

University of Ljubljana
Faculty of Mathematics and Physics
Department of Physics

Matej Pregelj

Magnetic Properties of Two-dimensional Systems of
Magnetic Clusters with Triangular Geometry

Doctoral thesis

Adviser: Assist. Prof. PhD. Denis Arčon

Ljubljana, 2010

III

Univerza v Ljubljani
Fakulteta za matematiko in fiziko
Oddelek za fiziko

Matej Pregelj

Magnetne lastnosti dvodimenzionalnih sistemov
magnetnih skupkov s trikotno geometrijo

Doktorska disertacija

Mentor:izr. prof. dr. Denis Arčon

Ljubljana, 2010

ACKNOWLEDGEMENT

I would first like to acknowledge the financial support of the Slovenian Ministry for Higher Education, Science and Technology through the Young Researcher educational program.

Second, I would like to thank my mentor, Denis Arčon for his continuous guidance, support and for being a true mentor in every respect. I would also like to thank Andrej Zorko for all the stimulating discussions and valuable hints, given during the process of making this Thesis. My thanks go also to Janez Dolinšek for giving me an opportunity to become a member of the Magnetic Resonance Group, as well as Robert Blinc and Igor Muševič, the former and current heads of the Solid State Physics department at “Jožef Stefan” Institute, Ljubljana, for accepting me in the department.

I would also like to express my sincere gratitude to Oksana Zaharko from Paul Scherrer Institute, Villigen, Switzerland, for introducing me to diffraction experiments, neutron as well as x-ray, teaching me how to interpret their results, as well as for our long-lasting collaboration in the field of magnetism in lower dimensions.

I am also grateful to Helmuth Berger from Ecole Polytechnique Federale de Lausanne, Lausanne, Switzerland, for growing beautiful single crystals and exceptionally pure powder samples used in this investigation.

I thank my co-workers Peter Jeglič and Tomaž Apih for introducing me to nuclear magnetic and quadrupolar resonance technique and help with the interpretation of the obtained data. My thanks go also to Tone Gradišek for help with the NQR experiment and Zdravko Kutnjak for performing the zero-field dielectric measurements and help with the setup for magnetic-field dependence.

I thank Matej Komelj from the Department for Nanostructured Materials at “Jožef Stefan” Institute for density functional calculations of the electric field gradients at Br sites.

Last but not least, I thank Zvonko Jagličić and Marko Jagodič from Institute of Mathematics, Physics and Mechanics, Ljubljana, for performing magnetic susceptibility and specific heat measurements and help with magnetic-field dependent dielectric measurements.

ABSTRACT

The impact of magnetic frustration on the magnetic ground state of two-dimensional systems of magnetic clusters with triangular geometry, as well as magnetic and electric properties of these systems is explored in this Thesis. The emphasis is on compounds, which include p -element cations that are in the oxidation state where they have lone pair electrons, in particular Te^{4+} in two recently synthesized $\text{FeTe}_2\text{O}_5\text{Br}$ and $\text{Ni}_5(\text{TeO}_3)_4\text{Br}_2$ systems. Both systems have layered monoclinic structures build of magnetic clusters composed of two triangles, i.e., edge sharing in iron while face sharing in nickel system.

Bulk magnetic response and magnetic transition temperatures were studied by low-field magnetic susceptibility and high-field magnetic torque and magnetization measurements. Low-temperature magnetic ground state and temperature dependence of the correlation length above the Néel transition were determined by neutron scattering experiments, while inelastic scattering was used to study spin waves. Temperature dependence of the spin correlation functions, magnetic anisotropies, exchange interactions, spin-gap and magnon spectra were investigated via local probe techniques, i.e., electron and nuclear magnetic, and nuclear quadrupolar resonance. Additionally, muon spin relaxation was measured to probe evolution of short- and long-range ordered phases. Finally, dielectric measurements were employed to study ferroelectric properties.

This way the magnetoelectric multiferroic state with coexisting electric polarization and incommensurate amplitude modulated magnetic structure has been discovered in the $\text{FeTe}_2\text{O}_5\text{Br}$ system. The explanation, derived using representation theory, is given by a novel mechanism based on exchange-striction involving sliding of the amplitude modulated magnetic waves, consequently inducing off-centre distortions of the superexchange bridging Te^{4+} ions and thus enforcing polarization of Te^{4+} lone pair electrons. Finally this results in macroscopic electric polarization, which can be suppressed when magnetic field of ~ 4 T is applied along the incommensurate direction. Just above the multiferroic phase, additional high-temperature incommensurate magnetic phase, showing no trace of ferroelectricity, was found. Moreover, short-range ordering effects persist far above the Néel temperature indicating strong magnetic frustration and low-dimensionality of the $\text{FeTe}_2\text{O}_5\text{Br}$ system.

On the other hand, magnetic ground state of the $\text{Ni}_5(\text{TeO}_3)_4\text{Br}_2$ system was found to be planar, with canted magnetic moments. It preserves the inversion symmetry of the crystal lattice and thereby excludes the possibility for macroscopic electric polarization. The relatively simple magnetic structure is ascribed to the fact that the magnetic anisotropies, determined from fits of antiferromagnetic resonance to the molecular field model and Kubo-Tomita theory, are strong, thus favouring long-range magnetic ordering over geometrical frustration. When magnetic field was applied perpendicular to the crystal layers, spin-flop like transition was observed at around ~ 11 T, which is according to the molecular field calculations followed by a second transition at ~ 24 T. The estimated high-field magnetic structure however breaks the inversion symmetry and thus open the possibility for ferroelectric order.

Keywords: low-dimensional, triangular topology, frustration, magnetoelectric, magneto-striction, phase diagram, spin flop, neutron diffraction, dielectric constant, magnetic resonance, quadrupolar resonance, magnetic anisotropy

PACS: 75.25.+z, 75.80.+q, 77.80.-e, 77.84.-s, 75.50.Ee, 81.30.Bx, 76.50.+g

POVZETEK

V tej disertaciji je predstavljen vpliv magnetne frustracije na osnovna magnetna stanja dvodimenzionalnih sistemov magnetnih skupkov s trikotno geometrijo, kakor tudi njihove magnetne in električne lastnosti. Poudarek je na spojinah, ki vsebujejo katione v oksidacijskem stanju, kjer imajo nevezne elektronske pare. Posvetili smo se predvsem Te^{4+} kationom v dveh nedavno sintetiziranih sistemih – $\text{FeTe}_2\text{O}_5\text{Br}$ in $\text{Ni}_5(\text{TeO}_3)_4\text{Br}_2$. Oba omenjena sistema imata plastoviti monoklinski strukturi zgrajeni iz magnetnih skupkov sestavljenih iz dveh trikotnikov, ki si v Fe sistemu delita celo stranico v Ni sistemu pa zgolj vogal.

Makroskopski magnetni odziv kot tudi temperature magnetnih prehodov smo preučevali z meritvami magnetne susceptibilnosti v nizkem magnetnem polju in meritvami magnetnega navora in magnetizacije v visokih poljih. Nizkotemperaturno osnovno magnetno stanje in temperaturno odvisnost magnetnih korelacij nad magnetnim prehodom smo določili z elastičnim nevtronskim sipanjem, medtem ko smo z meritvami neelastičnega sipanja raziskovali spinske valove. Temperaturno odvisnost spinskih korelacijskih funkcij, magnetnih anizotropij, izmenjalnih interakcij, spinske vrzeli in magnonskega spektra pa smo študirali z lokalnimi tehnikami, t.j. elektronsko in jedrsko magnetno ter jedrsko kvadrupolno resonanco. Dodatno smo za preučevanje razvoja magnetnega reda kratkega in dolgega dosega uporabili še muonsko spinsko relaksacijo. Na koncu smo opravili še dielektrične meritve, s katerimi smo spremljali feroelektrične lastnosti vzorcev

Na ta način smo v $\text{FeTe}_2\text{O}_5\text{Br}$ sistemu odkrili magnetoelektrično multiferroično stanje, kjer soobstajata električna polarizacija in inkomenzurabilni amplitudno moduliran magnetni red. Razlaga, izpeljana s pomočjo reprezentacijske analize, je podana z novim mehanizmom, ki temelji na izmenjalni-skrčitvi in vključuje drsenje amplitudno moduliranih magnetnih valov. Slednje privede do izven-centričnih deformacij superizmenjalnih mostov, ki vsebujejo Te^{4+} katione, in s tem vsili polarizacijo Te^{4+} neveznih elektronskih parov. Končni rezultat je makroskopska električna polarizacija, ki pa jo v polju ~ 4 T vzdolž inkomenzurabilne osi lahko izničimo. Tik nad multiferroično fazo smo opazili tudi visokotemperaturno inkomenzurabilno fazo, ki pa ne kaže feroelektričnih lastnosti. Dodatno smo opazili magnetne efekte reda kratkega dosega že visoko nad temperaturo magnetnega prehoda, kar odraža tako močno frustracijo kot tudi nizkodimenzionalnost $\text{FeTe}_2\text{O}_5\text{Br}$ sistema.

Po drugi strani so magnetni momenti v osnovnem stanju $\text{Ni}_5(\text{TeO}_3)_4\text{Br}_2$ sistema urejeni v ravnini, znotraj katere pa so različno zasukani. To stanje ohranja simetrijo inverzije kristalne mreže in s tem izniči možnost razvoja makroskopske električne polarizacije. Relativno preprosto magnetno strukturo pripisujemo dejstvu, da so magnetne anizotropije, določene na podlagi opisa antiferromagnetne resonance z modelom molekularnega polja in Kubo-Tomita teorije, močne in dajejo prednost magnetnemu redu dolgega dosega pred geometrijsko frustracijo. Ko smo dodali polje pravokotno na kristalne plasti, smo opazili blag spinski preskok pri ~ 11 T, temu pa naj bi po izračunih molekularnega polja sledil še drugi prehod pri ~ 24 T. Predvidena struktura te faze (v visokem polju) zlomi simetrijo inverzije in s tem odpre možnost za razvoj feroelektrične ureditve.

Ključne besede: nizkodimenzionalen, trikotna ureditev, frustracija, izmenjalna-skrčitev, fazni diagram, spinski preskok, nevtronsko sipanje, dielektrična konstanta, magnetna resonanca, kvadrupolna resonanca, magnetna anizotropija

Contents

1	Introduction.....	1
2	Theory.....	5
2.1	Origin of magnetism	5
2.1.1	Historical overview of research of magnetism.....	5
2.1.2	Microscopic theory of magnetism.....	5
2.1.3	Magnetic moments of transition metal ions.....	6
2.2	Spin Hamiltonian	7
2.2.1	Interactions with local environment	7
2.2.2	Interactions between magnetic moments	8
2.3	Order in magnetic materials.....	11
2.3.1	Antiferromagnetism	11
2.3.2	Incommensurate magnetic order.....	12
2.3.3	Frustration.....	13
2.4	Magnetic excitations	14
2.4.1	Antiferromagnetic resonance.....	15
2.5	Magnetoelectric coupling in frustrated magnetic systems.....	17
2.5.1	Ferroelectricity	17
2.5.2	Magnetoelectric multiferroics.....	18
2.5.3	Magnetoelectric coupling.....	20
3	Experimental	23
3.1	Magnetic resonance techniques	23
3.1.1	Electron spin resonance	24
3.1.2	Nuclear magnetic and quadrupolar resonance.....	28
3.2	Specific heat	34
3.2.1	Lattice heat capacity.....	34
3.2.2	Magnetic contributions to the heat capacity	35
3.2.3	Data acquisition.....	36
3.3	Magnetization measurements	36
3.3.1	Superconducting quantum interference device.....	37
3.3.2	Magnetic torque measurements.....	37
3.4	Magnetic neutron scattering.....	38
3.4.1	Neutron sources	38
3.4.2	Neutron detection	39
3.4.3	Neutron scattering cross sections	39

3.4.4	Polarisation analysis	43
3.4.5	Neutron scattering instruments	45
3.5	μ SR Spectroscopy	48
3.5.1	Production, life, and decay of the muon	48
3.5.2	Experimental geometries.....	50
3.5.3	Depolarization and relaxation functions	51
3.5.4	μ SR instruments	53
3.6	Dielectric measurements.....	54
3.7	Thermal expansion	54
3.8	X-ray single crystal diffraction	55
4	FeTe ₂ O ₅ Br system	57
4.1	Crystal Structure	57
4.2	Magnetic characterization of the paramagnetic state	60
4.2.1	Magnetic susceptibility	60
4.2.2	Electron spin resonance.....	63
4.2.3	Specific heat.....	66
4.3	Low-temperature magnetic ordering	67
4.3.1	Neutron scattering.....	67
4.3.2	μ^+ spin relaxation	70
4.3.3	Nuclear quadrupolar resonance	73
4.3.4	Summary of the magnetic ordering.....	79
4.4	Ferroelectric transition and its relation to magnetism.....	80
4.4.1	Thermal expansion measurements	80
4.4.2	X-ray diffraction experiments.....	80
4.4.3	Dielectric measurements.....	81
4.4.4	Theory of the magnetoelectric coupling	82
4.5	Phase diagram – measurements performed in applied magnetic field	85
4.5.1	Specific heat measurements.....	85
4.5.2	Magnetic susceptibility measurements in the applied magnetic field.....	86
4.5.3	Nuclear magnetic resonance	87
4.5.4	Neutron diffraction in the applied magnetic field.....	92
4.5.5	Thermal expansion in the applied magnetic field	95
4.5.6	Dielectric measurements in the applied magnetic field.....	95
4.5.7	Phase diagram – summary.....	96
4.6	Low-energy excitations.....	97

4.6.1	Inelastic neutron scattering.....	97
4.7	Summary and conclusion	99
5	$\text{Ni}_5(\text{TeO}_3)_4\text{Br}_2$	101
5.1	Crystal structure	101
5.2	Magnetic properties in zero and low magnetic field	103
5.2.1	Magnetization measurements in low magnetic fields	103
5.2.2	Neutron diffraction in zero-field	104
5.3	Measurements in the applied magnetic field	106
5.3.1	Heat capacity measurements.....	106
5.3.2	Magnetization and magnetic-torque measurements	108
5.4	Antiferromagnetic resonance.....	110
5.4.1	Temperature dependence.....	110
5.4.2	Frequency and field dependence	111
5.4.3	Angular dependence	112
5.5	Calculations and discussion.....	112
5.5.1	Magnetic ordering and anisotropies	112
5.5.2	The phase diagram	113
5.5.3	Molecular-field model	114
5.5.4	Calculations of the single-ion anisotropies	115
5.5.5	Calculations of the spin parameters.....	116
5.6	Summary and conclusion	119
6	Concluding remarks.....	121
7	Bibliography.....	123
8	Extended abstract in Slovene (Razširjen prevod v slovenščini).....	131
8.1	Uvod	131
8.2	$\text{FeTe}_2\text{O}_5\text{Br}$ sistem.....	133
8.2.1	Magnetne lastnosti paramagnetne faze	133
8.2.2	Nizkotemperaturna magnetno urejena faza	134
8.2.3	Ferroelektrični prehod in njegova povezava z magnetizmom	136
8.2.4	Fazni diagram – meritve narejene v zunanjem magnetnem polju.....	137
8.2.5	Povzetek	138
8.3	$\text{Ni}_5(\text{TeO}_3)_4\text{Br}_2$ sistem	139
8.3.1	Magnetne lastnosti v nizkih magnetnih poljih	139
8.3.2	Meritve v magnetnem polju.....	139
8.3.3	Meritve antiferromagnetne resonance.....	140

8.3.4	Izračuni.....	140
8.3.5	Povzetek.....	141
8.4	Končne ugotovitve.....	141

1 Introduction

In the last few decades, low-dimensional spin systems have been intensively studied, as they often exhibit novel unusual magnetic ground states, which can provoke new fascinating magnetic phenomena, e.g., spin liquid phases in Haldane chains (1), (2). This is even more pronounced, when competing spin-spin interactions are introduced, imposing so called magnetic frustration. In fact, magnetic frustration is believed to be strongly connected to the magnetic properties of the superconductivity in two-dimensional cuprates (3) and oxypnictides (4), strong magnetoelectric coupling in multiferroic materials (5), (6), (7), as well as an amazing degeneracy of the magnetic ground states, found in systems of spins arranged in Kagomé (8), (9), (10), Shastry-Sutherland (11), (12) and some other triangular patterns. For all these systems it is typical that because of their special arrangement of the magnetic moments – mostly triangular – or because of the competition between different magnetic interactions, all of the exchange interactions in the system cannot be satisfied simultaneously (13). The resulting magnetic frustration can lead to a strong degeneration of the ground state and thereby promote the role of the quantum fluctuations. On the other hand, such systems are extremely sensitive to perturbations, e.g., magnetic anisotropies of the Dzyaloshinski-Moriya and antisymmetric exchange interaction type, which can lift degeneration, open a gap in the excitation spectrum, suppress quantum fluctuations, and stabilize a long-range magnetically ordered state. As a result, physical realizations of frustrated low-dimensional magnetic systems are usually very complex and have intriguing magnetic properties. Therefore, knowledge about such systems significantly expands the asset of physical means, required to push forward the technological boundaries. However, since many of the encountered phenomena have not yet been completely understood, there is an intensive ongoing search for novel model systems, which will put the existing theories to the test.

Until recently, most magnetically frustrated physical systems were identified based on topological considerations from structural data bases, i.e., searching for so called geometrical frustration, while the attempts to systematically design novel systems via new synthesis concepts were surprisingly rare. However, during the past few years, novel synthesis approaches for finding new low-dimensional spin frustrated inorganic compounds has been developed. One of the synthesis strategies that has proved to be very successful, is the use of so-called lone pair cations. For lone pair cations it has already been demonstrated by Galy et al. (14) that the effective volume of the lone pair electrons is approximately the same as the volume of an O^{2-} ion. Consequently, these elements, when mixed with a transition metal in the presence of halogen ions, can be regarded as “chemical scissors” (15), used for reducing the number of the superexchange pathways between the magnetic ions and consequently prefer to form a low-dimensional structure.

The actual synthesis concept (16) is based on forming oxohalides involving *p*-element cations that are in the oxidation state where they have stereochemically active lone pair electrons (e.g., Te^{4+} , Se^{4+} , As^{3+} , and Sb^{3+}). The presence of stereochemically active lone pair electrons will allow for asymmetric or one-sided coordination around the lone pair cation. In addition also such a strong Lewis acid (e.g., Te^{4+}) preferably only forms bonds to oxygen while the transition metal cations bond to both oxygen and halides in an oxohalide environment. As a result, both the stereochemically active lone pair and the halide ions will function as terminating species opening up the structures and increase the possibilities for low-dimensional arrangements. This synthesis concept has been successfully applied in search for new compounds with reduced dimensionality in the arrangement of late transition metal cations, as several such compounds have been found; for example, $Cu_2Te_2O_5X_2$ ($X = Cl, Br$) (17), $CuSb_2O_3Br$ (18), and $Cu_4Te_5O_{12}Cl_4$ (19).

Remarkably, lone pair electrons were also found to be carriers of the electric polarization in the numerous ferroelectric materials, for instance Bi^{3+} in the $BiMnO_3$ (20). In fact, the general belief is that since lone pair

electrons are stereochemically active, they can be easily polarised and are thus considered as the primary driving force behind the off-centre structural distortions, essential for the formation of electric polarization in these materials. Thus they seem to be convenient candidates to induce both magnetic frustration as well as electric polarization, which might result in coupling between the magnetic and electric orders.

Practical realization of coexisting magnetic and ferroelectric order was found in so called multiferroic materials (21), (22), (23), (24), (25). In case of strong magnetoelectric coupling, ferroelectric polarisation can be switched by the magnetic field (5), (6) or *conversely* magnetic order can be controlled by the electric field (7), thus holding a great promise for future devices in the field of spintronics and data storage (26), (27). The observed behaviour was typically encountered in complex magnetic structures with broken inversion symmetry, i.e., in systems in which ferroelectric polarisation develops simultaneously with incommensurate spiral magnetic order (28). Actually, it is generally accepted that the spiral magnetic order, which removes a centre of inversion and thereby allowing the ferroelectric order, is essential for the occurrence of a nonlinear magnetoelectric effect in perovskite-type manganites $RMnO_3$ (29) (R -rare earth element) and in $Ni_3V_2O_8$ oxide (30). In spite of that, in the extensive search for novel magnetoelectric multiferroics, lone pair electrons have been typically considered solely as a source of electric polarization, and not as a tool for forming frustrated low-dimensional magnetic geometries, which might lead to complex magnetic structures with broken inversion symmetry. Magnetically frustrated materials possessing lone-pair electrons thus, in view of magnetoelectric coupling research, represent almost completely unexplored field.

The main question, which motivated the work presented in this thesis, is hence, what is the impact of magnetic frustration on the magnetic ground state of two-dimensional systems of magnetic clusters with triangular geometry, exploration of their magnetic and electric properties with the aim to understand how different degrees of freedom, such as spin, charge, or orbital, order and couple in reduced dimensions with topological frustration. During our research, we also paid attention to interesting new phenomena, which might be at some point applicable for a general use. Our investigation is dedicated to the systems containing the p -element cations that are in the oxidation state where they have stereochemically active lone pair electrons, in particular Te^{4+} . The presence of Te^{4+} lone pair electrons is responsible for reduced number of superexchange pathways between the magnetic ions and consequently leads to low-dimensional crystal structures. Additionally, we hope that the presence of lone pair electrons will promote the affinity of these systems to form off-centre crystal distortions, which might eventually lead to macroscopic electric polarization.

More precisely, the goal of this work is to explore the influence of Te^{4+} lone pair electrons in recently synthesized $FeTe_2O_5Br$ (31) and $Ni_5(TeO_3)_4Br_2$ (15) systems. These systems were derived according to the above presented synthesis concept, using Te^{4+} lone pair electrons as so called "chemical scissors". Both systems have a layered monoclinic structure build of magnetic clusters. In the first case, Fe^{3+} ($S = 5/2$) ions are coupled via oxygen bridges in geometrically frustrated $[Fe_4O_{16}]$ clusters. In the second case, however, the basic building blocks are $[Ni_5O_{17}Br_2]$ units, with Ni^{2+} ($S = 1$) being the magnetic ion. In both examples clusters consist of triangularly arranged magnetic ions, while the expected superexchange interaction is antiferromagnetic, as proposed in the first reports (31), (15) relying on the magnetic susceptibility measurements. Magnetic ordering is thus expected on different levels: within the clusters, within the layers, and finally three-dimensional magnetic order below 11 K and 29 K for $FeTe_2O_5Br$ (31) and $Ni_5(TeO_3)_4Br_2$ (15) respectively. Finally, we note that in $FeTe_2O_5Br$ system all superexchange interactions between Fe^{3+} ($S = 5/2$) ions involve Te^{4+} ions, having lone pair electrons, thus forming a potential bridge between magnetic and electric degrees of freedom.

Here we briefly summarize our main experimental findings. The most important result is that the $\text{FeTe}_2\text{O}_5\text{Br}$ system was found to be multiferroic, i.e., in this system at low temperatures macroscopic electric polarization is induced by the incommensurate amplitude modulated magnetic structure (32). The investigation of the crystal structure implies that the emergence of electric polarization is accompanied by the shift of the Te^{4+} lone pair electrons, corroborating with the hypothesis stating that electric polarization should result from off-centre distortions driven by lone pair electrons. The novel magnetoelectric coupling mechanism involving exchange-striction has been proposed, which is based on the sliding of the neighbouring incommensurate amplitude modulation waves, thereby breaking the inversion symmetry of the crystal lattice and thus opening the possibility for electric polarization. Further, we found that low-temperature multiferroic phase is actually preceded by another high-temperature incommensurate magnetic phase. Since in this phase no trace of ferroelectricity has been detected, we assume that inversion symmetry is still present. Moreover, when magnetic field is applied along the incommensurate direction, high-temperature phase vanishes around 4 T as well as electric polarization in the low-temperature phase (33), giving a direct proof of strong magnetoelectric coupling. In other words, we found that electric polarization in $\text{FeTe}_2\text{O}_5\text{Br}$ system can be shut down with the applied magnetic field, which is of great interest from a view of novel spintronic devices. The $\text{FeTe}_2\text{O}_5\text{Br}$ system thus represents a novel class of multiferroic compounds and expands strong magnetoelectric coupling, so far found only in helicoidal/spiral magnetic structures, also to amplitude modulated structures. This finding dramatically expands the number of candidates for room-temperature magnetoelectric effect, which is essential for large scale technological applications.

On the other hand, the investigation of the $\text{Ni}_5(\text{TeO}_3)_4\text{Br}_2$ system reveals that magnetic structure of this system is less complex and that it preserves the inversion symmetry of the crystal lattice. Hence the possibility of macroscopic polarization is excluded. Fits of the field and angular dependence of antiferromagnetic resonance to the molecular field model imply that lower level of magnetic frustration and consequently simpler magnetic structure are results of strong magnetic anisotropies. In addition, applied magnetic field, perpendicular to the crystal layers, was found to induce spin-flop like transition at around 11 T. Furthermore, according to the molecular field calculations, assuming the estimated magnetic anisotropies, another transition is predicted at ~ 24 T. The estimated magnetic structure of this phase, however, breaks the inversion symmetry, thus opening the possibility for ferroelectric order.

In short, our study is in agreement with working hypothesis, stating that low-dimensional magnetic systems might indeed develop complex magnetic structures and that lone pair electrons in such systems are likely to carry electric polarization. Thus it encourages us to pursue the search for interesting magnetic phenomena in the field of low-dimensional geometrically frustrated magnetic materials, possessing lone pair electrons.

2 Theory

2.1 Origin of magnetism

2.1.1 Historical overview of research of magnetism

Earliest reports about magnetism came from Aristotle, who attributed the first scientific discussion of magnetism to Thales (approximately 625 to 545 BC) (34). In China, the first mentioning of magnetism originates from fourth century BC (Book of the Devil Valley Master) (35). Concerning the actual use of magnetism, the ancient Chinese scientist Shen Kuo (1031-1095) was the first person to write about the magnetic needle compass, and by the 12th century the Chinese were known to use the lodestone compass for navigation. In 1269 Peter Peregrinus de Maricourt wrote the *Epistola de magnete*, the first extant treatise describing the properties of magnets, while in 1600 William Gilbert published his *De Magnete, Magneticisque Corporibus, et de Magno Magnete Tellure* (On the Magnet and Magnetic Bodies, and on the Great Magnet the Earth). In this work he concluded from his experiments that the Earth was itself magnetic and that this was the reason compasses pointed north.

An understanding of the relationship between electricity and magnetism began in 1819 with work by Hans Christian Oersted, a professor at the University of Copenhagen, who discovered that an electric current could influence a compass needle. This landmark experiment is today known as Oersted's Experiment. Several other experiments soon followed, with André-Marie Ampère, Carl Friedrich Gauss, Michael Faraday, and others finding further links between magnetism and electricity. James Clerk Maxwell synthesized and expanded these insights into Maxwell's equations, unifying electricity, magnetism, and optics into the field of electromagnetism. In 1905, Einstein used these laws as an initial condition in his theory of special relativity (36), requiring that the laws held true in all inertial reference frames.

Electromagnetism has continued to develop into the twentieth century, being incorporated into the more fundamental theories of gauge theory, quantum electrodynamics, electroweak theory, and finally the standard model. The microscopic theory of magnetism, on the other hand, had to wait for the advent of quantum mechanics in early twentieth century.

2.1.2 Microscopic theory of magnetism

Magnetism, at its root, arises from two sources. First, electric currents, or more generally moving electric charges, create magnetic fields. In classical electromagnetism, therefore, magnetic moment is described as a current loop. If there is a current I around area $|d\vec{S}|$ then the magnetic moment $d\vec{\mu}$ is given by (37)

$$d\vec{\mu} = I|d\vec{S}| \quad (2.1)$$

and the magnetic moment has the units of Am^2 . The length of the vector $d\vec{S}$ is equal to the area of the loop while its direction is normal to the loop and in a sense determined by the direction of the current around the loop. The second source lays within the elementary particles themselves, i.e., many particles have nonzero "intrinsic" (or "spin") magnetic moments, just as many particles, by their nature, have a certain charge.

In magnetic materials the most important source of magnetic phenomena are the electrons. More precisely, magnetism originates from their orbital angular motion around the nucleus (\vec{L}), as well as their intrinsic magnetic moment (\vec{S}). Together, these two contributions sum up into a magnetic moment

$$\vec{\mu} = \mu_B(\vec{L} + g_0\vec{S}). \quad (2.2)$$

Here $g_0 = 2.0023$ is the free-electron g -factor and $\mu_B = 9.274 \times 10^{-24} \text{ Am}^2$ is the Bohr magneton, defined as $e\hbar/2m_e$, where $e = -1.602 \times 10^{-19} \text{ As}$ is the electron charge, $\hbar = 1.055 \times 10^{-34} \text{ Js}$ is the Planck constant divided by 2π and $m_e = 9.109 \times 10^{-31} \text{ kg}$ is the electron mass. We note that the expression for $\vec{\mu}$ changes when magnetic ion is situated in some specific surrounding, for instance, a crystal lattice. The other potential sources of magnetism are much less important, for example, the nuclear magnetic moments of the nuclei in the material are typically thousands of times smaller than the electrons' magnetic moments.

Normally, the countless electrons in a material are arranged such that their magnetic moments (both orbital and intrinsic) cancel out. This is due, to some extent, to electrons combining into pairs with opposite intrinsic magnetic moments, as a result of the Pauli Exclusion Principle, or combining into "filled subshells" with zero net orbital motion. In both cases, the electron arrangement is such that it exactly cancels the magnetic moments from each electron. However, when d -orbitals (transition metal ions) or f -orbitals (rare-earth ions) are only partly filled, individual atoms can carry a non-zero magnetic moment.

2.1.3 Magnetic moments of transition metal ions

To understand the occurrence of the magnetic moment in transition metal ions, let us recall how d -orbitals are filled with electrons. It is very common that d -orbitals are divided into two classes: three t_{2g} orbitals, which point between x , y , and z axes (Figure 1a) and two e_g orbitals, which point along the axes (Figure 1b). In crystal, the degeneracy of d -orbitals will be removed by an electric field derived from neighbouring atoms – the so called crystal field (CF) (37).

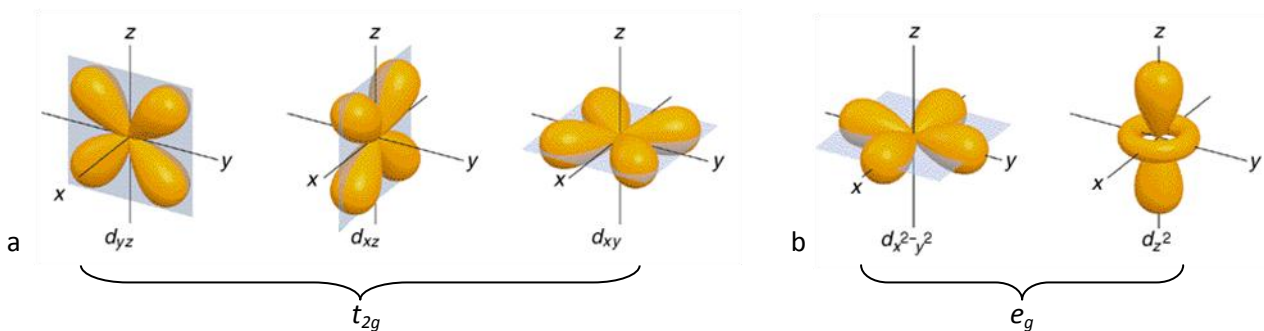


Figure 1: Five d -orbitals: (a) three t_{2g} and (b) two e_g orbitals.

Here are some basic concepts. Suppose that transition metal ion sits in octahedral environment surrounded by neighbouring ions with p -orbitals, aligned along the x , y , and z axes (oxygen for instance). The overlap with p -orbital will be different for t_{2g} and e_g orbitals as evident from Figure 2 (37).

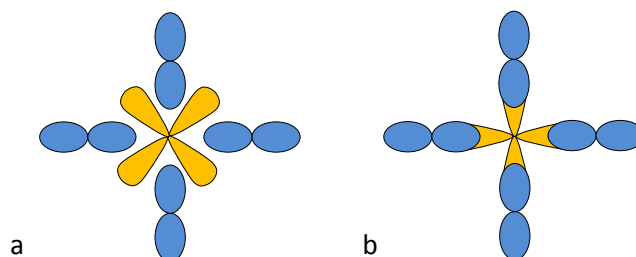


Figure 2: Overlap of the d -orbitals (orange) with the p -orbitals (green): (a) t_{2g} and (b) e_g orbitals.

Since the overlap is larger for e_g orbitals, the corresponding increase in the electrostatic energy will be larger compared to t_{2g} orbitals. As a result the fivefold degeneracy of d -orbitals is lifted by shifting t_{2g} orbitals to lower and e_g orbitals to higher energies (Figure 3a), i.e., the t_{2g} and e_g orbitals are split by the crystal field

splitting. Consequently the filling of the d -orbitals goes as follows. In case of a small CF splitting, the electrons simply obey Hund's rules, i.e., electrons will inhabit d -orbitals singly as far as possible (up to five). After that they will have to pair up – due to the Pauli exclusion principle only two electrons with the opposite spin can fill the same orbital (Figure 3b). The result is so called high-spin electronic configuration. On the other hand, if CF is strong, the splitting of the energy levels might be greater than the electronic repulsion. This results in the so called low-spin configuration. Now the electrons completely fill energetically favourable orbitals before they inhabit the less favourable ones (Figure 3c) (37).

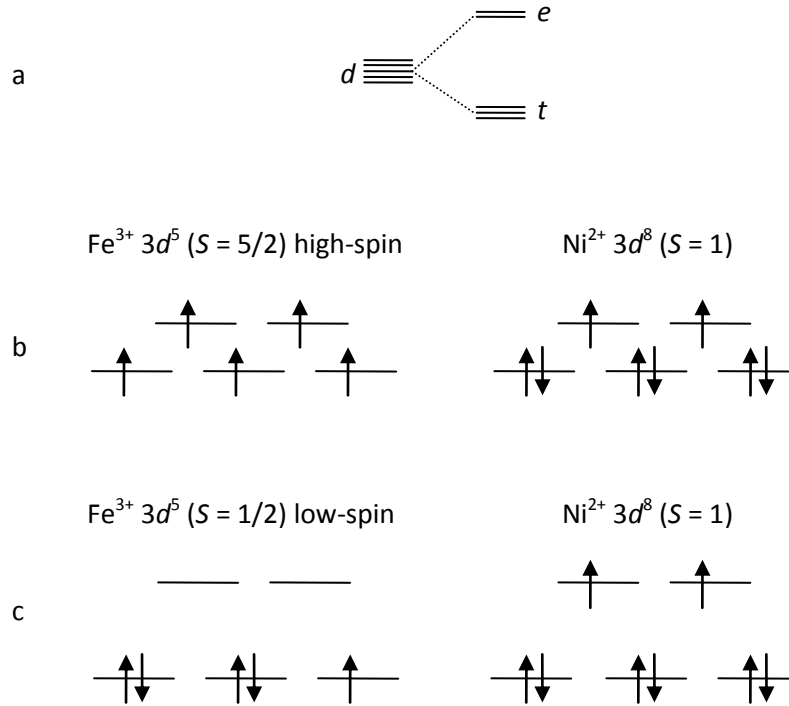


Figure 3: (a) Splitting of the energy levels of the d -orbitals in the octahedral environment and filling of the atomic d -orbitals in $\text{Fe}^{3+} 3d^5$ with 5 d -electrons and $\text{Ni}^{2+} 3d^8$ with 8 d -electrons: (b) high-spin configuration and (c) low-spin configuration. Please note that for Ni^{2+} , the crystal field splitting has no impact on electronic spin configuration.

For instance, Fe^{3+} with $3d^5$ electronic configuration can be switched by CF between high-spin $S = 5/2$ and low-spin $S = 1/2$ configuration (Figure 3b,c). In contrast, Ni^{2+} ion has eight $3d$ electrons and therefore its $S = 1$ spin configuration is independent of the CF.

2.2 Spin Hamiltonian

2.2.1 Interactions with local environment

As already explained above, magnetic ion, which interacts with its surroundings, is in a state different from a free-ion state. In transition metals the interaction of the paramagnetic ion with its diamagnetic neighbours (CF) competes with the direct electrostatic interaction and splits the degenerated energy levels of a given orbital momentum of the ion, \vec{L} , resulting in either high-spin or low-spin configuration. Moreover it often causes “quenching” of the expected values of this operator, $\langle \vec{L} \rangle = 0$ (38), which reduces the relative “size” of the spin-orbit (LS) coupling with respect to the crystal-field. Nevertheless, LS coupling written as $H_{LS} = \lambda \vec{L} \cdot \vec{S}$ for the states of orbital momentum, \vec{L} , and spin momentum, \vec{S} , (39) and the Zeeman energy, corresponding to the energy of the magnetic moment in the applied magnetic field \vec{B}_0 , $H_Z = \mu_B (g_0 \vec{S} + \vec{L}) \cdot \vec{B}_0$, can be considered as further perturbations. Here μ_B is the Bohr magneton, $g_0 = 2.0023$ is the free-electron g -factor

and λ is the LS coupling constant. As a result, we get the effective Hamiltonian, which has for a non-degenerate orbital ground state $|0\rangle$ split-off by the crystal field, the following form (40):

$$H_S = \sum_{\alpha,\beta} \mu_B g_0 B_\alpha (\delta_{\alpha,\beta} - \lambda \Lambda_{\alpha,\beta}) S_\beta - \lambda^2 S_\alpha \Lambda_{\alpha,\beta} S_\beta - \mu_B^2 B_\alpha \Lambda_{\alpha,\beta} B_\beta, \quad (2.3)$$

where α and β represent Cartesian components and the components of the tensor $\underline{\Lambda}$ are defined as

$$\Lambda_{\alpha,\beta} = \sum_n \frac{\langle 0|L_\alpha|n\rangle \langle 0|L_\beta|n\rangle}{E_n - E_0}. \quad (2.4)$$

Here the sum runs over all the excited states corresponding to a given shell. Since a spin wave-function is independent of an orbital wave function, \vec{S} is left as an operator in equation 2.3. While the fact that the last term does not involve any spin component, allows us to exclude it from the forthcoming analysis. The first term in equation 2.3 introduces the anisotropic g -factor tensor with components $g_{\alpha,\beta} = g_0(\delta_{\alpha,\beta} - \lambda \Lambda_{\alpha,\beta})$, which define the compact form of the Zeeman interaction

$$H_Z = \mu_B \vec{S} \cdot \underline{g} \cdot \vec{B}_0. \quad (2.5)$$

The second term is the origin of the single-ion anisotropy. It represents the anisotropy energy for the spin direction and can be written in the local frame, in which it takes a diagonal form, as

$$H_{cf} = D_{cf} S_z^2 + E_{cf} (S_x^2 - S_y^2). \quad (2.6)$$

The anisotropy parameters D_{cf} and E_{cf} are related to the principal values of the $\underline{\Lambda}$ -tensor as

$$D_{cf} = -\left(\Lambda_{zz} - \frac{1}{2}(\Lambda_{xx} + \Lambda_{yy})\right) \lambda^2, \quad (2.7)$$

$$E_{cf} = -\frac{1}{2}(\Lambda_{xx} - \Lambda_{yy}) \lambda^2. \quad (2.8)$$

As a result, the terms in the effective Hamiltonian, equations 2.5 and 2.6, lift the degeneracy and define the so-called fine structure in the energy levels of magnetic ion. It is worth mentioning that the single-ion anisotropy Hamiltonian has no effect on systems with $S = 1/2$, as they do not have a degenerated ground state.

In addition, the electrons are affected also by the interaction with the nuclear magnetic moments, which are approximately thousand times smaller than the electronic ones. Hence, in magnetically dense systems, this interaction is typically very small compared to the interactions with the external magnetic and crystal fields, associated with electron spin and the electrons' orbital angular momentum. Consequently this interaction is denoted as hyperfine interaction, resulting in energy shifts typically orders of magnitude smaller than the fine structure. In spite of a relatively weak effect of this electron-nuclear hyperfine interaction on the ionic energy levels, it can be very precisely determined from the nuclear magnetic resonance (NMR), as it will be presented latter in the Experimental section (page 28). Accordingly, detailed information about the electronic magnetic moments of the magnetic ions can be obtained from NMR.

2.2.2 Interactions between magnetic moments

Beside the interaction of the paramagnetic ion with its diamagnetic neighbours (CF) and nuclear magnetic moments, another type of interaction that a magnetic moment of the magnetic ion encounters in a crystal is an interaction with magnetic moments of other magnetic ions. Here we list the interactions, which can allow magnetic moments of magnetic ions in a solid to communicate and potentially evolve a long-range order.

2.2.2.1 Magnetic dipolar interaction

The most obvious interaction to consider is the magnetic dipole-dipole interaction. The magnetic dipoles $\vec{\mu}_1$ and $\vec{\mu}_2$ separated by \vec{r} have energy equal to:

$$E = \frac{\mu_0}{4\pi r^3} \left[\vec{\mu}_1 \cdot \vec{\mu}_2 - \frac{3}{r^2} (\vec{\mu}_1 \cdot \vec{r})(\vec{\mu}_2 \cdot \vec{r}) \right], \quad (2.9)$$

which depends on their separation as well as their mutual alignment. For instance the magnitude of this interaction for typical values encountered in solid magnetic materials, $\mu_i = 1\mu_B$ and $r = 1 \text{ \AA}$, is approximately $\mu_0\mu_B^2/4\pi r^3 \sim 10^{-23} \text{ J}$, which is equivalent to about 1 K in the temperature. Since lots of materials orders magnetically at much higher temperatures (some around 1000 K), the magnetic dipolar interaction is too weak to be considered as the leading interaction in most of the magnetic materials.

2.2.2.2 Exchange interaction

The main driving mechanism responsible for the occurrence of the long-range magnetic order is actually the exchange interaction. Even though exchange interaction is nothing more than electrostatic interaction, arising because charges of the same sign cost energy when they are close together and save energy when they are apart, one needs to use the tools of quantum mechanics to describe this phenomenon. The general idea is that the two electrons have to be either in symmetric or antisymmetric state in order to behave properly under the operation of particle exchange. For electrons the overall function must be antisymmetric hence the spin state can be either antisymmetric singlet ($S = 0$) in case of symmetric spatial state or symmetric triplet ($S = 1$) in case of antisymmetric spatial state. After some algebraic manipulation, it can be shown (37), (41) that the spin-dependent term of the effective exchange spin Hamiltonian is:

$$H = -2J\vec{S}_1 \cdot \vec{S}_2, \quad (2.10)$$

where J is the exchange coupling constant, which is actually half of the energy difference between singlet and triplet spin state. This equation is relatively simple to derive for two spins, but its generalization to a many body system is far from trivial. In spite of that, it is known that such interactions are active between all neighbouring spins, formally described with the Heisenberg Hamiltonian:

$$H = -2 \sum_{i>j} J_{ij} \vec{S}_i \cdot \vec{S}_j. \quad (2.11)$$

Here $i > j$ avoids the “double-counting”. Based on the sign of the J we distinguish between the ferromagnetic ($J > 0$) interactions, which tend to coalign the interacting moments, and antiferromagnetic ($J < 0$) interactions, favouring the oppositely aligned moments.

Although the exchange interaction between the two neighbouring magnetic atoms, so called direct exchange, seems the most obvious route for the exchange interaction to take, the reality in physical situations is rarely that simple. Very often the direct exchange is too weak to run the magnetic properties of the system, because of the insufficient overlap between the neighbouring magnetic orbitals. In rare earths, for instance, the $4f$ electrons are strongly localized and lie very close to the nucleus, with little probability density extending further than about a tenth of the interatomic spacing. Even in transition metals, such as Fe, Co, Ni, where the $3d$ orbitals extend further from the nucleus, it is extremely difficult to justify why direct exchange should lead to the observed magnetic properties.

In fact, the exchange mechanism which is responsible for the magnetic properties in majority of non-metallic magnetic solids is known as superexchange (42). It can be defined as an indirect exchange interaction between two non-neighbouring magnetic ions, which is mediated by a non-magnetic ion (ligand) between

them. It arises because there is a kinetic energy advantage for antiferromagnetism, i.e., the antiferromagnetic coupling lowers the energy of the system by allowing the electrons to become delocalized over the whole magnetic structure, thus lowering the kinetic energy.

Finally we list the Goodenough-Kanamori-Anderson (GKA) rules, which are a set of guidelines for estimating the sign and relative magnitudes of superexchange interactions (42), (43), (44), and can be summarised as follows:

1. Generally interactions in magnetic oxides will be antiferromagnetic.
2. The exchange between e_g electrons on different ions connected by a 180° bond is stronger than that between the t_{2g} electrons.
3. A small ferromagnetic coupling can occur for interaction between t_{2g} electrons separated by a 90° bond, or by e_g and t_{2g} electrons separated by a 180° bond.
4. Completely filled shells with an equal number of up and down spins do not contribute to the superexchange interaction.

These rules were experimentally verified for many transition metal oxide compounds (41), (45).

2.2.2.3 Higher order exchange interaction contributions

Sometimes, in addition to the isotropic part of the exchange interaction, anisotropic as well as antisymmetric parts need to be taken into the account. These are on the other hand determined by relativistic effects, i.e., by the admixture of the excited into the ground state by spin-orbit coupling. We note that in case of transition metal ions, spin-orbit coupling can be treated as a perturbation (due to the “quenching” of L).

In the first order perturbation one can derive the antisymmetric anisotropic exchange interaction, so-called Dzyaloshinsky- Moriya (DM) interaction, which takes the form

$$H_{DM} = \sum_{i,j} \vec{D}_{ij} \cdot (\vec{S}_i \times \vec{S}_j). \quad (2.12)$$

Such antisymmetric form of the spin interaction was first suggested by Dzyaloshinsky, purely from the symmetry arguments, to account for the phenomenon of the occurrence of weak ferromagnetism (46). A microscopic derivation of this interaction was later given by Moriya (47) together with the symmetry restraints that the Dzyaloshinsky-Moriya vectors \vec{D}_{ij} must obey. The symmetry arguments are based on the crystal space group symmetry, i.e., considering that two ions 1 and 2 located at points A and B , respectively, and the point bisecting the straight line AB is denoted by C , the following rules are obtained (47):

1. When a centre of inversion is located at C , $\vec{D}_{ij} = 0$.
2. When a mirror plane perpendicular to AB passes thorough C , $\vec{D}_{ij} \parallel$ mirror plane or $\vec{D}_{ij} \perp AB$.
3. When there is a mirror plane including A and B , $\vec{D}_{ij} \perp$ mirror plane.
4. When a two-fold rotation axis perpendicular to AB passes through C , $\vec{D}_{ij} \perp$ two-fold axis.
5. When there is an n -fold axis ($n > 1$) along AB , $\vec{D}_{ij} \parallel AB$.

In short, these rules are often summarized as (12), (48)

$$\vec{D}_{12} \propto \sum_i \vec{n}_{1i} \times \vec{n}_{i2}, \quad (2.13)$$

where \vec{n}_{1l_i} is a normalized vector connecting the magnetic moment on site 1 with the ion l_i , \vec{n}_{l_i2} is a normalized vector connecting the ion l_i with the magnetic moment on site 2, and i runs over all bridging ions.

Further, the result of the second order perturbation calculation is the symmetric anisotropic exchange. In its principal frame this interaction can be written as

$$H_{aniso} = \sum_{i,j} d_{ij} S_i^z S_j^z + e_{ij} (S_i^x S_j^x - S_i^y S_j^y). \quad (2.14)$$

This interaction is also called the pseudo-dipolar interaction because of the formal similarity of its form with the dipolar interaction.

The size of the two anisotropic terms can be estimated as $|\vec{D}_{ij}| \sim (\Delta g/g) \cdot J_{eg}$ and $d \sim (\Delta g/g)^2 \cdot J_{eg}$, where Δg accounts for the g -shift from the free electron value. Here the J_{eg} is not the simple exchange integral between the ground state of the two interacting ions, J , considered in the isotropic part of the exchange interaction, but is rather the exchange interaction with the excited state (41), (40). Hence the assumption $J_{eg} \sim J$, giving a simple estimation for D and d is valid only in case of orbitally nondegenerate ground states, e.g., in Mn^{2+} , Gd^{3+} or organic radicals, for which Δg is almost exactly 0. On the other hand, for systems with degenerated states (with significant $\Delta g/g$) J_{eg} interaction can be completely different from J , i.e., it can have different sign and different intensity. For this reason estimations for D and d have to be made with extreme circumspection. Furthermore, the estimation of the size of the DM vectors suffers a further faultiness. Namely, as already stressed, it critically depends on the local symmetry. For instance, if there is a centre of inversion present in the midpoint of two coupled spins the DM interaction will be identically equal to zero.

2.3 Order in magnetic materials

The above presented interactions can effectively produce strong internal magnetic fields, leading to a particular type of magnetic ordering below certain temperatures. Considering only the leading exchange or superexchange interactions, the simplest magnetic order is so called ferromagnetic one, where all magnetic moments in the system are parallel due to the positive sign of J . However, already when $J < 0$ is considered, far more complicated magnetic orders can be anticipated, depending on the spatial arrangement of the magnetic moments; and one can imagine what happens when additional terms in spin Hamiltonian are realized. In other words, the magnetic structure is defined by the geometrical arrangement of the magnetic ions as well as the type of the interactions between the magnetic moments. We note that second order phase transitions are always associated with the reduction of symmetry; thereby magnetic ordering is to some extent defined by the symmetry of the paramagnetic state.

2.3.1 Antiferromagnetism

If the exchange J is negative the simplest possible ordering is the two sublattice antiferromagnetic structure. Such a state is considered as two interpreting sublattices, on one of which the magnetic moments point up and down on the other. The nearest neighbours of each magnetic moment will then be entirely on the other sublattice.

Let us now consider the effect of strong magnetic field on antiferromagnet, with $T = 0$ to avoid any complications from thermal fluctuations. If the magnetic field is large enough, it must eventually dominate over any internal molecular field and force all the magnetic moments to lie parallel to each other. However, as the field is increased, although the final result is clear, the route to that state depends strongly on the direction of the applied field with respect to the initial orientation of the sublattice magnetization, so-called easy axis. This orientation is determined by the single-ion anisotropy imposed by the crystal field, which

causes that magnetic susceptibility is different if we apply the field parallel or perpendicular to the easy axis. In the latter case the magnetic moments are being turned in the direction of the field (Figure 4a); beyond certain field B_{C1} all the moments point in the direction of the applied field. On the other hand, if the applied field is parallel to the magnetic moments, they do not turn until the applied field exceeds critical value B_{SF} (Figure 4b), determined by the strength of the crystal field and the exchange interaction. At that point magnetic moments snap into different configuration (Figure 4b); this phenomenon is called spin-flop transition. Beyond this point the magnetic moments are being turned in the direction of the field, up to $B_{C2} > B_{SF}$, when all the spins are aligned along the external field.

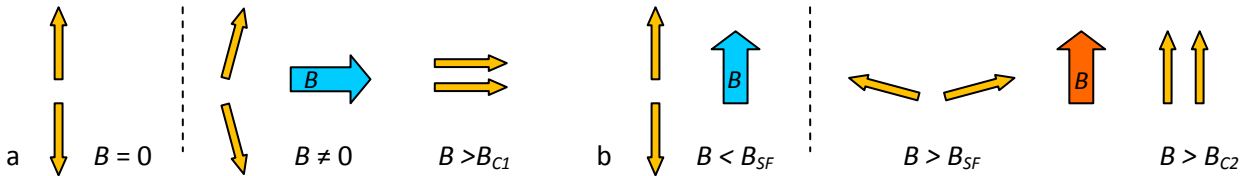


Figure 4: Magnetic moments in antiferromagnet: (a) external field perpendicular to the easy axis, (b) external field parallel to the easy axis.

In contrast to ferromagnet, antiferromagnets have often more feasible magnetic ground state configurations, where the number of possibilities strongly depends on the crystal lattice (Figure 5). In other words, the actual magnetic ordering is strongly defined by the spatial arrangement of the magnetic ions. In extreme, one can even imagine a geometry, where exists a competition between the magnetic interactions. So, in case when all of the interactions cannot be simultaneously satisfied, frustration is a plausible result. This might lead to far more complex magnetic structures, with canted as well as amplitude modulated magnetic moments.

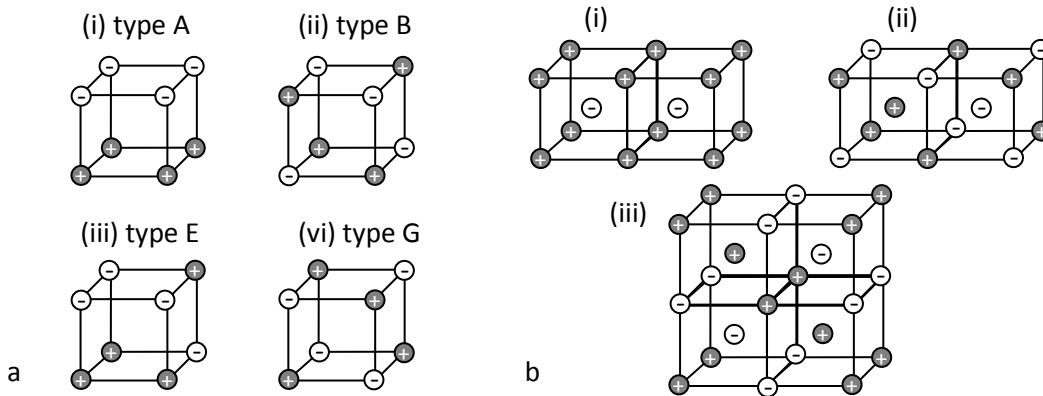


Figure 5: (a) Four types of antiferromagnetic order, which can occur on simple cubic lattice. The two possible spin states are marked + and -. (b) Three types of the antiferromagnetic order, which can occur on body-centred cubic lattice.

2.3.2 Incommensurate magnetic order

On the other hand, complex magnetic structures can be also realized, when magnetic interactions of different sign are assumed. The resulting competition between the magnetic interactions leads to frustration of the magnetic moments, since all the interactions cannot be satisfied at the same time. Nevertheless, the magnetic moments will try to order in a manner that will minimize the system's magnetic energy, which often drives the system into an incommensurate magnetic state. For instance, let us consider a simple one-dimensional chain, where J_1 indicates the exchange interaction between the nearest-neighbouring magnetic moments and J_2 is the interaction between the next-nearest-neighbours (Figure 6a). If the exchange interaction is isotropic, the energy of the system can be written as

$$E = -2S^2(J_1 \cos \vartheta + J_2 \cos 2\vartheta), \quad (2.15)$$

where ϑ is the angle between the neighbouring magnetic moments along the chain and S is the spin operator. The energy is minimized when $\partial E / \partial \vartheta = 0$, which yields

$$(J_1 + 4J_2 \cos \vartheta) \sin \vartheta = 0. \quad (2.16)$$

Solutions for this are either $\sin \vartheta = 0$, which implies $\vartheta = 0$ or $\vartheta = \pi$ (ferromagnet or antiferromagnet), or

$$\cos \vartheta = -J_1/4J_2. \quad (2.17)$$

Obviously this solution corresponds to helical/spiral magnetic ordering and is favoured over either ferromagnetism or antiferromagnetism when $J_2 < 0$ and $|J_1| < 4|J_2|$ (Figure 6b). In general, the pitch of the spiral is arbitrary, i.e., it is not necessary commensurate with the lattice parameter, and hence in case of incommensurate modulation along the so called “magnetic wave vector” \vec{q} (Figure 6) no two magnetic moments in a chain will have exactly the same spin orientation.

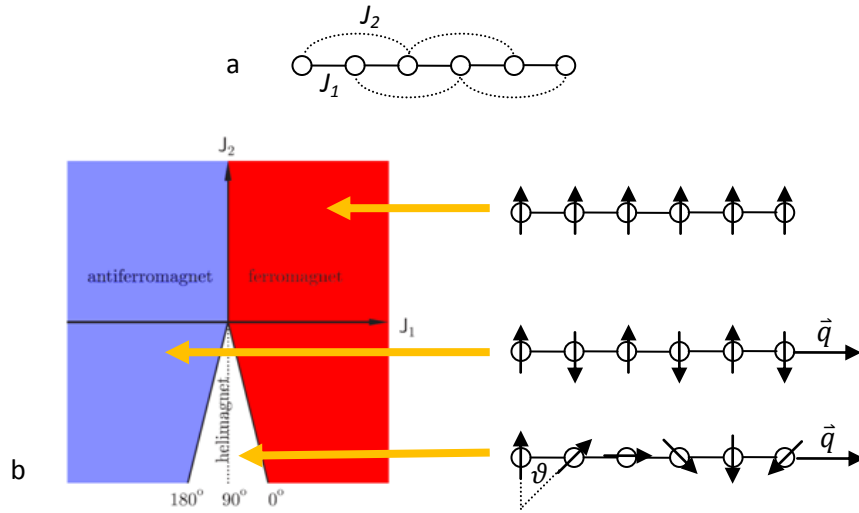


Figure 6: (a) A simple one-dimensional chain, where J_1 indicates the exchange interaction between the nearest-neighbouring magnetic moments and J_2 is the interaction between the next-nearest-neighbours. (b) The phase diagram for this model (37) and corresponding magnetic orders.

We note that competing exchange interactions can produce also incommensurate amplitude modulated magnetic structures, where amplitude of the magnetic moments is altered instead of their orientation. In such arrangements so called spin waves are observed, where at particular points in the crystal magnetic moments are completely suppressed while at some they are fully developed. Such magnetic ordering was found in several rare-earth manganites, for instance TbMnO_3 (49), ErMn_2O_5 and TbMn_2O_5 , (50), and Er_3Sn_3 (51).

2.3.3 Frustration

As already implied, ordinary two sublattice antiferromagnetic ordering is being altered in so called geometrically frustrated antiferromagnetic materials. In such compounds the magnetic interactions between spins are frustrated by their geometric arrangement in the crystal lattice. In other words, a magnetic system of classical or quantum spins is frustrated when all interactions among the spin pairs cannot have simultaneously their optimal values. Typical for these systems is that they remain magnetically disordered even when cooled well below the ordering temperature, naively expected from the strength of pairwise interaction. On the other hand, in such systems, short-range magnetic correlations often persist far above the long-range ordering temperature, forming small islands of magnetically ordered regions. Typical

geometrically frustrated systems are so-called spin glasses (52), where magnetic moments are randomly distributed through the whole crystal matrix.

The simplest example of a frustrated system is when three spins are mutually antiferromagnetically coupled: once two spins orient in the opposite directions the third one cannot be antiparallel to both of them (Figure 7) and thus at least one antiferromagnetic interaction is unsatisfied. It is also obvious that system is degenerated, which makes the system's ground state very sensitive to thermal fluctuations. For this reason, long-range magnetic ordering occurs at lower temperature, as in non frustrated magnetic arrangement.

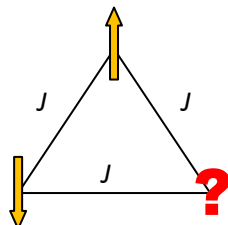


Figure 7: Frustration in three spin system.

Now imagine spins lying on a triangular lattice (Figure 8a). What will be the ground state of such a system? The answer is far from being trivial, since there are a variety of different spin configurations, with minimal energy, which cannot satisfy all the pairwise interactions simultaneously. The consequence is that the system does not exhibit long-range magnetic ordering, as expected from the strength of the exchange interactions. The tendency of a system to minimize its entropy makes frustrated systems very sensitive to perturbations, i.e. all the anisotropic interactions become more pronounced. Consequently crystal field anisotropy, dipolar interactions, deviations from scalar Heisenberg exchange, further-neighbour exchange, and impurities or inhomogenities can all transform the favoured ground states and shift the spectral weight of excitations.

The concept of frustration can be extended to other geometries as well. Beside triangular lattice (Figure 8a), frustration is also encountered in so called Kagomé lattice (Figure 8b), in ordinary square lattice, when the diagonal interactions are present and in certain 3D geometries (Figure 8c,d,e). The frustration can be brought in to the system also with the competition between the nearest and next-nearest neighbours, as suggested above for a case of one-dimensional chain with next-nearest neighbour interactions (Figure 6).

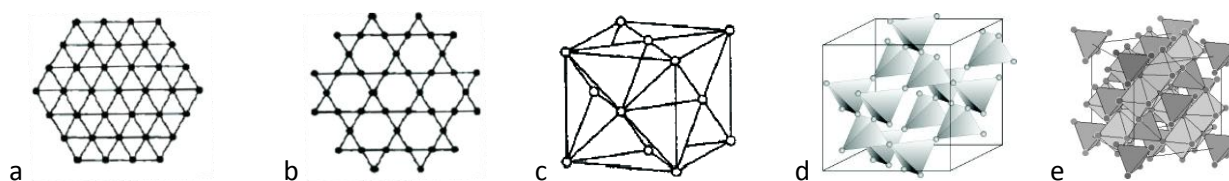


Figure 8: Frustrated 2D geometries: (a) triangular, (b) Kagomé and frustrated 3D geometries: (c) fcc cubic, (d) pyrochlore, (e) spinel

Unfortunately real systems, which correspond to any of these theoretical geometries, are very rare or they are limited to a certain building block of a compound, e.g., part of the unit cell.

2.4 Magnetic excitations

In this section we focus on the low-energy magnetic excitations encountered in the magnetically ordered systems. At $T = 0$, the physical systems are typically considered as static (even though in systems with degenerate or nearly degenerate ground states quantum fluctuations are likely to occur). However, with increasing temperature the order is disturbed by thermally excited excitations, e.g., excitations from magnetic ground state into a higher energy magnetic state, quantized as magnons. Such excitations are

typically characterized by a dispersion relation, i.e., a relationship between angular frequency ω and wave vector \vec{q} (equivalently between energy $\hbar\omega$ and momentum $\hbar\vec{q}$). The crucial feature of the dispersion relation is that $\omega = 0$ at $\vec{q} = 0$ and hence excitation of such a mode (so called ‘‘acoustic mode’’) does not cost any energy when the wavelength $\lambda = 2\pi/q$ is long enough, i.e., there is no energy gap to leap across from the ground state of the system ($\omega = 0$, $\vec{q} = 0$) to the lowest excited state. Whenever you have broken a continuous global symmetry (as you do when you make a solid from a liquid or a ferromagnet from a paramagnet) it is possible to produce long-wavelength excitations in order parameter (typically magnetization in magnetically ordered system) for vanishingly small energy cost, so called Goldstone modes.

For instance, the Goldstone modes of a ferromagnet are called spin waves. These are waves of precession of the magnetic moments. We note however, that in spite of the fact that in a simple isotropic ferromagnet the energy gap in the dispersion relation at $\vec{q} = 0$ is zero, the situation changes when anisotropic or antiferromagnetic interactions are considered.

2.4.1 Antiferromagnetic resonance

Here we present a simple molecular field approach to magnetic excitation spectrum in the antiferromagnet, which is measured as antiferromagnetic resonance (AFMR). The basic advantage of the molecular field theory is that it does not treat each spin in the physical system (where there is typically $\sim 10^{20}$ spins) and interaction with its neighbours individually, but it rather groups spins into sublattices (in the simplest case 2), and only then the interaction between these two is considered. This way, calculations of the AFMR become tractable and even relatively easy to solve. However this comes with a cost of losing all detailed information about the interactions between the spins in the individual sublattice and the difference in their local environments.

Let us now assume the magnetic structure, which can be described by a two oppositely aligned magnetic sublattices, so that the nearest neighbours of each magnetic moment are entirely on the other sublattice, and a simple uniaxial anisotropy. Hence the spin Hamiltonian in the applied magnetic field is:

$$H = 2 \sum_{i>j} J_{ij} \vec{S}_i \cdot \vec{S}_j + \mu_B g \vec{B}_0 \cdot \sum_i \vec{S}_i + D_{cf} \sum_i S_{iz}^2, \quad (2.18)$$

where indices i and j runs over all the spins in the system, J_{ij} is the antiferromagnetic exchange between the nearest-neighbouring spins, D_{cf} is the crystal field anisotropy constant, and \vec{B}_0 is the applied magnetic field. On the other hand, the expression for the free energy F states that $e^{-F/k_B T} = \sum_n e^{-E_n(B)/k_B T}$, where k_B is the Boltzmann constant and the sum runs over the n possible states with the energy $E_n(B)$ depending on the magnetic field B . Assuming, that at $T = 0$ K the system is in its ground state, we can write

$$F = 2 \sum_{i>j} J_{ij} \vec{S}_i \cdot \vec{S}_j + \mu_B g \vec{B}_0 \cdot \sum_i \vec{S}_i + D_{cf} \sum_i S_{iz}^2. \quad (2.19)$$

Further, assuming that magnetic moments within the same sublattice have the same orientation, resulting in a net-average sublattice magnetization $\vec{M}_l = -Ng\mu_B \sum_k \vec{S}_k$, where, l denotes the sublattice and k runs over the N magnetic ions in l -th sublattice, we obtain the following expression for the magnetic free energy:

$$F = 2A \vec{M}_1 \cdot \vec{M}_2 + \vec{B}_0 \cdot \sum_l \vec{M}_l + \sum_l K_l M_{lz}^2, \quad (2.20)$$

where $A = 2zJ/(g\mu_B)^2$, and $K_l = 2D_{cf}/(g\mu_B)^2$.

Based on the obtained expression for the magnetic free energy and knowing the magnetic structure of the system, i.e., magnitudes and orientations for \vec{M}_l , we can calculate the molecular field $\vec{H}_l = \partial F / \partial \vec{M}_l$ acting on the sublattice magnetization \vec{M}_l and solve the equations of motion:

$$\frac{d\vec{M}_l}{dt} = \gamma(\vec{M}_l \times \vec{H}_l). \quad (2.21)$$

Assuming that the time dependent part of magnetization oscillates as $e^{i\omega t}$, the resonant frequencies are simply the eigenvalues of the matrix, with $3l \times 3l$ elements (equation 2.21) (for each sublattice magnetization there are three spatial coordinates). In order to make calculations manageable we make the following approximations (53), (54). We assume that the deviations of each magnetization from the equilibrium value are small; hence we keep only the components, perpendicular to it. Consequently we can write each sublattice magnetization as $\vec{M}_l = \vec{M}_{0l} + \vec{m}_l(t)$, where \vec{M}_{0l} represents the equilibrium orientation and $\vec{m}_l(t) = \vec{m}_l e^{i\omega t}$ the oscillating part, perpendicular to it. The next step is to tailor the \vec{H}_l field according to the former assumption. Hence the molecular field acting on the sublattice magnetization $\vec{M}_l(t)$ can be written as $\vec{H}_l(t) = \vec{H}_{0l}(\vec{M}_{0l}) + d\vec{H}_l(\vec{m}_l(t))$. As a result equation 2.21 can be rewritten as:

$$\begin{aligned} \frac{d\vec{m}_l}{dt} &= \gamma[(\vec{M}_{0l} + \vec{m}_l) \times (\vec{H}_{0l} + d\vec{H}_l)] \\ &= \gamma[(\vec{M}_{0l} \times \vec{H}_{0l}) + (\vec{M}_{0l} \times d\vec{H}_l) + (\vec{m}_l \times \vec{H}_{0l}) + (\vec{m}_l \times d\vec{H}_l)]. \end{aligned} \quad (2.22)$$

The first term on the right is equal to zero, since the equilibrium orientation of l -th magnetization is perpendicular to molecular field acting on it. In sense of the molecular field theory we also neglect the last term as it oscillates with an angular frequency 2ω and we expect it to be small compared to the other contributions. What we achieved is that oscillating part of each sublattice magnetization is linearly dependent on the oscillating parts of the remaining sublattice magnetizations. On top of that, the oscillating part of each sublattice magnetization is perpendicular to its equilibrium orientation, so we can describe it only with two components instead of three. The result is that we are able to reduce $3n$ nonlinear equations to set of $2n$ linear equations, which can be solved for a reasonable number of sublattice magnetizations.

By using this asset of equations and mathematical tools, the leading terms of the spin Hamiltonian of a particular system can be determined. For instance, the crystal field anisotropy, resulting in the single-ion anisotropy, the Dzyaloshinski-Moriya interaction, or similar terms in the effective Hamiltonian, usually introduces a gap in the magnon spectra. The properties of the gap can be explored by studying the field dependence of the electron spin resonance. In case we are dealing with a single crystal, the nature of the spin-lattice coupling can be further studied by applying the field in different crystallographic directions.

As an example we write here the resulting resonant frequencies for our two-sublattice model with uniaxial single-ion anisotropy (55), (56):

$$\omega(B) = \omega(0) \pm \gamma B. \quad (2.23)$$

In equation 2.23 $\omega(0) = \gamma \sqrt{B_A(B_A + B_E)}$, where B_A is the magnetic anisotropy field and B_E is the exchange field, corresponding to the single-ion anisotropy $D_{cf}(E_{cf})$ (equations 2.7 and 2.8) and the exchange interaction J , respectively. We stress that zero field degeneracy can be removed by Dzyaloshinsky- Moriya or additional competing exchange interactions.

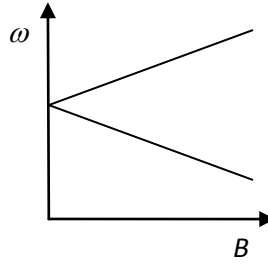


Figure 9: Frequency dependence of the resonant frequencies for two-sublattice model with uniaxial single-ion anisotropy described by equation 2.23.

In practice it has been shown that in addition to the antiferromagnetic resonance one needs to make a number of additional experiments in order to get enough data to determine numerous free parameters. One of the most important additional experiments is neutron scattering. This technique gives detailed information about the equilibrium spin arrangement. However, since this method is time-consuming, the measurements are usually made only in zero-field. Therefore, magnetization measurements in external field are indispensable, as they provide information about possible spin-flop transitions and orientations of the easy, hard and intermediate directions, when also angular dependence is performed.

2.5 Magnetolectric coupling in frustrated magnetic systems

Very interesting and attractive phenomenon encountered in magnetically frustrated materials is the magnetolectric (ME) coupling. In principle, the ME coupling is a rather rare phenomenon, which is typically very weak. However, strong ME coupling was found in systems with cycloidal or transverse conical structures (28), which are often a consequence of magnetic frustration, e.g., in the ME multiferroic TbMnO_3 . Hence, the discovery of spin-driven ferroelectricity in this compound in 2003 (5) has ignited extensive research activities focused on the ferroelectric properties of frustrated magnetic systems.

2.5.1 Ferroelectricity

In order to understand magnetolectric coupling, one should first know why the electric polarization in ferroelectric state develops at all. According to the formal definition, a ferroelectric material is one that undergoes a phase transition from a high-temperature phase that behaves as an ordinary dielectric (so that an applied electric field induces an electric polarization, which goes to zero when the field is removed) to a low-temperature phase that has a spontaneous electric polarization, whose direction can be switched by an applied field. Comparison with the ferromagnets reveals that they have many analogous properties, with the electric polarization, \vec{P} , corresponding to the magnetization, \vec{M} ; the electric field, \vec{E} , corresponding to the magnetic field, \vec{H} ; and the electric displacement, \vec{D} , corresponding to the magnetic flux density, \vec{B} .

The origin of the ferroelectricity lies within the fact that any lattice of oppositely signed point charges is inherently unstable (21). However, the short-range repulsions between adjacent electron clouds can stabilize the electronic structure, as in case of ionic materials. The existence or absence of ferroelectricity is hence determined by a balance between these short-range repulsions, which favour the nonferroelectric symmetric structure, and additional bonding considerations, which might stabilize the ferroelectric phase. Here one can see the resemblance to the establishment of the magnetic order in frustrated magnetic materials, where long-range ordering is also achieved through a competition between the opposing magnetic interactions. Similarly, in ferroelectric compounds the short-range repulsions dominate at high temperature, resulting in the symmetric unpolarized state. As the temperature is decreased, the stabilizing forces, associated with the polarization of the ions as they are displaced, become stronger than the short-range repulsive ion-ion interactions, and the polarized state becomes stable even in the absence of an

applied field. In short, in order to ensure the stability of ferroelectric order, the system should exhibit an antisymmetric spatial distortion, i.e., the spatial inversion symmetry has to be broken.

The most widely studied ferroelectrics are perovskite-structure oxides, ABO_3 , which have the prototypical cubic structure shown in Figure 10a. The cubic perovskite structure is characterized by a small cation, B , at the centre of an octahedron of oxygen anions, with large cations, A , at the unit cell corners. According to Hill (21) a simple phenomenological explanation of the ferroelectricity for a typical ferroelectric perovskite oxide consists of two complementary phenomenological models. The small B cation in ferroelectric perovskite oxides should always be able to lower its energy by shifting along one of the (111) directions (unless strain in the lattice stabilizes a different displacement). This leads to the characteristic “double-well” potential energy for the position of the small cation as a function of position between the oxygen anions, C , as shown in Figure 10b. At high temperatures, away from the phase transition temperature, the order-disorder model is applicable, which states that the B cations are always displaced along one of the cube diagonals, i.e., displacements along all possible (111) directions are allowed. At low temperatures the soft-mode model should be applied, stating that the B cation displacement is stable only at low temperatures. Above the Curie temperature, there is a restoring force that tends to push the B cation back to the centre. As the temperature is reduced, the phonon associated with this restoring force (the so-called “soft-mode” phonon) becomes weaker, until at the Curie temperature its frequency is zero and the displacement occurs spontaneously.

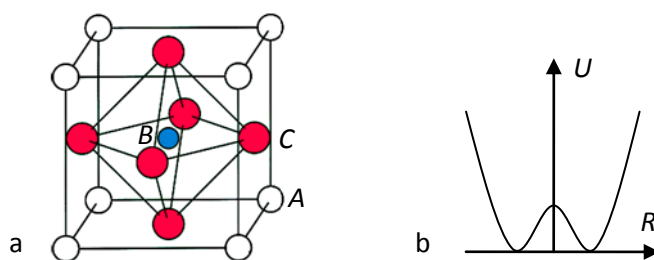


Figure 10: (a) Cubic perovskite structure. The small B cation (in blue) is at the centre of an octahedron of C oxygen anions (in red). The large A cations (white) occupy the unit cell corners. (b) Characteristic double-well potential energy U as a function of the position of the B cation between the oxygen anions in perovskite ferroelectrics R .

A significant observation is that most perovskite ferroelectrics contain B ion in a d^0 state (for instance Ti^{4+} in the $ATiO_3$). The role of lone pair electrons of the ions in the d^0 state in the perovskite ferroelectrics was extensively studied by the density functional theory (DFT) with the local density approximation (LDA) (20). The calculations indicate that the lone pair electrons are stereochemically active, i.e., are easily polarisable, and are the primary driving force behind the structural distortions essential for the formation of electric polarization in these materials. At high temperatures, the lone pair electrons are more or less symmetrically distributed around the d^0 , whereas below the ferroelectric transition the lowest unoccupied energy levels - d states - hybridize with O $2p$ ions, which results in a lobe-like asymmetric distribution of the lone pair electrons. Moreover, calculations reveal that all lone pair electrons shift in the same manner, which manifests in the macroscopic electric polarization.

2.5.2 Magnetoelectric multiferroics

Intuitively, strongest magnetoelectric coupling is expected to be found in systems, where simultaneously (anti)ferromagnetic and ferroelectric ordering occur. Such materials, exhibiting a phase where at least two ferroic orders (ferroelectricity, (anti)ferromagnetism or ferroelasticity) are developed, are named multiferroics (Figure 11) - in our case magnetoelectric multiferroics. Their allowed physical, structural, and electronic properties are restricted to those that occur both in (anti)ferromagnetic and in ferroelectric

materials. Here we list the limiting factors, which might prevent the simultaneous occurrence of (anti)ferromagnetism and ferroelectricity and would help us answer the question – why magnetoelectric multiferroics are so rare?

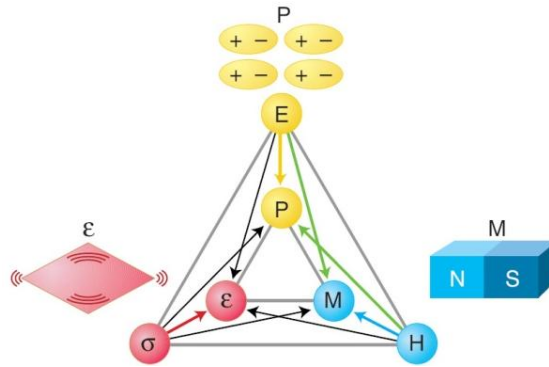


Figure 11: Phase control in ferroics and multiferroics (57). The electric field E , magnetic field H , and stress σ control the electric polarization P , magnetization M , and strain ζ , respectively. In a ferroic material, P , M , or ζ are spontaneously formed to produce ferromagnetism, ferroelectricity, or ferroelasticity, respectively. In a multiferroic, the coexistence of at least two ferroic forms of ordering leads to additional interactions. In a magnetoelectric multiferroic, a magnetic field may control P or an electric field may control M (green arrows).

A primary requirement for the existence of ferroelectricity is a structural distortion from the prototypical high-symmetry phase that removes the centre of symmetry and allows an electric polarization. There are 31 point groups that allow a spontaneous electric polarization, \vec{P} , and 31 that allow a spontaneous magnetic polarization, \vec{M} (27). Thirteen point groups (1, 2, 2', m, m', 3, 3m', 4, 4m'm', m'm'2', m'm'2', 6', and 6m'm') are found in both sets, allowing both properties to exist in the same phase. The number of possible point groups increases further if also antiferromagnetic ordering is considered. Hence, the total number of possible crystal structures (the total number of Shubnikov point groups is 122), it is far from being insignificant, and many candidate materials that are not in fact ferromagnetic and ferroelectric exist in one of the allowed symmetries. Therefore, it is unlikely that symmetry considerations are responsible for the scarcity of ferromagnetic ferroelectric materials.

The second possible limitation is the conductivity of the sample. By definition, a ferroelectric material must be an insulator (otherwise, an applied electric field would induce an electric current to flow, rather than cause an electrical polarization). Ferromagnets, although not required to have specific electrical properties, are often metals, for example, the elemental ferromagnets Fe, Co, and Ni and their alloys. Therefore, one could assume that the lack of the simultaneous occurrence of magnetic and ferroelectric ordering is simply the result of a dearth of magnetic insulators. However, considering also ferrimagnets, weak ferromagnets, or antiferromagnets, this argument no longer holds, because most of the listed materials are, in fact, insulators. Therefore, it appears that we cannot blame the lack of magnetically ordered ferroelectrics simply on a shortage of magnetically ordered insulators.

We already noted that the common perovskite oxide ferroelectric materials have a formal charge corresponding to the d^0 electron configuration on the B cation. Clearly, if there are no d electrons creating localized magnetic moments, then there can be no magnetic ordering of any type, either ferro-, ferri-, or antiferromagnetic. It appears, however, that in most cases, as soon as the d shell on the small cation is partially occupied, the tendency for it to make a distortion that removes the centre of symmetry is eliminated. This could be the result of numerous effects, including size, the tendency to undergo a different, more dominant distortion, electronic properties, magnetic properties, or an arbitrary combination of the

above. Apparently, there are lots of reasons, which seem to explain why the coupling between the magnetic order and electric polarization is usually small and rare.

In a last decade, however, a way around these limitations was found, as strong ME coupling has been discovered in complicated magnetic structures, typical for magnetically frustrated systems. Here, spatial inversion symmetry is usually broken only after magnetic order sets in, which thereby enables the development of electric polarization. Still, large ME effect is limited to the temperatures far below room temperature, necessary for practical applications. Thus, the ongoing research is now focused on the quest for room-temperature ME effect. In this respect, Eerenstein *et al.* (24) encourage to study magnetic materials with reduced dimensionality, since one- or two-dimensional magnetic order regularly persists to much higher temperatures than three-dimensional order does.

2.5.3 Magnetolectric coupling

The explanation for the observed strong ME effect lies in the crystal structure of the exemplary systems (for instance $ReMnO_3$, where Re is rare-earth) (5), (25). For these compounds it is typically that their crystal structure has the spatial inversion symmetry, while their magnetic ordering does not. Hence, when magnetic order sets in the spatial inversion symmetry is broken and non-centrosymmetric lattice distortions are induced through exchange-striction, leading to the presence of electric polarization, while bypassing the d^0 condition. As it turns out, magnetic ordering without magnetic inversion symmetry is often driven by the presence of magnetic frustration imposed by the competing exchange interactions.

2.5.3.1 Phenomenological approach to magnetolectric coupling

Several phenomenological theories, based on symmetry considerations, have been proposed to explain such phenomena (58), (59), (60). In these theories the free energy F is calculated using Ginzburg-Landau type continuum field theory in terms of an applied magnetic field \vec{H} , whose i -th component is denoted H_i , and an applied electric field \vec{E} , whose i -th component is denoted E_i . Note that this convention is unambiguous in free space, whereas E_i within a material encodes the resultant field that a test particle would experience. Let us consider a non-ferroic material, where both the temperature-dependent electrical polarization $P_i(T)$ ($\mu\text{C}/\text{cm}^2$) and the magnetization $M_i(T)$ (μ_B per formula unit, where μ_B is the Bohr magneton) are zero in the absence of applied fields and there is no hysteresis. This allows us to write F for an infinite, homogeneous and stress-free medium under the Einstein summation convention in S.I. units as (24):

$$F(E, H) = \frac{1}{2} \epsilon_0 \epsilon_{ij} E_i E_j + \frac{1}{2} \mu_0 \mu_{ij} H_i H_j + \alpha_{ij} E_i H_j + \frac{\beta_{ij}}{2} E_i H_j H_k + \frac{\gamma_{ij}}{2} H_i E_j E_k + \dots \quad (2.24)$$

Here, the first term on the right hand side describes the contribution resulting from the electrical response to an electric field, where the permittivity of free space is denoted ϵ_0 , and the relative permittivity $\epsilon_{ij}(T)$ is a second-rank tensor that is typically independent of electric field E_j in non-ferroic materials. The second term is the magnetic equivalent of the first term, where $\mu_{ij}(T)$ is the relative permeability and μ_0 is the permeability of free space. The third term describes linear magnetolectric coupling via $\alpha_{ij}(T)$; the third-rank tensors $\beta_{ijk}(T)$ and $\gamma_{ijk}(T)$ represent higher-order (quadratic) magnetolectric coefficients.

In the present scheme, all magnetolectric coefficients incorporate the field independent material response functions $\epsilon_{ij}(T)$ and $\mu_{ij}(T)$. The magnetolectric effects can then easily be established in the form $P_i(H_j)$ or $M_i(E_j)$. The former is obtained by differentiating F with respect to E_i , and then setting $E_i = 0$. A complementary operation involving H_i establishes the latter. One obtains:

$$P_i = \alpha_{ij}H_j + \frac{\beta_{ij}}{2}H_jH_k + \dots, \quad (2.25)$$

$$\mu_0 M_i = \alpha_{ij}E_i + \frac{\gamma_{ij}}{2}E_jE_k + \dots. \quad (2.26)$$

In ferroic materials, the above analysis is less rigorous because $\varepsilon_{ij}(T)$ and $\mu_{ij}(T)$ display field hysteresis. Moreover, ferroics are better parameterized in terms of resultant rather than applied fields (61). This is because it is then possible to account for the potentially significant depolarizing/demagnetizing factors in finite media, and also because the coupling constants would then be functions of temperature alone, as in standard Landau theory. In practice, resultant electric and magnetic fields may sometimes be approximated (7) by the polarization and magnetization respectively.

Eventually, the coupling between electric polarisation \vec{P} and magnetisation \vec{M} is constrained by symmetry relations, as behaviour of these two quantities under the system's symmetry operations as well as time reversal and spatial inversion is well defined. Additionally, free energy F is a scalar, and thereby demands that the ME coupling term in F is invariant to all symmetry operations. In the end, this gives an estimate about which P_i and M_i components might play a role in the magnetoelectric coupling. In order to explain the ME coupling in different magnetic arrangements, several coupling terms, involving different P_i and M_i components, were proposed. For instance, Mostovoy (58) developed an explanation for the occurrence of the electric polarization in incommensurate cycloidal structures, while Betouras et al. (59) predicted that electric polarization can be found also in commensurate magnetic orderings. The main difference between these two theories is that the former assumes a spatially homogeneous electric polarisation, whereas the latter allows spatial variation of \vec{P} within the material. To sum up, based on the knowledge of the crystal and magnetic symmetry of the magnetoelectric multiferroic one can predict a possible orientation of the electric polarization and on contrary, the orientation of the electric polarization reflects the symmetry of the magnetic system.

2.5.3.2 Microscopic mechanism of the magnetoelectric coupling

The microscopic mechanism of the magnetoelectric coupling is not yet fully understood, since there still exist several rival hypotheses. One possible candidate is the so-called 'inverse Dzyaloshinskii-Moriya' mechanism (62), (63), where a structural distortion lowers the energy of a spiral chain when there is a Dzyaloshinskii-Moriya exchange interaction between spins. In other words, in order to promote chiral magnetic ordering, all ligand ions move in parallel, thereby increasing the antisymmetric Dzyaloshinskii-Moriya exchange interaction. The resulting electric polarisation has the form

$$\vec{P} \propto \vec{r}_{ij} \times (\vec{S}_i \times \vec{S}_j), \quad (2.27)$$

where \vec{r}_{ij} is the vector connecting the i -th and j -th spins, which have spin \vec{S}_i and \vec{S}_j respectively.

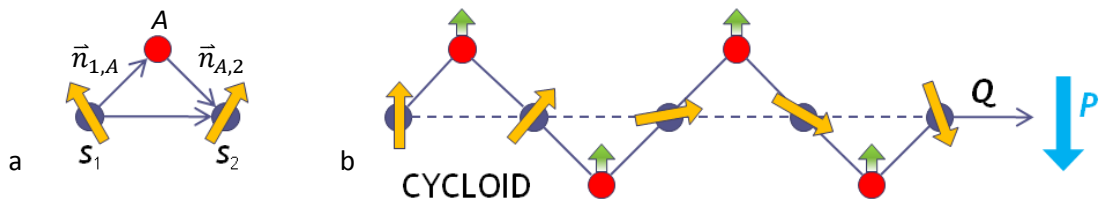


Figure 12: (a) Scheme of magnetic ions coupled by antisymmetric Dzyaloshinskii-Moriya exchange interaction via the exchange pathway determined by ligand ion A and vectors $\vec{n}_{1,A}$ and $\vec{n}_{A,2}$. (b) Effect of the inverse Dzyaloshinskii-Moriya mechanism: in order to promote chiral magnetic ordering, all ligand ions move in parallel, thereby increasing the antisymmetric Dzyaloshinskii-Moriya exchange interaction, and eventually induce macroscopic electric polarization \vec{P} .

The above result is strictly valid only for systems with just one magnetic ion per unit cell, and a magnetic propagation vector that is parallel to the lattice vector. Nevertheless, the underlying physics should be similar for more complicated systems. The same result is arrived at when a flow of electron spin through a material, i.e., spin supercurrent, is considered (62). Both these mechanisms are applicable only for cycloidal or conical magnetic structures, where the magnetic ordering is chiral.

On the other hand, for the occurrence of the electric polarization in the collinear magnetic structures, alternative explanations (64), (65), (66), (67) were proposed. These theories are based on the so called “exchange-striction” magnetoelectric coupling mechanism, which assumes that the structural distortion, responsible for the ferroelectric polarization, occurs in order to minimize the superexchange interaction; i.e., in order to reduce the overall magnetic energy, the ligand ion, forming the superexchange bridge, is assumed to shift, thereby modifying the bond angle, θ , (Figure 13) and consequently change the strength of the superexchange interaction. Hence the electric polarization can be written as

$$P \propto (\vec{S}_i \cdot \vec{S}_j). \quad (2.28)$$

Compared to the inverse Dzyaloshinskii-Moriya ME coupling mechanism, the exchange-striction is expected to be stronger, since isotropic superexchange coupling interaction is typically stronger compared to the antisymmetric Dzyaloshinskii-Moriya coupling.

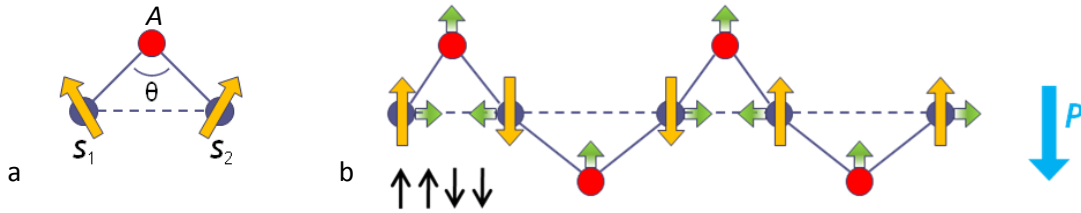


Figure 13: (a) Scheme of magnetic ions coupled by isotropic superexchange interaction via the superexchange pathway determined by ligand ion A and angle θ . (b) Effect of the exchange-striction mechanism: to promote the up, up, down, down magnetic ordering, all ligand ions move in parallel, thereby changing the bond angle and consequently the strength of the superexchange interaction, and eventually induce macroscopic electric polarization \vec{P} .

In conclusion, we stress that for large electric as well as magnetic responses, one should seek systems with crystal structures, where magnetic ions with large moments (for instance Fe^{3+} with d^5 electrons and $S = 5/2$) are superexchange-coupled via ions with empty d -orbitals, having easily polarisable lone pair electrons (for instance Te^{4+} with $5s^25p^0$ electronic configuration).

3 Experimental

In this chapter we will briefly introduce the experimental techniques used in course of our investigation of magnetic and electric properties of two-dimensional systems of magnetic clusters with triangular geometry. We have utilized local probe techniques (such as nuclear magnetic resonance, electron magnetic resonance and mu-ion spin relaxation), diffraction techniques (x-ray and neutron diffraction) and bulk measurements (specific heat, thermal expansion, electric polarization, dielectric and magnetic susceptibility measurements).

3.1 Magnetic resonance techniques

Magnetic moment $\vec{\mu}$ in an applied magnetic field \vec{B}_0 experiences torque and being fixed it will start to precess at an angular frequency $|\gamma B_0|$, where γ is the gyromagnetic ratio. This behaviour is described by so called Bloch equation of motion:

$$\frac{d\vec{\mu}}{dt} = \gamma(\vec{\mu} \times \vec{B}_0). \quad (3.1)$$

As a consequence, a system of magnetic moments in a magnetic field can absorb energy at this frequency, i.e., one may observe a resonant absorption of energy from radiofrequency (rf) field, if tuned to the correct frequency. This brought to the general expression - magnetic resonance, which stands for magnetic resonance absorption experiments performed on an ensemble of magnetic moments within the investigated specimen.

In practice the applied rf field is typically linearly polarized (along the x-axis) and perpendicular to the static magnetic field \vec{B}_0 (along the z-axis), which leads to an extra transverse magnetization written in the laboratory frame as

$$M_x(t) = M_x^{rot} \cos \omega t + M_y^{rot} \sin \omega t = (\chi' \cos \omega t + \chi'' \sin \omega t) B_{rf}, \quad (3.2)$$

where $M_x^{rot} \propto \sum_i \mu_{ixy}$ is the amplitude of the transverse component of the magnetization, ω and B_{rf} is the frequency and amplitude of the oscillating rf field, while the χ' and χ'' are the real and imaginary parts of rf susceptibility $\chi = \chi' + i\chi''$. Considering now that the signal acquisition in the magnetic resonance techniques is associated with the measurements of the power absorbed in the sample. In particular, change of the real part of the complex impedance of the sample $\Delta R/R = Q\chi''$, where Q is the quality factor depending on the experimental setup, is being measured. Thus the actually acquired quantity is

$$\chi''(\omega) = \frac{\omega V}{2k_B T} \int_{-\infty}^{\infty} \langle M_x(t) M_x(0) \rangle e^{-i\omega t} dt. \quad (3.3)$$

We note that the above expression is written in the high-temperature limit, when the energy of thermal fluctuations is much larger than the Zeeman energy splitting and $\langle \dots \rangle$ denotes the thermal average.

This expression can be further simplified according to the general quantum-mechanical description of the magnetic resonance introduced by Kubo and Tomita (68) back in fifties. Basically they developed a linear-response theory, where the response of the system of magnetic moments depends linearly on the external disturbance. The authors split the spin Hamiltonian into two parts, the term

$$H_0 = H_{ex} + H_Z \quad (3.4)$$

and the magnetic anisotropy part

$$H' = H_{cf} + H_{DM} + H_{aniso} + \dots, \quad (3.5)$$

which was then treated as a perturbative correction. The important point in this theory is that the Hamiltonians within the former term commute with each other, while they do not commute with the Hamiltonians included in the latter term. This way, the magnetization operator in equation 3.2 can be transformed into interaction representation as $\tilde{M}(t) = e^{-iH_0 t/\hbar} M(t) e^{iH_0 t/\hbar}$. Taking into account also the operators relations $\langle \tilde{M}^\pm(t) \tilde{M}^\pm(0) \rangle = 0$ allows one to rewrite the equation 3.3 into the form

$$\chi''(\omega) = \frac{\omega V}{8k_B T} \int_{-\infty}^{\infty} (\langle \tilde{M}^+(t) \tilde{M}^-(0) \rangle e^{-i(\omega-\omega_0)t} + \langle \tilde{M}^-(t) \tilde{M}^+(0) \rangle e^{-i(\omega+\omega_0)t}) dt. \quad (3.6)$$

Here, $\omega_0 = g\mu_B B_0/\hbar$ denotes the angular Larmor frequency determined by static magnetic field $\vec{B}_0 || z$. Hence, the first term in equation 3.6 is resonant absorption that takes place at $\omega = \omega_0$, while the second occurs at $\omega = -\omega_0$. In fact, in the limiting case when there is no magnetic anisotropy ($H' = 0$), the spectrum would simply consist of two δ -functions. The time dependence of the correlation functions $\langle \tilde{M}^\pm(t) \tilde{M}^\pm(0) \rangle$ due to anisotropy is thus responsible for the finite linewidths, lineshifts and the shape of the absorption spectra, and is thus of great importance in magnetic resonance experiments.

According to the Kubo-Tomita derivation, when the resonance at $\omega = -\omega_0$ is neglected, the normalized spin-resonance absorption spectrum can be expressed as the Fourier transform of the relaxation function $\varphi(t) = \langle \tilde{M}^+(t) \tilde{M}^-(0) \rangle / \langle M^+ M^- \rangle$,

$$I(\omega) = \int_{-\infty}^{\infty} \varphi(t) e^{i(\omega-\omega_0)t} dt. \quad (3.7)$$

In the case of Gaussian random processes the relaxation function is approximated by

$$\varphi(t) = e^{-\int_0^t (t-\tau) \psi(\tau) d\tau}, \quad (3.8)$$

where the spin correlation function $\psi(\tau) = \langle [\tilde{H}'(\tau), M^+(0)] [M^-(0), \tilde{H}'(0)] \rangle / \hbar^2 \langle M^+ M^- \rangle$ (the square brackets $[A, B]$ denote the commutator of the operators A and B) fluctuates on the time scale of the spin correlation time τ_c , yielding a Gaussian function

$$\psi(\tau) = \psi(0) e^{-\tau^2/2\tau_c^2}. \quad (3.9)$$

This result indicates that the lineshape strongly depends on the length of the correlation time and can consequently vary between Gaussian and Lorentzian lineshapes (as discussed in section 3.1.1.1).

3.1.1 Electron spin resonance

The electron magnetic resonance is usually associated with the absorption of magnetic moments corresponding to localized or itinerant electrons. In principle, such absorption can be seen in the case of paramagnetic compounds containing transition elements with incomplete inner shells, in ordinary metals, in magnetically ordered systems, and in case of imperfect insulators, which may trap electrons or holes. In this respect the expression electron spin resonance (ESR) is assigned to the experiments with paramagnetic species in the case when magnetic moments originate primarily from the spin momentum, as in iron-group metals, as well as for the resonant absorption in ferromagnetically or antiferromagnetically ordered state (12).

In practice, the ESR technique provides additional information to the data obtained by bulk magnetic susceptibility measurements, such as SQUID (section 3.3.1). ESR can reveal the development of electronic spin correlations in magnetic solids, the development of internal magnetic fields, or the coupling to the

crystal lattice. This is due to the fact that electrons serve as local probes in the ESR measurements so that spectra directly reflects fluctuations of the local magnetic fields present at a particular site in the crystal.

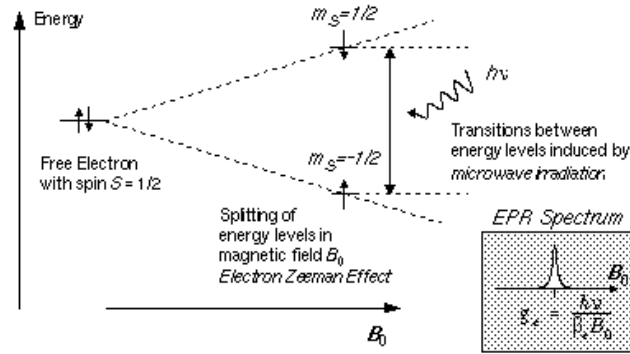


Figure 14: Sketch of ESR resonant absorption. With increasing magnetic field electron levels are being split hence when frequency of microwave irradiation match the energy of the splitting absorption occurs. An ESR spectrum is therefore recorded by measuring the magnetic field dependence of the resonant absorption.

In paramagnetic resonance experiment one usually observes the splitting of the energy levels of the paramagnetic centre with $S = \pm 1/2$ due to the external magnetic field (Zeeman effect) (Figure 14). Hence, when applying a fixed electromagnetic radiation while increasing the external magnetic field from zero, at certain value, absorption will occur, i.e., the energy gap divided by Planck constant, between the up and down orientation will match with the applied electromagnetic radiation

$$\nu = \Delta m_S \frac{g\mu_B}{h} B_0. \quad (3.10)$$

Here h is Planck constant, $\Delta m_S = 1$ is the difference between spin quantum numbers for up and down orientation, $g = \hbar\gamma/\mu_B$, where \hbar is $h/2\pi$, is the so-called g -factor and B_0 is the strength of the external magnetic field. At that point absorption in the system dramatically increases what is detected in the ESR experiment as the absorbed microwave power. The obtained ESR spectrum contains lots of information. For instance, the position of the resonance frequency (g -factor) indicates the strength of the local magnetic fields at the spin position and thus helps to identify the species of the magnetic ions, to which resonating magnetic moments correspond. The width of the spectrum is associated with the spin-spin and spin-lattice relaxation processes, while the intensity of the signal depends on the number of resonating magnetic moments as well as probability for the excited transitions. Finally, the complete shape of the spectrum (distribution of resonating frequencies) holds information about the on-site magnetic anisotropies as well as the nature of the relaxation processes etc. Much more about the strength of the spin-spin and spin-lattice coupling, as well as magnetic anisotropies can be learned from temperature and angular dependences of these ESR spectral parameters.

3.1.1.1 Exchange narrowing of the absorption spectra

In this section we focus on the effects of the exchange interaction J on the ESR spectrum. For electron spin the correlation time τ_c is determined by co called exchange frequency ω_e , i.e., $\tau_c = 1/\omega_e \sim \hbar/J$, since in the interaction picture the anisotropic Hamiltonian H' (equation 3.5) is modulated by the isotropic exchange interaction. As the exchange coupling constant in principle spans over a large interval of possible values, it is worth testing two limiting cases of the magnitude of the electron correlation time with respect to the parameter t describing the decay of the relaxation function. In the case when the spin correlation function decays slowly ($t \ll \tau_c$) the spin correlation function can be replaced by the second moment of the absorption spectrum

$$M_2 = \hbar^2 \psi(0) = \langle [H', M^+] [M^-, H'] \rangle / \langle M^+ M^- \rangle, \quad (3.11)$$

which yields a Gaussian-shaped relaxation function and consequently also Gaussian profile of the absorption spectrum. The peak-to-peak linewidth of the derivative ESR spectrum is in this case given by

$$\delta B_{pp}^G = \frac{2}{g\mu_B} \sqrt{M_2}. \quad (3.12)$$

In the second limiting case, usually encountered in real systems, the spins fluctuate very rapidly ($t \gg \tau_c$) due to large exchange coupling constant with respect to the observed linewidths. The integral defining the relaxation function in equation 3.6 can then be approximated by

$$\int_0^t (t - \tau) \psi(\tau) d\tau = \psi(0) \left(t \int_0^{t \rightarrow \infty} e^{-\tau^2/2\tau_c^2} d\tau - \int_0^{t \rightarrow \infty} \tau e^{-\tau^2/2\tau_c^2} d\tau \right) \sim \sqrt{\frac{\pi}{2}} \psi(0) \tau_c t, \quad (3.13)$$

which sets the relaxation function as an exponentially decaying function. The Fourier transform consequently yields the Lorentzian lineshape of the absorption spectrum with the peak-to-peak linewidth

$$\delta B_{pp}^L = \sqrt{\frac{\pi}{6}} \frac{2}{\hbar g \mu_B} M_2 \tau_c \sim \sqrt{\frac{\pi}{6}} \frac{2}{g \mu_B} \frac{M_2}{J}. \quad (3.14)$$

It should be stressed that the Lorentzian shape is expected for frequencies when $(\omega - \omega_0) \ll \omega_e$, or equivalently for magnetic fields $(B - B_0) \ll \hbar \omega_e / g \mu_B$, while the decay is faster in the tails of the spectrum, since it is determined by the relaxation function time dependence around $t = 0$ (41). This fact ensures finite values of the second moment, contrary to the second moment of the purely Lorentzian line that diverges. The second aspect to be highlighted is the occurrence of the exchange narrowing in the case of rapid electronic spin fluctuations. Namely, a comparison of equations 3.12 and 3.14 clearly demonstrates that the Lorentzian linewidth is suppressed with respect to the Gaussian one by approximately the factor of $\sqrt{M_2}/J$.

However, for broad lines (with the peak-to-peak width of the order of the resonance field B_0), both circular polarizations of the microwave irradiation, determining the resonances at $\pm B_0$ (equation 3.6), have to be taken into account (69),

$$\frac{dI}{dB} \propto \frac{d}{dB} \left[\frac{\delta B + 2r(B - B_0)}{4(B - B_0)^2 + \delta B^2} + \frac{\delta B + 2r(B + B_0)}{4(B + B_0)^2 + \delta B^2} \right]. \quad (3.15)$$

In this expression, the parameter δB denotes a linewidth, while r represents the amount of dispersion admixed into an absorption spectrum. In insulating materials, one usually encounters pure absorption Lorentzian lines ($r = 0$). However, asymmetric dispersive Lorentzians, i.e., Dysonian-like line shapes, can be observed if the dispersion contribution is admixed with the absorption. This is in general expected when the magnetic anisotropy of a particular system results in very broad ESR lines (of the order of B_{res}) due to nondiagonal terms of the susceptibility tensor (70). Alternatively, Dysonian line shapes are in general observed in metallic samples due to a skin effect (71).

3.1.1.2 Magnetic resonance in the vicinity of critical points

In principle, there are three different temperature intervals of interest, when performing magnetic resonance absorption experiments on magnetic solids, which undergo a transition to a magnetically ordered state below some critical temperature T_c . Namely, the high-temperature interval ($T \gg T_c$) where only short-range correlations potentially play a role, the temperatures just above the critical temperature ($T \geq T_c$), where precursor effects of long-range ordering are present, and temperatures below T_c , for which

appreciable internal magnetic field due to magnetic ordering are crucial for understanding the resonant spectra.

In the critical region there is an intrinsic difference between ferromagnetic and antiferromagnetic materials. That is, in ferromagnets the contribution of the spin correlations at wave-vector $\vec{q} = 0$ gets critically enhanced while these correlations are diminished in antiferromagnets. In fact, near the antiferromagnetic transition, staggered (alternating) correlations $\langle S_{q_0}^z S_{-q_0}^z \rangle$ at wave-vector \vec{q}_0 tend to dominate at zone centre. If looked at in the light of a snapshot picture, increasing clusters of ordered spins begin appearing, when approaching the transition point of the system. Also the mean-squared amplitudes of the staggered Fourier component of the magnetic moment distribution increases, which can be properly accounted for by the wave-length-dependent static susceptibility $\chi(\vec{q}, t = 0)$. On the other hand, also the dynamical aspect of the critical fluctuations is important. Namely, when approaching the transition temperature the average lifetime of a cluster of ordered spins will be increased. This effect, called the critical slowing-down of spin fluctuations, is expressed by the decrease of the relaxation rate $\Gamma(\vec{q}, T)$ of the spin correlation functions and, in effect, adds to the increased fluctuation amplitudes. Both the static and the dynamic effect contribute to a significant line broadening of the ESR absorption spectra in the vicinity of the phase-transition temperature, thereby according to reference (72) yielding the linewidth

$$\delta B \propto \frac{\langle S_{q_0}^z S_{-q_0}^z \rangle}{\Gamma(\vec{q}_0)} \xi^2, \quad (3.16)$$

where ξ is the correlation length.

3.1.1.3 Experimental apparatus

The typical X-band ($\nu = 9.4$ GHz) ESR spectrometer consists of an electromagnet with power supplies to generate and modulate a uniform magnetic field of several hundred mT (for X-band typically up to 1 T), as well as the components that generate and detect microwave power.

A static magnetic field is provided by an electromagnet with a current-regulated power supply. A homogeneous field is required for best results. A Hall probe, driven from a stable constant-current power system, with a digital multimeter reading the Hall voltage, is used to measure the value of the magnetic field between the poles of the magnet. The microwave system consists of a microwave power supply which uses a klystron. The output of the microwave power (several mw) supply is connected via rectangular waveguide (X-band 9.4 GHz) to a resonant cavity. The samples to be investigated are mounted in the middle of the cavity, where magnetic component of the microwave power has a maximum and is oriented perpendicular to the static field. A microwave diode, which detects the mw resides inside the same box as the power supply. The higher the quality of the resonant cavity the greater is the microwave field that can be obtained on the sample. The detection in X-band (9.4 GHz) is typically based on a detection of absorption of the microwave power. To minimize the noise from the mw diode in steady state measurements, a magnetic field modulation scheme with phase sensitive detection is usually employed. As a result, the detected signal appears as a first derivative (Figure 15b). The usually used modulation field has a modulation frequency of ~ 80 kHz and the amplitude up to 0.5 mT.

On the other hand, measurements at higher frequencies (up to several hundreds of GHz) are usually associated with high magnetic fields (several Tesla). Therefore, superconducting magnets are used, which are for convenience typically capable of sweeping the magnetic field. For instance at Magnetic Resonance Lab at National High Magnetic Field Laboratory, Florida, United States of America, one can reach frequencies

up to 660 GHz and magnetic fields of 15 T. Additionally, the detection technique is a bit different, since here no cavities are used, but simply intensity of the microwave beam, lighting through the sample, is measured.

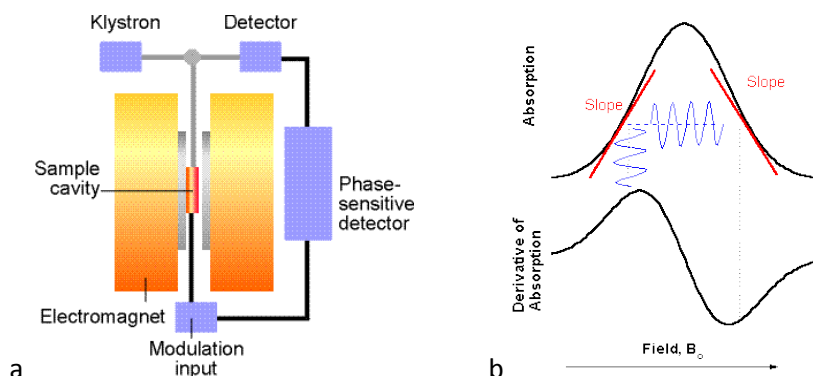


Figure 15: (a) ESR X-band experimental setup. (b) Effect of the modulation field on the detected signal.

3.1.2 Nuclear magnetic and quadrupolar resonance

In addition to the electron magnetic resonance, nuclear magnetic resonance (NMR) is also very useful local probe for studies of the electronic properties of solids. Its strongest point is that the nuclear resonance is being detected instead of electronic one, hence this experimental method provides a probe that is only weakly coupled to the electronic system, allowing for precise determination of the local magnetic fields present in the material under investigation. Because of the effectively weak coupling, which is usually much weaker than the leading Zeeman term, the NMR results are significantly easier to interpret compared to ESR. Hence one gets additional information to that obtained by ESR, where electrons directly serve as experimental probes. Nuclear magnetic resonance is sensitive to the time-averaged local magnetic fields through the position of the absorption lines as well as to certain spectral components of fluctuating fields, which affect the linewidth and the relaxation times of nuclei. We note that in contrast to ESR, we are not limited to transition metals, rare earths or other paramagnetic ions, but we can in principle probe any nuclei with reasonably large gyromagnetic ratio.

3.1.2.1 Origins of internal fields producing the frequency shifts of NMR spectra

The NMR spectrum of a certain species of nuclei in a material is strongly dependent on the nature of the investigated compound, i.e., a considerable difference is observed between nonmagnetic (38), (73) and magnetic materials, which can also exhibit ferromagnetic (74) or antiferromagnetic order (75). For instance, in nonmagnetic solids relatively small corrections to the energy of a nucleus in the external magnetic field are expected due to the dipolar field of other nuclei and atomic diamagnetism (tiny chemical shift of the resonant frequency). On the other hand, the electronic dipolar fields are several orders of magnitude larger than the corresponding nuclear fields, and the atomic hyperfine fields of magnetic ions are possibly even 10^6 times larger.

The internal fields at the nucleus, produced by the electronic spin moments, can be classified into three broad classes, depending on the nature of the atoms under investigation in the magnetic solid. In the first class of nuclei of nonmagnetic atoms, the main anisotropic addition to the Zeeman Hamiltonian $H_Z = -\gamma\hbar\vec{I}_i \cdot \vec{B}_0$ for the nuclei at site i with the nuclear gyromagnetic ratio γ usually originates from the dipole interaction between the nuclear spin \vec{I}_i and the average electronic spin moments of surrounding paramagnetic ions $\langle\vec{S}_j\rangle$. The static dipolar field B_d can be obtained from the dipolar Hamiltonian

$$H_i^d = -\gamma\hbar\vec{I}_i \cdot \vec{B}_d = \gamma\hbar\vec{I}_i \frac{\mu_0 g \mu_B}{4\pi} \sum_j r_{i,j}^{-3} [\langle \vec{S}_j \rangle - 3\vec{r}_{i,j}(\langle \vec{S}_j \rangle \cdot \vec{r}_{i,j})/r_{i,j}^2], \quad (3.17)$$

when the time-averaged value of the electronic spin $\langle \vec{S}_j \rangle$ is taken into account. In the equation 3.17 the summation extends over all magnetic sites j , which are at the distance $r_{i,j}$ from the nucleus. The static field is proportional to the time-average of the electronic magnetic moments and thus to the uniform magnetization of the system. In the paramagnetic phase, this interaction is nonzero only in the case of applied external magnetic field B_0 , which partially polarizes the electronic system. However, the dipolar magnetic field B_d and the external field are generally not parallel, due to the $(\langle \vec{S}_j \rangle \cdot \vec{r}_{i,j})$ term, which is even more pronounced if magnetic ordering sets in.

The second group are nuclei of paramagnetic ions, which are subjected to the intense hyperfine fields that arise from the interaction of the nucleus with electrons within the same paramagnetic ions. In addition to the dipolar Hamiltonian (equation 3.17), anisotropy terms of the form

$$H_i^{hf} = \vec{I}_i \cdot \underline{A}_i \cdot \langle \vec{S}_i \rangle \quad (3.18)$$

determine the properties of NMR absorption of the nucleus at site i . The static hyperfine magnetic field $\vec{B}_{hf} = -\underline{A}_i \cdot \langle \vec{S}_i \rangle / \gamma\hbar$ is usually so intense that it produces large lineshifts or even makes the resonant absorption experimentally unobservable (75). In the one-electron theory the hyperfine interaction can be expressed in the following form (76)

$$H_i^d = \frac{\mu_0 g \mu_B \gamma \hbar}{4\pi} \left(\frac{8\pi}{3} |\psi(0)|^2 \vec{I}_i \cdot \vec{S}_i - \frac{\vec{I}_i \cdot (\vec{S}_i - \vec{L}_i)}{r^3} + \frac{3(\vec{I}_i \cdot \vec{r})(\vec{S}_i \cdot \vec{r})}{r^3} \right). \quad (3.19)$$

The first term represents the Fermi contact interaction being nonzero only for s electrons, which have a nonzero probability of being found exactly at the point of the nucleus $|\psi(0)|^2 > 0$. In such case the last two terms are zero due to the spherical distribution of the electron density. These two terms are the orbital (L) and the spin dipole energy terms. For several electrons outside the closed shell the operators in equation 3.19 are taken as the sum operators for the entire ion. However, this conventional one-electron theory has its shortcomings, as it cannot predict hyperfine fields for ions which have net spin, but have no unpaired s electrons. In fact, if an ion is in the s orbital state and has a net spin, the spin and the orbital dipole contributions will be zero, however, the ion can still have appreciable local fields arising from the Fermi contact term. In Mn^{2+} this hyperfine field can be of the order of 70 T (76). The many-electron contribution to the hyperfine coupling includes the polarization effect involving core electrons. Namely, the incompletely filled shell with $L \neq 0$ distorts the closed shell and, in turn, causes an interaction with the nuclear magnetic moment (76). The calculation of the hyperfine tensor is thus far from being trivial, which is why it is usually taken phenomenologically as an anisotropic tensor and is not calculated from the first principles.

The last class joins nuclei of partially magnetic ions. For such materials there is an appreciable overlap between the wave functions of electrons of nominally nonmagnetic ions and those wave functions of electrons from paramagnetic ions. As a consequence a space redistribution of electrons at the nonmagnetic sites appears. This can be explained in the light of the amount of covalency present in bonds as follows. To the extent that an orbital of the paramagnetic ion is mixed with an orbital of the diamagnetic ion in the bonding function, it is reduced in the antibonding function. This means that, to the degree that bonding occurs, the unpaired electron in the antibonding orbital has the character of the initial orbital of the diamagnetic ion. Consequently, an imbalance at nonmagnetic ion characteristic of the symmetry of its initial orbital occurs in the sense that the unpaired electron in the antibonding orbital, with spin parallel to that of

the paramagnetic ion, can produce its characteristic hyperfine field. This way even at ions with paired s electrons there can be significant hyperfine coupling of the Fermi contact type (77). The effective hyperfine interaction can be written for partially magnetic ions as a sum of transferred hyperfine contributions

$$H_i^{hf} = \vec{I}_i \cdot \sum_j \underline{A}_{i,j} \cdot \vec{S}_j. \quad (3.20)$$

Here the sum runs over all the neighbouring paramagnetic sites j that affects the spatial distribution of electrons on the diamagnetic site i . From the size and the shape of the transferred hyperfine tensor $\underline{A}_{i,j}$ one can in principle deduce the orbital character and the extent of collaboration of the electrons from the diamagnetic species with the paramagnetic electrons in formation of the covalent bonding.

As demonstrated in this section, the line position reveals information on the time-averaged value of the local fields. The resonance frequency strictly follows the temperature evolution of the averaged spin moment when the coupling constants (dipolar and hyperfine) are assumed to be temperature independent. This is frequency shift can be written as

$$\delta\omega(T) = \omega(\infty) - \omega(T) = -\gamma\hbar\vec{I}_i \cdot \vec{B}_0 - \vec{I}_i \cdot \left(\gamma\hbar\vec{B}_d(T) + \sum_j \underline{A}_{i,j} \cdot \langle \vec{S}_j(T) \rangle \right), \quad (3.21)$$

where $\omega(\infty)$ is the resonating frequency due to \vec{B}_0 , \vec{B}_d is the static dipolar field of the surrounding ions, $\underline{A}_{i,j}$ is the hyperfine coupling tensor between nuclei and the electron orbiting around the same nuclei $j = i$ as well as electrons on the neighbouring paramagnetic $j \neq i$.

3.1.2.2 Quadrupolar interaction

Another major source of anisotropy in the case when $I \geq 1$ has to be introduced, i.e., the nuclear quadrupole interaction. This coupling arises from the interaction between nuclear quadrupole moment Q with the electric field gradient (EFG) tensor V_{ij} existing at the nucleus and is described by the Hamiltonian (73)

$$H_Q = \nu_Q h \left[3I_z^2 - I^2 + \frac{1}{2}\eta(I_+^2 + I_-^2) \right], \quad (3.22)$$

where $\nu_Q = eV_{zz}Q/4I(2I+1)h$, h is the Planck's constant, and I^2 , I_z^2 , I_+ and I_- are the nuclear spin operators. The above Hamiltonian is written in the principal frame of the EFG tensor with the principal values by convention taken as $|V_{zz}| \geq |V_{yy}| \geq |V_{xx}|$, while the asymmetry parameter is defined as $\eta = (V_{xx} - V_{yy})/V_{zz}$.

In case of a weak quadrupole interaction compared to the applied magnetic field, $\nu_Q \ll \nu_L$, for half-integer spins the central transition $\langle -1/2 | \leftrightarrow \langle 1/2 |$ is a delta-function at Larmor frequency ν_L while the satellite lines appear as symmetrically displaced delta-functions with respect to the central line.

On the other hand, when ν_Q is comparable or even larger than ν_L , the spectrum cannot be calculated by a simple perturbation theory. The complete Hamiltonian $H = H_z + H_Q$, introducing, Zeeman as well as quadrupolar interactions, has to be taken into the account. The actual eigenstates of such a system are then obtained by diagonalization of H and differ from the standard $\langle -1/2 |$, $\langle 1/2 |$, ... Moreover, in case of a strong EFG and reasonably large Q , magnetic resonance can be observed even in the absence of an external field. This phenomenon is called nuclear quadrupole resonance (NQR).

3.1.2.3 Calculations of the NMR/NQR spectra

To obtain the correct spectral intensity, probability of a certain nuclear spin transition has to be considered. This probability is given by the square of the matrix element responsible for the transition between two states,

$$W_{m-1,m} \propto |\langle m-1 | I_+ | m \rangle|^2 = I(I+1) - m(m-1). \quad (3.23)$$

For the abovementioned reason the heights of the satellite lines are suppressed with respect to the central line or can even be completely wiped out, especially if a distribution of the electric field gradient is present.

Here we give show basic steps for the diagonalization of the nuclear spin Hamiltonian, which consists of Zeeman term, dipolar interaction with the surrounding electronic spins, transferred hyperfine coupling with the closest magnetic ions, and finally quadrupolar interaction. We neglect the ordinary hyperfine interaction, as we are interested in spectra of nonmagnetic nuclei.

First of all, for a convenience, we rewrite the quadrupolar Hamiltonian (equation 3.22) written in the principal frame of the EFG tensor in to the form of the laboratory frame, where z-axis is oriented along the applied magnetic field and V_{ij} now corresponds to the EFG tensor \underline{V} components in the laboratory frame:

$$H_Q = \frac{eQ}{4I(2I+1)} [V_0(3I_Z^2 - I^2) + V_{+1}(I_- I_Z + I_Z I_-) + V_{-1}(I_+ I_Z + I_Z I_+) + V_{+2}(I_-)^2 + V_{-2}(I_+)^2], \quad (3.24)$$

where $V_0 = V_{zz}$, $V_{\pm 1} = V_{zx} \pm iV_{zy}$, $V_{\pm 2} = \frac{1}{2}(V_{zz} - V_{yy}) \pm iV_{xy}$. This means that when crystal is rotated V_{ij} change as:

$$\underline{V} = \underline{R} \cdot \underline{\tilde{V}} \cdot \underline{R}^{-1}, \quad (3.25)$$

where

$$\underline{\tilde{V}} = \begin{bmatrix} \tilde{V}_{xx} & 0 & 0 \\ 0 & \tilde{V}_{yy} & 0 \\ 0 & 0 & \tilde{V}_{zz} \end{bmatrix} \quad (3.26)$$

with $\tilde{V}_{xx} + \tilde{V}_{yy} + \tilde{V}_{zz} = 0$ is the EFG tensor written in the EFG principal axes system, and \underline{R} is the appropriate rotation matrix. Next, we write the complete Zeeman term for a local field in the local frame:

$$H_Z = -\gamma \hbar \vec{I}_i \cdot \left(\vec{B}_0 + \sum_j A_{i,j} \cdot \vec{S}_j + \frac{\mu_0 g \mu_B}{4\pi} \sum_k r_{i,k}^{-3} [\vec{S}_k - 3\vec{r}_{i,k}(\vec{S}_k \cdot \vec{r}_{i,k})/r_{i,k}^2] \right), \quad (3.27)$$

where first term corresponds to applied magnetic field \vec{B}_0 , the second to the transferred hyperfine coupling with the closest magnetic ions (j) and the last term to the dipolar interaction with the electronic spins (k) within a limiting distance (up to several tens of nm, depending on the magnitude of the magnetic moments). We stress that j runs only over the closest magnetic ions (typically $j = 1$), while for calculating the dipolar interaction with the satisfactory precision, one must take into the account all the spins within a few crystallographic unit cells, depending on their magnitude – meaning that k can easily be of the order of 100. Finally the complete $H = H_Z + H_Q$ Hamiltonian can be diagonalized. This allows us to calculate the system's eigenstates as well as the transition frequencies and their probabilities (equation 3.23). Since the relative orientations between the applied magnetic fields, dipolar field, and transferred hyperfine field change, one has to do the described procedure separately for each crystal orientation, when calculating angular dependences.

3.1.2.4 Relaxation processes

As noted earlier, the observability of the nuclear magnetic resonance in magnetic material depends on the magnitude of certain spectral components of the fluctuating local fields or equivalently the fluctuating electron spin correlation functions. The amplitude of the fluctuations varies with the degree of order in the electronic system and is therefore quite temperature dependent. The general expressions for line broadening and spin-lattice relaxation, in the case of large exchange coupling, were derived by Moriya (78), using the Kubo-Tomita general theory of magnetic resonance. In principle, the general theory, presented in beginning of the section 3.1, applies also to the case of the nuclear magnetic resonance. However, for clarity we will speak here in the language of local fields arising from the interaction of the nucleus with the surrounding electrons instead of magnetizations.

The fluctuations in the local field are defined as $\vec{b}(t) = \vec{B}_{loc}(t) - \langle \vec{B}_{loc} \rangle$. As already explained, the time-averaged field contributes to the shift of the resonance frequency while the fluctuations, on the other hand, are themselves responsible for finite homogeneous linewidth. As it was already presented in equation 3.7, a normalized absorption line in NMR experiments can be expressed in terms of the relaxation function of transverse nuclear magnetization $M(t)$, with angular Larmor frequency being $\omega_0 = |\vec{B}_0 + \langle \vec{B}_{loc} \rangle|$. The relaxation function $\varphi(t)$ is related to the correlation function (79)

$$\psi(\tau) = \gamma^2 \left(\langle \{b_z(\tau)b_z(0)\} \rangle + \frac{1}{2} e^{i\omega_0\tau} \langle \{b_+(\tau)b_-(0)\} \rangle \right), \quad (3.28)$$

through the familiar expression given by equation 3.6. By agreement the index z again denotes the direction of the external magnetic field and $\{AB\}$ stands for the symmetrised product of two operators. Once again, as with ESR (section 3.1.1.1), if the electron correlation time is small compared to the spin-spin relaxation time, the exponent of the relaxation function will be a linear function of time. Lorentzian lineshape is then expected. The expression for the spin-spin relaxation time, which is related to the full width at half height (FWHH) of the absorption spectrum in the frequency units as $\Delta\nu = 1/(\pi T_2)$ in the picture of the homogeneous broadening, can be derived to have the following appearance

$$\frac{1}{T_2} = \gamma^2 \int_0^\infty \left(\langle \{b_z(\tau)b_z(0)\} \rangle + \frac{1}{2} \langle \{b_x(\tau)b_x(0) + b_y(\tau)b_y(0)\} \rangle \cos(\omega_0\tau) \right) d\tau. \quad (3.29)$$

Introducing the spectral density of the fluctuating local field

$$J_{\alpha\beta}(\omega) = \frac{1}{\pi} \int_{-\infty}^\infty \langle \{b_\alpha(\tau)b_\beta(0)\} \rangle \cos(\omega\tau) d\tau, \quad (3.30)$$

the equation (3.29) can be rewritten as

$$\frac{1}{T_2} = \frac{\pi\gamma^2}{2} \left(J_{zz}(0) + \frac{1}{2} J_{yy}(\omega_0) + \frac{1}{2} J_{xx}(\omega_0) \right). \quad (3.31)$$

The first term represents contributions, arising from the secular part of the perturbing Hamiltonian, defining the local field while the transverse correlation functions represent the nonsecular part. The spin-spin relaxation thus probes dynamic as well as static components of the local magnetic fields. The spin-lattice relaxation, on the other hand, is governed solely by the transverse fluctuations

$$\frac{1}{T_1} = \gamma^2 \int_0^\infty \left(\langle \{b_x(\tau)b_x(0) + b_y(\tau)b_y(0)\} \rangle \cos(\omega_0\tau) \right) d\tau = \frac{\pi\gamma^2}{2} \left(J_{yy}(\omega_0) + J_{xx}(\omega_0) \right). \quad (3.32)$$

Consequently, it is affected only by the fluctuations of the local magnetic fields at the Larmor frequency. Since electron correlations normally persist for much shorter times than the nuclear Larmor period, the nuclear relaxation times are simply determined by the spectral density of fluctuating field at zero frequency.

The magnetic field fluctuations are of course correlated to electronic spin fluctuations through equations 3.17-3.20. To be precise, if we write a coupling term between a nuclear spin \vec{I}_i at site i and the ionic spin \vec{S}_j at site j in the general form (accounting for the hyperfine as well as the dipolar coupling)

$$H_i^{hf} = \vec{I}_i \cdot \sum_j \underline{A}_{i,j} \cdot \vec{S}_j \quad (3.33)$$

and identify electron spin fluctuations from the equation spin polarization as fluctuations $d\vec{S}(t) = \vec{S}(t) - \langle \vec{S} \rangle$, the expressions for the nuclear relaxation times governed by the coupling to the system of paramagnetic electrons can be transformed into the following general form

$$\begin{aligned} \frac{1}{T_1} &= \frac{1}{2\hbar} \int_{-\infty}^{\infty} \sum_{j,k} \sum_{\mu,\nu} (A_{i,j}^{x,\mu} + iA_{i,j}^{y,\mu}) (A_{i,k}^{x,\nu} - iA_{i,k}^{y,\nu}) \langle \delta S_j^\mu(\tau) \delta S_j^\mu(0) \rangle \cos \omega_0 \tau \, d\tau, \\ \frac{1}{T_2} &= \frac{1}{2\hbar} \int_{-\infty}^{\infty} \sum_{j,k} \sum_{\mu,\nu} \left((A_{i,j}^{x,\mu} + iA_{i,j}^{y,\mu}) \right. \\ &\quad \left. + \frac{1}{2} e^{i\omega_0 t} (A_{i,j}^{x,\mu} + iA_{i,j}^{y,\mu}) (A_{i,k}^{x,\nu} - iA_{i,k}^{y,\nu}) \right) \langle \delta S_j^\mu(\tau) \delta S_j^\mu(0) \rangle \cos \omega_0 \tau \, d\tau. \end{aligned} \quad (3.34)$$

The temperature dependence of the NMR relaxation times in magnetic solids can be in principle obtained by calculating the time dependence of the electron spin correlation functions. In this respect, the NMR analysis demands less theoretical efforts than ESR. This is due to the fact that nuclear resonance strictly samples local properties in magnetic solids. That is, a nucleus at a particular site resonates independently of other nuclei, which is due to the linearity of the nuclear perturbing Hamiltonian in the electronic spin operators. Its resonance spectrum is determined by electronic fluctuations and correlations, sensed at a particular wave-vector (79). It is the same argument that explains why only the knowledge of two-spin correlation functions is needed in NMR, while ESR in its essence requires the information about the four-spin correlation functions. In the above-presented way also the nuclei can serve as an experimental probe for detecting the temperature evolution of the spin correlations in the spin system of the paramagnetic electrons.

At the end of this chapter, few words on the effect of the nonmagnetic mechanism (i.e., the quadrupole coupling) on the nuclear relaxation are in place. The influence of this interaction on the shift of the resonance line has already been highlighted from the static point of view. However, one has to include dynamical aspect for this coupling to be able to induce relaxation. In liquids such feature is provided by rapid reorientations of molecules, which produces fluctuations of local electric field gradients. On the other hand, for the quadrupole coupling to be effective in inducing relaxation in solids phonons have to be taken into account. Such lattice vibrations modulate EFG tensors. It is well established that the spin-lattice relaxation times, for instance, should scale linearly with the temperature if direct phonon processes are dominant, which account for the single phonon creation or annihilation processes. On the other hand, if the phonons are inelastically scattered on the spin system as in the case of the Raman processes, the increase of the relaxation rate is much steeper (T^2 to T^7 depending on the temperature with respect to the Debye temperature) (73).

3.1.2.5 NMR/NQR signal acquisition

There are two basic concepts of NMR signal acquisition, the “continuous wave” spectroscopy, which is in principle very similar to the ESR technique, and the so called “Fourier transform” spectroscopy. Nowadays, most of NMR the research is based on the Fourier transform technique, which will be presented below (Figure 16).

A short radiofrequency square pulse of a given carrier frequency contains a range of frequencies centred about the carrier frequency, with the range of excitation (bandwidth) being inversely proportional to the pulse duration. The restricted range of the NMR frequencies made it relatively easy to use short (millisecond to microsecond) radiofrequency pulses to excite the entire NMR spectrum. Applying such a pulse to a set of nuclear spins simultaneously excites all the single-quantum NMR transitions. In terms of the net magnetization vector, this corresponds to tilting the magnetization vector away from its equilibrium position (aligned along the external magnetic field). The out-of-equilibrium magnetization vector precesses about the external magnetic field vector at the NMR frequency of the spins. This oscillating magnetization vector induces a current in a nearby pickup coil, creating an electrical signal oscillating at the NMR frequency. This signal is known as the free induction decay and contains the vector-sum of the NMR responses from all the excited spins. Finally, in order to obtain the frequency-domain NMR spectrum (NMR absorption intensity vs. NMR frequency) this time-domain signal (intensity vs. time) must be Fourier transformed.

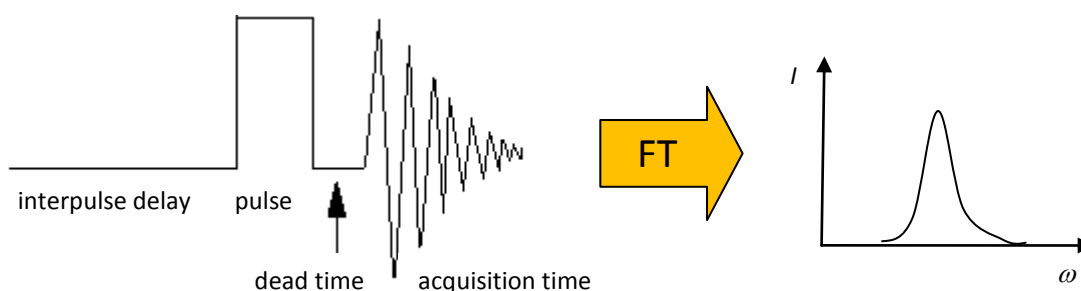


Figure 16: Schematic plot of the “Fourier transform” NMR spectroscopy. The basic acquisition process can be described with a one pulse sequence, which consists of interpulse delay, radiofrequency pulse, dead time and acquisition time. The pulse tilts the spins away from equilibrium position, the dead time is needed for the electronics to stabilize, the acquisition time is the time when signal is recorded, and the interpulse delay serves to allow the spin system to relax back towards equilibrium. Finally, the signal is transformed by Fourier transformation to obtain frequency-domain NMR spectrum.

3.2 Specific heat

One of the most important thermodynamic properties of the magnetic system is its specific heat. In particular, specific heat is very sensitive to any phase transition, whether it is structural or purely magnetic, since such thermal effects typically manifests as anomalies in the specific heat. Moreover, other magnetic contributions can be noticed, as for instance certain single-ion anisotropies, magnetic excitations, etc. This is because all these phenomena are associated with the decrease or increase of the system’s entropy. But first of all, in order to isolate the magnetic part, lattice contribution has to be discussed.

3.2.1 Lattice heat capacity

Every physical substance whether it contains magnetic ions or not, exhibit a lattice heat capacity, which accounts for the unavoidable presence of the lattice vibrations. This is also the basis for the Debye theory of lattice heat capacity. With decreasing temperature, lattice vibrations relaxes, resulting in a smooth monotonic reduction of the lattice heat capacity, which eventual achieves zero at $T = 0$ K. It is this fact that causes so much interest to investigate magnetic systems at low temperatures, for then magnetic contribution constitutes a much larger fraction of the whole.

In a Debye model, the lattice vibrations (phonons) are assumed to occupy the $3N$ lowest energies of a harmonic oscillator. As a result, the Debye lattice specific heat is written as (80):

$$C_{latt} = 9Nk_B(T/\theta_D)^3 \int_0^{T/\theta_D} x^4 e^x / (e^x - 1)^2 dx, \quad (3.35)$$

where $x = \hbar\omega/k_B T$ and $\theta_D = \hbar\omega_{max}/k_B$ is called Debye temperature (k_B is the Boltzmann constant). For temperatures up to $\sim \theta_D/10$, this can be relatively well approximated as $C_{latt} \sim (T/\theta_D)^3$, whereas for higher temperatures one often considers also corrections with higher odd powers.

3.2.2 Magnetic contributions to the heat capacity

In the first step, magnetic heat capacity can be divided in to two parts. Above the magnetic transition temperature T_N , a high-temperature series expansion of exchange-coupled spin contribution to the entropy has to be considered, which describes the increase in the heat capacity due to short-range magnetic correlations far above T_N and is typically described with (80), (81)

$$C_{short} = AT^{-2}, \quad (3.36)$$

where $A > 0$. On the other hand, below T_N , we have a contribution of the long-range ordering effects C_{long} .

In case when lattice specific heat follows T^3 law in the measured temperature region, the total specific heat above the T_N can be described as $C_{latt} + C_{short} = BT^3 + AT^{-2}$. This way an approximate estimation for $C_{latt} \sim BT^3$ is obtained. However, to be more precise, one needs to consider the complete expression for C_{latt} (equation 3.35). It is even more convenient if one can measure the specific heat of an isostructural nonmagnetic compound, which should give a very good estimation for C_{latt} . Essentially, after subtracting the lattice contribution we are left with the magnetic contribution alone.

Analyzing C_{mag} at very low temperatures using the spinwave theory can determine if the long-range magnetic ordering of a target material is ferromagnetic or antiferromagnetic. The specific heat due to the spin-wave excitation, C_{SW} , is expressed by (81), (82):

$$C_{SW} \propto T^{d/n}, \quad (3.37)$$

where d stands for the dimensionality of the magnetic lattice and n the exponent in the dispersion relationship: $n = 1$ for antiferromagnets and $n = 2$ for ferromagnets. This expression can be further improved by considering that long-wavelength spin waves are excited at low temperatures, and hydrodynamic Heisenberg spin-wave theory (83) can be applied assuming also the field dependence of the spin-wave gap Δ (82):

$$C_{SW} = B_{SW} T^{d/n} \int F(\Delta, G, H, T) dx, \quad (3.38)$$

where the integral $\int F(\Delta, G, H, T) dx = \int_{(\Delta g\mu_B H)/k_B T}^{\infty} [x^2 e^x / (e^x - 1)^2] [x - (\Delta + g\mu_B H)/k_B T]^{1/2} dx$, and constant B_{SW} depends on the spin-wave stiffness and molar volume of the compound.

Finally, the magnetic transition entropy, ΔS_{mag} , is obtained directly from C_{mag} after calculating the integral (84)

$$\Delta S_{mag} = \int_0^T C_{mag} d(\ln T). \quad (3.39)$$

The integration over the complete temperature interval should yield $\Delta S_{mag} = R \ln(2S+1)$, where R is the gas constant and S is the electron spin, which corresponds to entropy difference between totally disordered spins, at high temperatures, and perfectly ordered spins, at $T = 0$ K.

Moreover, from the temperature dependence of ΔS_{mag} the dimensionality of magnetic ordering can be determined, i.e., whether the system has two or three-dimensional (2D or 3D) magnetic lattice. When the value of ΔS_{mag} is divided into two terms, such as the magnetic entropy values below T_N ($\Delta S_{mag-lower}$) and above T_N ($\Delta S_{mag-upper}$), the ratio of $\Delta S_{mag-lower}/\Delta S_{mag}$ for the magnetic lattices of the 3D Ising, 2D Ising, and 3D Heisenberg types are 81 %, 44 %, and 62 %, respectively (81). This is due to the presence of the short-range ordering effects above T_N , i.e., the lower is the dimensionality of the system further above T_N short-range correlations develop, resulting in a significant $\Delta S_{mag-upper}$.

3.2.3 Data acquisition

The specific heat measurements of small samples are typically performed on a so called physical property measurement system (PPMS), which measure the heat capacity at constant pressure

$$C_p = \left(\frac{dQ}{dT} \right)_p. \quad (3.40)$$

The machine (Figure 17a) controls the heat added and removed from a sample while monitoring the resulting change in temperature. The measurements are acquired by so called thermal relaxation process is illustrated on Figure 17b.

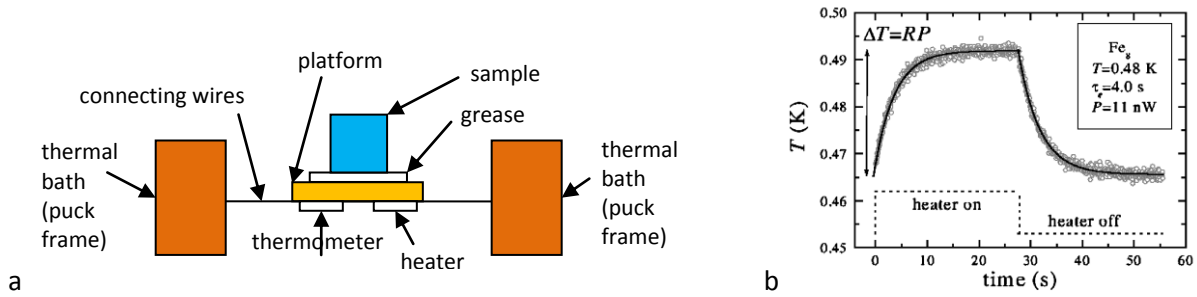


Figure 17: (a) PPMS setup for specific heat measurements, and (b) signal acquired by thermal relaxation method.

The simplest model to analyse the thermal relaxation data assumes that the sample and the sample platform are in good thermal contact with each other and are at the same temperature. Within this model the temperature of the platform as a function of a time obeys the equation

$$C_{total} \frac{dT}{dt} = -K_w(T - T_b) + P(t), \quad (3.41)$$

where C_{total} is the heat capacity of the sample and platform, K_w is the thermal conductance of the supporting wires, T_b is the temperature of the thermal bath, and $P(t)$ is the power applied by the heater. The solution of this equation is given by exponential functions with a characteristic time-constant equal to C_{total}/K_w .

3.3 Magnetization measurements

There are quite a few methods to measure the sample's magnetization. However, for measurements in magnetic field up to ~ 12 T the most commonly employed technique, which is also the most sensitive, uses a superconducting quantum interference device (SQUID). On the other hand, in order to measure magnetization in high magnetic fields, i.e., above the critical field of the SQUID superconductor (typically above 12 T), magnetic torque measurements are a very popular choice.

3.3.1 Superconducting quantum interference device

Nowadays, the most commonly used superconducting quantum interference device (SQUID) has two Josephson junctions (two superconductors linked by a non-conducting barrier) in parallel in a superconducting loop, which makes the Josephson effect possible (Figure 18). In the absence of any external magnetic field, the input current I is split equally into the two branches. Now, consider a small amount of applied external magnetic flux. This induces screening current I_s that generates the magnetic field to cancel the applied flux. As a result, the current in one of the branches of the superconducting loop is in the direction of I , and is equal to $I/2 + I_s/2$ and in the second branch is in the opposite direction of I and is equal to $I/2 - I_s/2$. As soon as the current in any one of the branches exceeds the critical current for the Josephson junction, the superconducting ring becomes resistive and a voltage appears across the junction. It is known that the flux enclosed by the superconducting loop must be an integer number of the flux quanta ϕ_0 . Hence if the external flux exceeds $\phi_0/2$, the SQUID instead of screening the flux, energetically prefers to increase it to ϕ_0 . The screening current now flows in the opposite direction. Thus the screening current changes direction every time the flux increases by half integer multiples of ϕ_0 , what makes the critical current I_c oscillate as a function of the applied flux. If the input current is more than I_c , then the SQUID always operates in the resistive mode and the voltage in this case is a function of the applied magnetic field and the period equal to ϕ_0 (85) (Figure 18). As a result, the increase of the magnetic field can be monitored by counting the oscillations of the SQUID voltage.

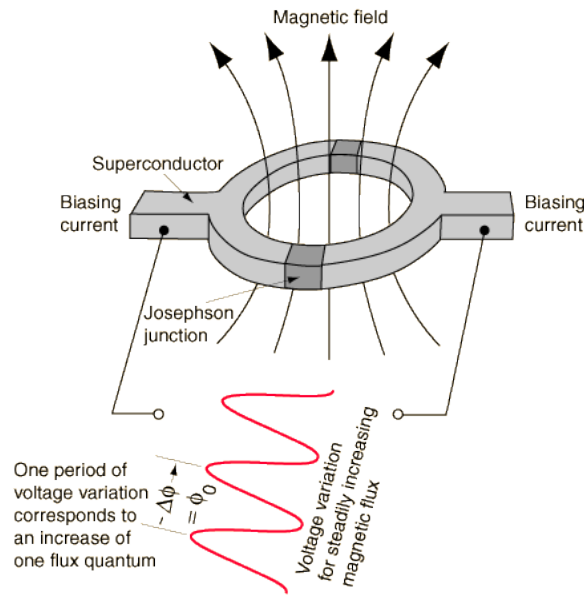


Figure 18: Basic design of SQUID magnetometer (86).

3.3.2 Magnetic torque measurements

Magnetic torque measurements are particularly useful for single crystal samples, where standard SQUID technique fails, e.g. in strong applied magnetic fields. The general principle behind the magnetic torque measurements is that a sample mounted on a flexible beam (cantilever) will respond to the application of a quasi-static magnetic field by experiencing force and torque, which deflects the beam. This technique was developed by Brooks et al. (87) at MIT in 1980s. The magnitude of the force \vec{F} and torque $\vec{\tau}$ are related to the samples magnetization \vec{M} and applied magnetic field $\vec{B}||z$ in the following way

$$\vec{F} = \vec{M} \cdot \frac{d\vec{B}}{dz}, \quad (3.42)$$

$$\vec{\tau} = \vec{M} \times \vec{B}. \quad (3.43)$$

The deflection of the beam is proportional to $\vec{\tau}$ and can be measured in a number of ways: (i) capacitively (88), (ii) piezo-resistively (89), (iii) optically (e.g. via diffraction grating), etc. If the magnetic moment of a sample is anisotropic, then measurements of the torque are more sensitive than force measurements in the experimentally achievable field gradients. Hence, measurements are typically performed in a zero-field gradient, which further suppress induced magnetic force and promotes the torque response. Sensitivity of such torque magnetometer depends on the stiffness of the flexible beam material, the sensitivity of the cantilever to temperature fluctuations and mechanical vibrations, the quality of the measuring instrumentation, and the magnitude of the applied magnetic field. Typical sensitivities for magnetic moment range from 10^{-10} Am^2 to 10^{-12} Am^2 for a torque measured at 20 T. Our experiments were performed at Grenoble High Magnetic Field Laboratory (GHMFL), France, where the cantilever is metallic and has lateral dimensions of approximately $3 \times 4 \text{ mm}^2$, while it is thinner than 0.1 mm. It is mounted on a fulcrum above the conductive plate, which serves as the opposite site of the capacitor (Figure 19).

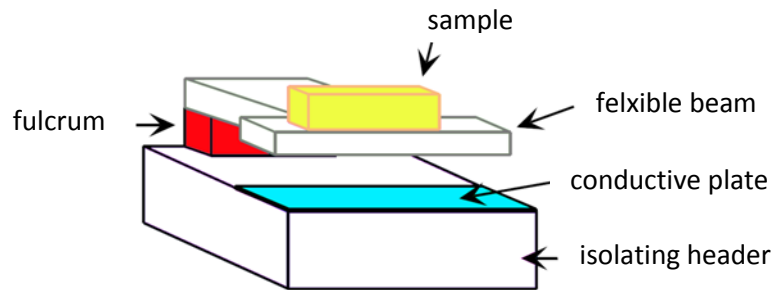


Figure 19: Here, basic parts of the cantilever magnetometer are shown. The sample is attached to the flexible beam (typically with varnish or vacuum grease). The flexible plate is metallic and typically thinner than 0.1 mm. The conductive plate serves as the opposite part of the capacitor, and is permanently attached to the header, which is typically made of fibreglass. The fulcrum is either part of a flexible plate or a part of the header.

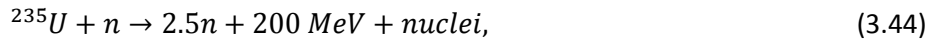
The interpretation of the data is more or less straight forward, since the measured magnetic torque directly reflects the behaviour of the magnetization. However, the determination of the exact magnetization is rather tricky. First, in order to dismount the sample, the cantilever has to be dismounted as well. Since the consecutive mounting is always done in a slightly different manner, the measurements are not completely repeatable and, therefore, making the exact calibration of the system's sensitivity unfeasible. Second, when magnetic field is applied, the cantilever tilts due to the resulting magnetic torque. As the actual torque is being dependent on the tilting angle, the estimation of the exact value of magnetization is rather difficult.

3.4 Magnetic neutron scattering

The main advantage for the use of neutrons to investigate magnetic properties is that they do not carry the electric charge, while they have an intrinsic magnetic moment. Therefore they interact only with magnetic moments (via magnetic dipole-dipole interaction) and atoms' nuclei (via contact interaction), avoiding the strong electromagnetic interaction with surrounding charges. As a consequence they can easily penetrate the sample and form a scattering pattern that is a combination of both, nuclear as well as magnetic, contributions. Hence we get information about the crystal and magnetic structure simultaneously.

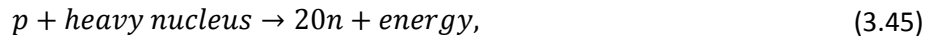
3.4.1 Neutron sources

There are two methods currently employed to generate neutrons for use in scattering experiments, each with its pros and cons. The first method is nuclear fission, occurring in a traditional nuclear reactor with uranium described with the following equation:



where the kinetic energy (200 MeV) is distributed among the resulting particles so that the total momentum is conserved. A reactor at a neutron scattering facility would be designed to produce an excess of neutrons beyond that required to maintain the chain reaction, and it is these excess neutrons which are used for scattering. The main advantage of a reactor source is that it produces a high flux of neutrons at a steady rate.

The other method of generating neutrons for scattering is with a spallation source. Accelerated protons strike a heavy metal target, and the impact of the proton beam triggers a nuclear reaction:



i.e., after each impact of proton 20 to 30 neutrons are expelled. The spallation process is the excitation and neutron emission of the target until it achieves a stable nuclear state. Such a source typically produces a much lower flux of neutrons than a reactor.

3.4.2 Neutron detection

The main advantage of neutrons that they interact rather weakly with matter, on the other hand, present a problem when it comes to detecting scattered neutrons. Neutrons are not charged so they cannot be detected using radiation detectors which rely on direct gas ionisation. Instead the neutrons need to cause some other atom to emit charged particles which will ionise a gas and therefore be electronically detectable. The standard way of doing this is to use a chamber filled with ${}^3\text{He}$ gas, which then undergoes the following reaction:



so that p , with kinetic energy of 0.77 MeV, ionise the gas and give rise to a signal, proportional its initial kinetic energy, which can be distinguished from signals at different energies arising from gamma rays entering the detector, for example. The ${}^3\text{H}$ nucleus eventually decays to form another ${}^3\text{He}$ nucleus and an electron, so the supply of helium in the detector does not need to be replenished.

It is important to know the flux of neutrons incident on the sample, especially given that this will vary depending on the value of the incident energy. Therefore, the incident flux is measured using a monitor, which is simply a rather inefficient neutron detector. Additionally, the monitor's efficiency is inversely proportional to the incident neutron wavevector k_i . Hence, when the final wavevector k_f is fixed, the normalization of detector counts to the monitor count rate already includes the correction for the k_f/k_i term in equation 3.68.

3.4.3 Neutron scattering cross sections

The derivation of the following results can be found in more detail in, for example, the book by Squires (90). Here we review only the important results which are stated without their associated proofs.

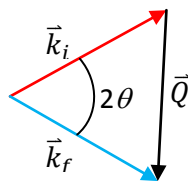


Figure 20: The scattering triangle, relating the incident and final wavevectors to the scattering wavevector.

A neutron scattering event must conserve both total momentum and energy, and these simple rules provide a starting point for the theory of neutron scattering. Energy conservation gives us

$$E_i - E_f = \frac{\hbar}{2m_N} (\vec{k}_i^2 - \vec{k}_f^2) = \hbar\omega, \quad (3.47)$$

where E_i and E_f are respectively the incident and final energies of the neutron, \vec{k}_i and \vec{k}_f are the incident and final neutron wavevectors and $\hbar\omega$ is the energy of an excitation in the sample. Meanwhile momentum conservation gives us

$$\vec{Q} = \vec{k}_f - \vec{k}_i, \quad (3.48)$$

where \vec{Q} is the scattering wavevector. The process is shown schematically in Figure 20. In practice, vectors \vec{k}_i and \vec{k}_f are determined by monochromators – large single crystals, where a particular Bragg diffraction is chosen, while \vec{Q} is assumed from equation 3.48. Taking together equations 3.47 and 3.48 allows us to calculate from a given scattering event the wavevector and energy of the excitations (or static order if $\hbar\omega$ is zero) in the sample.

The quantity measured during a neutron scattering experiment is the double differential cross-section:

$$\frac{d^2\sigma}{d\Omega dE} = \frac{\left(\begin{array}{l} \text{total number of neutrons scattered per unit time into the solid} \\ \text{angle } d\Omega \text{ in the direction } \theta, \phi \text{ with energy between } E \text{ and } E + dE \end{array} \right)}{d\Omega dE \Phi}, \quad (3.49)$$

where the total incident neutron flux is given by Φ . For elastic scattering we do not include the dE term in the denominator, i.e. we are only interested in the differential cross-section $\left(\frac{d\sigma}{d\Omega}\right)$. This is justified because the probability for elastic scattering event is several orders of maximum greater compared to inelastic one, which renders the differentiation with respect to energy redundant. So in both nuclear and magnetic elastic scattering it is $\left(\frac{d\sigma}{d\Omega}\right)$ that is of interest.

3.4.3.1 Nuclear elastic scattering

The coherent nuclear elastic scattering cross section is given by

$$\frac{d\sigma}{d\Omega} = N \frac{(2\pi)^3}{V_0} |F_N(\vec{Q})|^2, \quad (3.50)$$

where N is the number of unit cells in the crystal, V_0 is the volume of the unit cell and F_N is the nuclear structure factor given as

$$F_N(\vec{Q}) = \sum_j \vec{b}_j e^{i\vec{Q}\cdot\vec{r}_j} e^{-W_j(\vec{Q}, T)}, \quad (3.51)$$

where the sum runs over all atoms j , \vec{r}_j is the position of the j -th atom, and \vec{b}_j is the nuclear scattering length of the j -th atom. The Debye-Waller factor W_j for the j -th atom takes into account that atoms are not frozen to their lattice sites, but rather they undergo a certain amount of thermal motion about an equilibrium position. In other words, with increasing temperature the thermal motion increases, and consequently reduces the intensity of the Bragg peaks, which is parameterised by the Debye-Waller factor. For a Bravais crystal the Debye-Waller factor is defined as

$$W_j(\vec{Q}, T) = \frac{1}{2} \langle (\vec{Q} \cdot \vec{u}_j(T))^2 \rangle, \quad (3.52)$$

where $\vec{u}_j(T)$ is the thermal displacement of atom j from its equilibrium position.

Note that the cross section stated in equation 3.50 is that for coherent nuclear scattering. There is also an incoherent cross section that gives rise to an isotropic background scattering, which must be subtracted from any data before analysis is performed.

3.4.3.2 Magnetic elastic scattering

Let us now consider the scattering of neutrons by magnetic interactions. Neutrons have a magnetic moment

$$\vec{\mu}_n = -g_n \mu_N \vec{\sigma}, \quad (3.53)$$

where μ_N is the nuclear magneton, $g_n = 1.913$, and $\vec{\sigma}$ is the Pauli spin operator with values ± 1 . The magnetic interaction potential operator $\hat{V}_M(\vec{r})$ between neutrons and the local magnetic field $\vec{B}(\vec{r})$ in a material (e.g. resulting local magnetic field from magnetic moments in the lattice) is given by

$$\hat{V}_M(\vec{r}) = \vec{\mu}_n \cdot \vec{B}(\vec{r}). \quad (3.54)$$

However, the cross section must contain terms which are functions of wavevector \vec{Q} rather than spatial coordinate \vec{r} , so the Fourier transforms, $\hat{V}_M(\vec{Q}) = \int \hat{V}_M(\vec{r}) e^{i\vec{Q}\cdot\vec{r}} d\vec{r}$ and $\vec{B}(\vec{Q}) = \int \vec{B}(\vec{r}) e^{i\vec{Q}\cdot\vec{r}} d\vec{r}$, are used:

$$\hat{V}_M(\vec{Q}) = \vec{\mu}_n \cdot \vec{B}(\vec{Q}). \quad (3.55)$$

Now we want to expand the expression for $\vec{B}(\vec{r}) = \nabla \times \vec{A}(\vec{r})$, considering that the magnetic vector potential $\vec{A}(\vec{r})$, which gives rise to the magnetic field, results from a single unpaired electron:

$$\vec{A}(\vec{r}) = \frac{\mu_0 \vec{\mu}_e \times \hat{r}}{4\pi r^2}. \quad (3.56)$$

Here \hat{r} is a unit vector in the direction of the vector \vec{r} , where the latter defines the distance from the magnetic moment $\vec{\mu}_e$. Taking into the account also vector algebra explained in reference (91), $\vec{B}(\vec{r})$ can be finally written as

$$\nabla \times \left(\frac{\vec{\mu}_e \times \hat{r}}{r^2} \right) = \frac{1}{2\pi^2} \int \hat{q} \times (\vec{\mu}_e \times \hat{q}) e^{i\vec{q}\cdot\vec{r}} d\hat{q}. \quad (3.57)$$

Eventually we can rewrite the equation 3.55 as

$$\hat{V}_M(\vec{Q}) = -\mu_0 \vec{\mu}_n \cdot \vec{M}_\perp(\vec{Q}), \quad (3.58)$$

where $\vec{M}_\perp(\vec{Q})$ is the component of the electron's magnetic moment (due to spin and orbital contributions) perpendicular to the scattering wavevector, such that

$$\vec{M}_\perp(\vec{Q}) = \hat{Q} \times [\vec{\mu}_e(\vec{Q}) \times \hat{Q}], \quad (3.59)$$

where \hat{Q} is a unit vector pointing in the direction of the scattering wavevector \vec{Q} .

We must now consider the implications of the fact that the neutrons, which are magnetically scattered by electrons, will not necessarily consist of a spherical wave. So to formulate scattering cross sections, which assume that the incident and scattered beams are plane-waves, a correction factor must be applied. In order to avoid the complicated form for the magnetisation $\vec{M}(\vec{Q})$ in equation 3.59, we make the dipole approximation, which enables the use of the dipole moment of the scattering electrons $\vec{\mu}$ instead. Assuming also that for a $3d$ ion the orbital angular momentum L is often quenched, making the total angular momentum J not a good quantum number, magnetisation can be written as

$$\vec{M}(\vec{Q}) = -g\mu_B f(\vec{Q})\vec{S} = f(\vec{Q})\vec{\mu}, \quad (3.60)$$

where \vec{S} is the spin quantum number, and $f(\vec{Q})$ is the magnetic form factor. If we denote the normalised spin density on an atom by $\rho_S(\vec{r})$, then the form factor is defined, for the spin-only case, as the Fourier transform of $\rho_S(\vec{r})$ (92),

$$f(\vec{Q}) = \int d^3\vec{r} e^{i\vec{Q}\cdot\vec{r}} \rho_S(\vec{r}). \quad (3.61)$$

The derivation of the explicit form of the magnetic form factor $f(\vec{Q})$ is rather complicated and is omitted here for brevity. For a full derivation see the work of Freeman (93). However, $f(\vec{Q})$ for a pure $(x^2 - y^2)$ orbital can be approximated analytically using Bessel functions as (94)

$$f(\vec{Q}) = \langle j_0(\vec{Q}) \rangle - \frac{5}{7}(1 - 3 \cos^2 \beta) \langle j_2(\vec{Q}) \rangle + \frac{9}{56} \left(1 - 10 \cos^2 \beta + \frac{3}{35} \cos^4 \beta \right) \langle j_4(\vec{Q}) \rangle. \quad (3.62)$$

Here β is the angle between the scattering wavevector and the axis perpendicular to the $(x^2 - y^2)$ orbital plane (z axis), while the expectation values of the Bessel functions are approximated in terms of sums of exponentials with suitable coefficients (91) as

$$\begin{aligned} \langle j_0(s) \rangle &= A e^{-as^2} + B e^{-bs^2} + C e^{-cs^2} + D, \\ \langle j_{n>0}(s) \rangle &= (A e^{-as^2} + B e^{-bs^2} + C e^{-cs^2} + D) s^2. \end{aligned} \quad (3.63)$$

Here s is defined as

$$s = \frac{\sin \theta_s}{\lambda} = \frac{|\vec{Q}|}{4\pi}, \quad (3.64)$$

where θ_s is the Bragg angle at the sample, and λ is the wavelength of the incident neutrons.

Note that for a spherical charge density (i.e. $L = 0$, so spin-only) equation 3.61 simplifies considerably to

$$f(\vec{Q})_{spherical} = \langle j_0(\vec{Q}) \rangle. \quad (3.65)$$

For magnetic elastic scattering:

$$\frac{d\sigma}{d\Omega} = N \frac{(2\pi)^3}{V_{mag}} \left(\frac{g_n r_0}{2} \right)^2 \sum_{\alpha\beta} (\delta_{\alpha\beta} - \hat{Q}_\alpha \hat{Q}_\beta) \langle F^{(\alpha)}(-\vec{Q}) \rangle \langle F^{(\beta)}(\vec{Q}) \rangle, \quad (3.66)$$

where N is the number of magnetic unit cells, V_{mag} is the volume of the magnetic unit cell, $r_0 = 2.8 \times 10^{-15}$ m is the classical electron radius, the sum over α and β is a sum over all combinations of two Cartesian axes (i.e. xx, xy, xz, \dots), \hat{Q}_α is the α component of \hat{Q} , and $\delta_{\alpha\beta}$ is the Kronecker delta. $F^{(\alpha)}(\vec{Q})$ is the α component of the magnetic unit cell structure factor, given by

$$F^{(\alpha)}(\vec{Q}) = \sum_j \mu_j^{(\alpha)} f_j^{(\alpha)} e^{i\vec{Q}\cdot\vec{r}_j} e^{-W_j(\vec{Q}, T)}, \quad (3.67)$$

where the sum runs over all atoms, $\mu_j^{(\alpha)}$ is the α component of the magnetic moment of the j -th atom, and $f_j^{(\alpha)}$ is the α component of the magnetic form factor of the j -th atom.

3.4.3.3 Magnetic inelastic scattering

Let us consider now the case of an inelastic scattering process, i.e. one in which the neutron gains or loses energy during the scattering process. The cross section for magnetic inelastic scattering, in the dipole approximation for the case of spin-only scattering, is given by

$$\frac{d^2\sigma}{d\Omega dE} = \left(\frac{g_n r_0}{2}\right)^2 f^2(\vec{Q}) e^{-2W(\vec{Q}, T)} \frac{k_f}{k_i} \sum_{\alpha\beta} (\delta_{\alpha\beta} - \hat{Q}_\alpha \hat{Q}_\beta) S^{\alpha\beta}(\vec{Q}, \omega), \quad (3.68)$$

where $S^{\alpha\beta}$ are the space and time Fourier transforms of the time dependent spin-spin correlation functions

$$S^{\alpha\beta}(\vec{Q}, \omega) = \frac{1}{2\pi\hbar} \int_{-\infty}^{\infty} \sum_{j,j'} e^{i\vec{Q}\cdot(\vec{r}_j - \vec{r}_{j'})} e^{-i\omega t} \langle S_{j'}^\alpha(0) S_j^\beta(t) \rangle dt, \quad (3.69)$$

where $S_{j'}^\beta(t)$ is the β -component of the spin at site j' at time t , and $\langle \dots \rangle$ denotes an average over the initial states of the system. This expression can be considerably simplified if we consider a system where the excitations are out of the ground state only. (Strictly speaking this means a system is at zero temperature, however, for non-zero temperatures the described simplification is still a good approximation provided that the excited state lies at energy greater than $k_B T$ above the ground state.) The ground state has wave function $|0\rangle$ and energy E_0 , and the spin-spin correlation function is given by

$$S^{\alpha\alpha}(\vec{Q}, \omega) = \sum_{\lambda} |\langle \lambda | S^\alpha(\vec{Q}) | 0 \rangle|^2 \delta(\hbar\omega - E_0 - E_\lambda), \quad (3.70)$$

where the sum is over all eigenstates $|\lambda\rangle$ of the final state of the system with energy E_λ . $S^\alpha(\vec{Q})$ is the Fourier transform of the α -component of the spin S_j^α .

3.4.4 Polarisation analysis

Spin-flip (SF) refers to when the spin state of the neutron is flipped from up to down, or vice versa, and non-spin-flip (NSF) refers to when the spin state of the neutron remains unchanged during scattering. In general the scattering cross section is given by

$$\frac{d^2\sigma}{d\Omega dE} \propto |\langle k_f S_f | \hat{V} | k_i S_i \rangle|^2, \quad (3.71)$$

where the initial and final neutron states are labelled by their wavevectors k_i and k_f , and their spin states S_i and S_f respectively. \hat{V} is the scattering potential, which contains contributions from both, nuclear and magnetic potentials.

The coherent nuclear cross section is proportional to

$$\langle S_f | \hat{V}_{nuc}^{coh}(\vec{Q}) | S_i \rangle = \hat{V}_{nuc} \langle S_f | S_i \rangle, \quad (3.72)$$

where $\langle S_f | S_i \rangle = 0$ for spin-flip (SF) scattering ($S_i \neq S_f$), or $\langle S_f | S_i \rangle = 1$ for non-spin-flip (NSF) scattering ($S_i = S_f$). Therefore all coherent nuclear scattering is in the non-spin-flip channel.

Recall equation 3.58, which gives the Fourier transform of the magnetic scattering potential. Writing out the dot product explicitly

$$\hat{V}_M(\vec{Q}) = \sum_{\alpha} \mu^\alpha M_{\perp}^\alpha(\vec{Q}). \quad (3.73)$$

We define the quantisation direction as z and calculate the matrix elements involving $\hat{V}_M(\vec{Q})$ for the various different spin-flip states as follows.

Table 1: The matrix elements for different polarisation scattering events.

Transition	Matrix element
$ \uparrow\rangle \rightarrow \uparrow\rangle$	$\langle S_f \hat{V}_M(\vec{Q}) S_i \rangle = M_{\perp}^z(\vec{Q})$
$ \downarrow\rangle \rightarrow \downarrow\rangle$	$\langle S_f \hat{V}_M(\vec{Q}) S_i \rangle = M_{\perp}^z(\vec{Q})$
$ \uparrow\rangle \rightarrow \downarrow\rangle$	$\langle S_f \hat{V}_M(\vec{Q}) S_i \rangle = M_{\perp}^x(\vec{Q}) + iM_{\perp}^y(\vec{Q})$
$ \downarrow\rangle \rightarrow \uparrow\rangle$	$\langle S_f \hat{V}_M(\vec{Q}) S_i \rangle = M_{\perp}^x(\vec{Q}) - iM_{\perp}^y(\vec{Q})$

The equations in Table 1 allow us to determine which component of the magnetic scattering can be observed with a given flipper channel and polarisation direction. These rules can be summarised as follows:

1. No component of spin parallel to \vec{Q} may be detected.
2. In the SF channel only those components of spin perpendicular to the polarisation \vec{P} , subject to (1), may be detected.
3. In the NSF channel only those components of spin parallel to \vec{P} may be detected, subject to (1).

This then allows us to calculate the component of a static spin or a fluctuating spin in the three possible orthogonal directions. Let us define N as the coherent nuclear scattering arising from structural Bragg peaks, phonons etc. This scattering does not depend on neutron spin polarisation and does not flip the neutron spins, so it is divided equally between the three orthogonal NSF polarisation channels. Finally we can write the master equations for the polarization dependent partial differential cross-section according to Blume and Maleyev (95), (96), (97):

$$\sigma \equiv \frac{d^2\sigma}{d\Omega dE} = N + M^y + M^z - P_0^x C + P_0^y R^y + P_0^z R^z \quad (3.74)$$

and for the final polarization vector

$$\begin{aligned} \vec{P}' &= \underline{\tilde{P}}\vec{P} + \vec{P}'', \\ \sigma \underline{\tilde{P}} &= \begin{pmatrix} (N - M^y - M^z) & iI^z & -iI^y \\ -iI^z & (N + M^y - M^z) & M_{mix} \\ iI^y & M_{mix} & (N - M^y + M^z) \end{pmatrix}, \\ \sigma \vec{P}'' &= \begin{pmatrix} C \\ R^y \\ R^z \end{pmatrix}. \end{aligned} \quad (3.75)$$

Here $\underline{\tilde{P}}$ is the polarization tensor, which describes the rotation of the initial polarization vector \vec{P}_0 in the scattering process, \vec{P}'' is the polarization created in the scattering process at the sample, $M^{y,z}$ are y and z components of the magnetic contribution ($\propto \langle \vec{M}_{\perp}^{y,z}(\vec{Q}) \rangle^2$), $R^{y,z}$ and $I^{y,z}$ are real and imaginary parts of the nuclear-magnetic interference term ($\propto \langle F_N(\vec{Q}) \rangle \langle \vec{M}_{\perp}^{y,z}(\vec{Q}) \rangle$), while C and M_{mix} are chiral and mixed magnetic contribution ($\propto \langle \vec{M}_{\perp}^y(\vec{Q}) \rangle \langle \vec{M}_{\perp}^z(\vec{Q}) \rangle$), which are explicitly written in reference (97). We stress that all terms included in equations 3.74 and 3.75 are determined by the sample properties that are described solely by the nuclear structure factor F_N and the magnetic interaction vector $\vec{M}_{\perp}(\vec{Q})$, as described above.

Consequently the spherical polarimetry measurements are very useful for study of non-collinear magnetic structures. For such compounds it is often impossible to distinguish between different possible magnetic structures by other techniques because they are not able to determine the directional information held in magnetic structure factors. Additionally, it is useful for investigation of hybrid correlation functions in inelastic neutron scattering in compounds where nuclear and magnetic degrees of freedom or different magnetic degrees of freedom interfere (98).

3.4.5 Neutron scattering instruments

Here we give a short overview of the neutron scattering instruments, which were used during our study.

3.4.5.1 Powder diffractometer DMC

The cold neutron powder diffractometer DMC at Swiss spallation neutron source SINQ, at Paul Scherrer Institute (PSI), Switzerland is a flexible instrument for efficient neutron powder diffraction studies in the fields of crystallography, solid state physics, chemistry and material science, in particular for the determination of weak magnetic intensities. Special features are the position sensitive detector, the oscillating radial collimator system and the large diversity of available sample environment devices. DMC is complementary to the high-resolution diffractometer and is designed for high-intensity performance.

In a conventional neutron powder diffractometer, at a continuous source, a beam of monochromatic neutrons is incident upon a sample and the scattered neutron intensity is measured as a function of the scattering angle 2θ (Figure 21). The monochromatic incident beam is produced by Bragg reflection from an appropriate single crystal monochromator. The neutron count-rate is measured in more detectors, covering a broad 2θ interval. Masks and collimators restrict the spatial and angular widths of the beam.

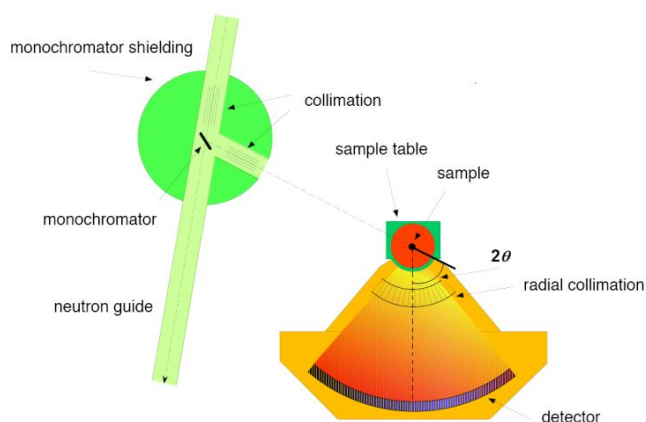


Figure 21: Experimental setup of powder diffractometer DMC at SINQ, at PSI, Switzerland (99).

In an ideal experiment the incident beam would have a single wavelength and unique direction, but there would be no intensity at the sample. In practice the incident beam has a narrow distribution of wavelengths and a narrow distribution of directions. The intensity at the sample is roughly proportional to the product of the widths of these distributions whereas the overall resolution of the instrument (assuming its design is optimized) is roughly proportional to one of the widths. Depending on the experiment the compromise between intensity and resolution will vary.

3.4.5.2 Single crystal diffractometer TriCS

The thermal neutron single crystal diffractometer TriCS at SINQ, at PSI is designed for investigations of commensurate and incommensurate crystal and magnetic structures as well as phase transitions driven by temperature, magnetic field or pressure. It is appropriate for samples with small-to-medium size unit cells (lattice parameter $< 20 \text{ \AA}$). The layout of the instrument is shown in Figure 22.

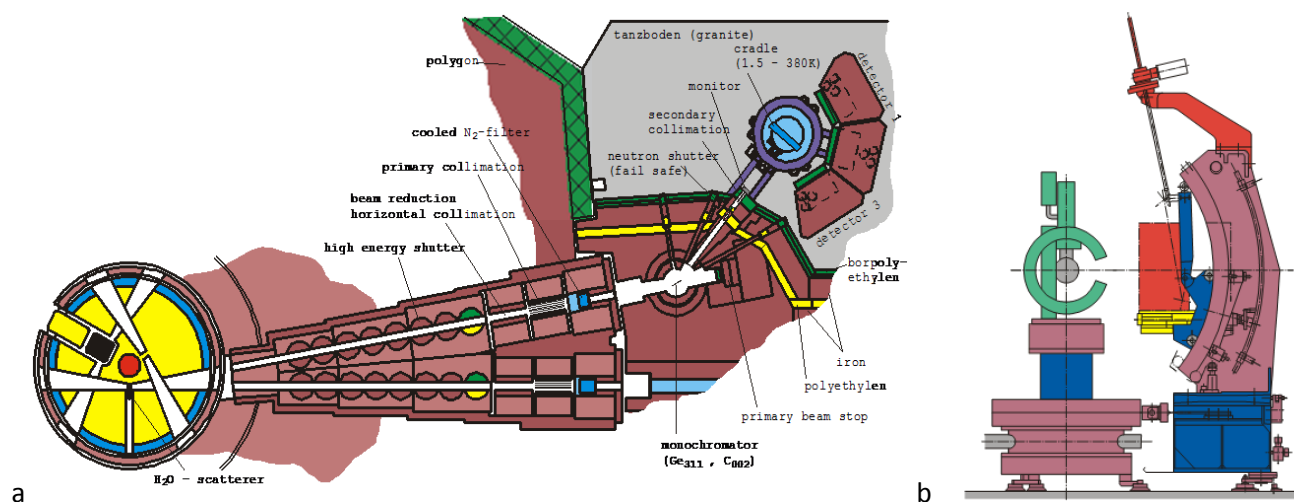


Figure 22: Single crystal diffractometer TriSC at SINQ, at PSI, Switzerland: (a) top view, (b) side view (99).

The incident white neutron beam first hits a monochromator crystal. The selected wavelength is not variable. It is equipped with 2 focusing monochromators: Ge₃₁₁ and C₀₀₂ for short (1.18Å) and long (2.3Å) wavelength and the possibility to select different reflections peaks however make it possible to select between a few different neutron wavelengths. The sample is held in a standard eulerian cradle, which allows rotating the sample into an arbitrary position. It is possible to use up to three position sensitive detectors held on detector holders or alternatively a single detector can be fixed to this setup. The detectors may be moved up and down on a sphere around the sample. This allows to access different lattice planes when the eulerian cradle has been replaced by some cryostat or other sample environment devices to heavy to be used in conjunction with an eulerian cradle.

3.4.5.3 Triple-axis spectrometer TASP

TASP, the triple-axis spectrometer (TAS) with cold neutrons is located at the end of the 1RNR14 neutron guide of the SINQ spallation energy source, at PSI. TASP provides incident neutrons with a wide range of wavevectors ($1.05 \lambda^{-1} < k_i < 3.8 \lambda^{-1}$) and allows for large momentum transfers (up to 20 meV). It offers the option of polarised neutron experiments with either longitudinal or XYZ polarization analysis and neutron spherical polarimetry. For these experiments TASP has the option of a Mu-metal Polarization Analysis Devise, MuPAD.

A broad range of problems in condensed matter can be explored with TASP, such as the study of magnetic and structural phase transitions and their associated fluctuations, superlattice reflections and critical exponents. It is well suited for the study of low-energy collective excitations with high energy and momentum resolution and due to the very high sensitivity of the polarized neutrons techniques, it is an excellent tool to investigate complex magnetic structures. In addition, using diffuse scattering at TASP one can investigate various effects of disorder.

The TASP is constructed as follows. The monochromator selects from a polychromatic beam of neutrons a monochromatic one by Bragg reflection, i.e., only neutrons of a given wavelength (energy) fulfil the Bragg condition. Collimators can be used to ensure that the beam does not diverge too much, and they take the form of parallel plates which are coated with a neutron-absorbing material. Despite this the width of the neutron beam is likely to be larger than the width of the sample, so in order to improve the signal-noise ratio diaphragms are placed before and after the sample. Diaphragms are also placed in front of the analyser and detector in order to allow full illumination whilst reducing spurious scatter entering the detector, further improving the signal-noise ratio. The sample may be mounted in a standard orange cryostat, in a dilution

refrigerator, or in a cryomagnet depending on the need. The analyser crystals work in much the same way as the monochromator, i.e., one can choose different wavelengths to determine the final neutron wavevector k_f .

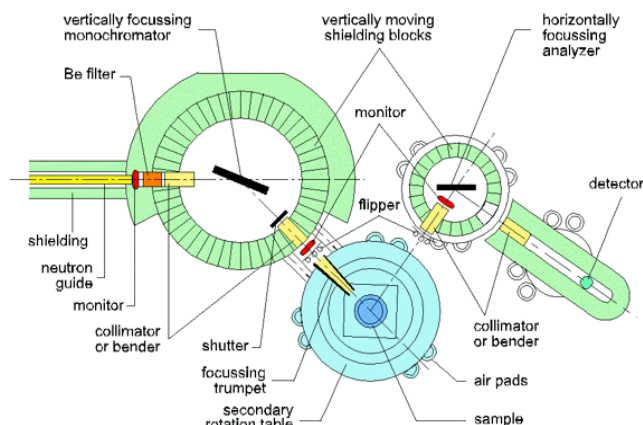


Figure 23: Layout of triple-axis spectrometer TASP at SINQ, at PSI, Switzerland (99).

3.4.5.4 Polarised neutron scattering

A variation on the basic TAS is the polarised neutron TAS, which works on the same principles as the basic TAS but has a few modifications. The basic idea behind these is to produce an incident beam of neutrons whose spins all point in the same direction. This is done by a polarising monochromator, which typically consists of ferromagnetic single crystals, arranged so that neutrons scatter off a particular Bragg planes, depending on the chosen wavelength. When the magnetic field is applied parallel to the monochromator surface, the spins in it will align parallel to the field. If the crystals are centrosymmetric the nuclear and magnetic structure factors for the particular peak are similar in value and the two kinds of scattering can interfere resulting in very good polarization. Eventually, this polarized flux hits the sample and by analysing the change in polarization state of the neutrons after scattering it is possible to measure scattering which is solely magnetic in origin.

The analysis of the scattered neutrons is based on so called flippers, which flip the neutron spin state from one eigenvalue to another, i.e. from spin up to spin down. The flipper is typically a radiofrequency coil, where a constant magnitude radio frequency magnetic field is applied parallel to the neutron beam while a static field applied perpendicular to the neutron beam varies in magnitude along the beam. For all neutron energies there will be some point in the flipper such that their Larmor frequency is equal to the radio frequency of the coil, thus resonance will occur and there will be a transition between the Zeeman split up and down states, i.e. a spin flip. A spin-flip magnetic scattering event would work as follows: the monochromator polarises the beam so that the spins are up, then the spins are flipped in the sample by interaction with a spin-1/2 magnetic moment/excitation (parallel to the neutron spin) so that the neutrons are now spin down. The flipper then changes the spin state of the scattered beam so that the magnetically scattered neutrons are spin up again. The analyser is then set to Bragg-reflect only spin up, so almost all of the non-magnetically scattered neutrons are not reflected into the detector, while the scattering from magnetic moments/excitations make up the vast majority of the neutrons arriving at the detector.

Our polarised neutron scattering data were collected in IN20, at Institute Laue Langevin, France. IN20 is a thermal beam three-axis spectrometer for inelastic scattering experiments in various sample environments (eg. magnets up to 15 T) and can be equipped with single-analyser-detector or Flatcone, with standard Helmholtz and CRYOPAD (zero-field) polarisation analysis. In latter case, instead of flippers, nutators are used, which adiabatically rotate the polarisation by two guide-field sections (axial and transverse) contained

in a single soft-iron cylinder for reducing the noise coming from the external components. The amplitude of the fields inside the nutator is 150 G, strong enough for assuring an adiabatic rotation of the polarisation.

3.5 μ SR Spectroscopy

The acronym μ SR stands for Muon Spin Rotation, Relaxation, or Resonance. μ SR is a widespread technique used in solid state physics and is closely related to NMR. The principle of the μ SR technique is quite simple. Positive muons are produced and implanted in a sample where they localize at a particular site. The local magnetic field \vec{B}_{loc} at this interstitial site exerts a torque on the muon spin ($S_\mu = 1/2$), so that the spin precesses around the local magnetic field with a frequency of $\omega = \gamma_\mu |\vec{B}_{loc}|$. Here $\gamma_\mu/2\pi = 135.53879$ (1) MHz T^{-1} is the gyromagnetic ratio of the muon. After a certain time, the muon decays and a positron is emitted, preferentially in the direction of the muon spin, at the moment of decay. The positron is detected. After collecting several million positrons the time-evolution of the polarization of an ensemble of muons can be reconstructed. The polarization function $P(t)$ reflects the spatial and temporal distribution of the magnetic field at the muon site. In this section a few elements of the μ SR technique will be elaborated on. A more detailed general description can be found in Refs. (100), (101). Experimental results on some exemplary materials can be found in Refs. (102), (103).

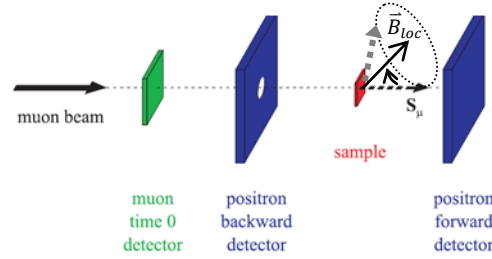


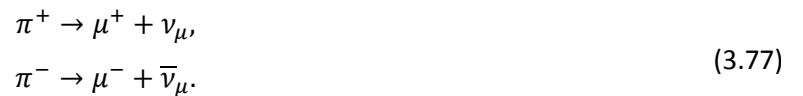
Figure 24: Experimental setup for μ SR consists of muon zero-time detector, as well as backward and forward positron detectors. In spite that the muon spin is actually antiparallel to the muon's momentum, they are drawn here in parallel for clarity. The arrows represent the Larmor precession of the muon spin in the local magnetic field \vec{B}_{loc} .

3.5.1 Production, life, and decay of the muon

The production of intense muon beams starts in large accelerators where protons (p) gain energies up to ~ 600 MeV. These highly energetic protons are aimed at a graphite or beryllium target. Several nuclear reactions take place between the protons and the protons and neutrons (n) of the target, leading to the production of pions (π):



where d stands for deuteron. The charged pions π^+ and π^- have an average life time of 26 ns and decay via a weak force process into the muons μ^+ and μ^- and the accompanying (anti-)neutrinos (ν_μ and $\bar{\nu}_\mu$):



The neutral pion π^0 plays no role in the μ SR technique, since it has a very short average life time of 0.089 fs before it decays into photons. In solid state physics almost all μ SR research is carried out using positive muons μ^+ .

Pions possess zero spin and neutrinos have a spin $S_\nu = 1/2$ polarized opposite to their momentum. Because angular momentum has to be conserved, the muon spin has to be antiparallel to its momentum in the rest frame of the pion. This allows the production of nearly 100 % polarized μ^+ -beam.

After production, the muons are directed to the μ SR instruments by electromagnetic guide fields using bending magnets and focussing quadrupole magnets. Along the path usually an electric and magnetic field separator is included to remove contaminant particles (mainly positrons) from the muon beam. After implantation in the sample the muon will thermalize. Along the first part of its track the muon thermalizes by energy exchange through ionizing host atoms and creating vacancies. This however does not influence the experimental results, since the final area of localization will not be affected. Along the last part of its track, the muon thermalizes by successive captures and dissociation of electrons from the host. The neutral bound state with an electron is known as muonium (μ^+e^-), an exotic light version of the hydrogen atom. In semi-conductors and insulators muonium can be stable, and it can even be incorporated in some organic materials. Finally, muonium dissociates and the muon will localize at an interstitial site. At its localization site, the muon magnetically interacts with the surrounding matter. The implantation and thermalization processes occur so rapidly (10^{-9} s) that depolarization is insignificant. The muon carries a relatively large magnetic moment, which even exceeds the proton's magnetic moment: $\mu_\mu = 3.2 \mu_p$. It therefore acts, as a very sensitive local magnetic field probe. Due to the absence of a quadrupolar electric moment ($S_\mu = 1/2$) the muon does not couple to electric field gradients.

The average muon life time is 2.2 μ s after which the muon decays into a positron e^+ via a three-body process

$$\mu^+ \rightarrow e^+ + \nu_e + \bar{\nu}_\mu, \quad (3.78)$$

where ν_e and $\bar{\nu}_\mu$ are the neutrinos and antineutrinos associated with the positron and the muon respectively. The decay positrons are emitted preferentially in the direction of the μ^+ spin, which allows a determination of the time evolution of the polarization. The probability distribution of the positron emission is given by

$$W_{e^+}(\theta) \propto (1 + a(E) \cos \theta), \quad (3.79)$$

where θ is the angle between the muon spin at the moment of decay and the direction in which the positron is emitted. In Figure 25 two characteristic angular patterns $W_{e^+}(\theta)$ are represented. The asymmetry parameter a depends on the energy of the positron. a increases monotonically with the positron energy and is 1 for the maximum positron energy $E_{max} = 52.83$ MeV. For $E = 0$, $a = -1/3$ and changes sign for $E = \frac{1}{2} E_{max}$. However, very few positrons are emitted with low energies and those, which are, will usually not be detected. When integrated over all energies one obtains $a = 1/3$ (100). The positron detectors used around the world in μ SR setups do not determine the incoming energy of the positrons and therefore one always measures the asymmetry parameter a averaged over all energies.

Because of their large kinetic energy (~ 30 MeV), the positrons are only weakly absorbed by the sample and cryostat walls. They are monitored and stored by detection electronics in a counts versus time histogram. The time histogram of the collected intervals is of the form

$$N_{e^+}(t) = N_0 e^{-t/\tau_\mu} [1 + aP(t) \cos \phi_{det}] + b, \quad (3.80)$$

where b is a time independent background, N_0 a normalization constant, and e^{-t/τ_μ} accounts for the μ^+ decay with the average decay time τ_μ . $P(t)$ reflects the time dependence of the μ^+ polarization and is normalized to unity for $t = 0$. The value of the initial asymmetry a depends on the experimental set-up and is in practice smaller than the theoretical value of $1/3$. Due to the finite solid angle of the detectors, energy dependent efficiency of detection and possible reduced beam polarization, a is usually $0.23 - 0.25$. The phase factor ϕ_{det} accounts for the angle between the initial muon polarization and the positron detector.

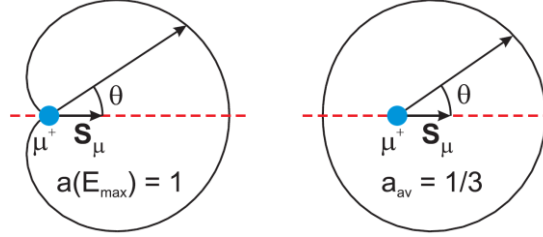


Figure 25: The angular distribution $W_{e^+}(\theta)$ of the decay positrons for the maximum positron energy of 52.83 MeV ($a = 1$) and integrated over all energies ($a = 1/3$).

3.5.2 Experimental geometries

In μ SR two types of experimental geometries are used. They are depicted in Figure 26. Measurements in zero magnetic field and in longitudinal field are performed with the same geometry. The positron detectors are set parallel and antiparallel to the initial beam polarization $\vec{S}_\mu(0)$. They are called the “forward” and “backward” detector, respectively.

By definition the magnetic field \vec{B}_{ext} is applied along the z direction. In the longitudinal geometry the field is applied parallel to the beam polarization $\vec{S}_\mu(0)$. The measured polarization function is called $P_z(t)$. In the transverse geometry \vec{B}_{ext} is perpendicular to $\vec{S}_\mu(0)$, which is then along x . The positrons are detected in a direction perpendicular to \vec{B}_{ext} , from which $P_x(t)$ is reconstructed as

$$\alpha P_x(t) = \frac{N_F(t) - \alpha N_B(t)}{N_F(t) + \alpha N_B(t)}, \quad (3.81)$$

Here $N_F(t)$ and $N_B(t)$ are the number of counts in the forward and backward detector and α is an experimental factor determined by detector efficiencies, exact experimental factors like distance between sample and detectors, cryostat, etc. It is measured by applying a transverse field (in the paramagnetic state) at exactly the same experimental conditions. With the correct α , $P_x(t)$ should oscillate symmetrically around zero.

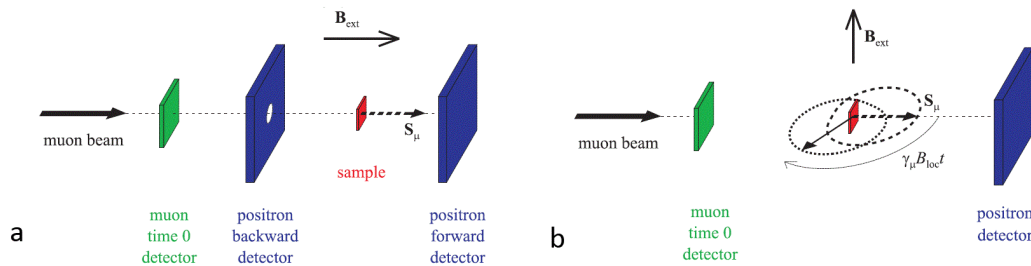


Figure 26: Two types of experimental geometry: (a) the longitudinal and (b) the transverse set-up. Although the muon spin is actually antiparallel to the muon’s momentum, here the muon spin is drawn parallel to the momentum for clarity. The arrows and cardioids in the transverse set-up represent the Larmor precession of the muon spin in the applied field and the accompanying angular positron distribution.

It should be noted that for e.g. a ferromagnet in zero field, with $\vec{S}_\mu(0)$ perpendicular to the local field, $P_x(t)$ is measured and not $P_z(t)$, although the measurements are performed in zero applied magnetic field. Physically for the muon spin there is no difference between a static externally applied magnetic field \vec{B}_{ext} or a constant field with its origin in the ferromagnetism of the compound under study.

3.5.3 Depolarization and relaxation functions

The polarization function $P_\alpha(t)$ ($\alpha = x, z$) extracted from the experiment contains the information on the magnetic distribution at the muon site and the time scale of the magnetic fluctuations. A few polarization functions will be discussed here, as far as they were used in this thesis. For a more extensive study, see e.g. references (102), (103).

3.5.3.1 Static magnetic fields

The starting point of all calculations is the consideration of a single muon spin in a static local magnetic field \vec{B}_{loc} oriented in an arbitrary direction. As explained before, the polarization function $P(t)$ is measured either along the x axis or along the z axis. Therefore $P_\alpha(t)$, with ($\alpha = x, z$), reflects the projection of $\vec{S}_\mu(t)$ along the x or z direction. The Larmor precession of a single muon spin and its projection along the α direction (depending on whether $\vec{S}_\mu(0) \parallel x$ or $\vec{S}_\mu(0) \parallel z$) are illustrated in Figure 27. If all muon spins precess in the same static magnetic field, oriented at an angle θ relative to the initial muon spin direction $\vec{S}_\mu(0)$, the Larmor equation yields

$$P_\alpha(t) = \cos^2 \theta + \sin^2 \theta \cos \omega_\mu t, \quad (3.82)$$

where $\omega_\mu = \gamma_\mu |\vec{B}_{loc}|$. The polarization $P_\alpha(t)$ describes a cone with the local field \vec{B}_{loc} as the axis of rotation. It is only the component of the muon spin perpendicular to \vec{B}_{loc} , which oscillates. The parallel component is time-independent. Both these components are projected onto the x or z direction, depending on the geometry. Equation 3.82 is the basic equation in μ SR.

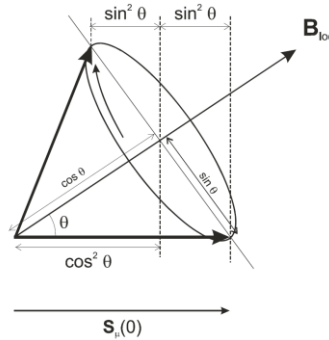


Figure 27: Muon spin precession describing a cone around a local magnetic field \vec{B}_{loc} . Here θ denotes the angle between the initial muon spin polarization and the local field.

Clearly, the assumption of a single magnetic field direction for all muons throughout the sample is a very simple model. Neglecting spin dynamics, the assumption is only encountered in single crystals of ferromagnets and antiferromagnets with a negligible volume fraction of domain walls. Helical structured magnets for example are excluded, since in different unit cells the local field at the muon site will have another direction. Obviously, the next step is to assume a field distribution at the muon site. It is easy to see that the polarization function $P_\alpha(t)$ can then be described by

$$P_\alpha(t) = \int f(\vec{B}_{loc}) [\cos^2 \theta + \sin^2 \theta (\cos \gamma_\mu |\vec{B}_{loc}| t)] d\vec{B}_{loc}, \quad (3.83)$$

where $f(\vec{B}_{loc})$ is the normalized magnetic field probability function. If only a single value of \vec{B}_{loc} is present, $f(\vec{B}_{loc})$ is a Dirac δ -function and equation 3.82 is recovered. For a polycrystalline ferromagnet with no preferred direction for the grains (“texture”) one can write $f(\vec{B}_{loc}) = 1/(4\pi B_0^2) \delta(|\vec{B}_{loc}| - B_0)$ to obtain

$$P_\alpha(t) = \frac{1}{3} + \frac{2}{3} \cos(\gamma_\mu B_0 t), \quad (3.84)$$

which is a simple oscillating function with a 1/3 shift coming from averaging of the $\cos^2 \theta$ term. A static distribution of local magnetic fields at the muon site, as the one arising from randomly oriented static nuclear magnetic moments through their dipole fields, can be very well approximated by a Gaussian field distribution because of the statistical law of large numbers. This distribution is isotropic and has zero average field, so no net precession is observed. Including an external magnetic field \vec{B}_{ext} parallel to z leads to

$$f(\vec{B}_{loc}) = \left(\frac{\gamma_\mu}{\sqrt{2\pi}\Delta} \right)^3 \exp\left(-\frac{(\gamma_\mu B_{loc}^x)^2}{2\Delta^2}\right) \exp\left(-\frac{(\gamma_\mu B_{loc}^y)^2}{2\Delta^2}\right) \exp\left(-\frac{\gamma_\mu^2 (B_{loc}^z - B_{ext})^2}{2\Delta^2}\right), \quad (3.85)$$

where $\Delta^2/\gamma_\mu^2 = \langle B_i^2 \rangle$ is the square of the width of the field distribution along the cartesian axis $i = x, y, z$. Introducing this function in equation 3.83 gives for the case of $B_{ext} = 0$ the well known Kubo-Toyabe function (Figure 28) (104)

$$P_{KT}(\Delta, t) = \frac{1}{3} + \frac{2}{3} (1 - \Delta^2 t^2) \exp\left(-\frac{1}{2} \Delta^2 t^2\right). \quad (3.86)$$

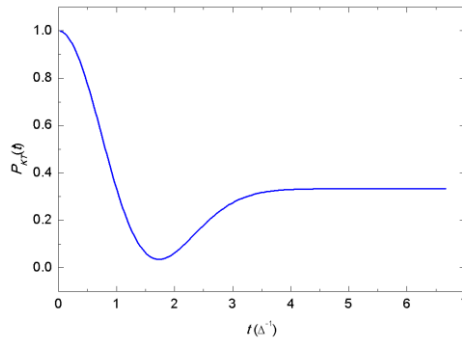


Figure 28: The Kubo-Toyabe function as given in equation (3.86).

3.5.3.2 Fluctuating magnetic fields

In contrast to the assumption of a static magnetic field at the muon site – static compared to the life time of the muon - the magnetic fields are in reality more often fluctuating on the muon time scale. This can be because of paramagnetic fluctuations above the magnetic ordering temperature, or because of spin waves below this temperature.

A mathematical description of the polarization function $P_\alpha(\nu, t)$ due to fluctuating magnetic fields can be obtained by applying the strong collision approximation. In this model, it is assumed that the local field \vec{B}_{loc} changes orientation and magnitude with a single fluctuation rate ν . According to Poisson statistics, the probability of j jumps within a time t is $\nu^j e^{-\nu t}$, where the time t_i of the i -th jump is arbitrary. The only restriction is that $t_1 < \dots < t_i < \dots < t_j < t$. After a “collision” the field is randomly chosen from the probability

distribution $f(\vec{B}_{loc})$ applicable to the compound under study and experimental conditions, without any correlation to the field before the collision. Before the first collision the polarization $P_\alpha(t)$ should be described by equation 3.83. After the first collision the ensemble of muons will further depolarize according to the same function but with an initial time zero at the time of collision. This process for multiple collisions is given by

$$P_\alpha(\nu, t) = e^{-\nu t} \left[P_\alpha(t) + \nu \int_0^t P_\alpha(t_1) P_\alpha(t - t_1) dt_1 + \nu^2 \int_0^t \int_0^{t_1} P_\alpha(t_1) P_\alpha(t_2 - t_1) P_\alpha(t - t_2) dt_1 dt_2 + \dots \right] \quad (3.87)$$

In general, this expression cannot be solved analytically and therefore one needs numerical computation. It is possible (105) to write this formula as

$$P_\alpha(\nu, t) = P_\alpha(t) e^{-\nu t} + \nu \int_0^t P_\alpha(\nu, t - t') P_\alpha(t') e^{-\nu t'} dt' \quad (3.88)$$

This equation is much easier to solve numerically, and is therefore used in the computations of $P_\alpha(\nu, t)$.

For ν/Δ sufficiently large, the Laplace transform can be used to find a useful approximate analytical expression. The resultant formula (105) is given by

$$P_z^{KT}(\nu, \Delta, t) = \exp \left[-\frac{2\Delta^2}{\nu^2} (e^{-\nu t} - 1 + \nu t) \right] \quad (3.89)$$

For very fast fluctuations with respect to Δ , $P_z^{KT}(\nu, \Delta, t)$ reduces to

$$P_z^{KT}(\nu, \Delta, t) = e^{-\lambda_z t} \quad \text{with } \lambda_z = 2\Delta^2/\nu. \quad (3.90)$$

This is the so-called motional narrowing limit.

For applied magnetic fields \vec{B}_{ext} the integrals in equation 3.83 can also be evaluated. For a transverse field, the approximation

$$P_x^{KT}(\nu, \Delta, B_{ext}, t) = \exp \left[-\frac{\Delta^2}{\nu^2} (e^{-\nu t} - 1 + \nu t) \right] \cos(\gamma_\mu B_{ext} t) \quad (3.91)$$

is valid for large enough ν/Δ . This formula is found via the Laplace transform (105) and is known in NMR as the ‘‘Abragam formula’’. It reduces to

$$P_x(\nu, \Delta, B_{ext}, t) = e^{-\lambda_x t} \cos(\gamma_\mu B_{ext} t) \quad \text{with } \lambda_x = \Delta^2/\nu \quad (3.92)$$

in the motional narrowing limit ($\nu/\Delta \gg 1$).

3.5.4 μ SR instruments

Muon beams are produced either as a continuous beam (PSI, Switzerland and TRIUMF, Canada) or as a pulsed one (ISIS, UK and KEK, Japan). For continuous beams every event is treated separately. A clock is started at the moment that a muon enters the sample. This clock is stopped when the corresponding decay positron is detected. The elapsed time is stored in a counts versus time histogram. For pulsed beams all muons come in at the same time t_0 . This pulse has however a finite width distributed around t_0 . Due to this uncertainty in t_0 continuous beams have a better time resolution than pulsed beams. The advantage of the

pulsed beams is their lower background. The background b of equation 3.80 is reduced since after the pulse the beamline is shut and no other muons enter the sample. The lower background leads to a longer time window for the pulsed beam sources. Typically, the time window of a pulsed beam source is twice as long as for a conventional continuous source.

All the μ SR measurements presented in this thesis have been carried out at PSI using the GPS, which uses surface muons. They are called like this, since they are obtained from the pions decaying at rest near the surface of the production target. The surface beam is fully polarized and monochromatic, with a kinetic energy of 4.1 MeV. Due to this small energy, the beam has a short stopping range $L_{eff} = c/\rho$, where c is around 160-200 mg/cm² and ρ the density of the compound in mg/cm³ (e.g., for FeTe₂O₅Br $L_{eff} \sim 35$ cm).

3.6 Dielectric measurements

The capacitance and the loss of a dielectric sandwiched in between two parallel electrodes can be written as $C = \epsilon\epsilon_0 A/d$ and $\tan \delta = \epsilon'/\epsilon''$, where ϵ_0 is the permittivity of free space, ϵ' and ϵ'' are the real part and imaginary part of the dielectric permittivity of the material, A is the area of the electrodes and d is the thickness of the sample. Peter Debye developed a model of dielectric relaxation by considering a delay of the response of a dipole under an alternating electric field due to a surrounding viscous medium (106). According to this model:

$$\epsilon(\omega) = \epsilon_\infty + \frac{\epsilon_s - \epsilon_\infty}{1 + i\omega\tau}, \quad (3.93)$$

where τ is the relaxation time associated with the orientation process, ϵ_s is the static permittivity (zero frequency limit), ϵ_∞ is the permittivity at optical frequencies, and ω is the (angular) frequency of the applied electric field. By separating the real part from the imaginary part in the Debye equation, one obtains:

$$\epsilon'(\omega) = \epsilon_\infty + \frac{\epsilon_s - \epsilon_\infty}{1 + (\omega\tau)^2}, \quad \epsilon''(\omega) = \frac{\omega\tau(\epsilon_s - \epsilon_\infty)}{1 + (\omega\tau)^2}. \quad (3.94)$$

This implies that in a Debye-like relaxation, ϵ' and ϵ'' show a step and a peak, respectively, at the relaxation frequency, τ^{-1} .

In practice, the dielectric constant is derived from the capacitance measurements acquired by LCR meter. This measures the impedance of the sample (plate, with electrodes on each side) by measuring the voltage across the part and the current through it. This is done for both the real and imaginary (90° phase shifted) components of the signals. The complex ratio of voltage to current is equal to the complex impedance. The processor calculates the various parameters, with capacity being one of them.

The quasistatic polarization (P) was determined from accumulated charge, measured by the Keithley 617 programmable electrometer, as described in references (107), (108).

3.7 Thermal expansion

High-precision measurements of the sample length as a function of temperature T or magnetic field B were performed on single-crystalline samples using the parallel plate capacitance method. The sample is connected to one of the plates, whereas the other plate is fixed. Because the capacitance C is given by

$$C = \frac{\epsilon A}{d}, \quad (3.95)$$

where d is the distance between the plates, A the area of the plates, and $\varepsilon = \varepsilon_r \varepsilon_0$ the dielectric constant of the medium between the plates, the length of the sample is inversely proportional to the capacitance. ε_0 is the dielectric constant of the vacuum and ε_r the dielectric constant of a medium, relative to ε_0 .

A schematic illustration of the parallel-plate capacitance method is shown in Figure 29. One can see that the upper capacitance plate is fixed while the lower is resting on the sample. The lower plate is positioned with springs, to ensure good contact with the sample. The bottom of the sample is placed on a plateau, fixed by a screw. The distance d between the two plates is chosen to be $\sim 100 \mu\text{m}$.

The coefficient of thermal expansion α is calculated by $\alpha = (1/L)(dL/dT)$, where L is the length of the sample. The linear thermal expansion of the sample is calculated by

$$\alpha_{sample} = -\frac{1}{L} \left(\frac{\Delta d}{\Delta L} \right)_{cell+sample} + \frac{1}{L} \left(\frac{\Delta d}{\Delta L} \right)_{cell+Cu} + \alpha_{Cu}, \quad (3.96)$$

where the first term corresponds to the change in the distance between the plates when the sample is mounted in the cell. The second term accounts for the so-called cell effect, i.e. the signal observed when a copper sample of the same length as the sample under investigation is mounted. This cell effect is found to reproduce very well. The last term is the linear thermal expansion of the copper of the cell.

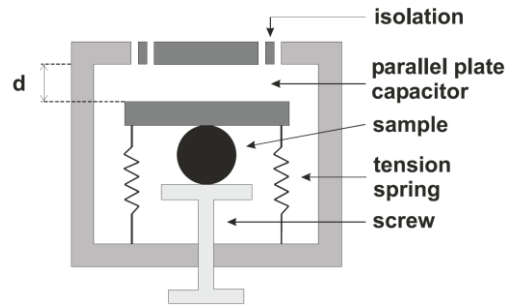


Figure 29: Schematic illustration of a parallel-plate capacitance cell to measure thermal expansion and magnetostriction. The two plates of the capacitor are electrically charged. The sample is pressed against the lower plate of the capacitor by turning the screw, on the bottom of the cell, tight. When the sample expands, it pushes the lower plate upwards, thereby enlarging the capacitance.

Because the capacitance can be measured very accurately, total length changes down to 0.05 \AA are measurable. This means that for samples of just 1 mm length, a resolution of $5 \times 10^{-8} \text{ K}^{-1}$ can be obtained in $\alpha(T)$ for a temperature step of $\Delta T = 0.1 \text{ K}$.

3.8 X-ray single crystal diffraction

X-ray single-crystal diffraction is a powerful technique used to identify crystal structures of compounds. The principle behind this technique is based on the constructive interference of x-rays, scattered from the illuminated sample. Hence the theoretical treatment is very similar as for elastic neutron diffraction, i.e., again the relative intensity of the diffraction peaks is mainly controlled by the structure factor, which is in this case denoted as

$$F_{hkl} = \sum_{n=1}^N f_n e^{2\pi i(hu_n + kv_n + lw_n)}, \quad (3.97)$$

where h , k , and l are the Miller indices of the scattering plane and u , v , and w are the reduced position indices of the N atoms in the unit cell. The atomic scattering factor f_n is a measure for the ability of an atom to scatter x-rays, relative to that of a single electron. The scattered intensity I is proportional to $|F_{hkl}|^2$.

As in neutron case, the sample is held in a standard eulerian cradle, which allows rotating the sample into an arbitrary position hence a broad range of the Bragg peaks can be reached. The measured intensity as a function of the scattering angle 2θ yields information on the spacing between planes of atoms in the crystal structure, as well as the sites of the atoms within the unit cell.

The accuracy, with which the lattice parameters of a compound can be determined, depends on the accuracy in the determination of 2θ . In this thesis (Chapter 4) the lattice parameters were measured with an uncertainty of 0.01 Å.

4 FeTe₂O₅Br system

In magnetic systems, where a competition between different magnetic interactions exists, resulting magnetic frustration is often resolved by adopting three-dimensional long-range incommensurate spiral magnetic order, e.g., by cycloidal and transverse conical structures (28), (see also Figure 6). The symmetry of such magnetic structures is very low and lacks the inversion centre. Thus, one can imagine that in magnetically ordered phase, crystals, which actually have inversion-symmetry built in the crystal structures, lose the global inversion symmetry and thereby pass the symmetry restrictions for the occurrence of the electric polarization. If electric polarization actually evolves, we talk about electric polarization induced by magnetic ordering, which is an archetypal example of strong magnetoelectric coupling. If this is the case, then magnetic and ferroelectric transitions occur simultaneously below certain ordering temperature. This is indeed what happens in the magnetoelectric multiferroic TbMnO₃, where electric polarization develops in parallel with evolution of cycloidal magnetic ordering, coming from geometrically frustrated spin arrangement. The discovery of spin-driven ferroelectricity in this compound in 2003 (5) has ignited extensive research activities focused on the ferroelectric properties of frustrated magnetic systems. It was soon realized, that the existing materials, where strong magnetoelectric coupling was observed are limited to the temperatures far below room-temperature, necessary for practical applications. Therefore, Eerenstein *et al.* suggested (24) that magnetic materials with reduced dimensionality should be also investigated for large magnetoelectric effects at high temperatures since one- or two-dimensional magnetic short-range order regularly persists to much higher temperatures than three-dimensional order does. In present, extensive research activities are devoted to the search for novel systems with strong magnetoelectric coupling, which might persist up to room temperature. This prompted us to investigate magnetic and ferroelectric properties of the FeTe₂O₅Br system (16), which has a crystal structure that implies both magnetic frustration and reduced dimensionality.

In this chapter we present our discovery of a new class of materials in which linear relationship between magnetisation and polarisation arises in a state in which magnetic moments with fixed direction vary periodically in magnitude, in clear contrast to the spiral magnetic structures (28). We find that in the layered FeTe₂O₅Br compound, comprised of iron tetramer clusters (16), a spontaneous electric polarisation appears simultaneously with a low-temperature long-range antiferromagnetic order (32). Below the transition temperature the Fe³⁺ ($S = 5/2$) magnetic moments on each crystallographic site order collinearly with an incommensurate amplitude modulation resulting from competing superexchange interactions (32). The spontaneous polarisation is ascribed to the Te⁴⁺ lone pairs that serve as superexchange bridges between iron tetramer clusters and thus couple the magnetic and ferroelectric order.

4.1 Crystal Structure

The first synthesis of the FeTe₂O₅Br compound was reported in 2006 by Becker *et al.* (16). The solid solution FeTe₂O₅Br crystallizes in a layered structure with a monoclinic unit cell (Table 2) and has calculated density of 5.213 g/cm³. The layers, which are stacked along the crystal a^* -axis, are connected only by weak van der Waals interactions so that each layer can be considered almost as an individual unit (Figure 30).

From the ions composing the FeTe₂O₅Br system two species stand out in particular. First there are Te⁴⁺ ($5s^25p^0$) cations with their stereochemically active lone pair electrons. The effective volume of the lone pair electrons is approximately the same as the volume of the O²⁻ ion (15). Consequently, these elements, when mixed with a transition metal in the presence of halogen ions, impose openings in the crystal structure and effectively reduce the dimensionality of the system. Hence they are often called “chemical scissors”. Additionally, lone pair electrons are typically found in ferroelectrics as they are easy to polarize and can under proper conditions contribute to the macroscopic electric polarization. A prototypical example is

BiFeO₃, where occurrence of electric polarization below $T_c \sim 800$ K is associated with a collective asymmetric distortion of the lone pair electrons. The other species we would like to bring into the light here are Fe³⁺ ($3d^5$) cations with the spin quantum number $S = 5/2$, as they are responsible for magnetic properties of the system.

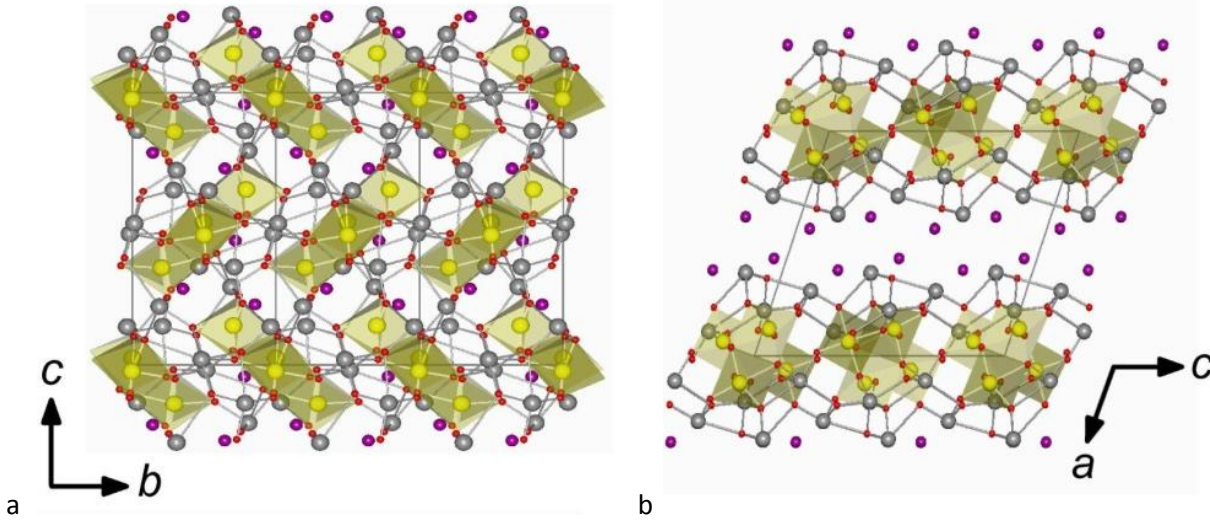


Figure 30: Crystal structure of FeTe₂O₅Br viewed along (a) a^* -axis and (b) b axis. Neighbouring layers (bc planes) are held together only by weak van der Waals interactions. The Fe³⁺, O²⁻, Te⁴⁺ and Br⁻ ions are denoted by yellow, red, grey and purple spheres, respectively.

Table 2: Basic crystallographic parameters for FeTe₂O₅Br system determined at 291(2) K (16).

Space group:	$P2_1/c$, (monoclinic)			
Lattice parameters	$a = 13.3964(8) \text{ \AA}$	$b = 6.5966(4) \text{ \AA}$	$c = 14.2897(9) \text{ \AA}$	$\beta = 108.118(6)^\circ$
Atomic coordinates:	Atom	x/a	y/b	z/c
	Te1	-0.10832(3)	-0.30965(6)	-0.71371(3)
	Te2	-0.36240(3)	0.46582(6)	-0.63843(3)
	Te3	-0.19700(3)	-0.01667(6)	-0.51910(3)
	Te4	-0.28016(3)	0.28811(6)	-0.35820(3)
	Fe1	0.11775(7)	-0.00147(12)	-0.02429(6)
	Fe2	-0.06206(7)	0.29481(12)	-0.14369(6)
	Br1	-0.43478(6)	0.71738(12)	-0.54336(5)
	Br2	-0.38242(6)	0.64507(13)	-0.27823(6)
	O1	0.0890(3)	0.2985(6)	-0.0521(3)
	O2	-0.0370(3)	0.9873(6)	-0.1031(3)
	O3	-0.2281(3)	0.5882(6)	-0.5908(3)
	O4	-0.2097(3)	0.2294(6)	-0.2245(3)
	O5	-0.1872(3)	0.4828(6)	-0.3778(3)
	O6	0.2108(3)	0.5527(6)	-0.1079(3)
	O7	0.1110(3)	0.7134(6)	0.0186(3)
	O8	0.0119(3)	0.7563(6)	-0.2462(3)
	O9	-0.0973(3)	0.5774(6)	-0.1362(3)
	O10	-0.3348(4)	0.2619(6)	-0.5450(3)

A detailed inspection of the crystal structure (16) reveals there are actually two crystallographically different Fe^{3+} positions (Table 2). Both of them have a distorted $[\text{FeO}_6]$ octahedral coordination. Four such octahedra are connected via edge sharing to form a $[\text{Fe}_4\text{O}_{16}]^{20-}$ unit where the four Fe^{3+} ions are in the same plane and form a rhomboid (see Figure 31). Each of the four Fe1-Fe2 pairs is linked via a double Fe-O-Fe bond (bonding angles of $95\text{-}110^\circ$, see Table 3). In addition, the two Fe1 sites are doubly bonded across the tetramer diagonal (bonding angle $\sim 102^\circ$, see Table 3). The similarity in bonding angles and distances suggests that the antiferromagnetic superexchange interaction between Fe1 and Fe2 moments, J_1 , should be similar to that between Fe1 and Fe1 moments, J_2 (16). Consequently, the structure of the iron tetramer can actually be described as two coupled triangles and therefore a competition between J_1 and J_2 is expected on the tetramer level.

Table 3: Fe-Fe distances and Fe-O-Fe angles within a $[\text{Fe}_4\text{O}_{16}]^{20-}$ group at 291 K (16).

X	3.159(1) Å		ξ	101.7(2) °		ψ	95.9(1) °
Y	3.343(1) Å		ξ'	99.5(2) °		ψ'	110.2(2) °
Z	3.435(2) Å					ζ	101.7(2) °

Let us now look at the coordination of Te^{4+} cations. There are four crystallographically different Te^{4+} cations. Considering the primary bonding distance of 2.66 Å for Te-O bonds and 3.22 Å for Te-Br bonds, all the Te cations can be described as having an asymmetric one-sided coordination with different number of ligands. Te1 is one-sided coordinated to three oxygens at distances around 1.89 Å, giving it a tetrahedral $[\text{Te1O}_3\text{E}]$ coordination, where E denotes the lone pair electrons. The Te2 cation coordinates two oxygens and one halide giving it a unique $[\text{Te2O}_2\text{BrE}]$ coordination. The present compound is the first where Te^{4+} has the classical one-sided three-coordination with both oxygen and a halide instead of only one of the two ligands (16). Te3 coordinate three oxygen anions at approximately 1.92 Å and two additional ones at 2.477(4) and 2.549(4) Å, which results in a one-sided $[\text{Te3O}_{3+2}\text{E}]$ coordination resembling a greatly distorted octahedron. Te4 has also three short Te-O distances of approximately 1.90 Å as well as two additional ligands, an oxygen anion at 2.549(4) Å and a bromine anion at 3.1146(8) Å, resulting in a distorted $[\text{Te4O}_{3+1}\text{BrE}]$ octahedral coordination. The four different Te polyhedra are connected via corner and edge sharing to form a $[\text{Te}_4\text{O}_{10}\text{Br}_2]^{6-}$ group (see Figure 31).

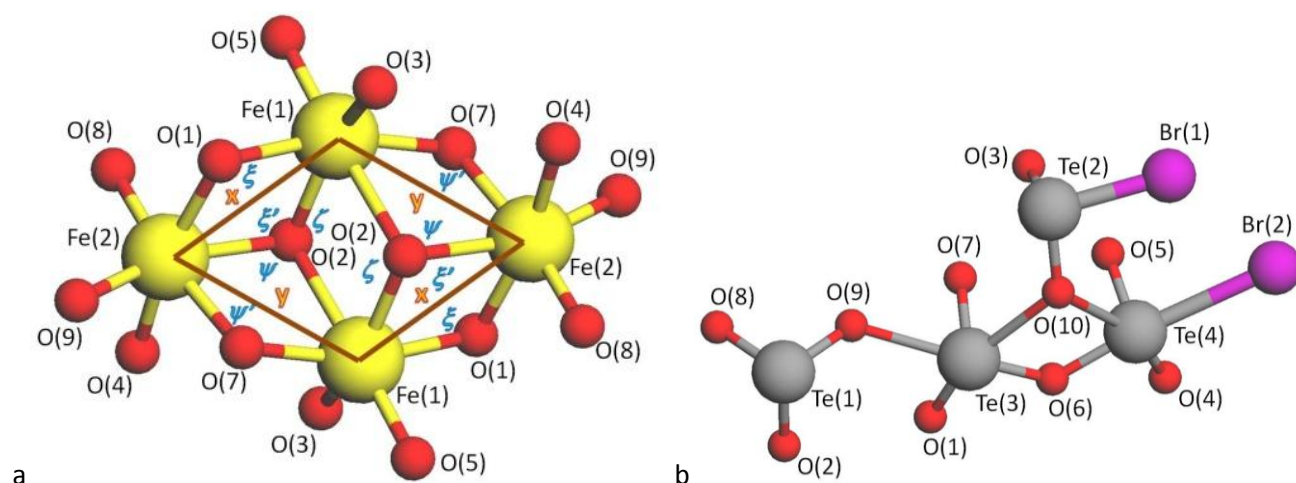


Figure 31: (a) Structure of a single $[\text{Fe}_4\text{O}_{16}]^{20-}$ basic building block. Two crystallographically non-equivalent Fe^{3+} sites, labelled Fe1 and Fe2, connect into the tetramer cluster, in which competition between different Fe1-Fe2 and Fe1-Fe1 magnetic superexchange interactions is anticipated. (b) Planar $[\text{Te}_4\text{O}_{10}\text{Br}_2]^{6-}$ group showing the various coordination polyhedra around the Te^{4+} cations.

Each layer in the crystal structure is made up of the two different building blocks; the $[\text{Fe}_4\text{O}_{16}]^{20-}$ groups (Figure 31a) and the $[\text{Te}_4\text{O}_{10}\text{Br}_2]^{6-}$ groups (Figure 31b). The $[\text{Te}_4\text{O}_{10}\text{Br}_2]^{6-}$ groups can be seen forming sublayers sandwiching the $[\text{Fe}_4\text{O}_{16}]^{20-}$ groups (see Figure 30), leading to a triangular array of $[\text{Fe}_4\text{O}_{16}]^{20-}$ clusters linked by $[\text{Te}_4\text{O}_{10}\text{Br}_2]^{6-}$ units. There are no bonds formed in between two different $[\text{Te}_4\text{O}_{10}\text{Br}_2]^{6-}$ groups nor between the two different $[\text{Fe}_4\text{O}_{16}]^{20-}$ groups. Instead the $[\text{Te}_4\text{O}_{10}\text{Br}_2]^{6-}$ groups are connected to the $[\text{Fe}_4\text{O}_{16}]^{20-}$ groups via common oxygens to build up charge neutral layers (see Figure 30). It is important to stress that all inter-cluster magnetic superexchange paths go through at least one of the Te^{4+} sites, thus providing an intimate link between the Fe^{3+} magnetic moments and the Te^{4+} lone pair electrons. Between the layers there are Br anions, which as well as the stereochemically active lone pair electrons of the Te^{4+} ($5s^25p^0$) cations protrude from the layers.

The shortest Fe-Fe distance in between two $[\text{Fe}_4\text{O}_{16}]^{20-}$ groups within the same layer is ~ 4.76 Å, while the shortest Fe-Fe distance in between two layers is ~ 10.1 Å. This large separation and the lack of direct bonds (only van der Waals forces connect the adjacent layers) in between the layers suggest that there are very weak magnetic interactions in between two layers and that the system can be well described as magnetically two-dimensional system.

With respect to NMR and NQR experiments, which were performed on Br nucleus, we finally make also a remark concerning the Br...-Fe exchange paths. Having in mind the primary bonding distance for Te-Br bonds (3.22 Å), the only atom close enough to Br1 is Te2, i.e., 3.212(1) Å, which is connected to Fe1 via O3. On the other hand, Br2 has two Te^{4+} cations just at the border of primary coordination sphere. The Te4 is 3.1146(8) Å away while the Te2 is 3.333(7) Å away, so we assume, that Br2 is coupled to Fe2 via Te4 and O4 and to two Fe1-sites via Te4 and O5 and via Te2 and O3. We thus anticipate that the Br NMR/NQR signal would give us rich information about the magnetic behaviour of ($S = 5/2$) Fe^{3+} magnetic moments.

4.2 Magnetic characterization of the paramagnetic state

The reduced dimensionality and the magnetic frustration within the iron tetramers, as well as their triangular arrangement in the crystal layers, suggest that $\text{FeTe}_2\text{O}_5\text{Br}$ may have interesting magnetic properties. Becker et al. (16) performed specific heat, magnetization measurements and Mössbauer experiments on powder samples, while we made a detailed investigation of single crystal samples. These have been studied using SQUID magnetisation, ESR, specific heat, neutron diffraction, ^{81}Br nuclear magnetic and quadrupolar resonance (NMR and NQR), μ^+ spin relaxation, dielectric susceptibility, x-ray diffraction, thermal expansion and inelastic neutron scattering.

4.2.1 Magnetic susceptibility

The magnetic susceptibility as a function of temperature was measured with a Quantum Design SQUID magnetometer MPMS-XL-5 equipped with a 5 T superconducting magnet. Zero-field-cooled and field-cooled susceptibilities were examined in the temperature interval between 300 and 2 K in a magnetic field of 0.1 T.

At high temperatures, i.e., above 100 K, the magnetic susceptibility χ follows the Curie-Weiss law for all crystal orientations (Figure 3a):

$$\chi_{mol} = \frac{C}{T - \theta_{CW}} + \chi_{dia}. \quad (4.1)$$

Here the $\chi_{dia} = -134.8 \times 10^{-5} \text{ Am}^2/\text{T mol}$ is a temperature-independent diamagnetic contribution for $\text{FeTe}_2\text{O}_5\text{Br}$ calculated from Pascal constants (Table 4) taken from Magnetochemistry by Selwood (109).

Table 4: Pascal's constants for selected ions (109).

Ion	Pascal's constants ($10^{-5} \text{ Am}^2/\text{T mol}$)
Fe	-12.8
Te	-37.3
O	-3.36
Br	-30.6
FeTe ₂ O ₅ Br	$-12.8 - 2 \times 37.3 - 5 \times 3.36 - 30.6 = 134.8$

The extracted Curie-Weiss temperature $\theta_{CW} = -125$ (20) K is not in the best agreement with the values presented by Becker et al. (16), where they observed anomalous behaviour around 250 K. Since we did not observe such anomaly in any of our numerous experiments, we suspect that it is an experimental artefact connected to the powder nature of the previous samples. Focusing back on our results, we note that there is no significant difference between zero-field-cooled and field-cooled runs. The high θ_{CW} indicates strong antiferromagnetic interactions between Fe³⁺ moments and the effective magnetic moment $\mu_{\text{eff}} = 6.15(5) \mu_B/\text{Fe}^{3+}$ obtained from the Curie constant, $C = 47(5) \text{ Am}^2/\text{T mol}$, is close to the calculated value $5.92 \mu_B$ expected for Fe³⁺ with a d^5 electronic configuration and a high-spin 6S ($S = 5/2$, $g = 2$) ground state. The small discrepancy indicates that the actual $g \sim 2.08(2)$. The low-dimensional magnetic character of FeTe₂O₅Br is reflected in a broad maximum of χ at ~ 50 K (minimum in Figure 32a). At much lower temperatures, i.e., at $T_N = 10.6(2)$ K, a pronounced change in the temperature dependence of χ is evident (Figure 32b), which indicates the development of a three-dimensional long-range magnetic ordering. The low-temperature susceptibility results (Figure 32b) show that χ is the smallest for magnetic field, $\vec{B} \parallel b$, implying that magnetic moments prefer ordering along the b -axis (easy axis), i.e., magnetization in this direction cannot increase significantly when magnetic field is applied. On the other hand, susceptibility is the largest when the magnetic field is applied along the c -axis, signifying that c -axis is so called intermediate axis and a^* -axis is so called hard axis, as the magnetic moments are not keen to rotate towards it. A large empirical frustration factor $f = |\theta_{CW}|/T_N \sim 11$ indicates a significant reduction of T_N compared to θ_{CW} , typically observed in strongly frustrated systems ($f > 10$) (110), and thus concurs with frustrated geometry of the FeTe₂O₅Br. On the other hand, T_N might be suppressed solely by the low-dimensional nature of investigated system (80), (111).

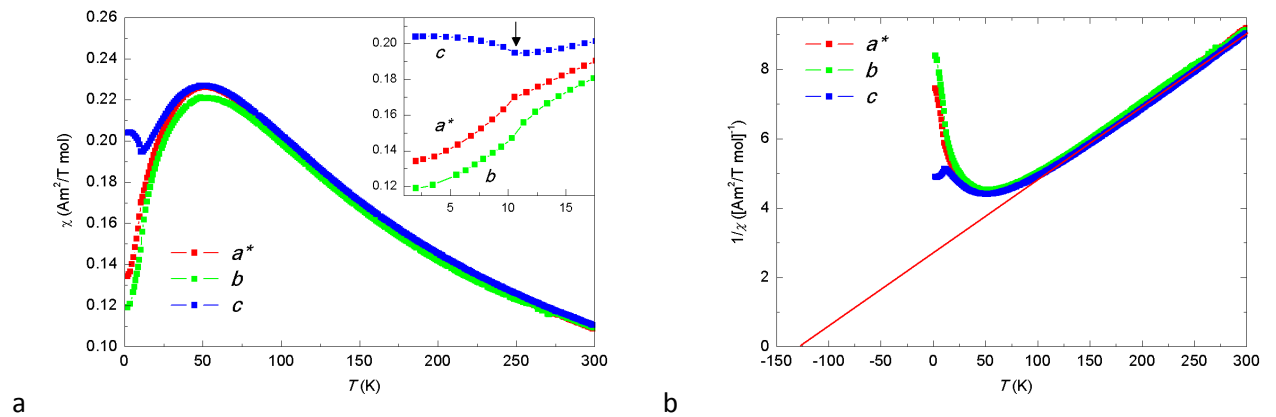


Figure 32: (a) Molar magnetic susceptibility for FeTe₂O₅Br measured along all three crystal directions in applied magnetic field of 100 Oe already corrected for diamagnetic contribution. Inset: magnetic susceptibility at low temperatures. Note a pronounced anomaly at the magnetic-phase transition temperature $T_N = 10.6(2)$ K marked with an arrow. (b) Inverse molar magnetic susceptibility for FeTe₂O₅Br. Thin solid line represents the Curie-Weiss behaviour above 100 K.

The discussed magneto-structural correlations of $\text{FeTe}_2\text{O}_5\text{Br}$ are evident from a comparison of intra Fe-Fe distances and Fe-O-Fe angles for the $[\text{Fe}_4\text{O}_{16}]^{20-}$ groups, listed in Table 3. The shortest inter Fe-Fe distances between the groups, 4.76 Å, are considerably larger than the intra group Fe-Fe distances. Therefore the spin cluster character of the material is promoted, which consequently suppresses the long-range ordering, i.e., the low transition temperature is likely a result of weak superexchange paths connecting the $[\text{Fe}_4\text{O}_{16}]^{20-}$ groups. Actually, the large variety of intra- and inter-group distances associated with competing interactions are the most probable cause for the large variation of magnetic energy scales given by the Curie-Weiss temperature (~ 110 K), the maximum position (~ 50 K) and the ordering effects (~ 10 K).

Based on the crystal structure Becker et al. (16) proposed a model assuming antiferromagnetic coupling J_1 connecting the Fe1 and Fe2 across the edges of the tetramer and J_2 between the opposite Fe1 across the diagonal of the tetramer. The appropriate Hamiltonian is hence:

$$H = -2J_1(\vec{S}_1 \cdot \vec{S}_3 + \vec{S}_2 \cdot \vec{S}_3 + \vec{S}_2 \cdot \vec{S}_4 + \vec{S}_1 \cdot \vec{S}_4) - 2J_2\vec{S}_1 \cdot \vec{S}_2 \quad (4.2)$$

for which the energy levels are given by (16):

$$E_{tet} = -J_1[S^T(S^T + 1) - S^I(S^I + 1) - S^{II}(S^{II} + 1)] - J_1[S^I(S^I + 1) - S_1(S_1 + 1) - S_2(S_2 + 1)], \quad (4.3)$$

where S^T , S^I , and S^{II} are the quantum numbers of the spin operators:

$$\vec{S}^T = \sum_{i=1}^4 \vec{S}_i, \quad \vec{S}^I = \vec{S}_1 + \vec{S}_2, \quad \vec{S}^{II} = \vec{S}_3 + \vec{S}_4. \quad (4.4)$$

For high-spin Fe^{3+} ($S_i = 5/2$), S^I and S^{II} can take the spin values 0, 1, 2, ..., 5. Using Van Vleck approximation (112), the effective magnetic moment μ_{eff} is given by:

$$\mu_{eff}^2 = g^2 \frac{\sum_{S^T} S^T(S^T + 1)(2S^T + 1)e^{\left(\frac{E_{tet}(S^T)}{k_B T}\right)}}{\sum_{S^T} (2S^T + 1)e^{\left(\frac{E_{tet}(S^T)}{k_B T}\right)}}. \quad (4.5)$$

For the susceptibility of the tetramer one obtains

$$\chi_{mol}^{tet} = \mu_0 \frac{N_A \mu_B^2 \mu_{eff}^2(T)}{3k_B T}. \quad (4.6)$$

To consider the coupling between the Fe tetramers, we apply a molecular field approach and calculate the susceptibility χ_{mol}^{MF} according to

$$\chi_{mol}^{MF} = \frac{\chi_{mol}^{tet}}{1 - \chi_{mol}^{tet} \frac{2z'J'}{N_A g^2 \mu_B^2}} + \chi_{dia}, \quad (4.7)$$

where $z'J'$ represents a mean superexchange coupling constant of Fe tetramers to z' neighbouring tetramer clusters and N_A is the Avogadro constant.

According to the presented model, Becker et al. (16) satisfactorily explained temperature dependence of χ measured on powder samples with $J_1 = -11.7$ K, $J_2 = -12.3$ K, and $z'J' = 17.4$ K. These parameters are consistent with the low-dimensional nature of the system, i.e., since $z' \sim 6$, the intercluster coupling J' is

approximately four times smaller compared to the intracluster coupling J_i . However, obtained parameters give little information about the nature of the magnetic groundstate. To sum up, based on the magnetic susceptibility measurements we can state that the magnitudes of intracluster interactions are of the order of ~ 10 K and ~ 4 times smaller for intercluster ones, but it is very difficult to be more specific, i.e., stating the exact $J_1 : J_2 : J'$ would be misleading.

4.2.2 Electron spin resonance

Continuous wave ESR experiments were performed in the X-band (9.5 GHz) on a home build spectrometer equipped with the Varian E-101 microwave bridge and HP 5350B microwave frequency counter. An Oxford ESR 900 continuous flow liquid He cryogen system was used for temperature-dependent measurements between 15 and 300 K. Temperature stability was better than 0.1 K.

At room temperature a single intense and almost symmetrical resonance has been observed in X-band ESR experiment for $\vec{B} \perp a^*$ (Figure 33b). Its calibrated room temperature intensity corresponds to $\chi_{\text{ESR}} = 8.5 \cdot 10^{-2}$ Am²/(T mol), which is close to the value measured in magnetization measurements (16). The resonance signal can be well simulated as a combination of absorption spectra with a small ($r \sim 0.1$) dispersion contribution (equation 3.15). This is most likely due to mixing of absorption and dispersion signals, frequently found in insulators with non-diagonal elements of the dynamic susceptibility (70). On the other hand, almost symmetric ($r \ll 1$) Lorentzian lineshape suggests that the exchange narrowing is effective and consequently blurs the difference between the two magnetically non-equivalent Fe³⁺ sites in the crystal structure. Therefore, the measured g -factor $g(\vec{B} \parallel a^*) = 2.008(1)$ represent only an effective g -factor value of the two chemically non-equivalent Fe³⁺ sites. We note that the measured g -factor is rather characteristic of a high-spin Fe³⁺ ($S = 5/2$) magnetic ions (16). The measured ESR linewidth $\delta B_{1/2} = 54.0$ mT for $\vec{B} \parallel a^*$ is large and is likely to be a consequence of strong magnetic anisotropies.

On Figure 33 we show a complete angular dependence of the basic X-band ESR signal parameters measured at room temperature, i.e., signal intensity, g -factor and linewidth. The intensity seems to be relatively insensitive to the orientation of the applied magnetic field, as it varies for ~ 10 % only. The g -factor also does not change much, as $g(\vec{B} \parallel a^*) = 2.008(1)$, $g(\vec{B} \parallel b) = 2.001(1)$, and $g(\vec{B} \parallel c) = 2.006(1)$. However, it shows unusual angular variation with the periodicity of 90° , which can be described for a^*b rotation as $y = A' + B'(3\cos^2(\alpha' - \alpha_0) - 1)^2$, where $A' = 1.9973(4)$, $B' = -0.0024(5)$ mT and $\alpha_0 = 11(1)^\circ$ (The fit is shown as a solid magenta line on Figure 33). This variation can have two possible origins. First, the admixture of the dispersion might influence the fit of the ESR line and second, the higher order terms in the g -factor can result in the angular variation with the periodicity of 90° (113). The linewidth is similarly insensitive to the orientation of the applied magnetic field when the magnetic field is rotated in the bc plane, but show large anisotropies in the a^*b and a^*c planes, changing from $\delta B_{1/2} = 54.0$ mT for $\vec{B} \parallel a^*$ to $\delta B_{1/2} = 85.0$ mT for $\vec{B} \parallel b$, c . The linewidth dependence can be empirically described as $A + B \sin^2 \alpha$, where A and B are fitting constants and the angle α denote the deviation from $\vec{B} \parallel a^*$ orientation. From fitting the angular dependence of the linewidth, we obtained for a^*b rotation $A = 33(2)$ mT and $B = 54(2)$ mT (The fit is shown as a solid magenta line on Figure 33). The value of the measured linewidth is rather surprising as magnetic anisotropies are not obvious in this system. Namely Fe³⁺ ($S = 5/2$) ions has typically quenched orbital angular momentum and thus suppressed LS coupling, responsible for the anisotropies such as single-ion anisotropy (equation 2.7). Nevertheless, the observed anisotropy of the linewidth might be a result of the higher order terms, where LS coupling between the excited states is assumed. Further studies are needed to understand this point.

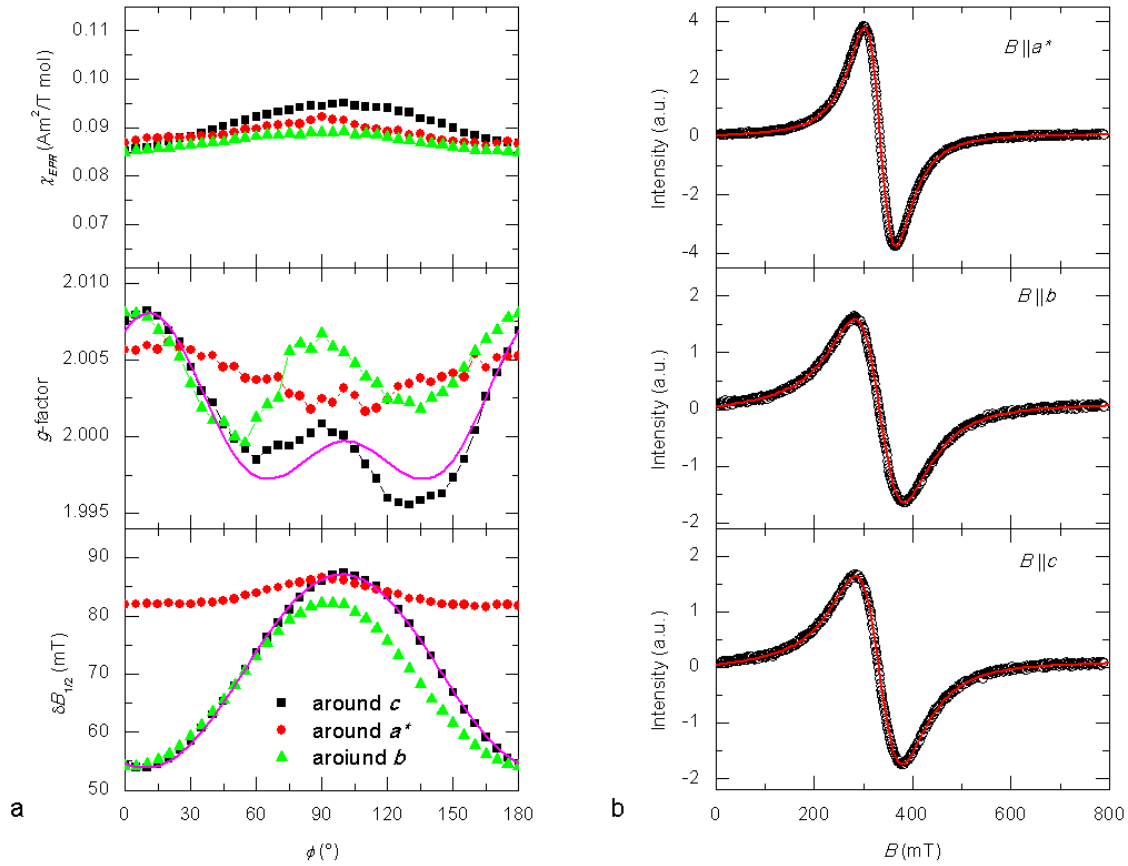


Figure 33: (a) Angular dependence of the ESR spectral parameters for all three crystal orientations of \vec{B} measured at room temperature. Solid lines represent fits to models described in text. (b) Measured spectra for all three orientations of the applied magnetic field. Solid lines are to models described in text.

Temperature dependence of the representative X-band ESR spectra measured on cooling is shown in Figure 34a for $\vec{B} \parallel a^*$. The spectrum retains nearly Lorentzian lineshape over entire temperature range even when the linewidth becomes comparable or larger than the resonant field. However, on cooling the ESR spectrum broadens and becomes virtually unobservable due to the extreme broadening for temperatures below ~ 20 K, i.e., already well above the Neel temperature T_N . This is likely the consequence of the developing short-range correlations, which imply a magnetically low-dimensional nature of the system, in agreement with the magnetic susceptibility measurements. Intensity of the ESR signal χ_{ESR} between the room temperature and ~ 130 K follows a Curie-Weiss dependence equation (4.1) for all three orientations, and the obtained values for θ_{CW} and C only marginally vary with the crystal orientation. For $\vec{B} \parallel c$ we find $\theta_{CW} = -151(10)$ K and $C = 38.8(3) \text{ Am}^2 \text{ K}/(\text{T mol})$ ($\mu_{eff} = 5.57(5) \mu_B$) and for $\vec{B} \parallel a^*$ $\theta_{CW} = -141(10)$ K, $C = 39.0(3) \text{ Am}^2 \text{ K}/(\text{T mol})$ ($\mu_{eff} = 5.56(5) \mu_B$). The linear fits of the inverse ESR susceptibility are represented by a solid line in the inset to Figure 34c. The obtained Curie-Weiss temperatures deviate from the values deduced from magnetic susceptibility data and the published SQUID data (16). This is most likely due to very large spectral linewidth compared to its resonant position, making it difficult to estimate the exact signal intensity. On the other hand, the effective magnetic moment estimated from the Curie constants ($\mu_{eff} \sim 5.6 \mu_B$) corroborates well with the magnetization data, as it departs only 10 % from the expected value ($\mu_{eff} = 5.92 \mu_B$) for $\text{Fe}^{3+} S = 5/2$.

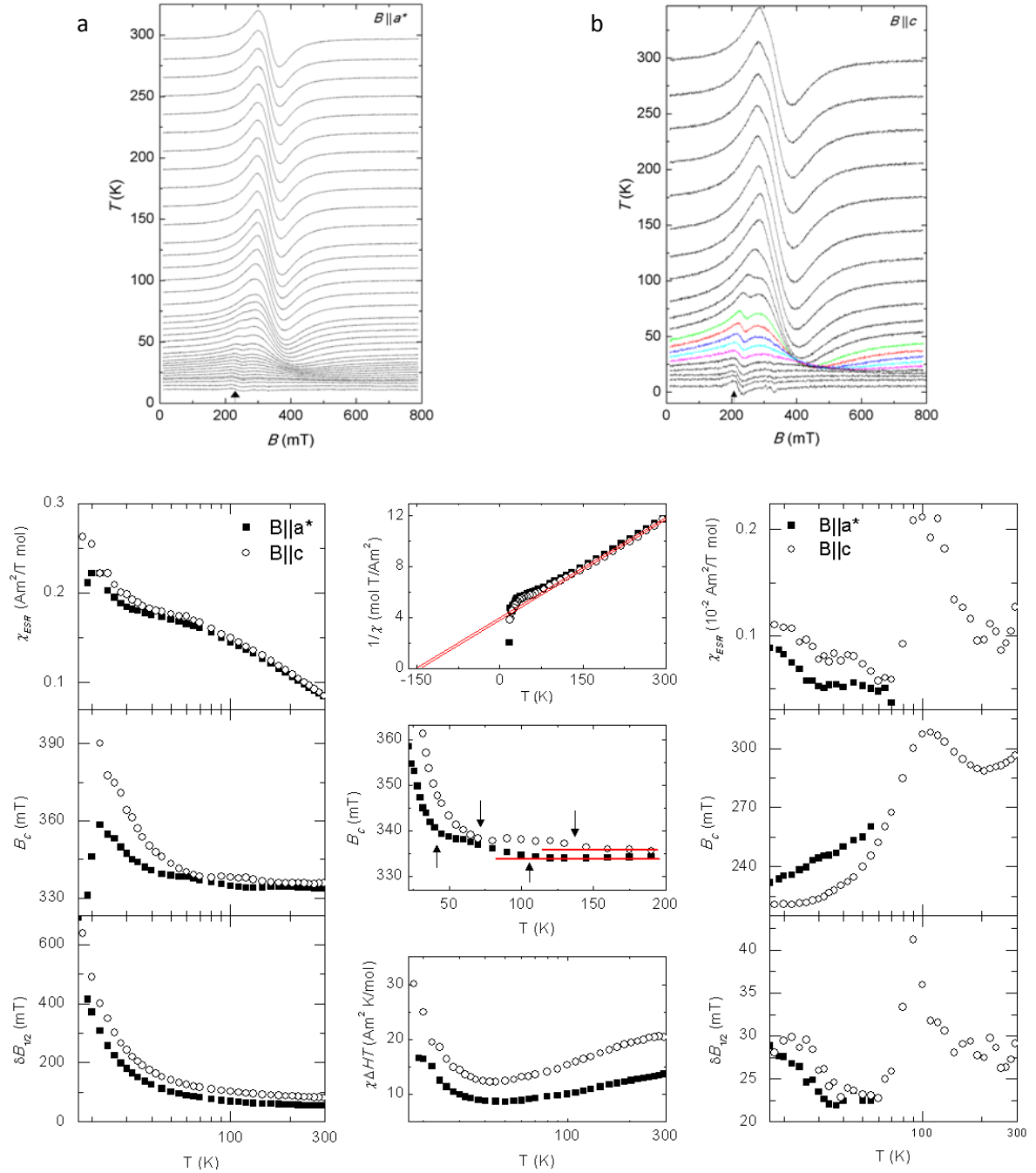


Figure 34: Above: temperature dependence of ESR spectra for (a) $\vec{B} \parallel a^*$ and (b) $\vec{B} \parallel c$. Below: temperature dependence of ESR spectral parameters for strong (left two columns) and weak (right column) signals.

Below ~ 70 K deviation from the Curie-Weiss behaviour becomes more significant, the $\chi_{ESR}(T)$ slightly flattens, but does not exhibit a maximum as observed in susceptibility measurements. Again, we believe that this is the consequence of the large linewidth, which makes the estimation of the ESR intensity increasingly difficult with decreasing temperature. This is evident from the temperature dependence of the ESR linewidth $\delta H_{1/2}$ (Figure 34c). With decreasing temperature the ESR linewidth for all crystal orientations monotonically increases in the entire temperature range. Below 100 K, linewidth starts to diverge and for instance at 20 K the linewidth amounts already 380(15) mT and 490(20) mT for $\vec{B} \parallel a^*$ and $\vec{B} \parallel c$ respectively. In order to test the development of the spin correlations with decreasing temperature, we show in the inset to Figure 34c temperature dependence of the parameter $\delta H_{1/2} \chi_{ESR} T$. This parameter should be in the paramagnetic state temperature independent, as spin correlations are not yet developed. With the onset of short-range

ordering and accompanying spin correlations we would thus expect $\delta H_{1/2} \chi_{\text{ESR}} T$ to increase. The measured $\delta H_{1/2} \chi_{\text{ESR}} T$ is actually very weakly temperature dependent between room temperature and 45 K. However, below $T \sim 45$ K ($\sim 4 T_N$), parameter $\delta H_{1/2} \chi_{\text{ESR}} T$ starts to increase with decreasing temperature, which is likely related to the development of two-dimensional spin correlations, in general agreement with the observed maximum in the magnetic susceptibility (Figure 32, (16)). We stress here, that such effects are not uncommon to two-dimensional antiferromagnets with pronounced magnetic anisotropies and geometrical frustration (114). In contrast to $\chi_{\text{ESR}}(T)$ and $\delta H_{1/2}(T)$ temperature dependences $B_c(T)$ is constant (334 mT for $\vec{B} \parallel a^*$ and 336 mT for $\vec{B} \parallel c$) to the accuracy of 0.5 mT between the room temperature and 150 K, where it slowly starts increase with decreasing temperature (Figure 34b). Below 150 K, a detailed inspection for $\vec{B} \parallel c$ reveals two inflection points. The first, at ~ 130 K, we ascribe to the mixing of the signal with the weak signal (marked with an asterisk in Figure 34a) and has no physical sense. However, the second one, at ~ 70 K, where B_c starts to shift significantly, possibly resembles the evolution of weak internal fields due to onset of the short-range magnetic ordering. At this point we stress that the weak signal observed at lower temperatures most likely corresponds to some paramagnetic impurity and its anomalous behaviour around 130 K (Figure 34b) is related solely to the overlap with the main ESR signal. On the other hand, for $\vec{B} \parallel a^*$ the weak signal is even fainter and can be noticed only below ~ 80 K. Hence, the first inflection of the $B_c(T)$ occurs only then. To our surprise the second inflection point, indicating the evident shift of the B_c , is found at significantly lower temperatures, i.e., at ~ 45 K. This suggests that the internal fields along the a^* start to evolve at lower temperatures, implying that short-range effects in this direction are delayed compared to $\vec{B} \parallel c$, in concurrence with the layered topology of FeTe₂O₅Br system. Clearly, the magnetic response is strongly anisotropic and depends on the orientation of the external magnetic field, i.e., at 30 K, for $\vec{B} \parallel a^*$ B_c is 355(5) mT and 378(5) mT for $\vec{B} \parallel c$.

4.2.3 Specific heat

Specific heat measurements were performed in the temperature range between 30 K and 0.3 K on the standard Oxford instruments PPMS setup with closed cycle cryostat, using the He3 “cooling machine” for reaching the temperatures below 1.5 K.

A sharp anomaly in the temperature dependence of the specific heat was found at T_N due to the onset of the magnetic ordering. In order to determine the temperature dependence of the magnetic heat capacity C_{mag} , C_{latt} has to be estimated first (following the procedure described in section 3.2). Since no diamagnetic isostructural compound is available, we simulated the raw heat-capacity data above the T_N with C_{latt} according to equation 3.35, which yielded $9Nk_B = 185$ J/(K mol) and $\theta_D = 120$ K (red line in Figure 35a). Unfortunately this estimation of the C_{latt} is very rough, since our data is limited to $T < 30$ K, whereas the short-range ordering effects are expected up to 50 K, where the maximum in the magnetic susceptibility is observed. Nevertheless, the obtained θ_D has a very reasonable value and is comparable to the values found in literature for doped telluride glasses (115), (116). In the next step, we subtracted the approximated lattice contribution from the raw heat-capacity data to obtain the magnetic contribution to the heat capacity C_{mag} (Figure 35b). The expected peak in C_{mag} at T_N is clearly visible, while the magnetic contribution to the heat capacity extends, well above T_N . This underlines the importance of the magnetic short-range ordering effects and confirms the low dimensionality of FeTe₂O₅Br. The experimentally obtained total entropy (equation 3.39) value 4.0(1) J/(K mol) (Figure 35b) represents only ~ 26 % of the value $R \ln(6) = 14.9$ J/(K mol) expected for the ordering of full magnetic Fe³⁺ ($S = 5/2$) moments, i.e., the obtained value correspond to only 1/8 of the full Fe³⁺ ($S = 5/2$) magnetic moment. This discrepancy is huge and is most likely the consequence of the naive estimation of the C_{latt} , where we assumed that the magnetic short-range ordering contribution above 25 K is negligible. Additionally, the peak in C_{mag} at T_N is very narrow and its integral is only marginal part

compared to the complete S_{mag} . The last two remarks bring us to the following conclusion: the short-range ordering starts to build up already above 30 K, therefore at T_N magnetic ordering within the layers is rather well developed and during the magnetic transition, when the long-range order is established, relatively small part of the entropy is released. We stress that no other anomaly was observed down to 0.3 K, implying there is no other phase transition.

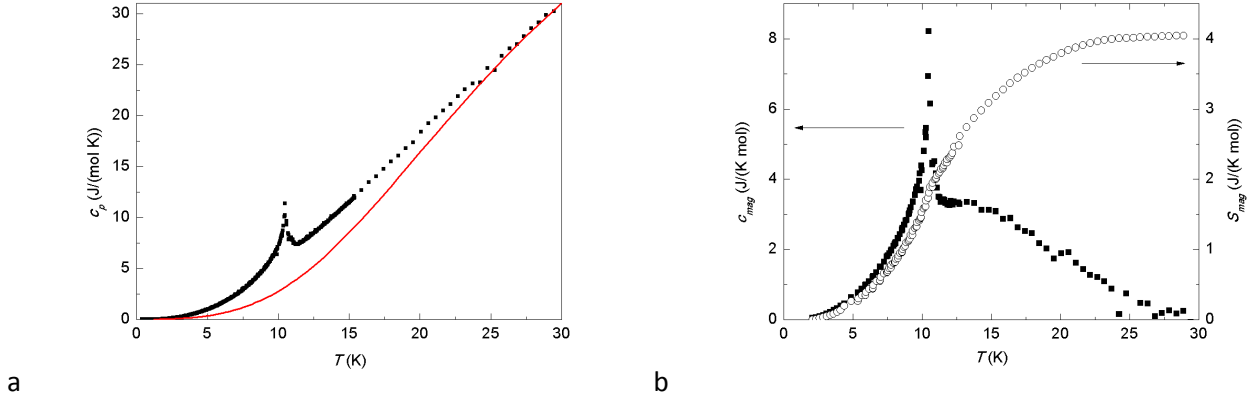


Figure 35: (a) Temperature dependence of measured specific heat, c_p , and calculated one according to the Debye approximation ($\theta_D = 120$ K and the scaling factor $9Nk_B = 185$ J/(mol K)). (b) Magnetic contribution to the specific heat (solid squares - left scale), obtained by subtraction of the estimated lattice contribution and derived magnetic entropy (empty circles - right scale).

4.3 Low-temperature magnetic ordering

In this section we present our investigation of the magnetic ordering in the FeTe₂O₅Br system. The study is based on the neutron scattering experiments accompanied by complementary techniques, such as μ^+ spin relaxation and nuclear quadrupolar resonance measurements.

4.3.1 Neutron scattering

In order to solve the low-temperature magnetic structure we carried out zero-magnetic-field single-crystal and powder unpolarised and polarised elastic neutron scattering experiments. All measurements using unpolarised neutrons were performed at the Swiss Neutron Spallation Source, Paul Scherrer Institute, Switzerland, while the spherical neutron polarimetry measurements were performed at the Institute Laue-Langevin, France.

4.3.1.1 Powder neutron diffraction

Magnetic wave vector has been determined by performing elastic neutron diffraction measurements in the temperature range between 1.5 K and 100 K on a powder sample of the isostructural FeTe₂O₅Cl system, where similar magnetic ordering is expected. Measurements were performed on 4 g of FeTe₂O₅Cl powder sample on DMC powder diffractometer ($\lambda = 2.46$ Å) at the Swiss Neutron Spallation Source (Switzerland) using the He cryostat. In order to expose the reflections in the diffraction pattern coming from the magnetic ordering (magnetic reflections), we subtracted the diffraction pattern measured at 20 K (above the T_N), from the one measured at 1.5 K (well below the T_N) (Figure 36a). Since the intensities of the reflections, coming from the scattering from the atom nuclei (nuclear reflections), do not change perceptibly in this temperature range, we obtained the magnetic scattering pattern (Figure 36a), reflecting the low-temperature magnetic structure.

In Figure 36b we show the temperature evolution of the magnetic-only scattering pattern, where nuclear part (20 K pattern) has already been subtracted. The temperature dependence of the diffraction pattern reveals that magnetic reflections suddenly emerge below T_N at the incommensurate positions described by

the wave vector $\vec{q} = (1/2 \ 0.463 \ 0)$. Discrepancy from the $(1/2 \ 1/2 \ 0)$ value indicates that the magnetic ordering along the b -axis does not match the crystal lattice, implying a complex magnetic structure, i.e., the magnetic structure is either cycloidal, helical or amplitude modulated.

On the other hand, comparison of the diffraction pattern measured at the 100 K and the one measured at 20 K, clearly indicates broad reflections (Figure 37), originating from the diffuse magnetic scattering due to the onset of the short-range magnetic correlations.

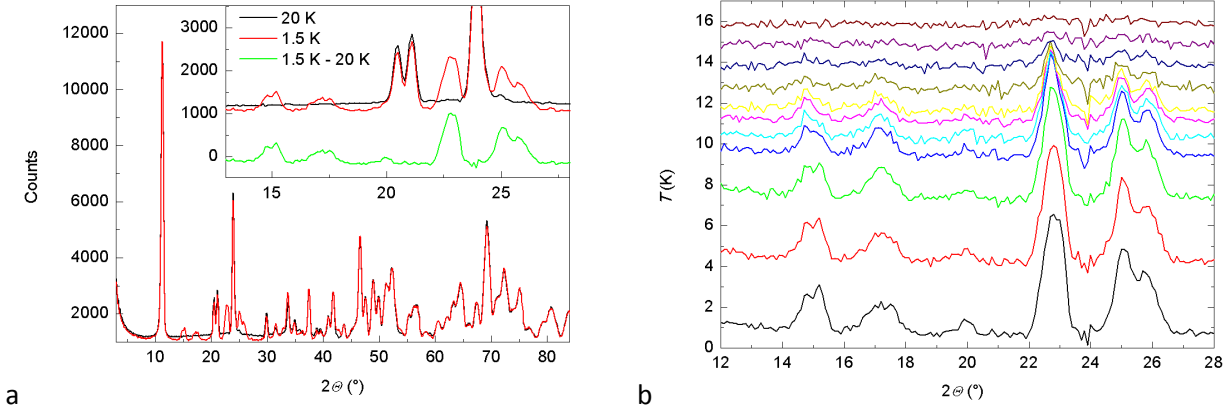


Figure 36: Powder neutron diffraction pattern for $\text{FeTe}_2\text{O}_5\text{Cl}$. (a) spectra measured at 20 K and 1.5 K, inset: subtraction of 20 K spectrum from 1.5 K one. (b) magnetic diffraction pattern obtained by subtraction of 20 K spectrum from spectra measured between 1.5 K and 16 K.

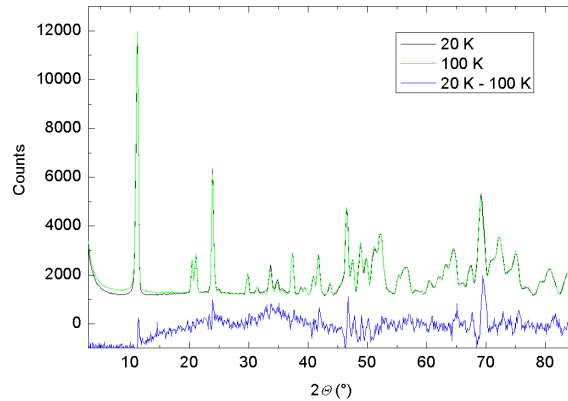


Figure 37: Diffuse magnetic scattering pattern (blue) obtained by subtraction of 100 K spectrum from the one measured at 20 K.

4.3.1.2 Single crystal neutron diffraction

We have continued our investigation of the low-temperature magnetic structure of the $\text{FeTe}_2\text{O}_5\text{Br}$ system by elastic neutron diffraction experiments conducted on the $\text{FeTe}_2\text{O}_5\text{Br}$ single crystals. The measurements were performed using close cycle refrigerator and four-circle mode of the single crystal diffractometer TriCS ($\lambda = 2.32 \text{ \AA}$) at the Swiss Neutron Spallation Source (Switzerland). To determine the magnetic structure factor for the low-temperature magnetic structure, we measured a data set of magnetic reflections at 5 K, where magnetic moments are almost fully developed. In order to ensure the correct relative intensities, magnetic reflections were measured in so called “omega-scan” manner. (Detector stands still, while the sample is being rotated around the vertical goniostat axis omega, i.e., omega scan is the one that goes perpendicularly to the in-plane scattering vector). This way integrated intensities of 41 magnetic reflections were collected. Unfortunately refinement of this data did not converge to a single solution. Therefore, to determine the exact magnetic structure, additional measurements were needed.

4.3.1.3 Polarized neutron scattering

A logical step was to employ polarized neutron scattering, as the neutron spherical polarimetry is the most sensitive method to determine the arrangement of magnetic moments (96), (117), (118). Data were measured on a $7 \times 5 \times 1.6 \text{ mm}^3$ single crystal with CRYOPAD II installed on the IN20 spectrometer ($\lambda = 2.34 \text{ \AA}$) at the Institute Laue Langeven (Grenoble, France). The crystal was mounted with the c -axis perpendicular to the scattering plane and cooled to 1.8 K in a He cryostat. Polarization matrices (Table 5) with elements P_{ij} , (i and j are different components of incoming ($i=x,y,z$) and outgoing ($j=x,y,z$) polarization, where x is parallel to the scattering vector and z is perpendicular to the scattering plane) were measured for 25 $hk0$ incommensurate reflections.

Table 5: As-measured polarization matrices P_{ij} (i - incoming, j - outgoing component of polarization) for two representative reflections measured at 1.8 K (32).

h	k	l	P_i	P_{ix}	P_{iy}	P_{iz}
1/2	-0.463	0	x	-0.85 (2)	0.05 (1)	0.04 (1)
			y	0.03 (1)	0.83 (1)	-0.09 (1)
			z	-0.00 (1)	-0.10 (1)	-0.77 (1)
3/2	1.537	0	x	-0.927 (4)	0.05 (1)	0.01 (1)
			y	0.01 (1)	0.863 (6)	0.34 (1)
			z	-0.04 (1)	0.38 (1)	-0.843 (6)

At first sight one can notice that the off diagonal components P_{yz} and P_{zy} are very small and slightly increase with increasing h or k suggesting that the c -component of magnetic moment is small.

The combined refinement of polarization components and integrated magnetic intensities (25 and 41 independent reflections, respectively) using the CCSL code (119) yields an excellent agreement between the experimental and calculated quantities (Figure 39). The best solution is an amplitude modulated model $S(i, k, l) = S_0 \cos(\vec{q} \cdot \vec{r}_i + \psi_{kl})$ with \vec{r}_i being the vector defining the origin of the i -th cell (32), (120). The modulation amplitude $S_0 = 4.02(9) \mu_B$ is the same for all iron sites in the unit cell, but each atom has its individual phase ψ_{kl} (Table 6). Magnetic moments of the same site are collinear (Figure 38) and almost orthogonal to the wave vector \vec{q} but their directions on adjacent Fe1 and Fe2 sites are slightly inclined at an angle of 7(3) deg (Table 6). We note that the incommensurate long-range magnetic order in $\text{FeTe}_2\text{O}_5\text{Br}$ likely emerges because of the competing interactions within the geometrically frustrated iron tetramers. Finally, we highlight that the refined magnetic structure has very low symmetry with only two symmetry elements, i.e., 1 and 2_{1y} - identity and twofold screw axis respectively, meaning that inversion symmetry of the crystal structure has been broken. Thereby a possibility for macroscopic electric polarization has been introduced.

Table 6: Parameters of the magnetic structure deduced from neutron diffraction experiments. The sites Fe12-Fe14 are obtained from Fe11 (0.1184(6), -0.001(1), -0.0243(7)) and Fe22-Fe24 from Fe21 (0.9386(6), 0.296(1), 0.8568(6)) by symmetry elements 2_{1y} , i , and $2_{1y}i$. Angles θ and φ , which describe the orientation of the iron magnetic moments, are defined with respect to the a^*bc coordinate system. Additionally, each spin has individual phase ψ_{kl} (deg), where index $k = 1, 2$ counts the sites and the second index $l = 1-4$ counts the atoms within the site.

	θ	φ	ψ_{k1}	ψ_{k2}	ψ_{k3}	ψ_{k4}
Fe11-14	100(1)	-52(3)	0	55(5)	-17(4)	260(10)
Fe21-24	100(1)	-45(3)	10(5)	113(5)	-10(11)	274(10)

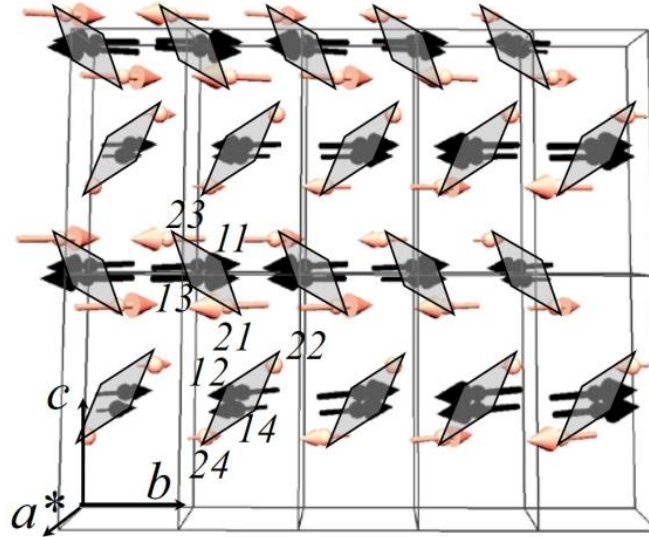


Figure 38: Low-temperature ($T = 1.6$ K) incommensurate magnetic structure obtained from the refinement of neutron diffraction data. Crystallographic positions of the Fe sites and their labelling are given in Table 6.

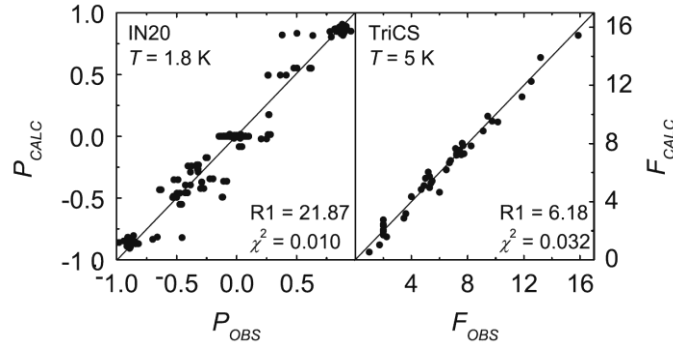


Figure 39: The agreement between the experimental and calculated quantities E: (left) components of neutron polarization matrices $E=P$ and (right) magnetic structure factors $E=F$. The reliability factors are defined as: $R1 = \Sigma \Delta E / \Sigma E$ and $\chi^2 = (\Delta E)^2 / (N_{\text{observables}} - N_{\text{parameters}})$.

4.3.2 μ^+ spin relaxation

In order to validate the magnetic structure model, we performed μ^+ spin relaxation (μ SR) measurements (121). Grinded polycrystalline samples were used in zero-field (ZF) as well as weak transverse-field (wTF 30 G) μ SR measurements. These were performed on the GPS spectrometer at the Paul Scherrer Institute, Villigen, Switzerland. Data were collected in the temperature range between 2 K and 60 K in a continuous-flow helium cryostat.

Typical wTF μ SR spectra are shown in Figure 40a. The muons that stop at interstitial sites in the sample are initially 100 % polarized and start precessing in the local magnetic fields \vec{B}_{loc} . In the paramagnetic phase μ^+ moments coherently precess around weak external magnetic field as shown by the slow oscillations of μ^+ asymmetry Figure 40a. However, in the magnetically ordered regions the internal magnetic field is much larger than wTF of 30 G and causes a reduction of the oscillations' amplitude after short initial times. The remaining oscillating amplitude reflects the portion of muons, which are not coupled to strong static internal magnetic fields. Its temperature evolution is shown in Figure 40b, which is obtained after fitting wTF relaxation data to

$$A_{TF}(t) = A_0 \cos(\gamma_\mu H_{wTF} t) e^{-\lambda_\tau t} + B. \quad (4.8)$$

Here A_0 denotes initial asymmetry, $\gamma_\mu/2\pi = 13.55$ kHz/G is muon gyromagnetic ratio, $H_{wTF} = 30$ G and $e^{-\lambda_T t}$ denotes transversal relaxation. B is time-independent background corresponding to a "1/3"-tail, originating from muons in the ordered phase whose polarization is parallel to internal field. Amplitude parameter A_0 decreases dramatically below the Neel temperature $T_N = 10.6$ K due to the development of static long-range magnetic order. Surprisingly, the residual oscillations, corresponding to the fraction of paramagnetic regions with rapidly fluctuating Fe^{3+} moments, are present even far below T_N . This suggests the coexistence of paramagnetic and magnetically ordered regions and could signalize a first-order magnetic transition. Then again, this fluctuations may account for the reduced size of Fe^{3+} moments observed in the neutron diffraction experiments, where the amplitude of the modulation waves is $S_0 = 4 \mu_B$, i.e. much less than it would be expected for a spin 5/2 system. It is rather unusual for a nearly classical spin system to display such fluctuations at very low temperatures; however, in $\text{FeTe}_2\text{O}_5\text{Br}$ the geometrically frustrated structure of $[\text{Fe}_4\text{O}_{16}]^{20-}$ spin clusters may be responsible for that. On the other hand, we notice also a considerable wTF amplitude reduction for $T > T_N$. This implies the presence of short-range order effects, which can be traced as high as ~ 20 K, i.e., to temperatures largely exceeding T_N . Such behaviour is expected in low-dimensional magnetic systems, which agrees with ESR, magnetization, and neutron diffraction data as well as the $\text{FeTe}_2\text{O}_5\text{Br}$ crystal structure and thus confirms the expectations of weak interlayer coupling in this compound.

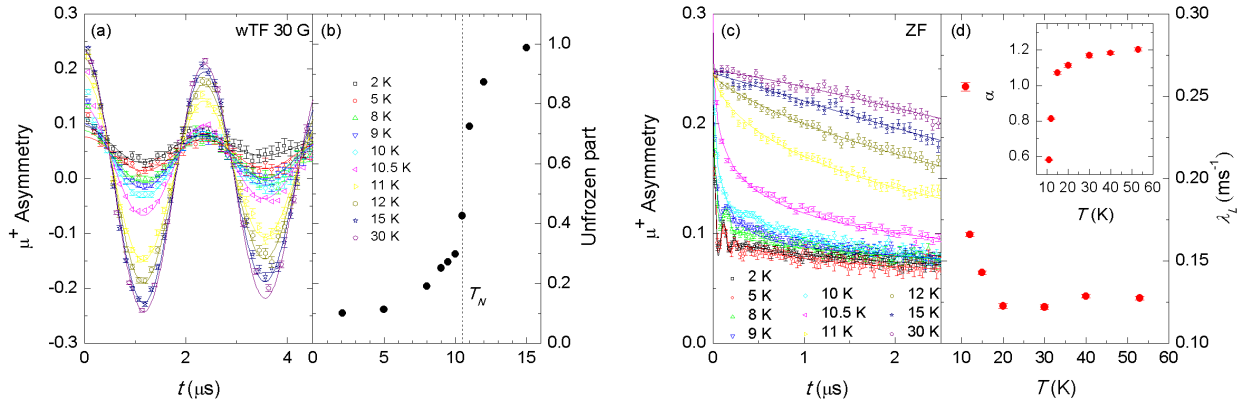


Figure 40: (a) Temperature dependence of weak transverse-field (30 G) μ^+ asymmetry decay in polycrystalline $\text{FeTe}_2\text{O}_5\text{Br}$. Solid curves represent fits to the model (equation (4.8)). (b) Temperature dependent "unfrozen part" representing the fraction of muons not detecting static internal magnetic fields. (c) Zero-field μ^+ SR decay in $\text{FeTe}_2\text{O}_5\text{Br}$. Solid curves above $T_N = 10.6$ K are fits to the stretched exponential model (equation (4.9)), and to the model incommensurate (equation (4.10)), below T_N . (d) Temperature dependence of the longitudinal μ^+ relaxation rate in the paramagnetic phase obtained from the stretched exponential fit. Inset shows the corresponding stretched exponent α .

Next we move to ZF μ SR. Monotonically decaying ZF spectra are recorded above T_N Figure 40c. These spectra can be simulated with the stretched exponential function

$$A_{SE}(t) = A_0 e^{-(\lambda_L t)^\alpha}, \quad (4.9)$$

where λ_L denotes the ZF longitudinal relaxation rate. Stretched exponent $\alpha = 1$ (Lorentzian relaxation) is typical for quickly oscillating electronic fields while $\alpha = 2$ (Gaussian relaxation) is regularly observed for static nuclear fields. In $\text{FeTe}_2\text{O}_5\text{Br}$ at around 50 K $\lambda_L = 0.13 \text{ ms}^{-1}$ and the exponent approaches $\alpha = 1.2$ (inset to Figure 40d), suggesting that both channels are active at high temperatures, whereas the dynamical relaxation channel is greatly enhanced when temperature is lowered towards T_N Figure 40d, i.e., $\alpha = 0.58$ and $\lambda_L = 0.26 \text{ ms}^{-1}$ at 11 K. We assign this to critical Fe^{3+} fluctuations, which are present up to $2T_N$ as implied

by short-range order effects observed in the wTF measurements. The small value of α in the vicinity of T_N , which is below 1, signals multiple non-equivalent μ^+ sites.

Below T_N clear oscillations are observed in ZF spectra Figure 41a, proving the presence of static internal magnetic fields of electronic origin. The low-temperature spectra reveal the presence of at least two oscillating frequencies Figure 41a, corresponding to two muon sites. This is in line with the symmetry of the little group of $\text{FeTe}_2\text{O}_5\text{Br}$ (section 4.4.4). Namely, magnetic order dismisses the inversion-center symmetry thus making pairs of crystallographically equivalent sites magnetically non-equivalent. Additionally, because the magnetic order is incommensurate, as evidenced by neutron diffraction, a distribution of muon precession frequencies is expected for each site.

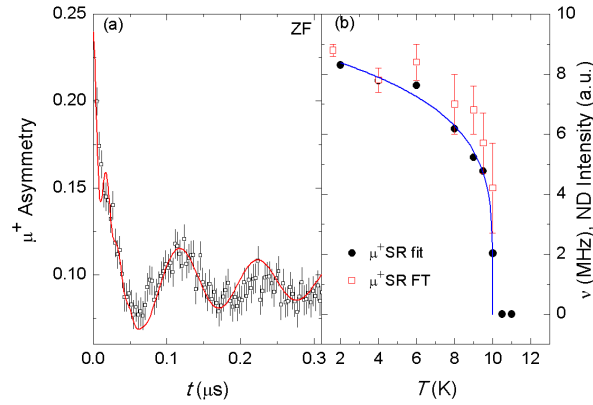


Figure 41: (a) Comparison of incommensurate model (equation (4.10)) with recorded ZF muon relaxation at 2 K. (b) Temperature dependence of + spin precession frequency obtained from ZF relaxation fits (solid circles) and Fourier transform (open squares), compared to the $|T - T_N|^\beta$ law with $\beta = 0.21$.

Unfortunately, the exact muon stopping sites in $\text{FeTe}_2\text{O}_5\text{Br}$ are not known, and consequently we could not calculate exact field distributions. Hence, in order to analyze the low-temperature ZF μ^+ data we assumed the model, corresponding to incommensurate spatially inhomogeneous magnetic fields, which are spread between 0 and H_{max} (122),

$$A_{ICM}(t) = \sum_{i=1}^2 A_0^i \left(\frac{2}{3} J_0(\gamma_\mu H_{max}^i t) + \frac{1}{3} \right), \quad (4.10)$$

where J_0 denotes the zero-order Bessel function of the first kind. The agreement between the experimental data and fit to equation (4.10) is good (Figure 41), which speak in favour of our magnetic structure model.

In (Figure 41b) we plot the temperature dependence of the μ^+ precession frequency of the component with the largest fraction and most obvious frequency, which can be explained with $|T - T_N|^\beta$ law (solid line in Figure 41b). The obtained $\beta \sim 0.21(5)$ reflects the evolution of the average amplitude of the local fields at one of the muon sites, which are induced by the evolving Fe^{3+} ($S = 5/2$) magnetic moments. In spite of that, it is naive to assume that the estimated β is the critical exponent of the magnetic order parameter, as we lack key experimental points in the vicinity of T_N , where $|T - T_N|^\beta$ law should actually apply. Additionally, we calculated Fourier transform (FT) of the μ^+ asymmetry curves and determined the average precession frequency of the same muon site from the first moment of the (FT) spectra. Not surprisingly, both approaches lead to qualitatively similar results.

In conclusion, local-probe wTF and ZF μ^+ SR measurements on the magnetoelectric $\text{FeTe}_2\text{O}_5\text{Br}$ compound revealed pronounced short-range ordering effects up to ~ 20 K. Below T_N a broad distribution of the local magnetic fields experienced by muons is found, confirming the incommensurate nature of the long-range magnetic order; however, details of the magnetic ordering cannot be extracted, since the exact muon stopping sites are unknown.

4.3.3 Nuclear quadrupolar resonance

In order to get additional information about the specific features of the low-temperature magnetic structure, we decided to measure nuclear quadrupolar resonance (NQR) on $^{79,81}\text{Br}$ nuclei. This phenomenon is observed since both Br nuclei have $S > 1/2$ and therefore have non-zero quadrupole moment, $Q(^{79}\text{Br}) = 31.3 \times 10^{-30} \text{ m}^2$ and $Q(^{81}\text{Br}) = 26.2 \times 10^{-30} \text{ m}^2$ ($^{79}\text{Q}/^{81}\text{Q} = 1.19$). For this reason, the energy levels are split in the electric field gradient (EFG) induced by the surrounding atoms and hence the resonant absorption might be observed even in the absence of an external field. However, when magnetic order in the studied compound is established, local magnetic field at Br site will appear and alter its NQR spectrum. Since local fields at Br site are a result of dipolar as well as hyperfine fields coming from Fe^{3+} ($S = 5/2$) magnetic moments, it is not trivial to extract the complete information about the magnetic ordering.

In order to find the NQR frequencies ν_Q , first EFG tensors for both Br sites (1,2) were calculated using density functional theory (DFT) (Table 7). For Br1 results yield rather small asymmetry parameter, $\eta = 0.09$, suggesting almost uniaxial form of the EFG tensor, while the calculated $\nu_Q = 154.97$ MHz is enormous. For Br2 on the other hand, the calculated, $\eta = 0.58$, reflects strongly anisotropic EFG, whereas the $\nu_Q = -42.32$ MHz is more than 3 times smaller. We stress, that DFT calculation results reflect the local surrounding of the Br sites, i.e., the Br1 has only one ion in the neighbourhood (section 4.1), which is probably the reason for almost uniaxial EFG and a small η , whereas the Br2 has two ions in the vicinity, causing the asymmetry and consequently result in a large η value.

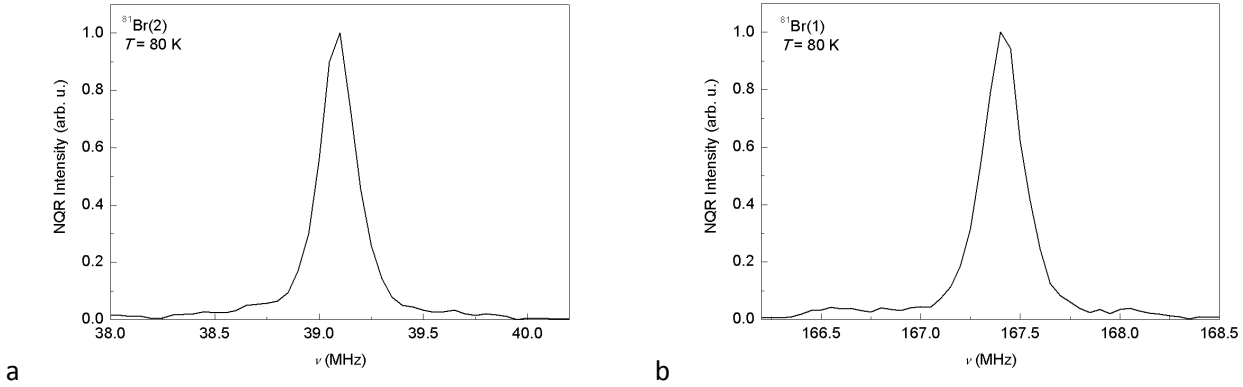
Table 7: Values for EFG tensors at Br1 and Br2 sites in units of 10^{21} V/m^2 in obtained by DFT calculations, where x, y, z correspond to a^*, b, c , respectively.

Br1			Br2		
-15.8353	13.9572	-14.8939	2.96904	0.47202	-2.45593
13.9572	7.00619	-34.5642	0.47202	3.35194	-10.6256
-14.8939	-34.5642	8.82908	-2.45593	-10.6256	-6.32098

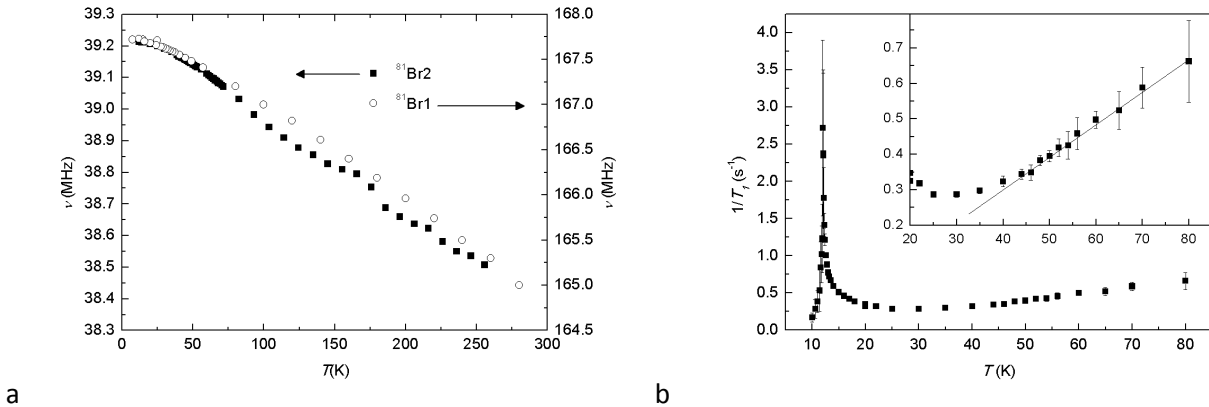
Based on the estimated resonance position values obtained from the DFT calculations, we were able to find in the paramagnetic state all four resonances for $^{81}\text{Br}_2$, $^{79}\text{Br}_2$, $^{81}\text{Br}_1$, and $^{79}\text{Br}_1$ (Figure 42a). The DFT calculations proved to be very accurate, as the calculated values deviated from the measured values for only $\sim 10\%$ (+8.3% for Br1 and -12% for Br2 site). In Table 8 we give some characteristic data for signals obtained at 80 K. All spectral lines can be reasonably well explained by a simple Gaussian distribution with the width of ~ 0.13 MHz. However, at both Br-sites, there is an additional broad, square like, contribution with a width of ~ 2 MHz and centred ~ 0.2 MHz lower in respect to the sharp line. This part contains approximately 20% of the whole signal intensity (Figure 42), and hence represents a considerable portion of the sample. Focusing now on the main part of the signal (sharp Gaussian line) and comparing the values for the spectral width $\delta\nu_{1/2}$, T_1 and T_2 for different isotopes, we can clearly state that the leading relaxation process at both crystallographic sites is magnetic. This comes from the fact that all three parameters scales almost exactly as $(^{79}\gamma/^{81}\gamma)^{-2} = 1.162$, where $^{79}\gamma = 10.6663 \text{ MHz/T}$ and $^{81}\gamma = 11.4978 \text{ MHz/T}$ are the gyromagnetic ratios, for ^{79}Br and ^{81}Br respectively.

Table 8: $^{79,81}\text{Br}$ NQR parameters obtained at $T = 80$ K.

Site	$^{81}\text{Br}2$	$^{79}\text{Br}2$	$^{81}\text{Br}1$	$^{79}\text{Br}1$
ν (MHz)	39.2	46.7	167.2	200.15
$\delta \nu_{1/2}$ (MHz)	0.119	0.141	0.143	0.167
T_1 (ms)	0.275 (0.025)	0.315 (0.05)	1.28 (0.05)	1.45 (0.11)
T_2 (μs)	215 (55)	265 (55)	290 (40)	320 (70)
$\delta \nu_{1/2} (^{79}\text{Br}2) / \delta \nu_{1/2} (^{81}\text{Br}2)$	1.185		1.168	
$T_1(^{79}\text{Br}2) / T_1(^{81}\text{Br}2)$	1.145 (0.29)		1.133 (0.13)	
$T_2(^{79}\text{Br}2) / T_2(^{81}\text{Br}2)$	1.233 (0.57)		1.100 (0.39)	

Figure 42: Temperature dependences of the ^{81}Br nuclear quadrupole resonance spectra at both crystallographically inequivalent positions (a) Br1 and (b) Br2, measured at 80 K.

Now we focus on the temperature dependence of the ^{81}Br signal. On cooling from room temperature to T_N , resonance position for both Br-sites monotonically shifts to higher frequencies (Figure 43a). This most likely reflects the lattice contraction, which manifests in an increase of the EFG. The resonance at Br2-site shifts for $\Delta \nu(\text{Br}2) \sim 0.8$ MHz, whereas at Br1-site $\Delta \nu(\text{Br}1) \sim 2.8$ MHz, hence the ration $\Delta \nu(\text{Br}1) / \Delta \nu(\text{Br}2) = 3.5$ is close to the ratio between the measured quadrupolar frequencies at room temperature $\nu_Q(\text{Br}1) / \nu_Q(\text{Br}2) = 4.3$.

Figure 43: (a) Temperature dependence of ^{81}Br NQR line position for Br1 and Br2 sites. (b) Temperature dependence of $1/T_1$ measured for ^{81}Br resonance at Br1-site. Inset: high-temperature region of $1/T_1$ emphasising the linear dependence indicated with solid line.

This implies that relative change of the EFG at both Br-sites is similar, suggesting that lattice distortions are also alike. To be precise, approximately 20 K above T_N , the shift slowly decreases, most likely due to the

onset of the short-range order correlations. This is even more obvious from the $1/T_1$ temperature dependence (Figure 43b). On cooling from room temperature a monotonic slowing down of magnetic relaxation is detected, i.e., $1/T_1$ is actually proportional to the temperature down to ~ 40 K (inset to Figure 43b). As evident from the equation 3.34 this indicates that in this temperature region the spin correlations are temperature independent, implying that we are in the paramagnetic regime. However, on further cooling $1/T_1 \propto T$ dependence is broken, which designates the development of spin correlations, most likely associated with the onset of short-range ordering within the crystal layers. This is even more pronounced below ~ 25 K, where the relaxation process speeds up and exactly at T_N , $1/T_1$ reaches a singularity, corresponding to the onset of long-range magnetic ordering. Of course, at T_N , NQR spectra dramatically changes. The sharp paramagnetic signal begins to fade away (Inset to Figure 44a), whereas a broad signal, with seemingly symmetrical U-shaped spectra (Figure 44) evolve. The observed U-shaped line can be explained by assuming a sinusoidal dependence of the NQR shift along the magnetic wave vector: $\nu_i = \nu_Q + \delta\nu_{IC} \cos(\vec{q} \cdot \vec{r}_i)$. Here ν_Q is the quadrupolar frequency and $\delta\nu_{IC} \cos(\vec{q} \cdot \vec{r}_i)$ is the shift due to the modulation of the local magnetic field arising from the coupling with nearby Fe^{3+} magnetic moments. In the case of commensurate order, $\cos(\vec{q} \cdot \vec{r}_i)$ would take discrete values and would result in a spectrum composed of a finite number of sharp lines. However, when magnetic order is incommensurate, $\cos(\vec{q} \cdot \vec{r}_i)$ takes all values between -1 and 1 so that the spectral intensity is continuously distributed between the two singularities, occurring at $\pm\delta\nu_{IC}$. Coming back to the experimental results, we can see that the width of the spectra at half maximum for the Br1-site is ~ 1.7 MHz, whereas the distance between the singularities is ~ 0.9 MHz. For Br2-site the spectra is broader, i.e., the width at half maximum is ~ 3 MHz, and the distance between the singularities is ~ 2 MHz. The splitting (between the singularities) implies that the projections of the hyperfine fields at the ^{81}Br sites to the principal axis of the EFG tensor are $B_{hf} = 0.08$ T and $B_{hf} = 0.094$ T for Br1 and Br2 sites respectively. Just 0.4 K below T_N the spectra change again, indicating a second magnetic transition. We note that from this point on we will name the temperature of the first magnetic transition T_{N1} , and T_{N2} the temperature of the second magnetic transition. So, above T_{N1} , the system is in the paramagnetic (PM) state, between T_{N1} and T_{N2} we have a high-temperature magnetic phase, which seem to be incommensurate (HT-ICM), and below T_{N2} low-temperature (LT-ICM) magnetic phases is present. In LT-ICM phase, spectrum at Br1-site develops even clearer U-shape with two very distinct singularities, characteristic for an incommensurate magnetic structure. Actually, at lowest temperature (4 K), spectrum is a bit more complicated. On the outside side of the singularities, now almost 3.1 MHz apart ($B_{hf} = 0.145$ T), two shoulders, which extent more than 1.5 MHz, evolve. Additionally, the spectral intensity seems to drop with the increasing frequency. In Figure 44c,d we plot the temperature evolution of splitting between the singularities, which give us an estimation of the hyperfine fields and consequently the magnitude of the evolving Fe^{3+} ($S = 5/2$) magnetic moments, i.e., magnetic order parameter. Obviously the magnetic order parameter displays a $(T_N - T)^\beta$ behaviour, though, due to the lack of the experimental points, the estimation of $\beta(\text{Br1}) = 0.26(4)$ and $\beta(\text{Br2}) = 0.40(5)$ might be misleading and difficult to interpret. Actually, both values should match; hence our uncertainty about meaningfulness of these values is justified. In contrast to Br1-site, for Br2-site the symmetry of the spectrum in the LT-ICM phase is lost. With decreasing temperature three different and almost completely separated U-shaped lines evolve (Figure 44b). At 9 K, the low-frequency line is well separated and has a U-shape with additional shoulders similar as the low-temperature Br1-line. Here the singularities are ~ 1.3 MHz apart, left shoulder extent for 0.8 MHz, whereas the right shoulder extent only for 0.5 MHz. The middle line seems to be the widest, as the two singularities are ~ 1.9 MHz apart. Here it is difficult to say much about shoulders since the line overlaps with the high-frequency one. This line has singularities separated for only ~ 0.8 MHz, and do not seem to have pronounced shoulders. At 4 K all three lines broadens even more. The lowest frequency line has singularities ~ 1.5 MHz apart and 1.2

MHz wide left and 0.6 MHz wide right shoulders. The middle line, with singularities ~ 2.8 MHz apart, now strongly overlaps with high-frequency line, which has singularities separated for ~ 1.2 MHz.

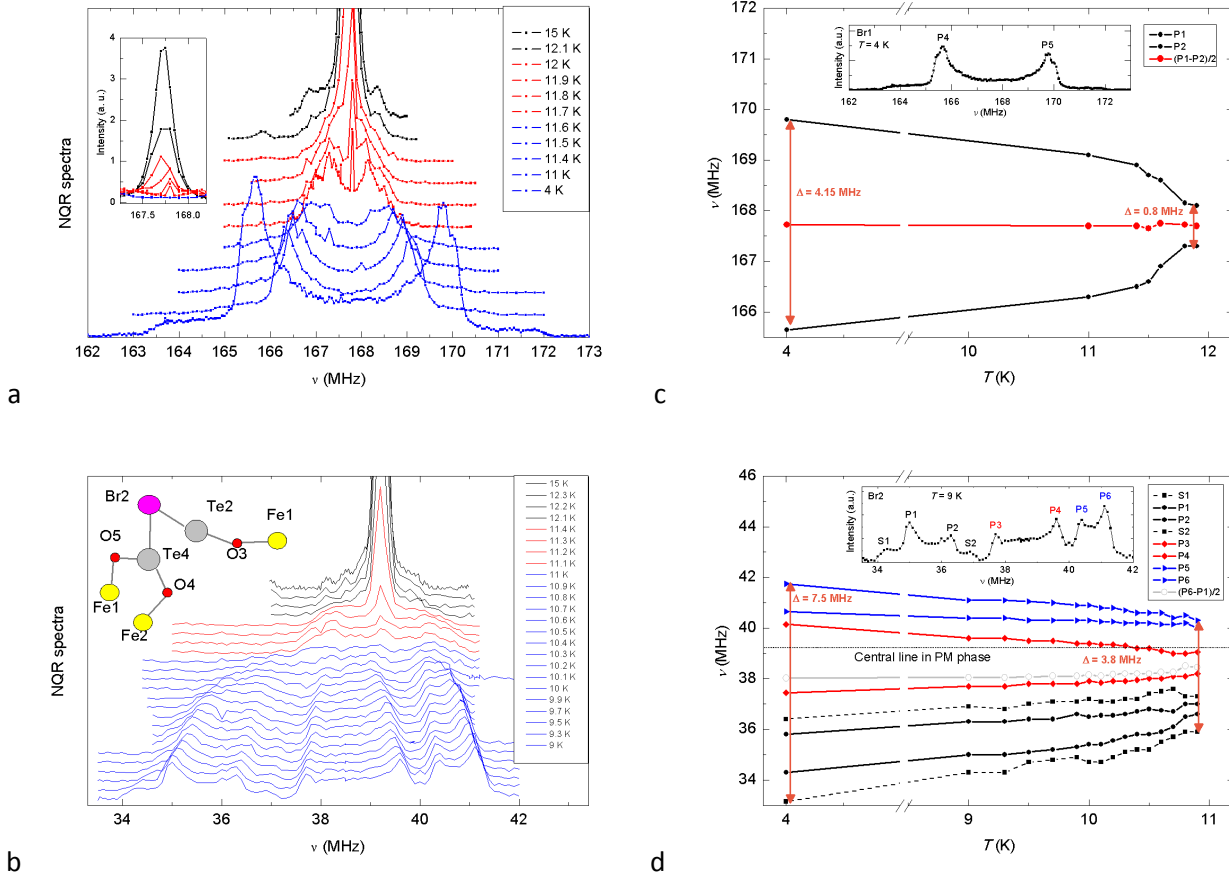


Figure 44: NQR spectra measured between 15 K and 4 K at (a) Br1-site and (b) Br2-site, and the temperature evolution of the singularities for (c) Br1-site and (d) Br2-site.

In order to understand the difference in the spectra for Br1 and Br2 sites in the LT-ICM phase, which magnetic structure is determined from the neutron diffraction, we first look at the crystal structure of our sample. As already mentioned in the section 4.1 the Br1 sites are coupled to only one Fe ion, while Br2 sites are coupled to three Fe ions. However, a simple explanation that coupling to one Fe site would result in one line and coupling to three Fe sites results in three lines is wrong. One must not forget that coupling to one or several magnetic ions cannot change the ν_Q and consequently split the spectra, i.e., the hyperfine coupling always result in a local magnetic field. However, this can have very complex spatial dependence. At this point we stress that in the magnetically ordered phase, magnetic moments at all Fe sites in the crystal unit cell (there are eight of them) have different phases of their amplitude modulation waves. Hence, we can expect that the resulting hyperfine fields at the Br2 sites might indeed have very complex spatial dependence, which can give rise to an unusual field distribution at Br2 site. In addition the calculated EFG tensor for Br2 site has a large η value, which furthermore contributes to the complexity of the NQR spectra. At last we should stress that the spectra are finally altered by dipolar fields, with an extraordinary spatial distribution.

To investigate the origin and nature of the observed spectra, we performed also detailed measurements of T_1 and T_2 relaxation times along the low-temperature spectra. We show ^{81}Br dependences of $1/T_1$ and $1/T_2$ for both Br sites on Figure 45. Obviously, both relaxation times have non-trivial frequency dependence which is in a way correlated with the spectral intensity. For Br2 site spin lattice relaxation $1/T_1$ seems to be inversely proportional to the spectral intensity, i.e., it has minima on top of the most pronounced spectral

singularities, where $1/T_1$ is 1.46(2)-2.02(2) ms^{-1} , while it increases up to 9(3) ms^{-1} (Figure 45) in between. Similar dependence is also found for spin-spin relaxation $1/T_2$, though its values are a bit larger, i.e., $1/T_2$ varies between 3.3(2) ms^{-1} on top of singularities to 20(5) ms^{-1} among them. Similar behaviour along all three lines implies that the spectrum actually corresponds to the crystallographically same site, and that its complex triple structure is merely the consequence of the non-trivial spatial dependence of the local magnetic field, resulting from hyperfine coupling with Fe^{3+} ($S = 5/2$) magnetic moments as well as their dipolar fields. At Br1 site, $1/T_1$ is almost an order of magnitude shorter and interestingly shows just the opposite behaviour. On top of each spectral intensity singularities it has maximum ($1/T_1 = 3.8(1) \text{ms}^{-1}$), while it has a minimum ($1/T_1 = 0.19(1) \text{ms}^{-1}$) in the middle. $1/T_2$ on the other hand, behaves almost exactly as at Br2 site. It is not much shorter and its minima coincide with spectral intensity singularities, reaching 2.1(4) ms^{-1} and 6.3(5) ms in between. We note that almost identical behaviour was found for ^{79}Br at both sites.

The explanation for the observed behaviour of $1/T_1$ at Br1 site might be the following. The maxima in the spectral intensity correspond to the Br sites in the vicinity of maximally developed Fe^{3+} ($S = 5/2$) magnetic moments, whereas the central part of the spectrum corresponds to the Br sites close to Fe's with almost no magnetic moment developed. This difference also influences the relaxation processes and hence reflects in the measured $1/T_1$. At sites, where Fe^{3+} ($S = 5/2$) magnetic moments are fully developed, the lowest energy excitations and therefore also the driving relaxation mechanism would be phasons. The phason represents the sliding of the incommensurate modulation wave and therefore corresponds to the Goldstone mode (gapless), recovering the broken translational periodicity of the ICM phase. Actually in real systems, discrete lattice effects and impurities may produce a locking of the modulation wave to the under lying lattice and hence introduce the gap in to the phason spectrum (123), making $1/T_1 < \infty$. On the other hand, at sites where Fe's have almost no magnetic moment developed the relaxation process is driven by amplitudons, i.e., the excitations of the amplitude of the Fe^{3+} ($S = 5/2$) magnetic moment. These excitations are expected to be more costly, since they have to compete with the superexchange interactions, hence also the expected $1/T_1$ is shorter. This interpretation is in agreement with the proposed incommensurate amplitude modulated magnetic structure of the LT-ICM, and thus corroborates with neutron diffraction measurements.

On contrary the observed relaxation rates at Br2 site cannot be so easily explained. We stress that the Br2 spectrum is a result of no-trivial local magnetic field, which is a combination of three hyperfine fields coming from different modulation waves and therefore varies in magnitude as well as in orientation. Hence the maxima and minima in the Br2 spectrum cannot be associated solely to the magnitude of Fe^{3+} ($S = 5/2$) magnetic moments, making it impossible to identify the relaxation process at specific spectral position.

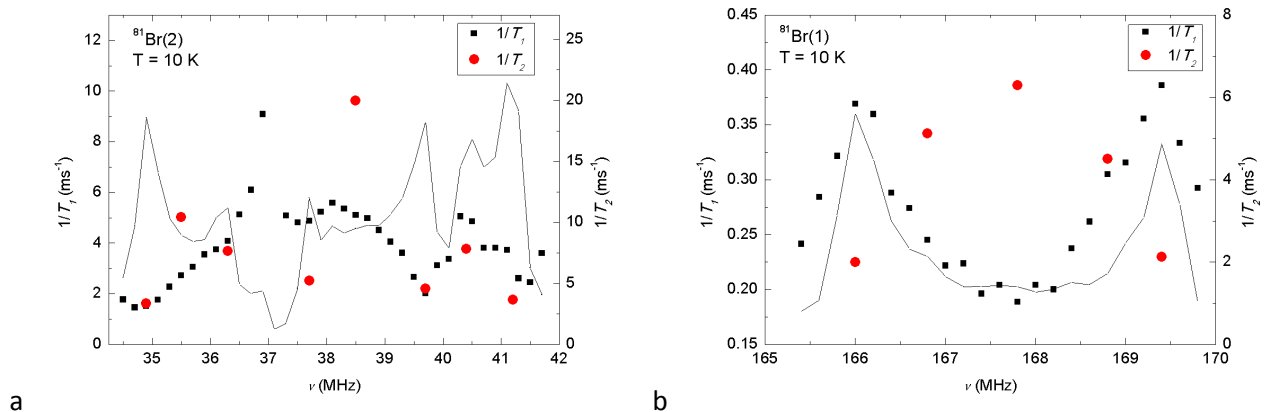


Figure 45: $1/T_1$ and $1/T_2$ relaxation rates measured along the ^{81}Br spectra for (a) Br2 and (b) Br1 sites.

Now we try to simulate the low-temperature NQR spectra considering the calculated EFG tensors (Table 7) scaled by the appropriate factors obtained from the deviation of the NQR resonances in the paramagnetic phase (+8.3 % for Br1 and -12 % for Br2 site) and the magnetic structure model obtained from the neutron diffraction measurements (Table 6). Calculations were performed according to the procedure explained in the section 3.1.2.3 considering different transferred hyperfine coupling tensors for each hyperfine pathway, dipolar fields produced by Fe^{3+} ($S = 5/2$) magnetic moments as well as calculated EFG tensors (Table 7). Hence we are left with 18 free parameters for Br2 site and 6 for Br1 site to describe the NQR spectra. The obtained fits for both Br sites are shown in Figure 46 (in case of Br2 we show the complete spectra for ^{81}Br as well as ^{79}Br since they overlap at low temperatures). In both cases all the major features (singularities and minima) are reproduced, though the agreement is much better for Br1 site. Obviously this is the consequence of a simpler spectrum as well as significantly smaller number of free parameters. In this respect, we are also confident that the obtained set of fitting parameters is the best solution. The obtained parameters for local magnetic field at Br-site per μ_B of the Fe^{3+} ($S = 5/2$) magnetic moment induced by hyperfine coupling are shown Table 9. However, the fit does not reproduce nicely the shape of the shoulders and intensities of singularities. This deviation might be the consequence of neglecting the broad part of the spectra observed in the paramagnetic phase (Figure 42) in our simulations. For Br2 spectra the deviations are even more pronounced. Even though we can reasonably well reproduce the shape of the spectrum, we have difficulties with positions of the calculated singularities and minima. In case of the third line (between 40 MHz and 42 MHz) strong discrepancy in the spectral intensity is observed, which might have an instrumental origin, since no such discrepancy is observed for the line at 48 MHz, coming from ^{79}Br , which should behave similar as ^{81}Br line.

Table 9: Obtained parameters for hyperfine coupling from fitting the NQR spectra in units of T/μ_B .

Br1-Te2-O3-Fe1			Br2-Te4-O4-Fe2			Br2-Te4-O5-Fe1			Br2-Te2-O3-Fe1		
0.124	-0.004	0.062	0.082	-0.165	0	0.041	-0.082	0	0.041	-0.082	0
-0.004	0.124	-0.004	-0.165	0.082	0.165	-0.082	0.041	0	-0.082	0.041	-0.082
0.062	-0.004	0.124	0	0.165	0.082	0	0	0.041	0	-0.082	0.041

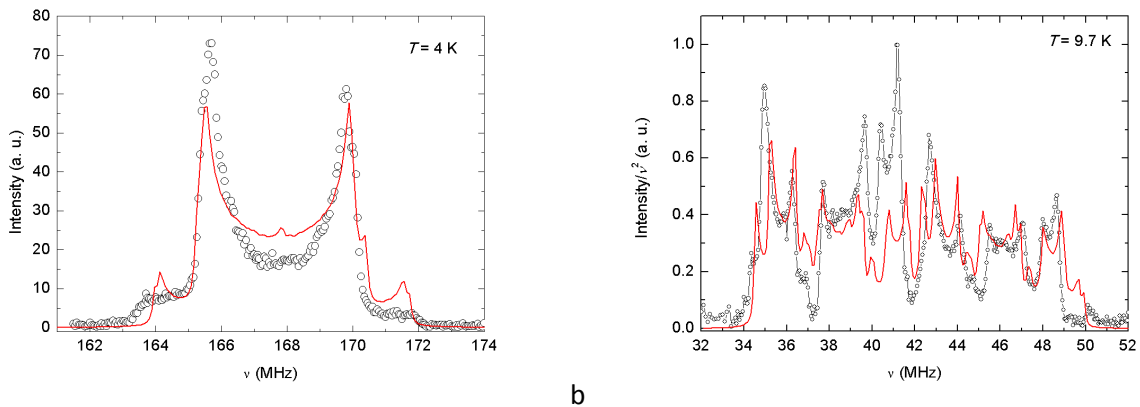


Figure 46: Low-temperature spectra (empty symbols) and fits (line), calculated as explained in text, (a) for Br1 and (b) for Br2 site.

In order to better understand the origin of so complex spectra, we make here a more pedagogic approach. Let us restrict to only one Br ion in its local environment neglecting any local magnetic field. Since Br nucleus has a quadrupolar moment, its energy levels will be split due to EFG produced by its diamagnetic neighbours (Figure 47). When local magnetic field is applied, these levels will shift, depending on the strength and

direction of the local magnetic field, according to equation 3.27 (Figure 47). Now imagine that each of the Br nuclei at a particular crystallographic site, e.g., Br12-site (the Br nuclei determined by Br1 position in Table 2 upon which two fold screw axis is applied), feels different local magnetic field. This is determined by the magnitude of the Fe^{3+} magnetic moment at a particular Fe-site coupled by a transferred hyperfine coupling. Considering that amplitude of magnetic moment is actually spatially modulated for our magnetic structure model, we end up with a distribution of the Br energy levels, which determine the distribution of the resonant frequencies shown in the left sides of Figure 48a and b, for Br12 and Br21 sites respectively. Finally, calculating also the probability for each magnetic transition according to equation (3.23) we obtain the predicted NMR spectra shown in the right sides of Figure 48a and b.

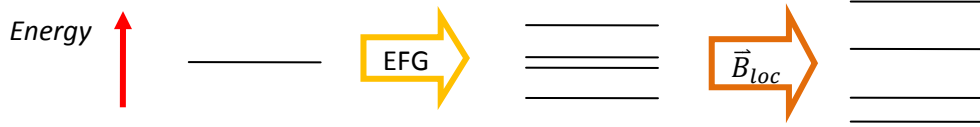


Figure 47: Splitting of the energy levels of for $S = 3/2$. For weak local magnetic fields, the splitting of the energy levels is mostly determined by the EFG, which is further altered by local magnetic field. In case that quadrupolar and Zeeman interactions are comparable, exact diagonalization of the complete Hamiltonian has to be performed to obtain correct eigen energies.

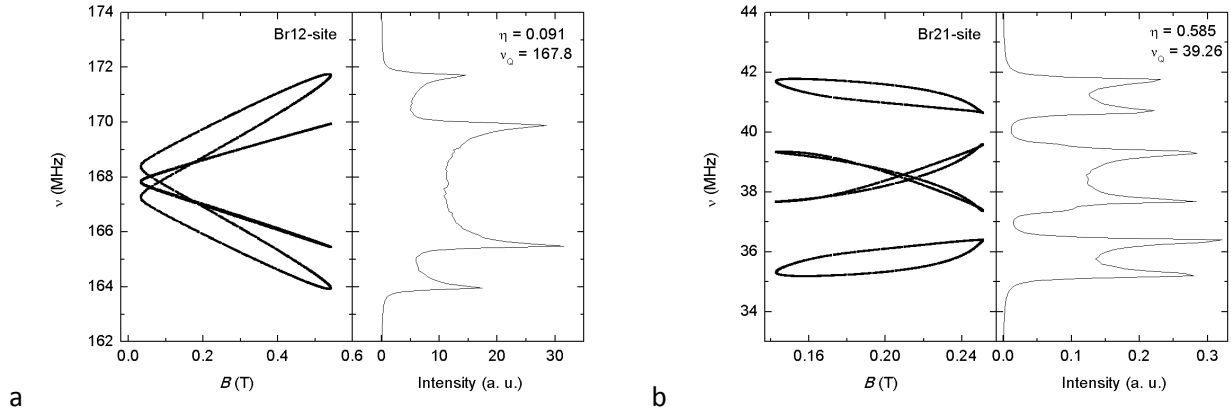


Figure 48: Simulated frequency distribution and spectra for individual (a) Br12 and (b) Br21 sites assuming the hyperfine coupling constants obtained from fit, as explained in text.

We must keep in mind that due to the complex magnetic structure, spectrum for Br1 as well as Br2 sites should be regarded as a sum of four inequivalent sites with different local field distributions. Additionally, in our fitting procedure we have considered also a correction of local fields due to dipole-dipole interactions.

To sum up, the complexity of the measured spectra (Figure 46) signify that local magnetic field at Br-site, which is a sum of dipolar and hyperfine fields, varies in amplitude as well as in orientation. Our analysis also shows that transferred hyperfine magnetic field at Br2 site should have a significant c -component, which is essential for the occurrence of three lines in the Br2 spectrum, thus implying the importance of the off-diagonal hyperfine coupling terms.

4.3.4 Summary of the magnetic ordering

On cooling, below ~ 20 K, the short-range order is indisputably reflected in the obtained data – diffuse neutron diffraction scattering, reduction of the magnitude of the μSR oscillations and increasing relaxation rate in NQR experiments. Below $T_{N2} = 10.6$ K, the system undergoes a magnetic transition into incommensurate transverse amplitude modulated magnetic ordering - LT-ICM phase - with eight amplitude modulation waves, all having different phases. This magnetic model is in agreement with μSR results and also explains the complex NQR spectra. We stress that above the LT-ICM there is a narrow interval of 0.4 K when the system is in the HT-ICM phase, which will be discussed more precisely in the section 4.5.

4.4 Ferroelectric transition and its relation to magnetism

Evidently, the magnetic structure has no inversion centre (Figure 38). This removes the symmetry restriction for the coexistence of ferroelectric and magnetic order.

4.4.1 Thermal expansion measurements

In order to investigate a potential existence of ferroelectricity and its impact on the crystal lattice, we performed thermal expansion measurements. The measurements were carried out along the c -axis, with magnetic field applied also along the c -axis in the temperature interval between 150 K and 4 K in two runs to check for reproducibility. The data were taken in warming up employing a low sweep rate of 1.5K/h.

In Figure 49a a complete temperature dependence of the thermal expansion parameter along c -axis, α_c , is shown. At high temperatures α_c is positive (at 140 K $\alpha_c = 10 \times 10^{-6} \text{ K}^{-1}$) and becomes reduced upon cooling, which imitates anticipated lattice expansion with increasing temperature (dotted line in Figure 49). However, on cooling below 70 K the α_c behaviour becomes anomalous. At ~ 50 K, α_c changes sign and exhibits a pronounced negative anomaly centred at 20 K. This means that cooling below 50 K is accompanied by an expansion of the c -axis lattice parameter. The 20 K anomaly coincides with the onset of short-range magnetic ordering detected by experimental techniques probing the magnetic response of the system presented in preceding sections. We thus have a first evidence for a spin-lattice coupling, which indicates a possible existence of a strong electromagnetic coupling.

A magnification of the data around 10 K, Figure 49b reveals a very sharp spike around ~ 10.5 K on top of the above-mentioned negative contribution. The shape of the transition is lambda like, indicating strong critical fluctuations, while its position nicely coincides with the magnetic transition temperature. Thus, we have a definite proof that the establishment of the long-range magnetic ordering is accompanied with crystal lattice distortion, implying a possible onset of electric polarization.

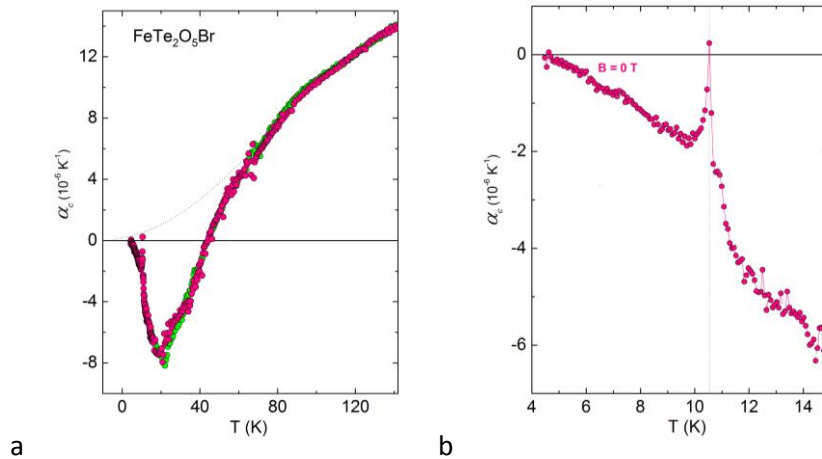


Figure 49: (a) Temperature dependence of the thermal expansion parameter along c -axis α_c . (b) Magnification of the low-temperature part.

4.4.2 X-ray diffraction experiments

To precisely monitor the changes in the crystal structure during the development of the long-range magnetic ordering and to locate the source of a potential electric polarization, we performed low-temperature single-crystal synchrotron x-ray diffraction experiments at the BM01A Swiss-Norwegian Beamline of ESRF (Grenoble, France). Data sets (typically 780 reflections per temperature point) were collected in the temperature range between 4.5 K and 35 K at a wavelength of 0.64 Å using a closed-cycle He cryostat mounted on a six-circle kappa diffractometer KUMA.

On cooling through the magnetic transition, no structural distortions, leading to measurable changes in the lattice symmetry or cell metrics, were found. However, the high-quality of the data allowed us to refine (124) the atomic positions and to deduce the interatomic distances at each measured temperature. The Fe-Te distances, revealed in Figure 50, show clearly distinguishable changes below 10 K, which confirm that the crystal lattice responds to the onset of magnetic order. This finding is important because, on one hand, Te^{4+} ions bridge the intercluster superexchange interactions and, on the other, Te^{4+} ions have lone-pair electrons. As already mentioned in the theory section, lone-pair electrons are often stereochemically active and easily polarisable. The observed structural anomalies therefore suggest a possible polarization of the Te^{4+} lone-pair electrons, which might result in the macroscopic electric polarization. However, the changes are tiny, in the range of 0.03 Å, thus rather small magnitude of electric polarization is expected.

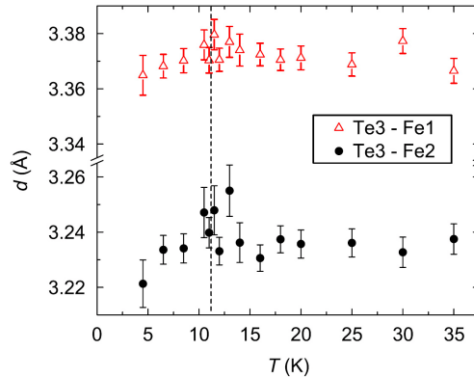


Figure 50: Temperature dependence of Fe-Te distances obtained from the refinement of the X-ray diffraction experiment.

4.4.3 Dielectric measurements

The structural investigation of the $\text{FeTe}_2\text{O}_5\text{Br}$ system (sections 4.4.1 and 4.4.2) evidently shows that changes in the crystal lattice coincide with the magnetic transition. We therefore decided to measure the temperature dependence of the dielectric constant, ϵ , and the electric polarisation, P . The complex dielectric constant $\epsilon^*(T, \omega) = \epsilon'(T, \omega) - i\epsilon''(T, \omega)$ was measured as a function of temperature and frequency ω by using an HP4282A precision LCR meter. The dielectric constant was scanned at few frequencies between 20 Hz and 1 MHz on cooling or heating the sample with the typical cooling/heating rates of 10 K/h in the various dc bias electric fields ranging from 0-3 kV/cm. The excitation electric ac field of 100-400 V/cm was applied along the a^* , b and c axes. The quasistatic polarization (P) was determined by electrometer charge accumulation measurements in a field cooling run. Here bias field of 10 kV/cm was used, which was several times higher than the coercive field (~ 1 kV/cm) in order to obtain saturated spontaneous polarization. Zero field ac dielectric measurements and ac dielectric measurements in the dc electric bias field were performed in the Oxford continuous flow liquid helium cryostat.

An extremely sharp peak in real part of dielectric constant, ϵ' , at $T_N = 10.5(1)$ K (Figure 51a) indicates a transition to a long-range ferroelectric (FE) state. At the same time, imaginary part of the dielectric constant, ϵ'' , is very small and not frequency dependent proving intrinsic nature of the observed transition. The ferroelectric state is unambiguously confirmed by the emergence of spontaneous polarisation (Figure 51c) measured using an electrometer charge accumulation technique (108), (107) and the reversal of spontaneous polarization with the electric field (Figure 51b). The spontaneous polarization is largest along the crystal c -axis, $P(c) = 8.5(2)$ $\mu\text{C}/\text{m}^2$, and is almost an order of magnitude smaller in a^* , $P(a^*) = 1.0(1)$ $\mu\text{C}/\text{m}^2$, while for the b direction it is below the sensitivity of our experimental equipment. Comparing the temperature dependence of P to the intensity of the magnetic (1/2 1.537 0) peak, I , it is obvious that the two transitions coincide (Figure 51c).

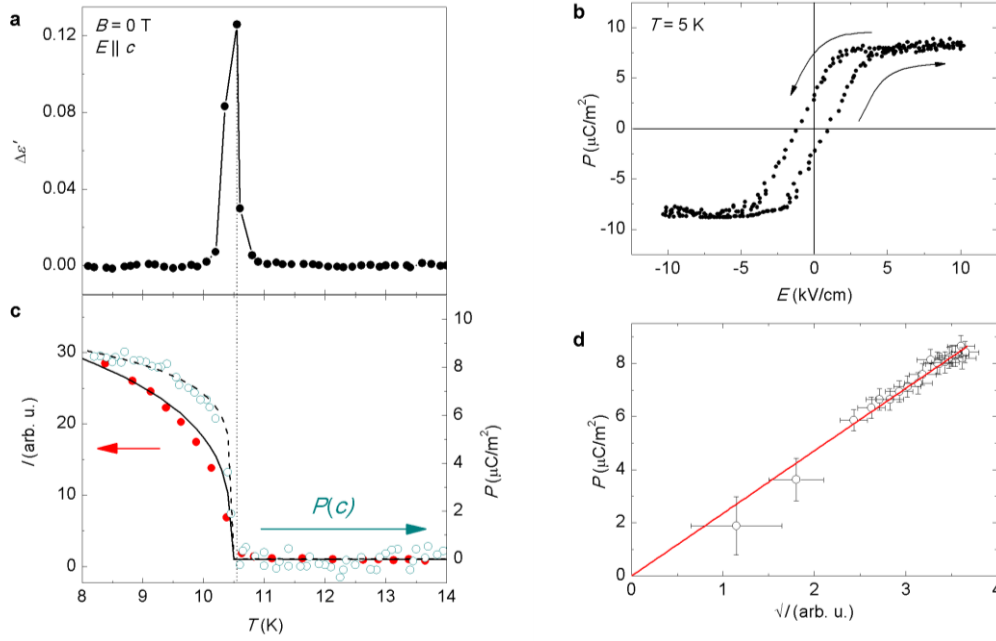


Figure 51: (a) Temperature dependence of the change in the dielectric constant $\Delta\varepsilon = \varepsilon(T) - \varepsilon(14\text{ K})$ measured for $\vec{E}||c$ in zero magnetic field. (b) Ferroelectric hysteresis loop for $\vec{E}||c$ measured at 5 K. (c) Temperature dependence of the spontaneous electric polarisation \vec{P} for $\vec{E}||c$ (open cycle, right-hand scale) and the intensity of the (1.5, 1.537, 0) neutron diffraction magnetic peak I (solid cycle, left-hand scale). I and P calculated from equations (4.14) and (4.15) are presented with solid line and dashed line, respectively, for $\beta = 0.15$. (d) A linear correlation between \sqrt{I} and P .

The sharpness of the anomaly in the ε' implies that the ferroelectric transition might actually be first-order one, meaning that the symmetry of the LT-ICM/FE phase might be completely different compared to the paramagnetic phase. This is in agreement with the temperature evolution of the ferroelectric order parameter P , which can be described with $P \propto (T_N - T)^\beta$, where $\beta = 0.17(2)$ is very small compared to the 0.23, 0.33 values typical for second order transitions for 2D and 3D ordering. However, there is no sign of the temperature hysteresis implying that the transition is at most weakly first transition, and hence we believe the symmetry relation between disordered and ordered magnetic phases is retained. We stress that when magnetic field was applied along the a^* direction, both the Néel-transition and the ferroelectric-transition temperatures simultaneously decrease (Figure 53, Figure 64), proving the presence of the magnetoelectric coupling in $\text{FeTe}_2\text{O}_5\text{Br}$.

Considering now also the observed structural anomalies (Figure 49, Figure 50), we suspect that the observed electric polarization is likely to originate from asymmetric distortions of the Te^{4+} lone-pair electrons induced by the onset of the LT-ICM phase, which brakes the global inversion symmetry. Moreover, the detected changes of the tetramer Fe-O interatomic distances imply that the coupling between polar and magnetic order parameters is likely mediated through Fe-O-Te-O-Fe intercluster superexchange. We stress, that the standard spin-current (62) and “inverse Dzyaloshinskii-Moriya” (63) models developed for spiral magnetic structures are unlikely to be active in $\text{FeTe}_2\text{O}_5\text{Br}$, since magnetic moments vary in amplitude and not in direction along \vec{q} . Alternatively, the exchange-striction model was frequently applied to magnetoelectrics with collinear magnetic order (64), (65), (66), (67).

4.4.4 Theory of the magnetoelectric coupling

The phenomenological explanation for the occurrence of the magnetoelectric effect in incommensurate helical or spiral magnetic phases has been given with thermodynamic potential terms of type $\vec{P} = [\vec{M}(\nabla \cdot \vec{M}) - (\vec{M} \cdot \nabla)\vec{M}]$ (58). For our magnetic structure (Table 6) we calculate that \vec{P} should lie in the a^*b

plane in striking contrast to the experimentally observed $\vec{P}(c)$ component. We next extended calculations by an additional $\vec{P} \cdot \nabla(\vec{M})$ term, which is important when \vec{P} is a sum of homogeneous and spatially modulated contributions (59). However, this additional term also cannot reproduce the correct \vec{P} direction. Hence, it appears that coupling terms, which work very well for helical or spiral magnetic orderings, cannot explain the appearance and the correct direction of the ferroelectric polarization in $\text{FeTe}_2\text{O}_5\text{Br}$.

In order to better understand the magnetoelectric coupling in $\text{FeTe}_2\text{O}_5\text{Br}$ we proceed first with the representation analysis. The crystal group of our system is $P2_1/c$, hence it has four symmetry elements: identity 1 (x, y, z), twofold screw axis 2_{1y} ($-x, 0.5+y, 0.5-z$), inversion centre ($-x, -y, -z$), and the combination of the last two – the mirror plane m_y ($x, 0.5-y, 0.5+z$). The star of the wave vector is formed by the two vectors \vec{q} and $-\vec{q}$, defining the little (magnetic) group, which is therefore composed of only two elements, namely 1 and 2_{1y} , i.e., inversion symmetry is lost. Consequently, the little group has two one-dimensional irreducible representations, Γ_1 and Γ_2 , and the $4(e)$ sites are split into two orbits (Table 10).

Table 10: Results of representation analysis for $\vec{q} = (0.5 \ 0.463 \ 0)$ in $P2_1/c$. Complex basis vectors of magnetic moments for atoms 1 (x, y, z) and 2 ($-x, y+1/2, -z+1/2$) from the same orbit ($\eta = e^{-i\pi q_y}$) for Γ_1 and Γ_2 .

Orbit/symmetry operation	Γ_1			Γ_2		
1 / 1	(1 0 0)	(0 1 0)	(0 0 1)	(1 0 0)	(0 1 0)	(0 0 1)
2 / 2_{1y}	($-\eta$ 0 0)	(0 η 0)	(0 0 $-\eta$)	(η 0 0)	(0 $-\eta$ 0)	(0 0 η)

The resulting Fourier components of the magnetic moment for atom 1 and 2 hence depend on the choice of the irreducible representation. Assuming that the magnetic moments lie in the ab -plane, we write the Fourier components of the magnetic moments for both atoms corresponding to Γ_1 and Γ_2 :

Fourier component (site)	Γ_1	Γ_2
$\vec{S}(\vec{q}, 1)$	$(M_{1x}, M_{1y}, 0)e^{i\phi_1}$	$(M_{2x}, M_{2y}, 0)e^{i\phi_2}$
$\vec{S}(\vec{q}, 2)$	$(-M_{1x}, M_{1y}, 0)e^{i(\pi q_y + \phi_1)}$	$(M_{2x}, -M_{2y}, 0)e^{i(\pi q_y + \phi_2)}$

Here, each representation is defined by a complex order parameter, which has its own phase ϕ_1 and ϕ_2 , and magnitude $|M_1|$ and $|M_2|$ for Γ_1 and Γ_2 respectively. Since the refined phase shift between the two magnetic moments from the same orbit (Table 6) differs from the $\pi q_y = 83^\circ$ value expected from the symmetry relations, we conclude that our magnetic model is a combination of both Γ_1 and Γ_2 :

Fourier component (site)	$\Gamma_1 + \Gamma_2$
$\vec{S}(\vec{q}, 1)$	$(M_{1x}e^{i\phi_1} + M_{2x}e^{i\phi_2}, M_{1y}e^{i\phi_1} + M_{2y}e^{i\phi_2}, 0)$
$\vec{S}(\vec{q}, 2)$	$(-M_{1x}e^{i\phi_1} + M_{2x}e^{i\phi_2}, M_{1y}e^{i\phi_1} - M_{2y}e^{i\phi_2}, 0)e^{i\pi q_y}$

Hence the important coupling term, which already takes into account observed orientations of \vec{P} and Fe^{3+} magnetic moments as well as the symmetry operations of the little group, is written as

$$V = i \sum_{\alpha, \beta} \varepsilon_{\alpha\beta} [S_{\alpha}(\vec{q}, 1)S_{\beta}^*(\vec{q}, 2) - S_{\alpha}^*(\vec{q}, 1)S_{\beta}(\vec{q}, 2)] P_c \quad (4.11)$$

Here $\varepsilon_{\alpha\beta}$ is the magnetoelectric coupling tensor, $\alpha, \beta = x, y$, and $S_{\alpha}(\vec{q}, i)$ is the Fourier component of the magnetic moments for Fe atoms $i = 1, 2$ (Table 10). Based on the proposed magnetoelectric coupling term

and the above derived Fourier components taken for a combination of Γ_1 and Γ_2 we can derive magnetic structure factor $\vec{M}_f(\vec{q}) = C[\vec{S}(\vec{q}, 1) + \vec{S}(\vec{q}, 2)]$ (C is a constant) and consequently write the expressions for neutron magnetic peak intensity $I = \vec{M}_f(\vec{q}) \cdot \vec{M}_f^*(\vec{q})$ and electric polarization P :

$$\begin{aligned}
I = |C|^2 & \left(2 \left[(|M_{1x}|^2 + |M_{1y}|^2 + |M_{2x}|^2 + |M_{2y}|^2) \right. \right. \\
& + \left. \left. (-|M_{1x}|^2 + |M_{1y}|^2 + |M_{2x}|^2 - |M_{2y}|^2) \cos(\pi q_y) \right] \right. \\
& + \left. \left[i(M_{2x}M_{1x}^* - M_{1x}M_{2x}^* + M_{2y}M_{1y}^* - M_{1y}M_{2y}^*) \cos(\phi_1 - \phi_2) \right. \right. \\
& - \left. \left. (M_{2x}M_{1x}^* + M_{1x}M_{2x}^* + M_{2y}M_{1y}^* \right. \right. \\
& \left. \left. - M_{1y}M_{2y}^*) \sin(\phi_1 - \phi_2) \right] \sin(\pi q_y) \right) \quad (4.12)
\end{aligned}$$

and:

$$\begin{aligned}
P = 2\varepsilon_{xx} & [i|M_{1x}|^2 \sin(\pi q_y) - M_{2x}M_{1x}^* e^{-i(\phi_1 - \phi_2)} + M_{1x}M_{2x}^* e^{i(\phi_1 - \phi_2)} - i|M_{2x}|^2 \sin(\pi q_y)] + \\
\varepsilon_{xy} & [(M_{1x}M_{1y}^* - M_{1x}M_{2y}^* e^{i(\phi_1 - \phi_2)} + M_{2x}M_{1y}^* e^{-i(\phi_1 - \phi_2)} - M_{2x}M_{2y}^*) e^{-i\pi q_y} - (M_{1x}^*M_{1y} - \\
& M_{1x}^*M_{2y} e^{-i(\phi_1 - \phi_2)} + M_{2x}^*M_{1y} e^{i(\phi_1 - \phi_2)} - M_{2x}^*M_{2y}) e^{-i\pi q_y}] + \\
\varepsilon_{yx} & [(-M_{1y}M_{1x}^* + M_{1y}M_{2x}^* e^{i(\phi_1 - \phi_2)} - M_{2y}M_{1x}^* e^{-i(\phi_1 - \phi_2)} - M_{2y}M_{2x}^*) e^{-i\pi q_y} - (-M_{1y}^*M_{1x} + \\
& M_{1y}^*M_{2x} e^{-i(\phi_1 - \phi_2)} - M_{2y}^*M_{1x} e^{i(\phi_1 - \phi_2)} - M_{2y}^*M_{2x}) e^{-i\pi q_y}] + 2\varepsilon_{yy} [-i|M_{1y}|^2 \sin(\pi q_y) + \\
& M_{2y}M_{1y}^* e^{-i(\phi_1 - \phi_2)} - M_{1y}M_{2y}^* e^{i(\phi_1 - \phi_2)} + i|M_{2y}|^2 \sin(\pi q_y)]. \quad (4.13)
\end{aligned}$$

Considering now that M_{1x} is real and $M_{1y} \propto iM_{1x}$ the expressions simplify to:

$$\begin{aligned}
I = 2|C|^2 & \left[(1 + D^2)(M_{1x}^2 + M_{2x}^2) + (-1 + D^2)(M_{1x}^2 - M_{2x}^2) \cos(\pi q_y) \right] \\
& - (-1 + D^2)M_{1x}M_{2x} \sin(\phi_1 - \phi_2) \sin(\pi q_y) \quad (4.14)
\end{aligned}$$

and:

$$\begin{aligned}
P = 2 & \left[D(\varepsilon_{yx} + \varepsilon_{xy})(M_{1x}^2 - M_{2x}^2) - 2(\varepsilon_{xx} - D^2\varepsilon_{yy})M_{1x}M_{2x} \sin(\phi_1 - \phi_2) \right] \cos(\pi q_y) \\
& - [(\varepsilon_{xx} - D^2\varepsilon_{yy})(M_{1x}^2 - M_{2x}^2) \\
& + 2D(\varepsilon_{yx} + \varepsilon_{xy})M_{1x}M_{2x} \sin(\phi_1 - \phi_2)] \sin(\pi q_y). \quad (4.15)
\end{aligned}$$

In order to explain observed temperature dependences for both, P and I , we assume that in the vicinity of the phase transition magnetic order parameters, $|M_1|$ and $|M_2|$, can be described with the simple power law ansatz $(T_N - T)^\beta$. At this point we stress that the phase difference between the two order parameters ($\phi_1 - \phi_2$) defines the phases of individual amplitude modulation waves ψ_{kl} determined from neutron diffraction experiment (Table 6). The temperature dependence of I and P is simulated (Figure 51b) by assuming temperature dependent $(\phi_1 - \phi_2)$ approaching low-temperature values for ψ_{kl} obtained from the neutron diffraction experiments. The agreement with the experiment is much worse, if $(\phi_1 - \phi_2)$ are kept constant. The above analysis suggests that sliding of the individual amplitude modulation waves, which also removes the centre of inversion at the magnetic phase transition, is responsible for the magnetoelectric effect in FeTe₂O₅Br. Opposed to the $P \propto I$ dependence reported for representative magnetically incommensurate systems (125), (126), (60), we find here the unusual proportionality between \sqrt{T} and P (inset of Figure 51b). Similar dependence in the low-temperature incommensurate spiral phase of Ni₃V₂O₈ (30) was explained with the saturation of the high-temperature magnetic order parameter already in the paraelectric phase. In contrast, the observed $P \propto \sqrt{T}$ scaling in FeTe₂O₅Br is reproduced within our model as a direct consequence of the temperature dependence of the amplitude modulation wave phases.

If the exchange-striction model applies to $\text{FeTe}_2\text{O}_5\text{Br}$, then the above coupling term (equation 4.11) suggests that the spin phonon coupling is provoked by the difference in the individual phases of spin modulation waves. Additional experimental and theoretical investigations are necessary to validate this suggestion.

4.5 Phase diagram – measurements performed in applied magnetic field

The existence of the magnetoelectric coupling should manifest in a pronounced effect of the applied magnetic field on the ferroelectric properties of the system and vice versa the electric field on the magnetic properties. However, the small value of the electric polarization on one hand and sizable Fe^{3+} ($S = 5/2$) magnetic moments on the other, imply that magnetoelectric effects would be more easily induced by applying the magnetic field. We thus decided to measure specific heat, magnetic susceptibility, single-crystal neutron diffraction, NMR and dielectric measurements in the applied magnetic field.

A detailed study reveal that there are actually two consequent magnetic transition ~ 0.4 K apart (Figure 65), as already indicated by NQR. Both magnetic transition temperatures are highly dependent on the strength and the direction of the applied magnetic field. Hence the magnetic phase diagram consists of three phases paramagnetic high-temperature phase – above T_{N1} , high-temperature phase, which is likely to be incommensurate (HT-ICM) – between T_{N1} and T_{N2} , and low-temperature incommensurate (LT-ICM) phase, which is also ferroelectric – below the T_{N2} .

4.5.1 Specific heat measurements

Specific heat measurements in the applied magnetic field were performed in the temperature range between 20 K and 2 K and 0 to 9 T on the standard Quantum Design PPMS setup with closed cycle cryostat at Paul Scherer Institute, Switzerland.

A detailed inspection reveals that even in the absence of an external magnetic field, the anomaly at 10.6 K actually has a structure. This gets even more pronounced, when external magnetic field is applied along the a^* -axis, as the anomaly clearly splits into two (Figure 52). With increasing magnetic field the high-temperature transition at T_{N1} shifts to higher, while the low-temperature transition at T_{N2} shifts to lower temperatures. The effect of the magnetic field is significant – $T_{N1} = 11.8(1)$ K and $T_{N2} = 9.4(1)$ K in the magnetic field of 9 T. This way the borders in the phase diagram for $\vec{B}||a^*$ can be drawn (Figure 65).

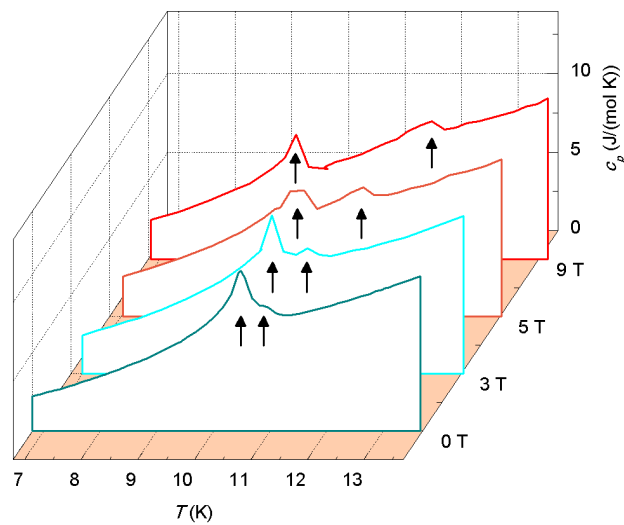


Figure 52: Temperature dependence of specific heat, c_p , measured in different applied magnetic fields applied along a^* axis. Please note that the zero-field anomaly at $T_N = 10.6(2)$ K splits into the high-temperature transition at T_{N1} shifting to higher and the low-temperature transition at T_{N2} shifting to lower temperatures with increasing magnetic field.

4.5.2 Magnetic susceptibility measurements in the applied magnetic field

To obtain an overview of the magnetic behaviour in the applied magnetic field up to 5 T, we performed a set of magnetic susceptibility measurements along all three crystal axes, namely a^* , b , and c . Again, measurements were performed in Quantum Design MPMS XL-5 SQUID magnetometer using He cooled cryostat. The results are shown in Figure 53. In the first column we show measured χ , in the second column we show the derivative of $\chi(T)$, $d\chi/dT$, and in third column we show the field evolution of the anomalies determined from the first two columns. Temperature dependence of χ for $\vec{B}||a^*$ measured in low magnetic field (0.01 T) exhibit an anomaly at 10.6 K, which is even clearer in $d\chi/dT$ plot (first row in Figure 53). When magnetic field is increased, this anomaly precisely mimics behaviour of the low-temperature peak in the specific heat measurements (Figure 52b), i.e., it shifts to lower temperatures and at 5 T it is found at 10.2(1) K. Hence we are confident that it reflects the T_{N2} magnetic transition. A precise observation of the $d\chi/dT$ plot reveals also a very minute change indicated by the dotted line in first plot in the second column of Figure 53, which seems to imitate the behaviour of the high-temperature peak in the specific heat measurements (Figure 52), corresponding to the T_{N1} transition. In case of $\vec{B}||b$, the response is even more interesting (second row in Figure 53). Here both transitions are relatively well resolved, especially in $d\chi/dT$ plot. In this case, the transition temperature of the high-temperature transition, T_{N2} , decreases with increasing field, while the T_{N1} appears to be field independent up to 3.75 T, where both anomalies seem to merge in to one sharp anomaly. From this point on, the increasing field shifts the remaining anomaly (at T_N) to the lower temperatures and at 5 T the T_N is already at 10.40(5) K. The observed response of the χ , therefore suggests that magnetic field applied along the b -axis narrows the HT-ICM phase, which at ~ 4 T finally disappears.

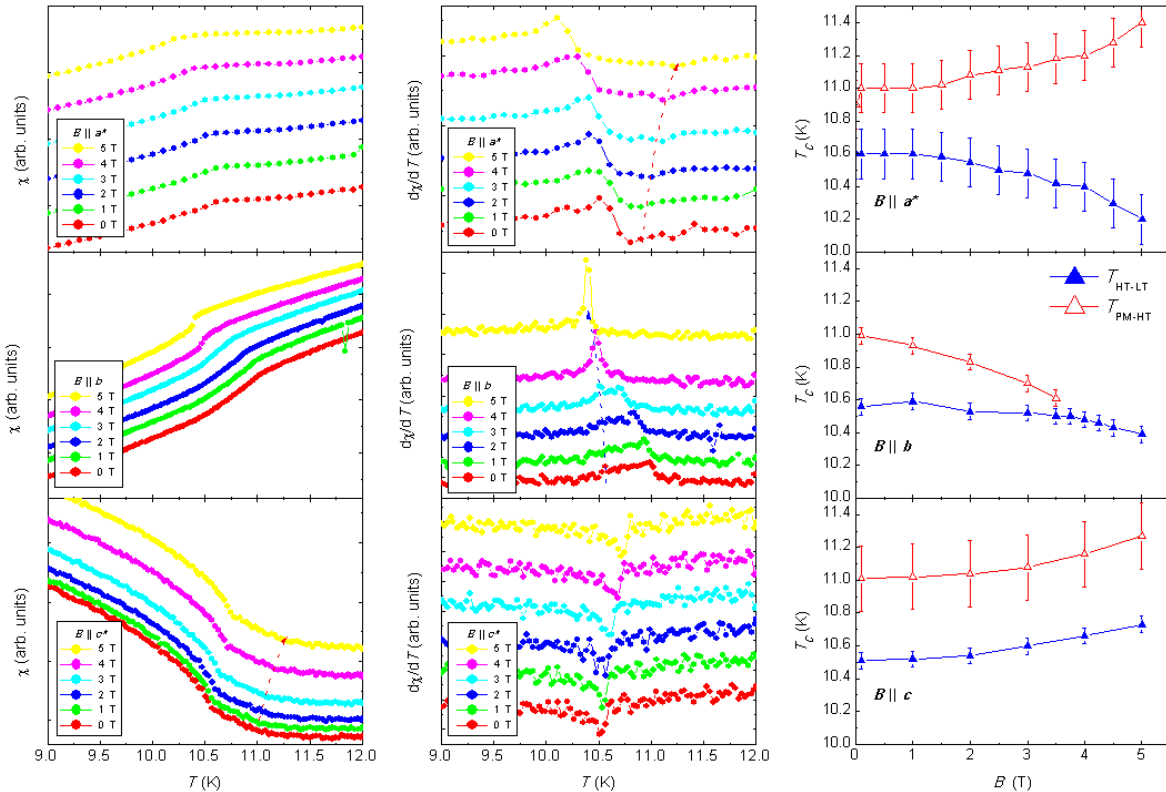


Figure 53: Magnetic susceptibility measured along all crystal axes. Measurements for different orientation of the applied magnetic field \vec{B} are shown in different rows (for $\vec{B}||a^*$ in first, $\vec{B}||b$ in second and $\vec{B}||c$ in last). First column of plots are stack plots of measured magnetic susceptibility χ , second column are stack plots of $d\chi/dT$, shown for easier estimation of transition temperatures, and in the third column estimated transition temperatures are shown.

When magnetic field is applied along the c -axis (last row in Figure 53), one anomaly is very clear, though now it shifts to higher temperatures with increasing magnetic field, i.e., from 10.50(5) K at 0.01 T it shifts to

10.73(5) K at 5 T. Again a precise investigation of the measured data unveils a second very weak anomaly χ at 11.0(2) K. This also seems to shift to higher temperature with increasing magnetic field, i.e., at 5 T it is observed already at 11.3(2) K.

The magnetic susceptibility measurements obviously agree with the NQR results, which imply that HT-ICM phase is magnetic. However the NQR spectra in this phase are relatively noisy, leaving the question about the nature of the magnetic ordering - “Is it really incommensurate or not?” - still open.

4.5.3 Nuclear magnetic resonance

In order to get a deeper insight about the nature of the HT-ICM magnetic phase $^{79,81}\text{Br}$ NMR measurements were carried out in magnetic fields of 9.4 T and 4.7 T applied along a^* as well as along c . The NMR technique has been successfully employed in the past to reveal characteristics of incommensurate magnetic states (127), since NMR spectrum directly image local magnetic field distributions. On Figure 54 we show single crystal $^{79,81}\text{Br}$ NMR spectrum measured in field of 9.4 T applied along a^* at 80 K, i.e., well above the magnetic transition. For this orientation each four of the Br1/Br2 sites are magnetically equivalent, and hence only two resonant absorption lines are expected for the central transition ($\langle -1/2 | \leftrightarrow \langle 1/2 |$). However, even a small deviation from this orientation breaks the twofold screw axis and thereby the site equivalency in to two pairs, within each the equivalency is ensured by the centre of inversion. Consequently in our experiment a pair of lines for Br2 site is observed (Figure 54). Based on the intensity ratios, expected resonant frequency positions, and the quadrupolar moments of ^{79}Br and ^{81}Br nuclei, we can explain the NMR spectra in the following way. The two pairs of narrow lines, whose Larmor frequencies (ν_L) are shifted from the ^{81}Br NMR reference frequency ($\nu_{ref} = 108.025$ MHz, $B = 9.4$ T) for -3 MHz and 3.5 MHz, correspond to the central transitions ($\langle -1/2 | \leftrightarrow \langle 1/2 |$) of ^{79}Br and ^{81}Br , respectively. Each of these pairs is accompanied by two pairs of satellite lines (related to $\langle 1/2 | \leftrightarrow \langle 3/2 |$ and $\langle -3/2 | \leftrightarrow \langle -1/2 |$ transitions), one approximately 10 MHz lower and the other ~ 6 MHz higher in respect to the central line. The resonant frequency ratio between the lower and the higher satellite line pairs for ^{79}Br and ^{81}Br , almost precisely coincides with the ratio of their quadrupolar moments. We did not find the Br1 resonance, in spite of a broad span of our frequency sweep. This is most likely due to a large $\nu_Q = 167.2$ MHz and small $\eta = 0.09$, determined from the NQR measurements and the DFT calculations respectively, which at 9.4 T results in an extremely broad (~ 125 MHz) range of possible Br1 resonance; especially when compared to the Br2, which extends ~ 10 MHz wide. In this respect our experimentally limited frequency span of “only” 40 MHz is rather small, i.e., one third of the whole Br1 range, and hence it is quite plausible that we have missed the Br1 signal. The line observed at ~ 24 MHz above the reference frequency most likely corresponds to the ^{125}Te resonance (inset to Figure 54).

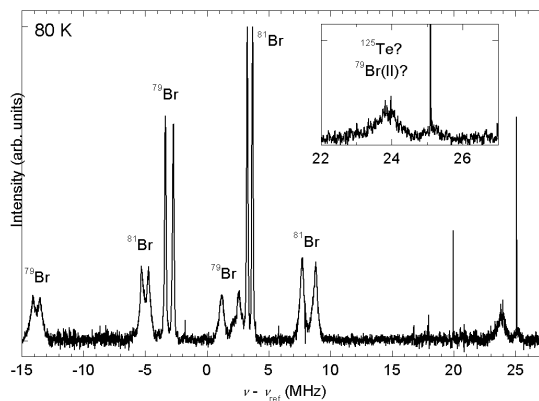


Figure 54: Representative ^{81}Br NMR spectra ($\nu_L = 108.025$ MHz, $B = 9.4$ T) measured for $\vec{B} || a^*$ at 80 K.

To check the reliability of the DFT calculations, we measured angular dependence of the ($-1/2 | -1/2$) transition of $^{81}\text{Br}2$ signal in the magnetic field applied in a^*c plane (Figure 55). At $\phi = 0^\circ$, \vec{B} was parallel to a^* . In order to compare the results with the calculated values we employed the procedure explained in the experimental section 3.1.2.3. If we assume that the isotropic hyperfine shift is $\Delta\nu(80\text{ K}) = 1.04\text{ MHz}$ and when we reduce the magnitude of the calculated EFG tensor (Table 7) for 12 %, as already determined from NQR results, we get almost perfect agreement between the experimental and calculated results (Figure 55). Moreover, considering the value for molar magnetic susceptibility at 80 K $\chi_{\text{mol}}(80\text{ K}) = 0.217\text{ Am}^2/(\text{T mol})$, the obtained hyperfine shift $\Delta\nu(80\text{ K}) = 1.04\text{ MHz}$, and γ^{81} the magnitude of hyperfine fields at Br2 per Fe^{3+} ($S = 5/2$) magnetic moment can be estimated to $\sim 0.267\text{ T}/\mu_B$. This result is close to the values obtained from the fitting of the NQR spectra (Table 9), and hence speaks in favour to the obtained set of parameters. Finally we note that very good agreement between the simulated and measured angular dependence implies that xz terms of the hyperfine coupling for Br2 site are almost insignificant as well as the induced dipolar fields, which would also complicate the angular dependence.

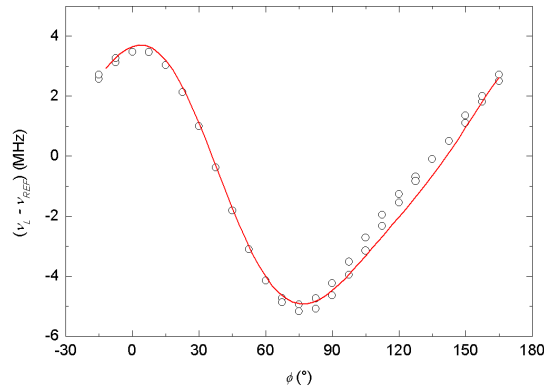


Figure 55: Resonance position of $^{81}\text{Br}2$ NMR as a function of rotating angle ϕ . The empty circles correspond to the peak positions of the ^{81}Br NMR central resonant line. The solid line is a simulation considering the 1.04 MHz isotropic hyperfine shift and the calculated EFG tensor reduced by 12 %.

Hereafter we readjusted the crystal orientation to ensure $\vec{B} || a^*$ and focus only on the ^{81}Br central transition. In the investigated frequency range we were able to detect also ^{79}Br satellite transition (marked with an arrow on Figure 56a). Temperature dependence of ^{81}Br central line and its satellite is shown on Figure 56a. Due to the weak signal the ^{79}Br satellite line appears only below 240 K, at $\sim 1\text{ MHz}$ above the ν_{ref} . The satellite line is significantly broader what imply that distribution of the EFG values along the crystal lattice is narrow, meaning that structural inhomogeneities in the investigated samples can be completely ignored. The resonant position of the central line closely mimics the magnetic susceptibility measurements (Figure 56b), i.e., $\delta\omega(T) \propto \chi(T)$. This can be understood in terms of the theory developed in section 3.1.2.1, equation 3.21, as a signature of the temperature independent transferred hyperfine coupling constant. On cooling from 300 K it shifts from 3 MHz to $\sim 3.6\text{ MHz}$ at 50 K, where it meets a broad maximum and further starts to decrease to $\sim 3.5\text{ MHz}$ at 13 K. Comparison with the magnetic susceptibility behaviour therefore give us an estimated shift of 1.04(2) MHz at 80 K due to the transferred hyperfine coupling, indicating that hyperfine fields due to Fe^{3+} ($S = 5/2$) magnetic moments at Br2 site are $\sim 0.1\text{ T}$. The satellite line shows a similar behaviour on cooling down to 50 K. In this range the satellite line shifts from 1 MHz at 240 K to 2.3 MHz at 50 K, i.e., significantly more than the central line. This corroborate with the generally accepted assumption that the satellite transitions are more susceptible to the change of the EFG tensor and indirectly to the lattice expansion/contraction. Below 50 K, in contrast to the central line, the satellite line continuous to shift to higher frequencies and reaches 2.55 MHz at 13 K. This implies that the evolving short-range order (SRO) has

a different impact on $\langle -1/2 | \leftrightarrow \langle 1/2 |$ and $\langle -3/2 | \leftrightarrow \langle -1/2 |$ ($\langle 1/2 | \leftrightarrow \langle 3/2 |$) transitions (Figure 56b), i.e., in case of central transition the resonance position is predominantly influenced by hyperfine field, while for satellite lines EFG tensor is the leading factor. Finally, the change of the intensity ratio between the central and the satellite line from ~ 1.7 at 200 K to ~ 1 at 13 K is most likely due to a different relaxation rates or different $\pi/2$ pulses.

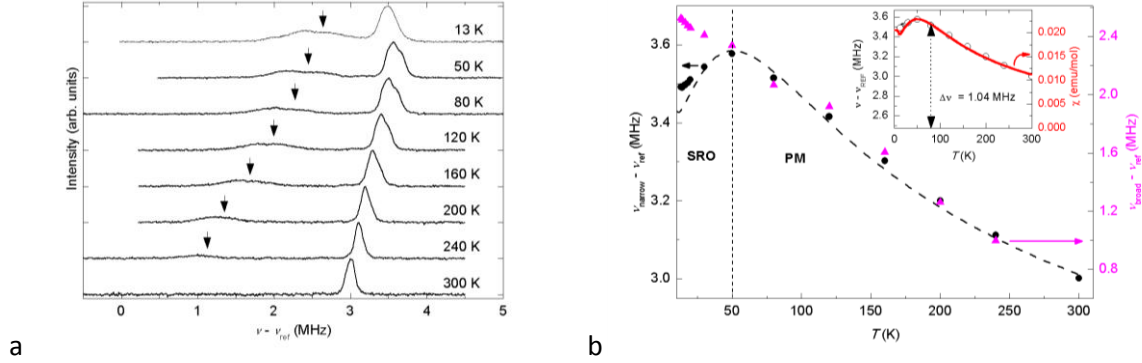


Figure 56: (a) Temperature dependence of the $^{79,81}\text{Br}_2$ NMR spectra ($\nu_L = 108.025$ MHz, $B = 9.4$ T) measured for $\vec{B} \parallel a^*$. (b) Resonance position of $^{81}\text{Br}_2$ central (solid circles) and $^{79}\text{Br}_2$ satellite (solid triangles) lines. A dashed line represents a rescaled temperature dependence of the magnetic susceptibility measured for $\vec{B} \parallel a^*$. Inset: estimation of the hyperfine fields, i.e., comparison of the $^{81}\text{Br}_2$ central resonance position (empty circles – left scale) and magnetic susceptibility (solid line – right scale).

Below $T_{N1} = 12.0(5)$ K the spectrum abruptly change. Each resonance broadens dramatically and develops two well pronounced singularities split by about 1.7 MHz (Figure 57). The splitting implies large hyperfine fields along the a^* at the ^{81}Br sites, $B_{hf} = 0.080$ T. The observed line-shape is similar to that observed in NQR and can be simulated by assuming a sinusoidal dependence of the NMR shift along the magnetic wave vector: $\nu_i = \nu_L(1 + \delta) + \delta\nu_{IC} \cos(\vec{q} \cdot \vec{r}_i)$, assuming incommensurate \vec{q} . Here ν_L is the Larmor frequency, δ includes chemical, quadrupole and Knight shifts and $\delta\nu_{IC} \cos(\vec{q} \cdot \vec{r}_i)$ is the part of the shift due to the modulation of the local magnetic field arising from the nearby Fe^{3+} moments. The ^{81}Br NMR line-shape (Figure 57) thus unambiguously proves that the intermediate magnetic structure of the HT-ICM phase is also incommensurate. On cooling through $T_{N2} = 9.0(5)$ K the splitting between the two singularities dramatically increases (Figure 57), indicating a sudden increase in local hyperfine fields to 0.176 T. However, the ^{81}Br line-shape remains characteristic of an incommensurate magnetic structure and is thus in full agreement with the neutron diffraction data.

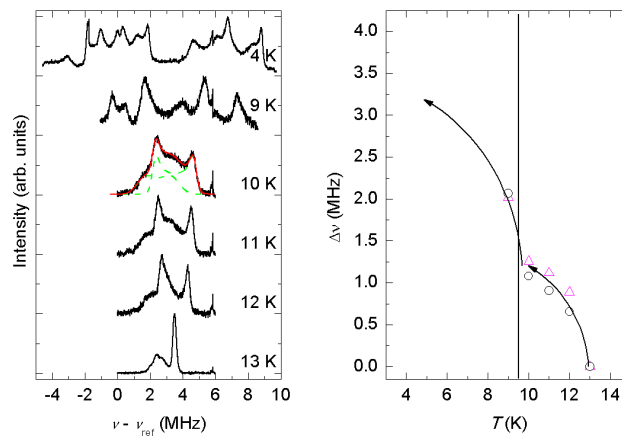


Figure 57: Left: in the paramagnetic phase ($T = 13$ K) two well separated $^{81}\text{Br}_2$ central and $^{79}\text{Br}_2$ satellite lines are observed. In the HT-ICM phase each resonance suddenly broadens and the measured line-shape is characteristic of incommensurate magnetic structure. The solid line is a line-shape fit to the model described in the text. In the LT-ICM phase ($T = 9$ K) line-shape still corresponds to incommensurate magnetic structure, but the local hyperfine fields at the Br sites dramatically increase. Right: temperature dependence of the gaps between the singularities for central (empty circles) and satellite (empty triangles) lines.

In addition to measurements at 9.4 T, we measured $^{79,81}\text{Br}$ spectra in the intermediate phase also at 4.7 T for $\vec{B}||a^*$ as well as for $\vec{B}||c$. This field is appropriate since we can track all the transitions for ^{79}Br and ^{81}Br in a relatively narrow frequency range. Our aim was to learn as much as possible about the magnetic behaviour in vicinity of T_{N1} and T_{N2} . Spectra measured between 20 K and 7 K are shown in Figure 58. We have followed the behaviour between 12 K and 8 K in very fine steps of 0.2 K in order to obtain enough points to draw a temperature dependence of the magnetic order parameter. Similarly to 9.4 T measurements the spectrum dramatically changes at $T_{N1} = 11.4$ K. Looking at the satellite line (marked with black arrow in Figure 58) one can clearly see how the line with decreasing temperature develops a U shape, characteristic for ICM magnetic structures. However in contrast to 9.4 T measurements, at T_{N2} , the satellite line seems to disappear. Yet on further cooling, it seems that there is some very broad signal reoccurring. There are two possible explanations. First is associated with the occurrence of the electric polarization P at T_{N2} , which originates from the electric charge redistribution. This is typically associated with small crystal lattice changes, which might strongly influence the EFG at the Br2 site. As already mentioned, the resonances of the satellite transitions depend very much on the EFG tensor and hence even a tiny change of the crystal lattice can either severely broaden the resonant line or even drastically change its position, what might explain the observed behaviour. However, NQR results imply that changes of the EFG below the ferroelectric transition are small; hence this effect is probably too small to explain the observed behaviour. Second explanation is associated with the relaxation times. Typically $1/T_1$ as well as $1/T_2$ diverges at T_N . Hence in case of very short T_2 just below the T_{N2} , we might not be able to detect the NMR signal. In order to peruse this idea, we have measured temperature dependence of the lattice relaxation time T_1 for both, satellite as well as central line (Figure 58d). T_1 for both, satellite and central, lines behaves exactly the same through the whole temperature range. At room temperature, $1/T_1 \sim 1.5 \times 10^{-3} \text{ s}^{-1}$ and is almost constant down to 100 K, where it starts to decrease and reaches minimum of $\sim 0.7 \times 10^{-3} \text{ s}^{-1}$ at ~ 17 K. On further cooling $1/T_1$ exhibits two sharp anomalies. The first maximum is found at $T_{N1} = 11.2$ K, and the second one at $T_{N1} = 10.2$ K, exactly coinciding with the observed magnetic transition temperatures. Since the NQR results indicate that lattice relaxation in $\text{FeTe}_2\text{O}_5\text{Br}$ is predominantly magnetic, i.e., $^{79}T_1/^{81}T_1 \propto (^{79}\gamma/^{81}\gamma)^2$, we associate this behaviour with evolving magnetic correlations, which dramatically speed up relaxation process in the vicinity of phase transitions.

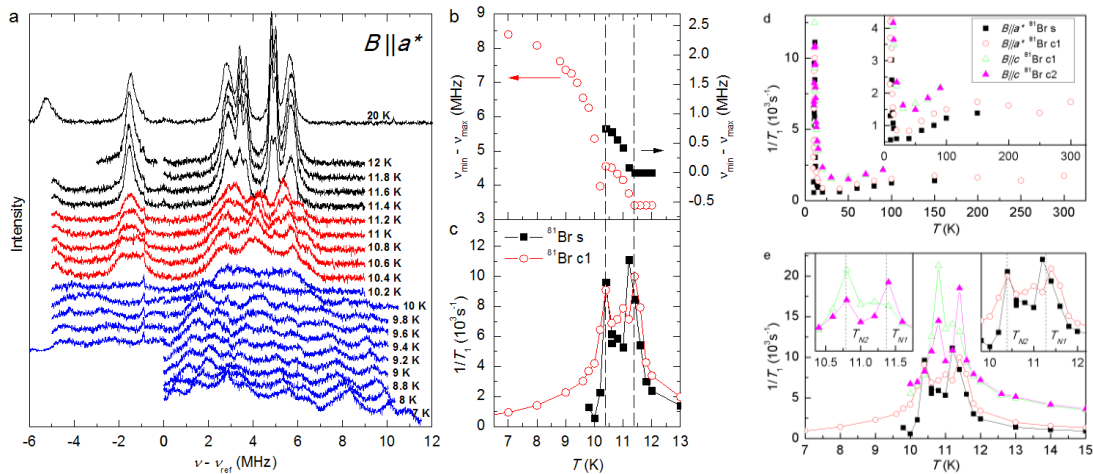


Figure 58: (a) Temperature dependence of the $^{79,81}\text{Br}$ NMR spectra ($\nu_l = 54.013$ MHz, $B = 4.7$ T) measured for $\vec{B}||a^*$. (b) Distance between the two farthest singularities for the $^{79,81}\text{Br}$ broad group of two pairs of central and two pairs of satellite lines (open red circles) and a single ^{81}Br satellite line (solid squares). (c) $1/T_1$ measured at ^{81}Br central (open red circles) and satellite (solid squares) line for $\vec{B}||a^*$. (d) and (e) temperature dependence of $1/T_1$ measured at satellite and central line.

Below T_{N1} we have measured T_1 on the central position of the line as well as its edge; however there is almost no difference what so ever. To attain some estimation about the temperature evolution of the

magnetic order parameter, we plot in Figure 58b distance between the two farthest singularities for the satellite line (in black) as well as the group of the satellite and central lines between the red arrows (in red).

For $\vec{B}||c$ ($B = 4.7$ T) the spectrum gets considerably more transparent, as the central lines of ^{81}Br and ^{79}Br lie far apart. Even more, also the splitting between the lines corresponding to the Br2 sites connected by the glide plane 2_{1y} , significantly increases. As a result, we can focus only on the two central lines corresponding to the ^{81}Br (Figure 59). At this point we again stress that each of these lines originate from two Br2 sites, connected by the centre of inversion. Therefore, in an ideal case, when the inversion symmetry gets broken each of this lines should split in to two. So what happens? In the paramagnetic state in addition to the two ^{81}Br central lines at -8.5 MHz and -11.8 MHz a broad resonance is observed at -9.7 MHz. This line is most likely one of the satellite lines for ^{79}Br or ^{81}Br . At $T_{N1} = 11.2$ K the spectrum suddenly changes. Both central lines change their shape from narrow Gaussian line into a U-shaped line, typical for a distribution of local magnetic fields, found in ICM modulated magnetic structures. This implies that the direction of the applied external magnetic field does not change the nature of the HT-ICM phase, which remains ICM, as for $\vec{B}||a^*$. The splitting between the two singularities is ~ 1 MHz, implying that the projection of the hyperfine fields on the c -axis is $B_{hf}(c) = 0.047$ T, what is almost half the size as found for the fields along the a^* . Surprisingly, the broad line, found at -9.7 MHz relative to the reference frequency almost completely disappears, what is in contradiction with the behaviour of the satellite lines when $\vec{B}||a^*$. There are at least two possible explanations for this disappearing: (i) the line we are looking at is not the satellite line, but it corresponds to Br1-site or ^{125}Te resonance, both of which might exhibit completely different behaviour; or (ii) the relaxation times for this transition become so fast, that we are not able to detect the signal. Only 0.4 K lower, at $T_{N2} = 10.8$ K, the second transition occurs. Spectrum again changes, though due to the weak signal (fast relaxation rates), it is very difficult to say much about detailed structure. For this reason we focus on the low-temperature spectra, i.e., at 7 K, where the specific features of the spectra are more obvious. It is quite clear that the two lines differ. This might be the result of the anticipated breaking of inversion symmetry, as explained above. According to this scenario each line split in to two, which still overlap, though in slightly different manner, since they are not symmetry related any more. As a result two broad lines with different shapes would be observed, exactly as in our experiment. However, some contribution to this discrepancy might also come from the broad line, which disappeared in HT-ICM phase, but develops again and asymmetrically overlaps with the central lines.

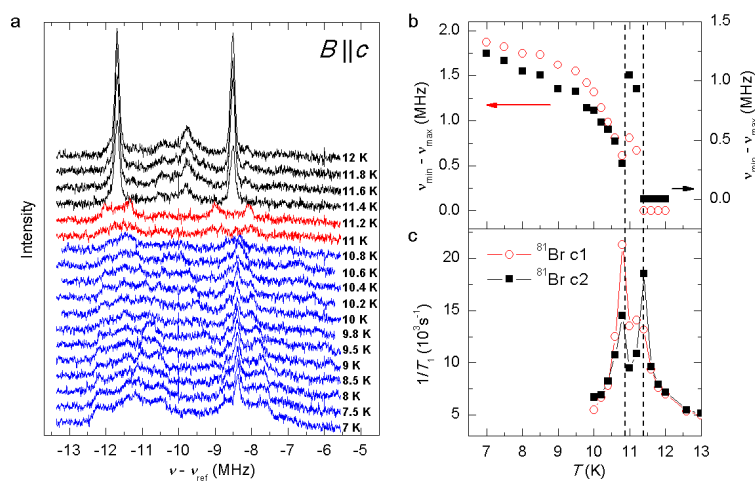


Figure 59: (a) Temperature dependence of the $^{79,81}\text{Br}$ NMR spectra ($\nu_L = 54.013$ MHz, $B = 4.7$ T) measured for $\vec{B}||c$. (b) Distance between the two farthest singularities for the $^{79,81}\text{Br}$ broad group of two pairs of central and two pairs of satellite lines (open red circles) and a single ^{81}Br satellite line (solid squares). (c) $1/T_1$ measured at ^{81}Br central (open red circles) and satellite (solid squares) line for $\vec{B}||c$.

To sum up, the NMR corroborates with NQR results and undisputedly confirms the incommensurability of the HT-ICM phase. However, we still have no indication about a detailed nature of the magnetic ordering – is it amplitude modulated as in LT-ICM or is it cycloidal, helical, etc. Nevertheless, it is likely that it is still inversion symmetric, which would mean that it is probably not ferroelectric.

4.5.4 Neutron diffraction in the applied magnetic field

In order to reveal the nature of the magnetic ordering in the HT-ICM phase and to get a better insight of what happens, when magnetic field is applied along b axis, we performed single crystal neutron diffraction for $\vec{B} \parallel a^*$ and $\vec{B} \parallel b$ in the applied magnetic field up to 6 T. Single-crystal diffraction experiments were performed on a $5 \times 4 \times 1 \text{ mm}^3$ single crystal on the single-crystal diffractometer TriCS ($\lambda = 2.32 \text{ \AA}$) at the Swiss Neutron Spallation Source, Paul Scherrer Institute, Switzerland, upgraded with the MA09 superconducting magnet (up to 6 T), when an external field was applied.

In the absence of an external magnetic field ($B = 0 \text{ T}$) the temperature dependences of the integrated intensity for three magnetic peaks, (0.5 0.463 -4), (0.5 0.537 -1), (1.5 0.537 -2), show the same behaviour (Figure 60, Figure 61a). They seem to mimic the evolution of the magnetic order parameter and they can be well explained below 9.8 K by the $I \propto M^2 \propto |T - T_N|^{2\beta}$ law, where M denotes magnetization and obtained β is $\sim 0.26(1)$. A detailed inspection, however, reveals that a weak magnetic peak can be observed already between 9.8 K and 10.2 K (Figure 60b) - before the establishment of the LT-ICM phase described by $|T - T_N|^{2\beta}$ dependence of the magnetic peak intensity. From the width of this temperature interval we assume it corresponds to the HT-ICM phase and consequently $T_{N1} = 10.2 \text{ K}$ and $T_{N2} = 9.8 \text{ K}$. We stress that in HT-ICM phase the intensity of (0.5 0.537 -1) peak is smaller compared to the other two (Figure 60b), implying a change in the magnetic structure. The discrepancy of the transition temperatures compared to the other experiments is most likely due to modified experimental setup used for the neutron diffraction measurements in an applied magnetic field, i.e., the position of the thermometer was almost 15 cm further away from the sample compared to the normal zero-field setup.

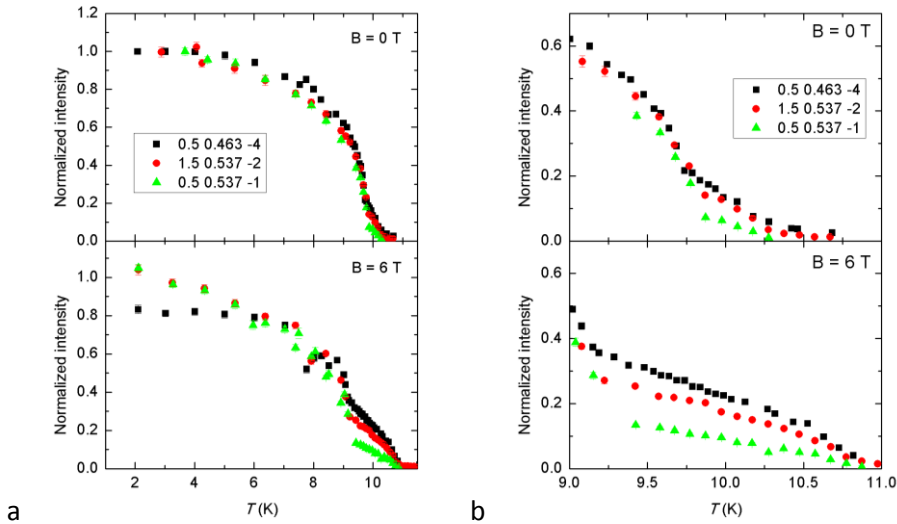


Figure 60: (a) Temperature dependences of normalized intensities of three magnetic reflections in $B = 0 \text{ T}$ and $B = 6 \text{ T}$ along a^* . (b) The same dependences magnified in the temperature interval of the HT-ICM phase.

As expected, in the magnetic field of 6 T applied along a^* , the temperature interval of the HT-ICM phase broadens and becomes very distinct (Figure 60b, Figure 61a). We stress that all magnetic peak intensities in the HT-ICM phase have fundamentally different temperature dependence compared to LT-ICM phase. The difference is evident from the critical exponent β in the expression $I \approx |T - T_N|^{2\beta}$, which is in LT-ICM phase \sim

0.26(1), whereas it is almost 0.35(2) in HT-ICM, i.e., magnetic peak intensity in the HT-ICM phase seems to be almost proportional to the temperature. The comparison of the obtained β to the critical exponent values known for some typical universality classes (Table 11) implies that the HT-ICM phase should be characterized as three-dimensional planar (3D XY) model, while LT-ICM corresponds to the two-dimensional planar (2D XY) class. These findings are in agreement with planar nature of the refined LT-ICM magnetic structure as well as layered crystal structure, whereas the proposed 3D character for HT-ICM phase is counterintuitive.

Table 11: Critical exponent β for some chosen universality classes.

Universality class	β	reference
2D Ising	1/8	(80)
2D XY	0.23	(128)
3D Ising	0.32	(129)
3D XY	0.35	(129)
3D Heisenberg	0.36	(129)

Moreover, if hypothetically the change of dimensionality would occur, one would expect this to happen in exactly the opposite sequence. Hence, we suspect that the obtained β might deviate from the correct value for the critical exponent. This is because the magnetic peak intensity I is not exactly proportional to the M^2 but it depends also on the phase shifts between the amplitude modulated waves, which have also their own temperature dependences, braking the simple $I \approx |T - T_N|^{2\beta}$ relation.

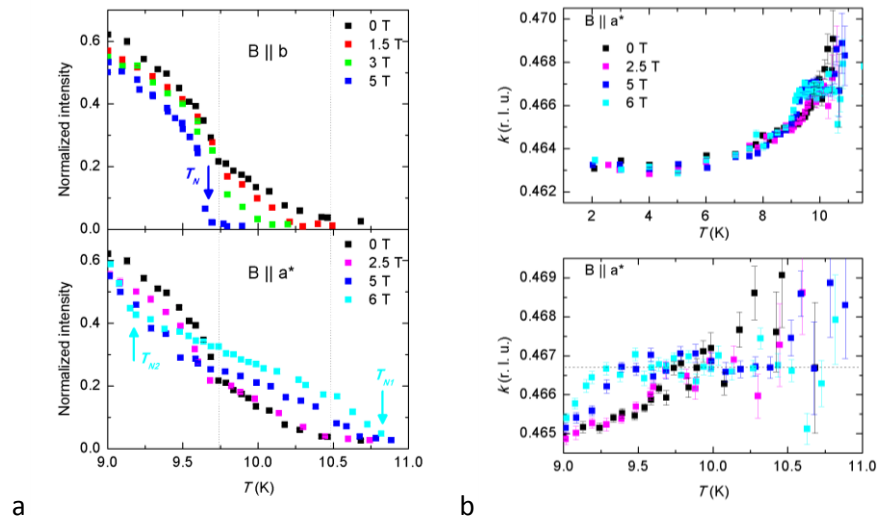


Figure 61: Temperature dependence of (a) normalized intensity of (0.5 0.463 -4) magnetic reflection in different magnetic fields applied along a^* and b axes, and (b) temperature evolution of the (0.5 0.463 -4) magnetic peak position in magnetic fields applied along a^* .

Similar to the magnetic peak intensity, behaviour of the magnetic peak positions can be also explained with $|T - T_N|^{2\beta}$ law, where $\beta \sim 0.26(1)$ (Figure 61b). For instance, position of the (0.5 0.463 -4) magnetic peak shifts with decreasing temperature to lower k values for approximately 0.004 r. l. u. The obvious resemblance between the behaviour of the peak position and its intensity implies that magnetic wave vector does actually depend on the amplitude of the Fe^{3+} ($S = 5/2$) magnetic moments, which might indicate that it is also involved in the magnetoelectric coupling mechanism. However, such behaviour is missing in the HT-ICM phase. Though it is difficult to say much about the temperature dependence of the peak position in the HT-ICM phase at $B = 0$, it is revealed when magnetic field is applied (Figure 61b). In contrast to the LT-ICM

phase, in HT-ICM phase magnetic peak positions are temperature independent and seem to be locked at 0.466(3) position.

The effect of the field applied along b axis is even more interesting, as expected from susceptibility measurements. Temperature dependences of the magnetic peak intensities for this case (Figure 61a) confirm implications of the magnetic susceptibility measurements that the temperature interval of HT-ICM phase shrinks with an applied magnetic field. Actually, at 5 T there is no sign of the temperature interval with linear (large β) evolution of the magnetic peak intensity, implying that the HT-ICM phase completely disappears.

In order to investigate the short-range ordering effects, we have performed h , k , and l -scans of some strong magnetic reflections above the T_{N1} . This way we can estimate the correlation lengths along all three crystal axes, since magnetic correlation lengths in a^* , b and c axes are proportional to the widths of the magnetic reflection measured in scans along h , k and l respectively, i.e., the magnetic correlation length along a^* axis, ξ_{a^*} , can be calculated from the width of the magnetic peak, f_{whm} , determined from the h -scan measurement as $\xi_{a^*} = 1/[\pi (f_{\text{whm}}[\text{r.l.u.}]/a^*)]$. Since $\text{FeTe}_2\text{O}_5\text{Br}$ is a layered system, with shortest interlayer Fe-Fe distances around 10 Å, the obvious question is how far above the T_{N1} the neighbouring layers feel each other. On Figure 62a we show a temperature dependence of the (3.5 0.463 0) magnetic peak intensity and width, when performing h -scans.

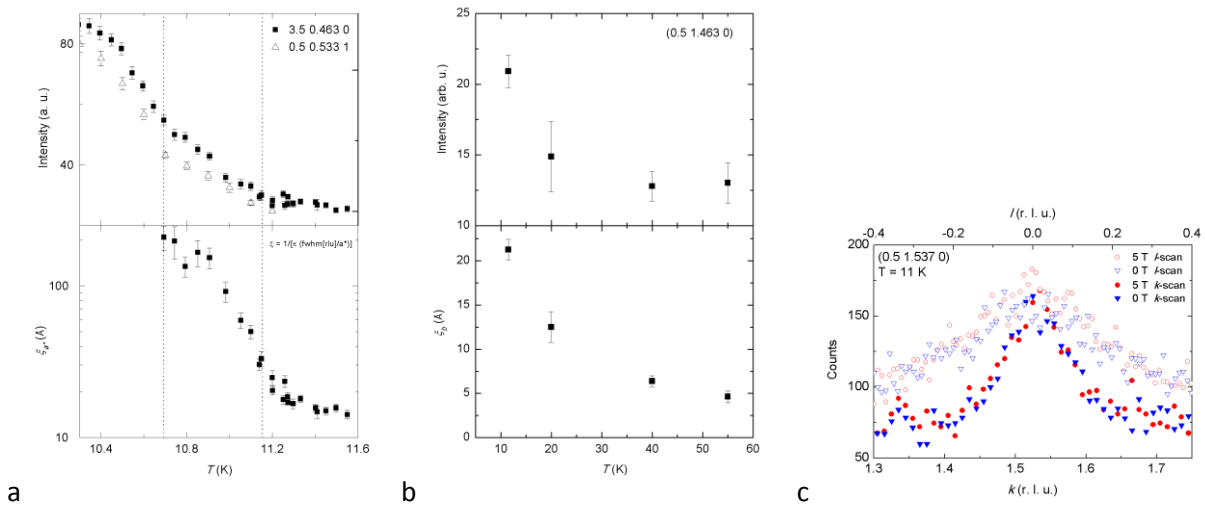


Figure 62: Correlation length measurements. (a) above: temperature dependence of the magnetic peak intensity clearly indicates two consecutive magnetic transitions, below: estimated magnetic correlation length along a^* determined from the width of magnetic peak obtained from h -scans. (b) above: temperature dependences of magnetic peak intensity of (0.5 1.537 0) magnetic peak and bottom: estimated magnetic correlation length along b axis, determined from k -scans. (c) Comparison of the magnetic peak (0.5 1.537 0) measured in k - and l -scans at 0 T and 5 T.

Obviously the correlation length starts to decrease already in the HT-ICM phase and at T_{N1} the ξ along a^* is just around 30 Å. Above the transition, ξ is further reduced and it drops below the interlayer Fe-Fe distance already at 11.6 K, i.e., 0.5 K above T_{N1} . We note that deviation of the T_{N1} compared to the previous measurements is strictly due to the used experimental setup. This implies that short-range ordering correlations between the neighbouring layers break up very soon, and the remaining short-range ordering effects observed by the other techniques should come from the intralayer correlations. To check this we have measured a k -scan temperature dependence of the (0.5 1.537 0) magnetic peak (Figure 62b). Just above the T_{N1} the estimated correlation length is ~ 20 Å. Comparing this to 4.76 Å, which is the minimal Fe-Fe inter-tetramer distance, we can assume that there are still strong correlations within the layers. In spite of

rather quick reduction of the correlation length, we are able to sense the magnetic peaks up to ~ 40 K in agreement with the ESR and magnetic susceptibility measurements. To get an estimate of the correlations along the c axis, l -scan of the (0.5 1.537 0) magnetic peak at 11 K was performed (Figure 62c). The comparison of the calculated correlation length ~ 13 Å and ~ 21 Å, measured along c and a^* respectively, most likely reflects the anisotropy in the intercluster superexchange. When magnetic field is applied (Figure 62c) nothing happens suggesting that magnetic field up to 5 T does not influence magnetic correlations. Considering the strong magnetic interactions (J 's are estimated to be around 10 K) and very high saturation fields (up to 5 T, the magnetization curve does not show any sign of saturation) this is actually the expected result.

4.5.5 Thermal expansion in the applied magnetic field

To investigate also the effect of the applied magnetic field on the crystal lattice, we measured thermal expansion parameter along the c -axis, α_c , with magnetic field applied also along the c -axis. The data were taken in warming up employing a low sweep rate of 1.5K/h.

In the applied magnetic field of 6 T, the peak position observed at ~ 10.5 K shifts to higher temperatures in agreement corroborating with the magnetic susceptibility as well as NMR. A detailed inspection of both measurements $B = 0$ T and 6 T reveals that in both temperature dependence runs there is a small anomaly approximately 0.4 K above the sharp peak, which might correspond to the magnetic transition from paramagnetic to HT-ICM phase. Hence we suggest that the sharp peak indicates the HT-ICM to LT-ICM transition and is associated with the onset of the electric polarization, which induces the detected lattice distortions. To clarify this point, dielectric response of the sample as well as information on the pressure dependence of the antiferromagnetic transition would be very helpful.

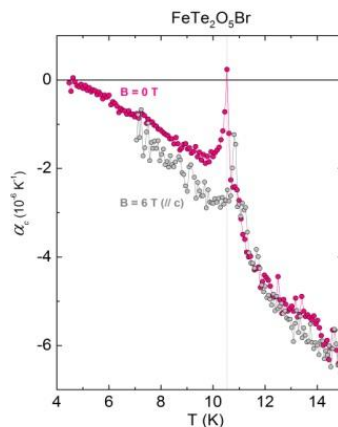


Figure 63: Thermal expansion parameter along the c -axis, α_c , measured in zero-field and in the applied magnetic field of 6 T.

4.5.6 Dielectric measurements in the applied magnetic field

To firmly prove the existence of the magnetoelectric coupling as well as to reveal what happens with the electric polarization in the HT-ICM phase and when magnetic field is applied along b axis, we performed an extensive investigation of the dielectric properties in the external magnetic field. In Figure 64 we show the complete dielectric response along c axis in magnetic fields up to 5 T. The ac dielectric measurements in the dc magnetic bias field were performed in the magnetic field of Quantum Design MPMS XL-5 SQUID magnetometer.

For magnetic field applied along a^* and c axes, the peak in the dielectric constant exactly mimics the behaviour of the T_{N2} determined from the magnetic susceptibility, NMR, neutron diffraction and thermal

expansion measurements. i.e., for $\vec{B}||a^*$ it shifts to the lower temperatures, while for the $\vec{B}||c$ it shifts to the higher temperatures; thus indicating that electric polarization is present only in the LT-ICM phase. In addition, this corroborates also with the NMR results for $\vec{B}||c$, suggesting that HT-ICM phase might still be inversion symmetric and thus incapable of inducing macroscopic electric polarization. We also notice that the magnitude of $\varepsilon'(B, T_{N2})$ at the transition temperature is weakly dependent on applied magnetic field. In Figure 64b we plot the magnetic field dependence of the height of the peak $\Delta\varepsilon'_{\max}(\vec{B}||a^*) / \Delta\varepsilon'_{\max}(B=0)$ demonstrating a weak but nonzero quadratic magnetolectric coupling.

On contrary, when magnetic field is applied along the b axis, the dielectric response is unexpected. Similar to $\vec{B}||a^*$ and $\vec{B}||c$ case, the dielectric peak follows the T_{N2} , but on top of that its intensity slowly decreases and eventually at ~ 4 T finally vanishes. The extinction of the singularity exactly coincides with the overlap of the anomalies observed in the $d\chi/dT$ as well as with the disappearance of the HT-ICM phase observed in the neutron diffraction experiment. This suggests that the existence of the HT-ICM phase is essential for the electric polarization in the LT-ICM phase. The disappearance of the electric polarization at 4 T for $\vec{B}||b$ implies that magnetic structure should also change. However, no noticeable anomaly was observed at this field in the magnetization curve as well as no significant change in the magnetic peak position and intensity was found. Obviously the changes responsible for the phenomenon are very small and difficult to observe. Hence a detailed investigation in higher magnetic field is needed to resolve this question.

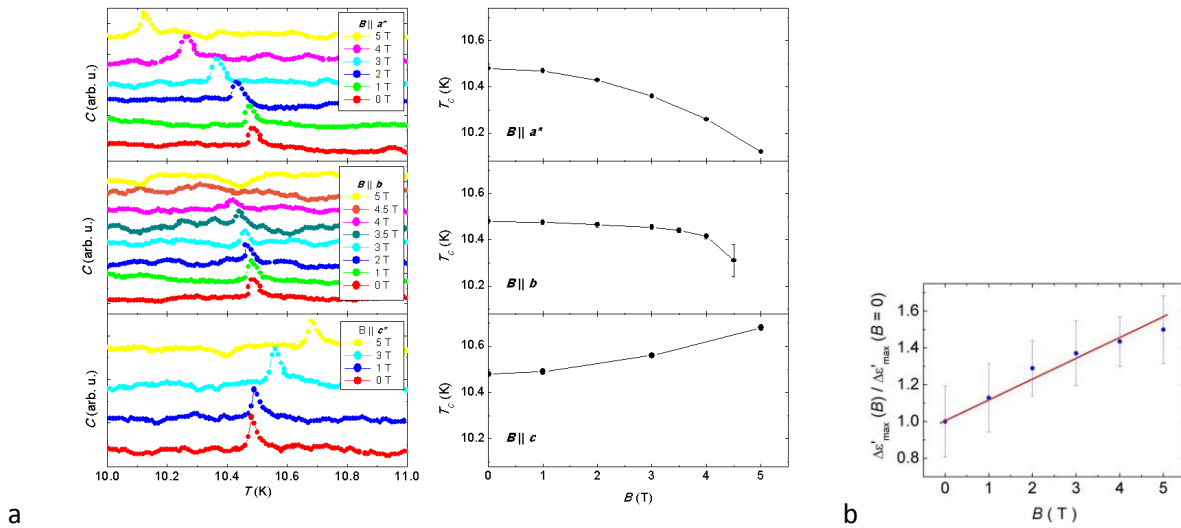


Figure 64: (a) Temperature dependence of the dielectric constant measured along c -axis in magnetic fields applied along all three crystal axes. First column show stack plots of as measured capacitance, C , of the sample, which mimics the behaviour of dielectric constant, while the second column show the estimated ferroelectric transition temperatures. (b) The normalized integrated intensity of dielectric constant as a function of applied magnetic field along the a^* direction.

4.5.7 Phase diagram – summary

Based on the presented measurements in the applied magnetic field we can plot the B - T phase diagram of the $\text{FeTe}_2\text{O}_5\text{Br}$ system (Figure 65). When magnetic field is applied along a^* -axis the upper transition temperature, T_{N1} , shifts up and the lower one, T_{N2} , shifts down, i.e., the gap between the two temperatures increases from ~ 0.4 K in the absence of the magnetic field to ~ 2.4 K at 9 T. Field dependent dielectric measurements show that ferroelectric transition temperature mimics the dependence of the low-temperature magnetic transition, suggesting that the electric polarization develops only in LT-ICM magnetic phase (Figure 65a). For $\vec{B}||c$ both transition temperatures moderately shift (for ~ 0.2 K) to higher temperatures with increasing field, keeping the width of the HT-ICM temperature interval almost field independent. Magnetic field applied along b -axis has even smaller impact on the transition temperatures – it

only slightly lowers T_{N1} (for ~ 0.1 K), while T_{N2} does not change at all. However, at ~ 4 T transition temperatures coincide and HT-ICM magnetic phase seems to disappear (Figure 65b). Moreover, at the same time electric polarization vanishes, which implies that also LT-ICM phase has changed (Figure 65b) into LT-ICM 2. This phase seems to be very similar to the low-field LT-ICM phase, as there is no noticeable anomaly in the magnetization curve as well as no significant change in the magnetic peak position and intensity.

At last we stress that above T_{N1} exists a broad region (up to $\sim 6 T_N$) where short-range ordering within the crystal layers is present, which we ascribe to low-dimensional nature of the system as well as geometrical frustration effects. However, the applied magnetic field does not seem to effect on it.

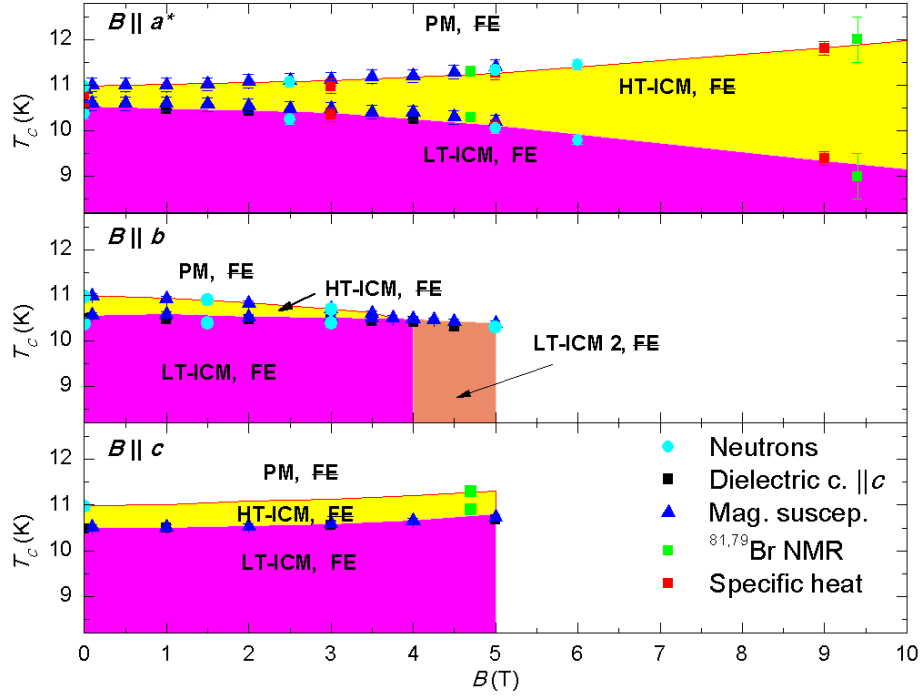


Figure 65: Complete temperature versus magnetic field phase diagram based on all performed measurements: specific heat (red squares), dielectric constant (black squares), magnetic susceptibility (blue triangles), neutron diffraction (cyan circles) and ^{81}Br NMR (green squares) measurements. Abbreviations PM and FE stand for paramagnetic and non-ferroelectric phase, respectively. High-temperature magnetically incommensurate phase (HT-ICM) for $T_{N2} < T < T_{N1}$ does not show a spontaneous polarization, while the low-temperature magnetically incommensurate phase (LT-ICM) for $T < T_{N1}$ coexists with the ferroelectric phase (FE) with polarisation aligned along c -axis. The LT-ICM phase is characterised by nearly transverse incommensurate magnetic order with magnetic wave vector $\vec{q} = (1/2, 0.4629, 0)$.

4.6 Low-energy excitations

Here we present our investigation of the low-energy excitation spectra of the $\text{FeTe}_2\text{O}_5\text{Br}$.

4.6.1 Inelastic neutron scattering

Inelastic neutron spectroscopy was performed on the TASP spectrometer at the Swiss Neutron Spallation Source, Paul Scherrer Institute, Switzerland using the arrangement of three $\text{FeTe}_2\text{O}_5\text{Br}$ single crystals coaligned within 1° , each with a size of approximately $10 \times 8 \times 2 \text{ mm}^3$, and the total mass of 1.2 g.

Investigation of spin excitations has been performed in the $hk0$ plane starting from the two magnetic peaks $-2.5 -0.5 \pm \delta$, where δ is 0.036 r.l.u. First we performed broad energy scans up to 7.5 meV, with the resolution of 0.6-0.8 meV for k selected between -1.5 and -0.45 and constant $h = -2.5$. The results (presented in Figure 66a) show that there are at least three excitation branches present. The low-energy branch (indicated by a black line and symbols in Figure 66a) rises from ~ 1 meV at $k = -0.5$ (-1.5) up to ~ 3.5 meV at k

= -1, where it overlaps with the higher energy excitations. In contrast the higher two branches at ~ 3.5 meV and ~ 5 meV (indicated by a red and green lines and symbols in Figure 66a) seem more or less k independent (dispersionless). At this point we stress that due to the experimental limitations the energy resolution was significantly better for scans above the magnetic peaks, i.e., $-1.5 < k < -1$ and $-0.5 < k < 0$, which is obvious from Figure 66a. In other words, our resolution ellipsoid was elongated along (k, E) .

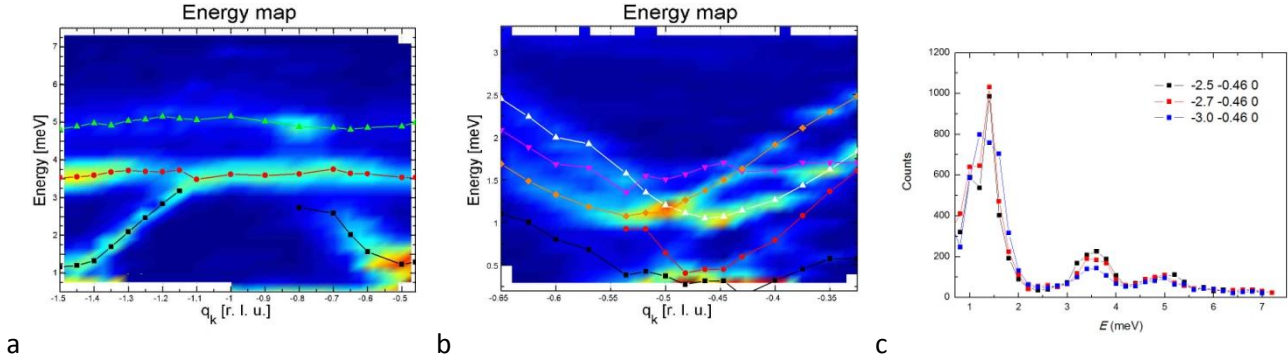


Figure 66: Energy map of the magnetic excitation spectra for varying k obtained from inelastic neutron diffraction experiment. (a) low-resolution map of the complete energy scale along k for $h = -2.5$ and $l = 0$ and (b) high-resolution map up to 3 meV recorded in the vicinity of the magnetic peaks $(-2.5 -0.5\pm\delta\pm\Delta k 0)$, ($\Delta k < 0.15$ r.l.u.). (c) Energy scans for $h = 2.5, 2.7$ and 3.0 for fixed $k = -0.5+\delta$ and $l = 0$.

A detailed inspection of the region between $k = -0.65$ and $k = -0.3$ and energy (E) of $E = 0.2$ meV and $E = 3.2$ meV was performed with the higher energy resolution setup ($dE = 0.2$ meV). The results are shown on Figure 66b. Again the effect of the resolution ellipsoid is apparent below $k = -0.5$. Nevertheless, inspection of the measured spectra reveals that the low-energy branch is actually composed of at least 5 branches. The strongest two, marked with white and orange on Figure 66b show a very similar behaviour and each of them seems to disperse from one of the two neighbouring incommensurate magnetic peaks. On the other hand, behaviour of the rest of the branches is more difficult to resolve, as they lack in intensity. It seems that the red mode closely follows the behaviour of the white and the orange, whereas the violet and the black seem to deviate, i.e., they appear to be less dispersing. Interestingly the most intense modes (white and orange) are gapped at 1 meV, while the Goldstone red and black modes are much weaker. This is very similar to the behaviour of the $\text{Cu}_2\text{Te}_2\text{O}_5\text{X}_2$ system (130). The dependence of the excitation spectra along h direction is shown on Figure 66c. As expected the excitations are here only weakly dispersing. The only change between the energy scans performed at $-2.5 -0.46 0$ and $-3.0 -0.46 0$ was that at higher h excitation modes have slightly broadened and weakened, indicating that indeed the energy level distribution along h is undisturbed.

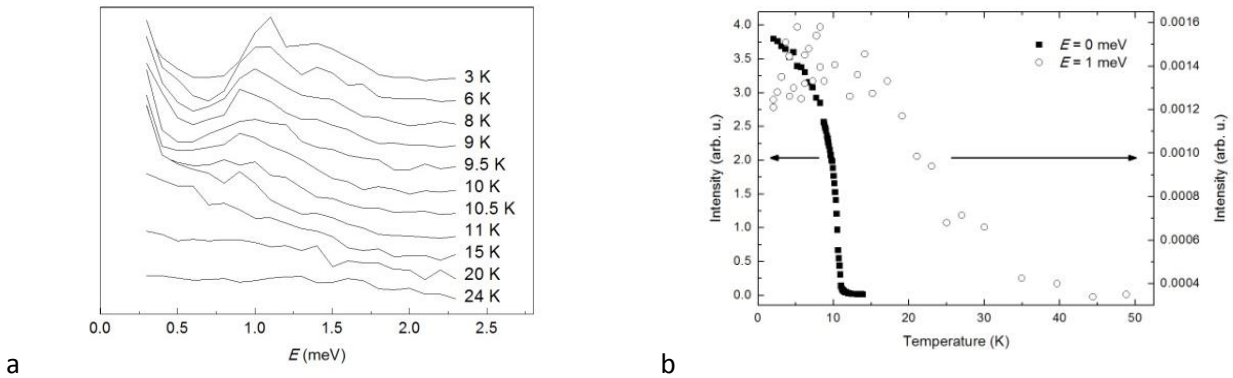


Figure 67: (a) Temperature dependence of the excitation spectra at $(-2.5 -0.536 0)$ magnetic peak position. (b) Temperature dependence of the scattered intensities measured at $(-2.5 -0.536 0)$ for elastic ($E = 0$ meV) and inelastic scattering ($E = 1$ meV).

Finally we measured also the temperature dependence of the excitations at the magnetic peak position $(-2.5 -0.536 \ 0)$ (Figure 67a). The results suggests that excitations at ~ 1 meV survive far above the magnetic transition ($T_M = 10.6$ K). The emergence of a strong diffuse scattering at the magnetic peak position above the transition temperature implies the closing of the energy gap. To investigate this assumption, a detailed inspection of the temperature dependence of the intensities (Figure 67b) was performed. Apparently the “1 meV” excitation does not weaken at the magnetic transition and it stays almost constant in intensity (but damped) up to 20 K and vanish only after 30 K. This suggests that the spin excitations gapped at ~ 1 meV, do not vanish at the magnetic transition and persist, damped and spatially on a short-range scale, up to $\sim 3T_N$, in agreement with the elastic neutron diffraction as well as other experimental techniques.

4.7 Summary and conclusion

In summary, we have discovered simultaneous emergence of ferroelectric and magnetic order in $\text{FeTe}_2\text{O}_5\text{Br}$ in the state with nearly transverse amplitude modulated incommensurate magnetic structure described by the wave vector $\vec{q} = (1/2 \ 0.463 \ 0)$. The ferroelectricity is ascribed to the polarization of Te^{4+} lone-pair electrons. The magnetoelectric effect and the unusual temperature dependence of the magnetic and ferroelectric properties are explained with the sliding of neighbouring amplitude modulation waves opening the possibility for the exchange-striction in the Fe-O-Te-O-Fe intercluster superexchange bridges.

Further we present a detailed B - T phase diagram which is determined by three phases, paramagnetic, incommensurate HT-ICM phase, and incommensurate amplitude modulated LT-ICM phase, where also electric polarization is present. Both magnetic transition temperatures show pronounced field dependence, as they shift up and down depending on the field orientation. The most interesting observation is that when the magnetic field is applied along the b -axis, above ~ 4 T HT-ICM phase disappears along with the electric polarization in the LT-ICM phase. This phenomenon remains unresolved and is yet to be investigated. We note that already far above ($6T_N$) the first magnetic transition short-range correlations are present, which are ascribed to the low-dimensional nature of the crystal and geometric frustration effects.

Finally we show the magnetic excitation spectra, which indicates that Goldstone modes are strongly suppressed, and that most intense excitations are gapped one. Moreover, these excitations does not vanish at the magnetic transition, as they persist, damped and spatially on a short-range scale, up to $\sim 3T_N$.

To conclude, our results suggest that two-dimensional systems of magnetic clusters with triangular geometry are a fruitful family of interesting physical phenomena, one of them being also a novel magnetoelectric coupling mechanism, based on the sliding of the neighbouring amplitude modulated magnetic waves.

Our results suggest to look for new magnetoelectrics in the vast family of M-T-O-X compounds ($M = \text{Cu, Ni, Fe, X} = \text{Cl, Br, I, T} = \text{Te, Se, Sb, Bi, Pb}$), as they frequently join strong magnetic frustration with the presence of T ions with lone-pair electrons.

5 Ni₅(TeO₃)₄Br₂

Intrigued by the discovery of the magnetoelectric coupling in the FeTe₂O₅Br system, we expand our study of low-dimensional magnetic systems with frustrated geometries to the Ni₅(TeO₃)₄Br₂ system. This system is a result of the same synthesis concept, as used in the case of FeTe₂O₅Br (16), (15), which is based on the fact that stereochemically active lone pair electrons in association with halide ions open up the structure and increase the possibility for low-dimensional arrangement of the transition metal cations. As already mentioned in the introduction, this way several new compounds have been found, e.g., Cu₂Te₂O₅X₂ (X = Cl, Br) (17), CuSb₂O₃Br (18), and Cu₄Te₅O₁₂Cl₄ (19), as well as Ni₅(TeO₃)₄X₂ (X = Br, Cl, I) (15). The new Ni₅(TeO₃)₄X₂ (X = Br, Cl, I) family was found to have triangular arrangement of Ni²⁺ (*S* = 1) magnetic moments within the [Ni₅O₁₇X₂] subunits and a layered topology of the Ni²⁺ sites, typical for frustrated antiferromagnet. In spite of this, the Ni²⁺ (*S* = 1) magnetic moments below *T_N* (29 K for X = Br) develop long-range antiferromagnetic order, which is expected to be rather complex due to the frustrated arrangement of the Ni²⁺ ions.

In this section we present our investigation of the magnetic ground state of Ni₅(TeO₃)₄Br₂ single crystal and its behaviour under the applied magnetic field down to 1.5 K and up to 23 T (131), (132), (133), (134). Extensive study included magnetization, magnetic torque, neutron diffraction, specific heat, and antiferromagnetic resonance measurements. A nonzero magnetic contribution to the heat capacity observed up to 2.3*T_N* is consistent with short-range magnetic ordering and the two-dimensional nature of the system. Below the *T_N* several antiferromagnetic phases were identified. The zero-field phase is characterized by a planar antiferromagnetic arrangement of the two in-layer neighbouring [Ni₅O₁₇Br₂] magnetic clusters within the magnetic unit cell. When the magnetic field is applied along the *a** crystal axis, a spin-flop-like transition to a phase with a complex out-of-plane arrangement of Ni²⁺ (*S* = 1) magnetic moments occurs at ~10 T. Using a molecular-field approach we were able to explain the magnetic field dependence of the antiferromagnetic resonance as well as predict the shift of the spin-flop like transition to higher fields with increasing temperature and the occurrence of a new magnetic phase with ferromagnetic ordering of [Ni₅O₁₇Br₂] magnetic clusters above 24 T. We ascribe the richness of the magnetic phases to strongly exchange-coupled clusters, being the basic building blocks of the investigated layered system. Estimated single-ion anisotropy, associated with the strongly distorted Ni-centered octahedra, has the same magnitude as the antiferromagnetic superexchange interaction, which obviously prevails over the geometrical frustration and leads to a long-range magnetic ordering below *T_N*. We note that in contrast to FeTe₂O₅Br, zero-field magnetic ground state of Ni₅(TeO₃)₄Br₂ preserves the inversion symmetry of the crystal lattice and thus rules out a possible ferroelectric behaviour. Nevertheless, the inversion symmetry is broken in the predicted high-field magnetic phase, hence electric polarization is in principle allowed.

5.1 Crystal structure

The Ni₅(TeO₃)₄Br₂ crystallizes in the monoclinic system (Table 12) (15). There are three different crystallographic nickel sites. Ni1 (Wyckoff site 4e) and Ni3 (in 8f) are octahedrally coordinated by oxygen atoms while Ni2 (in 8f) is connected to five oxygen atoms and one halogen atom. The three Ni-sites are connected via oxygen bridges to form some kind of a “claw” [Ni₅O₁₇Br₂] basic unit made of two connected triangles with Ni1 in the centre. The distances between Ni1-N2 and Ni1-Ni3 are 2.98 Å and 3.29 Å respectively, while the Ni2-Ni3 distances (2.8204(5) Å) are very short. This results in the Ni2-O-Ni3 bond angle below 90°, which according to the Goodenough-Kanamori rules (section 2.2.2.2) favours ferromagnetic superexchange interaction. In contrast, angles between the rest of the Ni-sites are in average larger than 90°, which likely result in the antiferromagnetic superexchange. As observed in Figure 68, one claw [Ni₅O₁₇X₂] is linked via eight corners to four of its next-nearest neighbours. This forms, due to the 2-fold axis and the glide plane *c*, rows, running alternatively along *y*, which build the NiO layers (Figure 68). Between

the Ni layers, $[\text{TeO}_3\text{E}]$ tetrahedrons are located (E denotes the $5s^2$ lone pair electrons of the Te^{4+} ions). Each tetrahedron shares three oxygen atoms with four adjacent basic entities $[\text{Ni}_5\text{O}_{17}\text{Br}_2]$, while in the space available between the Ni layers its lone pair E interacts with the halogen ions, i.e., this compound provides a new example in which lone pair-lone pair and lone pair-halogen interactions are observed.

Table 12: Basic crystallographic parameters for $\text{Ni}_5(\text{TeO}_3)_4\text{Br}_2$ system determined at 153 K (15).

Space group:	$C2/c$, (monoclinic)			
Lattice parameters	$a = 19.5674(2) \text{ \AA}$	$b = 5.2457(1) \text{ \AA}$	$c = 16.3084(9) \text{ \AA}$	$\beta = 125.289(1)^\circ$
Atomic coordinates:	Atom	x/a	y/b	z/c
	Te1	0.6216(1)	0.1846(1)	0.1358(1)
	Te2	0.3569(1)	0.7833(1)	0.1201(1)
	Br	0.2628(1)	0.1969(1)	-0.0983(1)
	Ni1	0.5	0.2531(1)	0.25
	Ni2	0.4136(1)	0.2834(1)	0.285(1)
	Ni3	0.5102(1)	0.7183(1)	0.1224(1)
	O1	0.4370(2)	0.0027(5)	0.1307(2)
	O2	0.6122(2)	0.8358(5)	0.2507(2)
	O3	0.4303(2)	0.1198(5)	-0.0700(2)
	O4	0.4252(2)	0.5055(5)	0.1458(2)
	O5	0.5394(2)	0.3333(5)	0.1432(2)
	O6	0.4087(2)	0.6447(5)	-0.0177(2)

To summarize, the triangular based Ni^{2+} topology of the $\text{Ni}_5(\text{TeO}_3)_4\text{Br}_2$ has all characteristics of frustrated systems, whereas on the other hand, all Ni^{2+} sites have strongly distorted octahedral environments and thus a significant magnetic anisotropy, which might prevail over the geometrical frustration and lead to a long-range magnetic ordering. We note that the crystal structure has a centre of inversion, thus, excluding a possibility for intrinsic ferroelectric behaviour. Nevertheless, this might change in case of the magnetic ground state with broken inversion symmetry.

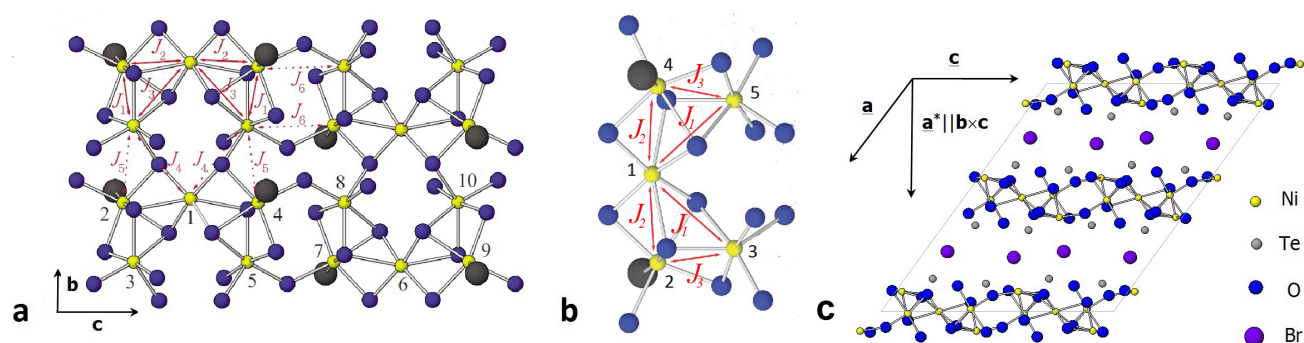


Figure 68: (a) The bc $\text{Ni}_5(\text{TeO}_3)_4\text{Br}_2$ layer with the notation of the superexchange interactions used in this work. Numbers from 1 to 10 indicate the numbering of magnetic sublattices used in our model. Te atoms are omitted for clarity. (b) The three Ni-sites are connected via oxygen bridges to form some kind of a "claw" $[\text{Ni}_5\text{O}_{17}\text{Br}_2]$ basic unit made of two connected triangles with Ni1 in the centre. (c) Projection of the crystal structure on the ac plane. Small yellow circles represent Ni, larger blue circles stand for oxygen, grey circles for Te, and violet ones indicate Br.

5.2 Magnetic properties in zero and low magnetic field

A high-temperature Curie-Weiss dependence of the magnetic susceptibility with the Curie-Weiss temperature of about $\theta_{CW} = -46$ K (15) suggested strong antiferromagnetic interactions between Ni^{2+} (electronic configuration $3d^8$) $S = 1$ spins. The preliminary magnetic susceptibility data (15) also found a small anomaly at low temperatures indicating a magnetic transition at around $T_N = 28$ K for $\text{Ni}_5(\text{TeO}_3)_4\text{Br}_2$ system ($T_N = 23$ K and $T_N = 30$ K for isostructural Cl and I systems, respectively). The observed hysteresis effects were assigned to the interplay of the random grain orientation of the powder samples with magnetic anisotropies of the spin system.

In order to answer the question how does geometrical frustration on the one hand and magnetic anisotropies on the other, influence the magnetic ground state and how this behaves under applied magnetic field, $\text{Ni}_5(\text{TeO}_3)_4\text{Br}_2$ single crystals were investigated by magnetization, neutron diffraction, antiferromagnetic resonance, heat-capacity, and magnetic-torque measurements (134), (135), (131), (133).

5.2.1 Magnetization measurements in low magnetic fields

Temperature dependence of the dc magnetic susceptibility measured in a field of 0.1 T is for different crystal orientations shown in Figure 69a. In a preliminary report Zorko et al. (135) found out that at high temperatures magnetic susceptibility χ follows the Curie-Weiss law with the Curie-Weiss temperature of about $\theta_{CW} \sim -50$ K and the Curie constant $C = 5N_A\mu_{eff}^2/3k_B \sim 77$ $\text{Am}^2\text{K/mol T}$ (mol of formula unit). They obtained the effective magnetic moment $\mu_{eff} = 3.5 \mu_B$, which for $S = 1$ spin system indicates a g -factor $g \sim 2.5$ in reasonable agreement with the value $g = 2.35$ obtained by Johnson et al. (15). The sign and the magnitude of the Curie-Weiss temperature suggest fairly strong predominantly antiferromagnetic interactions between Ni^{2+} moments. There is a small magnetic anisotropy present already at high temperatures, which was attributed to the anisotropy in the g factor. Our analysis of $1/\chi$ (Figure 69b) confirmed the above results, giving $\theta_{CW} = -44(5)$ K, $C = 75(2)$ $\text{Am}^2\text{K/mol T}$, ($\mu_{eff} = 3.45(5) \mu_B$).

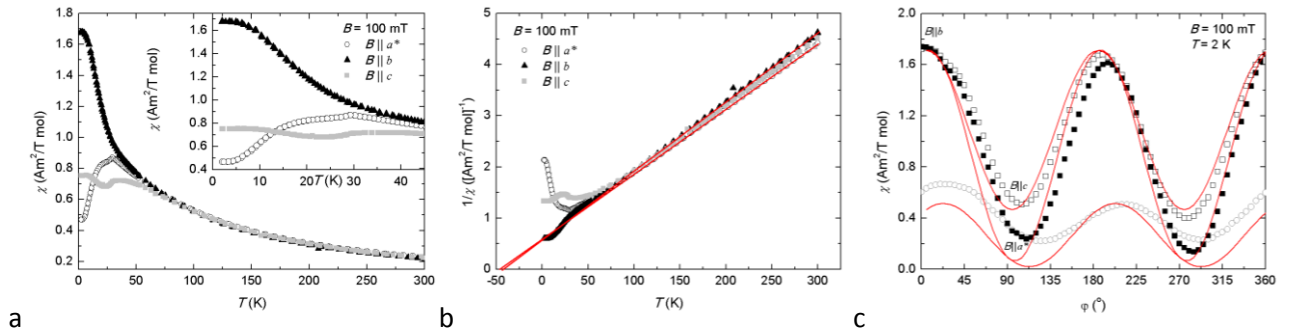


Figure 69: (a) The temperature dependence of dc magnetic susceptibility measured for different crystal orientations. In the inset, we show the expanded low-temperature region. (b) The temperature dependence of the inverse susceptibility for different crystal orientations. Solid lines present the high-temperature fit to the Curie-Weiss law. (c) The angular dependence of the magnetization measured at $T=2$ K for crystal rotations in the a^*c , a^*b , and bc planes. Solid lines are fits to the model described in the text.

A closer inspection of the low-temperature susceptibility data (inset of Figure 69a) reveals a small bump at $T_N = 29(1)$ K, reported already in the original article, where it was ascribed to the antiferromagnetic transition. Below T_N , a large anisotropy in the magnetic response was found. The magnetic moments, which are in low-fields orientated along the easy axis, bend easier along the field applied in the direction of the intermediate axis than along the field applied in the orientation of the hard axis. On the other hand, up to the spin-flop field they are almost insensitive to the changes of the magnetic field along the easy axis. Therefore, since the largest magnetization is measured along the b axis, we assign this axis as the crystalline effective intermediate axis, which also means that the crystalline a^*c plane is the plane of the easy and the

hard axes. Comparing the measurements taken with $\vec{B}||a^*$ and $\vec{B}||c$, we notice that the decrease of the magnetic susceptibility is larger for $\vec{B}||a^*$. Hence we conclude that this crystal axis is close to an effective crystalline easy axis, which leaves us with c as the effective hard axis. The complete temperature dependence of the magnetic susceptibility, however, signals even more complex picture of the magnetism in $\text{Ni}_5(\text{TeO}_3)_4\text{Br}_2$ single crystal. For instance, we notice a bump in the magnetic susceptibility at around $T = 12$ K, which could, for instance, originate from the different temperature dependence of the Ni sublattice magnetizations.

To determine the precise orientation of the magnetization easy and hard axes, we decided to measure the angular dependence of the magnetization (Figure 69c) at $T = 2$ K and $B = 0.1$ T. The magnetization is the largest for $\vec{B}||b$ confirming once again this axis as the intermediate axis (see above discussion for the argumentation). In the crystalline a^*c plane, the easy axis is tilted $\sim 30^\circ$ from the crystal a^* axis, while the hard axis is then $\sim 30^\circ$ from the c axis.

5.2.2 Neutron diffraction in zero-field

We now turn to the determination of the magnetic structure by neutron diffraction. A refinement of the crystal structure for $\text{Ni}_5(\text{TeO}_3)_4\text{Br}_2$ single crystal confirmed the structural model published in (15). Below T_N , new reflections of magnetic origin appeared at the positions of the C -centered lattice corresponding to the wave vector $\vec{q} = (0, 0, 0)$ (Table 13). The two strongest magnetic peaks (-201) and (-203) break the extinction rule $h0l: h, l=2n$, while the $hk0: h+k=2n$ rule is preserved.

Table 13: Selected observed and calculated squared magnetic structure factors F_{obs}^2 and F_{calc}^2 of $\text{Ni}_5(\text{TeO}_3)_4\text{Br}_2$ single crystal at 5 K corresponding to the model discussed in the text. The data set of 90 reflections with $h_{\text{max}} = 12$, $k = 0$, and $l_{\text{max}} = 13$ was used to refine the magnetic structure. The experimental setup limited our measurements to $h0l$ peaks only.

h	k	l	F_{obs}^2	F_{calc}^2	h	k	l	F_{obs}^2	F_{calc}^2
0	0	1	0.09	0.15	2	0	5	3.27	2.89
0	0	3	14.51	12.95	2	0	7	1.68	0.24
0	0	5	2.82	3.79	2	0	9	2.36	0.04
0	0	7	3.07	0.64	2	0	11	2.25	0.79
0	0	9	0.73	0.01	2	0	13	2.90	0.21
0	0	11	0.84	2.19	4	0	1	0.35	0.06
0	0	13	0.94	0.28	4	0	3	4.39	3.04
0	0	15	0.99	0.01	4	0	5	2.13	0.36
2	0	-1	30.43	29.49	4	0	7	0.86	0.43
2	0	-3	65.56	71.14	4	0	9	1.09	0.05
2	0	-5	0.96	1.86	4	0	11	1.00	0.26
-2	0	7	4.10	0.52	4	0	-1	12.00	11.77
2	0	-9	1.54	0.00	4	0	-3	60.73	59.33
2	0	-11	3.93	3.04	4	0	-5	11.51	7.26
2	0	-13	0.90	0.78	4	0	-7	1.23	1.86
2	0	1	1.51	0.01	4	0	-9	3.08	2.37
2	0	3	2.36	3.10	4	0	-11	1.23	2.07
					4	0	-13	1.51	1.98

Table 14: Irreducible representation Γ_4 of the wave vector group for $\vec{q}=(0, 0, 0)$ in the space group $C2/c$. The coefficients corresponding to the Wyckoff sites 4e are $x = 0.5, y = 0.2575, z = 0.25$ for Ni1 and those of 8f are $x = 0.4089, y = 0.2842, z = 0.0265$ for Ni2 and $x = 0.5095, y = 0.7191, z = 0.1213$ for Ni3.

4e						8f					
x	y	z	u	0	v	x	y	z	u	v	w
$-x+1/2$	$-y+1/2$	$-z+1/2$	$-u$	0	$-v$	$-x+1$	y	$-z+1/2$	u	$-v$	w
						$-x+1/2$	$-y+1/2$	$-z+1/2$	$-u$	$-v$	$-w$
						x	$-y+1$	$z+1/2$	$-u$	v	$-w$

To facilitate magnetic structure determination, representation analysis was performed with the program BASIREPS (136). The Fourier coefficients describing possible spin configurations can be written as linear combinations of irreducible representations of the wave vector group. The group of $\vec{q}=(0, 0, 0)$ does not split the 4e and 8f Wyckoff sites occupied by Ni^{2+} ions. The magnetic representations for the 4e and 8f sites are

$$\Gamma(4e) = 1\Gamma_1 + 1\Gamma_2 + 2\Gamma_3 + 2\Gamma_4, \quad (5.1)$$

$$\Gamma(8f) = 3\Gamma_1 + 3\Gamma_2 + 3\Gamma_3 + 3\Gamma_4. \quad (5.2)$$

The best agreement with experimental data was obtained for the irreducible representation Γ_4 (see Table 14) corresponding to the $C2'/c$ magnetic group. The moments of Ni^{2+} ions of the same Wyckoff site related by the inversion centre i' or by the glide plane c are oppositely aligned. The two-dimensional canted magnetic structure is presented in Figure 70a, the agreement between observed and calculated integrated magnetic reflection intensities is given in Table 13, and the refined values for Ni^{2+} moments are summarized in Table 15. We first note that the Ni^{2+} magnetic moments are confined in the ac plane with the major component along the (101) diagonal, reaching the values $2.16(9) \mu_B/\text{Ni}1$, $2.15(5) \mu_B/\text{Ni}2$, and $2.19(6) \mu_B/\text{Ni}3$ at 5 K. It is also clear from the refined magnetic structure that the Ni^{2+} moments are far from being collinear and the tilt from the c axis varies from site to site. There is, however, a tendency of the nearest Ni2 and Ni3 moments to align in the same direction and “opposite” to the Ni1 moment. We note that the refined magnetic structure (Figure 70a) is inversion symmetric, and thus excludes a possibility for magnetoelectric coupling necessary for the establishment of macroscopic electric polarization, in contrast to the behaviour found in the $\text{FeTe}_2\text{O}_5\text{Br}$ system.

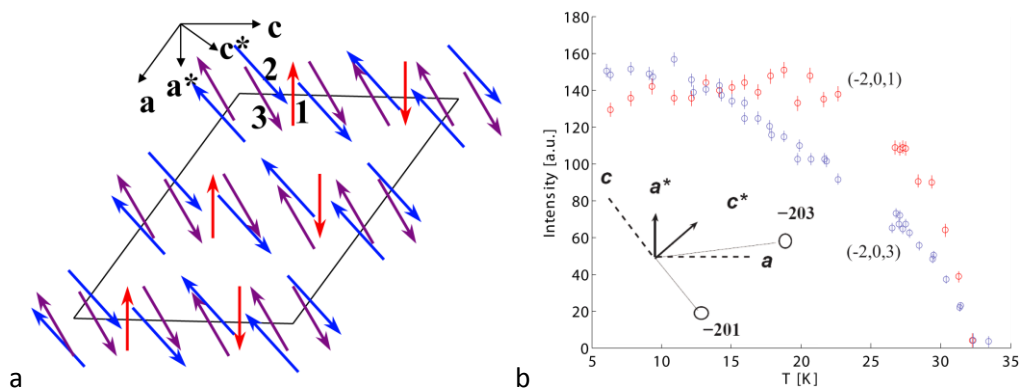


Figure 70: (a) The ac projection of the unit cell of the magnetic structure of $\text{Ni}_5(\text{TeO}_3)_4\text{Br}_2$. (b) Measured intensity of the (201) and (203) magnetic reflections of $\text{Ni}_5(\text{TeO}_3)_4\text{Br}_2$ single crystal as functions of temperature. Inset: The (-201) reciprocal lattice directions almost parallel to c , while the (-203) direction is almost parallel to the a axis.

Table 15: Refined parameters for the neutron data $\text{Ni}_5(\text{TeO}_3)_4\text{Br}_2$ in magnetically ordered state at $T = 5$ K and $T = 20$ K. μ is the ordered magnetic moment and θ the tilt from the c^* axis.

$T(\text{K})$	Ni-site	$\mu (\mu_B)$	$\theta (^\circ)$	$T(\text{K})$	Ni-site	$\mu (\mu_B)$	$\theta (^\circ)$
5	1	2.16(9)	241(2)	20	1	1.5(1)	242(4)
	2	2.15(5)	20(2)		2	1.90(7)	14(3)
	3	2.19(6)	32(2)		3	1.97(8)	23(3)
$R_M = 13.1\%$				$R_M = 18.8\%$			

The temperature evolution of the magnetic arrangement can be extracted from the temperature dependence of the (-201) and (-203) reflections and from the refinement of single crystal data collected at 5 and 20 K. Figure 70b shows that the (-201) and (-203) reflections have very different although correlated temperature dependences. When increasing temperature from 5 to 15 K, the intensity of the (-201) reflection, in contrast to the (-203) reflection, first slightly increases and for $T > 15$ K becomes stronger. Above 15 K, (-201) stays almost constant up to ~ 24 K and then dramatically reduces approaching T_N from below. Such behaviour correlates well with the temperature dependence of the magnetization measured for $\vec{B} \parallel c$ (Figure 69a). On the other hand, the temperature dependence of the (-203) intensity is much less dramatic and decreases with increasing temperatures as $A(1 - T/T_N)^{2\beta}$ with $\beta = 0.25(1)$. We note that $\beta = 0.25$ is typical for the stacked-triangular antiferromagnets (137). The observed temperature dependence of the intensities of the magnetic reflections can have two origins: either a gradual rotation of the moments or the nonuniform temperature dependence of the magnetic moment values of different Ni sites. Closer inspection of the magnetic structure factors of these two reflections shows that several factors determine such different temperature dependence. Firstly, due to the special position \vec{r} occupied by the Ni1 ions, the $\sin(2\pi\vec{h} \cdot \vec{r})$ contribution of this site adds up to the contributions of the other Ni sites for $\vec{h} = (-201)$ and is subtracted for (-203) . Secondly, as presented in the inset of Figure 70b, the (-201) reciprocal lattice direction is almost parallel to the c axis, while the (-203) direction is almost parallel to the a axis. Due to the dipole interaction between the neutron and the magnetic moments, only components perpendicular to the scattering vector contribute to scattered intensity. Therefore, the (-201) reflection is sensitive to the M_x component and (-203) to M_z . Finally, as the magnetic moment of Ni1 is oppositely aligned to the Ni2 and Ni3 moments, the decrease of the Ni1 moment would increase the (-201) magnetic intensity and decrease the (-203) one. Comparison of the magnetic arrangements refined at 20 K and 5 K in the $\text{Ni}_5(\text{TeO}_3)_4\text{Br}_2$ single crystal confirms that the temperature dependence of the Ni1 moment is different from those of Ni2 and Ni3. It decreases faster by $(67(5) \%)$ than the other two moment values $(87(4) \%)$ for Ni2 and $(92(4) \%)$ for Ni3, leading to different temperature dependences of the (-201) and (-203) reflections.

5.3 Measurements in the applied magnetic field

Increased susceptibility of frustrated systems to external perturbations, prompted us to investigate the influence of the applied magnetic field on the magnetic properties of the $\text{Ni}_5(\text{TeO}_3)_4\text{Br}_2$ system. Thus we performed a systematic study, including heat-capacity, magnetization, and magnetic-torque measurements. This allowed us to determine a magnetic phase diagram for this compound in the temperature range between 300 and 1.7 K and in magnetic fields from 0 up to 23 T.

5.3.1 Heat capacity measurements

Heat-capacity measurements were performed in the temperature range between 3 and 120 K in zero field (Figure 71a) and in applied magnetic fields B of 4, 6, and 9 T (Figure 71b). In zero field a sharp peak is detected at Néel temperature $T_N = 29$ K, where also the magnetic-susceptibility data indicate long-range

AFM ordering (135), (131). We stress that the transition temperature seems to be almost independent of the magnetic field — it only marginally decreases from 28.8(2) K at $B = 0$ T to 28.0(2) K at $B = 9$ T.

Temperature dependence of the heat capacity can be generally described as a sum of three contributions: $C_p = C_{latt} + C_{short} + C_{long}$ (81). Where C_{latt} stands for a phonon contribution to the heat capacity (84) and is calculated in the Debye approximation (equation 3.35). Short-range magnetic correlations far above T_N are typically described with $C_{short} \propto T^{-2}$ (equation 3.36) (81), (80), while below T_N long-range magnetic-ordering open a possibility for spin-wave excitations, resulting in the $C_{long} \sim T^{d/n}$ term. In case of a non-zero spin-wave gap, this expression can be improved resulting in the expression (equation 3.38) (82). At this point we remind the reader that parameter d denotes the magnetic lattice dimensionality, an $n = 1$ ($n = 2$) stands for antiferromagnetic (ferromagnetic) systems (81).

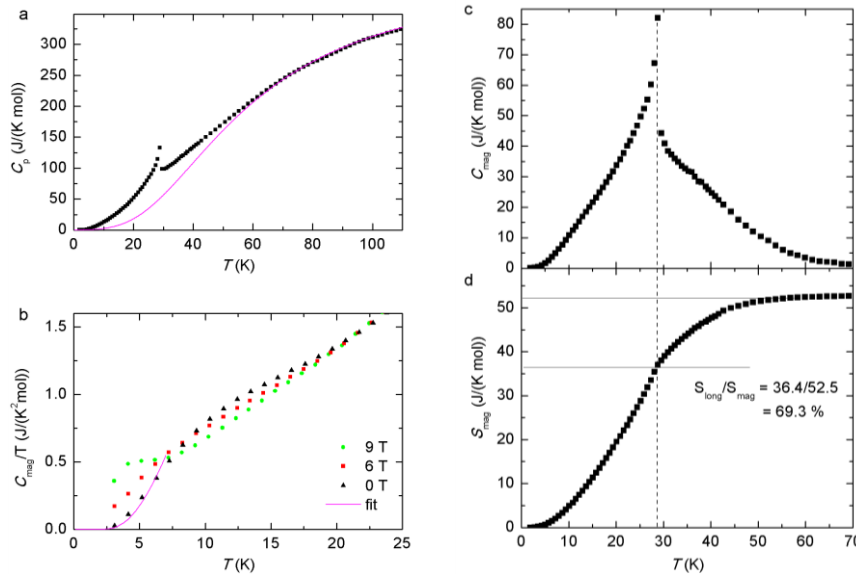


Figure 71: (a) Temperature dependence of the heat-capacity raw data (scattered symbols) and the fitted lattice contribution (solid line) with $\theta_D = 240(5)$ K and $N = 3.6(1) \times 10^{19}$. (b) Low-temperature dependences of magnetic contribution to the heat capacity for different magnetic fields: triangles for $B = 0$ T, squares for $B = 6$ T, and circles for $B = 9$ T. Solid line represents the fit for $B = 0$ T based on the expression for C_{long} , as described in the text. (c) Temperature dependence of the magnetic heat capacity measured in zero field obtained after subtraction of the phonon contribution from the raw data. (d) Integrated magnetic entropy contribution of the zero-field data.

As explained in the experimental section 3.2, in order to determine the temperature dependence of the magnetic heat capacity, i.e., $C_{mag} = C_{short} + C_{long}$, C_{latt} has to be estimated first. Since no diamagnetic isostructural compound is available, we simulated the raw heat-capacity data with C_{latt} well above T_N ($T > 3 |\theta_{CW}|$), where the contribution of C_{short} is expected to be marginal. Unconstrained fit to the expression for C_{latt} (equation 3.35) yielded $N = 3.6(1) \times 10^{19}$ and $\theta_D = 240(5)$ K (see solid line in the inset of Figure 71a). At this point we stress that N is consistent with the number of atoms in the studied crystal, while the Debye temperature is, in contrast to $\text{FeTe}_2\text{O}_5\text{Br}$ (120 K), closer to pure telluride glasses (115), (116) and also comparable to those found in different Ni alloys (138), (139). We subtracted the lattice contribution from the raw heat-capacity data to obtain the magnetic contribution to the heat capacity C_{mag} (Figure 71a). The expected peak in C_{mag} at T_N is clearly visible. Further, the magnetic contribution to the heat capacity extends up to $T \sim 70$ K, i.e., well above T_N . This underlines the importance of the magnetic short-range ordering effects and confirms the low dimensionality of $\text{Ni}_5(\text{TeO}_3)_4\text{Br}_2$.

The zero-field data below 7 K can be fitted with the expression for C_{long} (solid line in Figure 71c). In order to reduce the number of free parameters, we assume $n = 1$ (valid for AFM compounds) and $d = 2$ (layered

structure). Additionally, we take into account the spin-wave gap obtained from the AFMR measurements (section 5.4.2) $\delta\omega = 450$ GHz (131), which corresponds to $\Delta = 21.6$ K. Hence, B_{SW} remains as the only free parameter and the data simulation leads to $B_{SW} = 0.0842(1)$ J/(K³mol). The attempt to fit the low-temperature data with $d = 3$ (three-dimensional magnetic structure) failed to satisfactorily describe C_{mag} . We therefore conclude that the intralayer magnetic interactions are dominant in Ni₅(TeO₃)₄Br₂.

To properly account for the heat-capacity curves in applied magnetic field one should consider increasing population of lower energy states (140), which is beyond the scope of the proposed model. We highlight here the appearance of a very broad anomalous bump at $T \sim 10$ K in $B = 0$ T data, which shifts to lower T with increasing magnetic field. We tentatively ascribe it to a different temperature evolution of the magnetic moments at different Ni sites, as implied by the temperature evolution of the magnetic peaks in the neutron diffraction experiment (131).

The magnetic transition entropy ΔS_{mag} is obtained directly from C_{mag} after calculating the integral, $\Delta S_{mag} = \int_0^T C_{mag} d(\ln T)$. The experimentally obtained total entropy value 52(5) J/(K mol) (Figure 71b) reasonably well matches with the value $5R \ln(2S + 1) = 45.7$ J/(K mol) expected for the ordering of full magnetic Ni²⁺ ($S = 1$) moments. We stress that a considerable part ($\sim 30\%$) of the magnetic entropy develops at $T > T_N$, implying the importance of short-range ordering effects well above the magnetic transition temperature, most likely coming from the two dimensional correlations within the crystal layers.

5.3.2 Magnetization and magnetic-torque measurements

Adopting two different measuring techniques — direct magnetization and magnetic-torque measurements — we were able to follow the complete response of the magnetization \vec{M} along the three orthogonal axes $\vec{M}||a^*$ (M_{a^*}), $\vec{M}||b$ (M_b) and $\vec{M}||c$ (M_c), with the external magnetic field applied along the a^* crystal axis. The magnetization parallel to the magnetic field, M_{a^*} , was determined from magnetization measurements, which were performed up to 12 T between 1.5 and 10 K (Figure 72a).

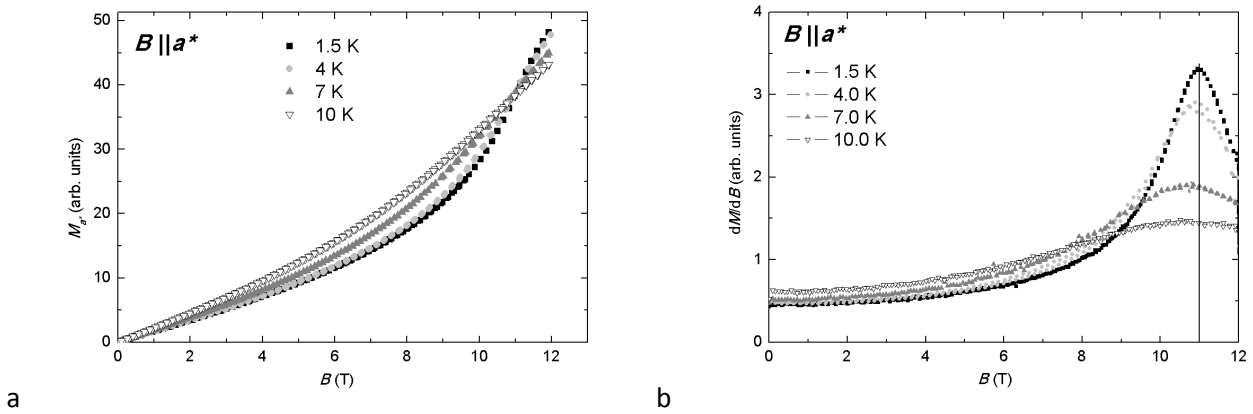


Figure 72: (a) Field dependence of the magnetization $M(B)$ (raw data) and (b) derivative of the magnetization curves, dM/dB , measured at different temperatures.

A well-pronounced inflection point in the $M(B)$ curve can be noticed and is clearly seen as a peak in the derivative dM/dB curves in Figure 72. The observed maximum of dM/dB is a result of a “spin-flop-like” transition at ~ 11 T, matching the estimation obtained from the AFMR measurements (131), (56). We notice that the spin-flop-like field shifts with increasing temperature to lower fields and that at the same time the maximum in dM/dB dramatically broadens (Figure 72b). This is likely the result of the increased thermal fluctuations of the magnetic moments. Such fluctuations reduce the static average of the moments’

amplitude, which lessens the effect of the magnetic anisotropies and consequently lowers the energy of spin-reorientation (lowers the magnetic transition field), as well as smear the transition over a broader magnetic field interval. Similar broadening with temperature was observed in the AFMR spectra (section 5.4) (134), (131).

To determine the response of the perpendicular magnetization (M_b and M_c) with respect to the applied field, $\vec{B} \parallel a^*$, magnetic-torque measurements were performed (Figure 73a and b). Due to experimental limitations, the magnetic field was applied only perpendicular to the cantilever surface, i.e., parallel to the crystal a^* axis. Hence, the magnetic torque $\tau = \vec{M} \times \vec{B}$ was measured only in b and c directions, which revealed qualitative responses of M_c and M_b , respectively. The actual response is measured as the capacitance C of the capacitor formed by the cantilever, holding the sample, and the fixed plate beneath (see section 3.3.2).

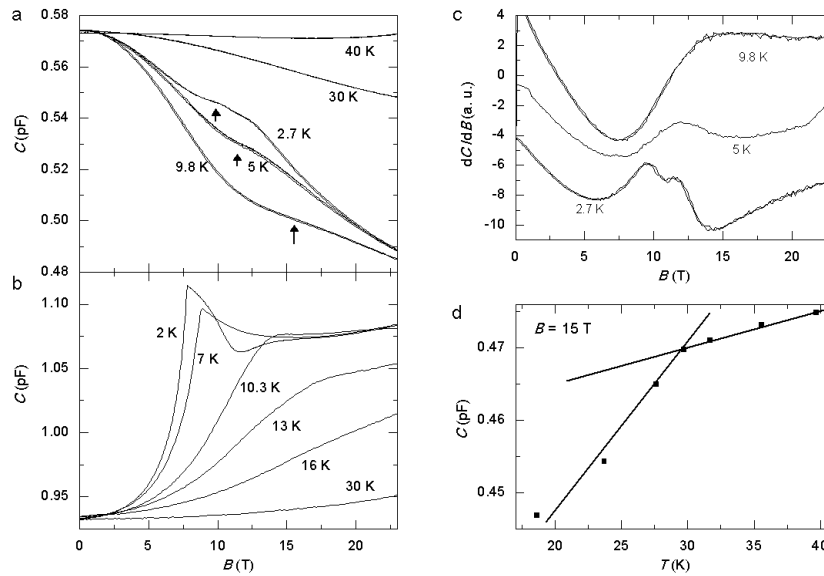


Figure 73: (a) Field and temperature dependencies of the capacity yielding the magnetic torque in the b direction (indicating the changes in M_c). The arrows reveal the inflection points. (b) Field and temperature dependencies of the capacity yielding the magnetic torque in the c direction, indicating the changes in M_b and (c) derivative dC/dB curves for typical torque measurements. (d) Temperature dependence of capacity $C(T)$ at 15 T; straight lines are guides for the eyes and help indicate the change in $C(T)$.

The measurements of the magnetic torque parallel to b , indicating the response of the component of the magnetization along the crystal c direction, M_c , show a pronounced change below 29 K, which can be associated with the Néel transition and is almost field independent up to 23 T. The transition is clearly seen in Figure 73d, where we plot $C(T)$ at 15 T. At lower temperatures (below 10 K), an inflection point is observable in the capacitance curves $C(B)$. This feature is manifested as a peak in the derivative dC/dB curves in Figure 73c. The field corresponding to the peak in these curves is in the range of the spin-flop-like transition (131), (133) and strongly depends on temperature as it shifts from 11.3 T at 3.7 K up to 16 T at 9.8 K. However, below 3.7 K, this peak in dC/dB curve splits and at 2.7 K we observe two well-defined peaks at 9.7 and 11.6 T.

In contrast to the field and temperature dependencies of M_c (Figure 73a), the component of the magnetization along the crystal b axis, M_b , (indicated by the magnetic torque in the c direction) does not exhibit any observable feature when going through the transition from paramagnetic (PM) to AFM states. This observation is consistent with our previous conclusions that in zero field the Ni^{2+} moments order in the ac crystal plane (131). Below 13 K, we start to observe an exceptionally sharp anomaly superimposed on the otherwise smooth capacity curves (Figure 73b). The magnetic field, corresponding to this feature, is strongly temperature dependent and monotonically decreases from 14 T at 10.3 K to 7.8 T at 1.8 K.

5.4 Antiferromagnetic resonance

In an attempt to shed some additional light on the magnetism of isostructural $\text{Ni}_5(\text{TeO}_3)_4\text{Cl}_2$ system, Mihaly et al. (56) performed a highfield electron magnetic resonance study for frequencies up to 3 THz. Several antiferromagnetic resonance modes were identified and their field-frequency relations were determined. In order to fit the antiferromagnetic resonance data, a collinear spin arrangement was assumed in a magnetic unit cell that is the same as the structural unit cell (56). However, since the Ni-centred octahedra are distorted in different ways, one would expect that the Ni^{2+} magnetic moments are not necessary collinear. This is supported also by our neutron diffraction results, which indicate that the magnetic ordering in the $\text{Ni}_5(\text{TeO}_3)_4\text{Br}_2$ system differs from collinear.

In order to learn more about the magnetic interactions and anisotropies in the $\text{Ni}_5(\text{TeO}_3)_4\text{Br}_2$ system, and to check the similarity to the $\text{Ni}_5(\text{TeO}_3)_4\text{Cl}_2$ system, we performed magnetic resonance measurements in magnetic fields up to 15 T and down to 4 K. Additionally we performed also angular dependence of the lowest frequency mode at 4 K.

5.4.1 Temperature dependence

Our attempts to detect electron paramagnetic resonance already in the paramagnetic phase, i.e., for $T > 29$ K, were not successful. We tried in a broad frequency range for resonance frequencies between 9.7 and 330 GHz. Apparently, the resonance is so broad that it is currently beyond the detection limit of our experimental equipment. On the other hand, we were able to detect the resonance in the antiferromagnetic phase Figure 74a but only for temperatures below 15 K, i.e., deep in the antiferromagnetic phase. The resonance signal measured at $\nu_L = 324$ GHz for $\vec{B} \parallel a^*$ and $T = 15$ K is very broad, as the peak-to-peak linewidth is 1.8 T. The resonance is also shifted towards lower fields (resonance field is 5.05 T) compared to the position expected for a usual Ni^{2+} $g \sim 2.5$ paramagnetic signal (11.45 T). The extra spike marked with asterisk in Figure 74a is due to the oxygen resonance and will be thus from now on ignored. The main resonance has nearly Lorentzian line shape (the spectra shown in Figure 74a are distorted due to the admixture of dispersion into our signal).

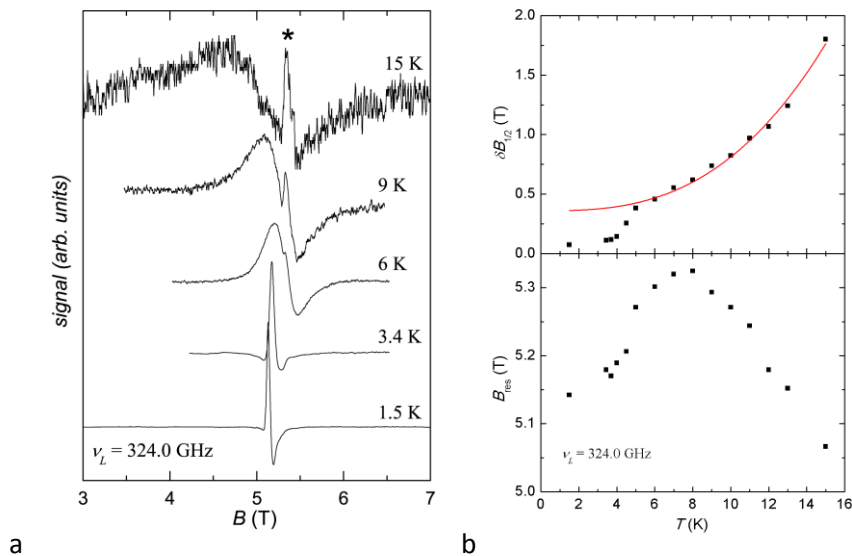


Figure 74: (a) The temperature dependence of the antiferromagnetic resonance line shape measured at a Larmor frequency $\nu_L = 324$ GHz. A narrow spike at $B = 5.3$ T (marked with asterisk) is due to the oxygen resonance. The temperature dependence of the (b) above: the linewidth (symbols), with fit to power law $T^{2.8}$ (solid line) and below: the centre of the antiferromagnetic resonance mode (symbols).

On cooling to low temperatures, the signal changes very dramatically. The first immediate observation is that the signal gets significantly narrower with decreasing temperature (Figure 74b). The linewidth at the half maximum decreases from $\delta B_{1/2} = 1.8(1)$ T at $T = 15$ K to $\delta B_{1/2} = 0.07(1)$ T at $T = 1.5$ K. Above $T = 15$ K, the linewidth shows nearly divergent dependence, and for this reason, we were not able to detect signal above this temperature. We also notice a small change in the slope in the temperature dependence of the linewidth at around $T = 5$ K. The observed temperature dependence between 15 K and 5 K can be phenomenologically described with a power law $\delta B_{1/2} \propto T^\gamma$, $\gamma = 2.8(3)$ (132), even though that AFMR linewidth is usually determined by four magnon scattering processes leading to T^4 dependence (141), (142). The deviation from the T^4 power law as well as the anomaly at $T = 5$ K thus probably reflect peculiarities in the magnon spectrum in $\text{Ni}_5(\text{TeO}_3)_4\text{Br}_2$.

The temperature dependence of the centre of the resonance is also very complex (Figure 74c). The resonance field first increases with decreasing temperature, reaching a maximum at $T = 8$ K. Below this temperature, the trend reverses and the centre of the line now shifts toward lower fields with decreasing temperature. Such temperature dependence of the centre of the line could signal a very complex temperature dependence of individual Ni^{2+} moments as already inferred from the neutron diffraction data.

5.4.2 Frequency and field dependence

In this section, we turn to the frequency dependence of the resonance signal described above. A full frequency dependence was measured at $T = 4$ K, i.e., well below T_N . A very typical observation for the resonance mode shown in Figure 74a is that the centre of the resonance shifts to higher resonance fields with decreasing resonance frequency (134). A full dependence of resonance-frequency–resonance-field relation for crystal orientation $\vec{B} \parallel \alpha^*$ is shown in Figure 75a. We note that such behaviour is very typical for the antiferromagnetic resonance modes. In fact, Mihaly et al. (56) found ten resonance modes in a frequency range up to 3 THz in $\text{Ni}_5(\text{TeO}_3)_4\text{Cl}_2$ system. Our mode corresponds to their lowest resonance mode. This particular mode softens with increasing field until $B = B_{sf}$. At spin-flop field, B_{sf} , the resonance field goes toward zero, and for $B > B_{sf}$, resonance frequency increases with resonance field again. From this data, we determine the spin-flop field to ~ 10.7 T, which is in agreement with magnetization and magnetic torque measurements. We also stress that we managed to detect the next higher resonance mode. At zero field, the two modes split into two branches, i.e., the zero-field frequency is for the lowest mode $\omega_1(0) = 450(5)$ GHz (equivalent to the thermal energy of ~ 21.6 K), while it is for the second mode $\omega_2(0) = 550(8)$ GHz. The zero-field frequencies and the splitting of the two lowest modes, $\omega_2 - \omega_1 = 100(8)$ GHz (equivalent to the thermal energy of ~ 4.8 K), confirm the importance of magnetic anisotropies in our system.

Assuming a case of a simple two-sublattice model, the zero-field resonance frequency is determined by magnetic anisotropy and superexchange field (equation 2.23), while the zero-field degeneracy of the modes can be removed by the presence of Dzyaloshinsky-Moriya interaction and the two modes should then vary as $\omega = \omega(0) \pm \gamma \sqrt{B^2 + B_{DM}^2}$, where B_{DM} is the field related to the strength of the Dzyaloshinsky-Moriya interaction, as pointed out already by Mihaly et al. (56). Considering the crystal structure of the $\text{Ni}_5(\text{TeO}_3)_4\text{Br}_2$ the Dzyaloshinsky-Moriya term can be present in all nearest-neighbour Ni-Ni superexchange interactions, since they all miss the centre of inversion. However, the direction of the Dzyaloshinsky-Moriya vector, connecting the magnetic moments on sites 1 and 2 over the ion l_i bridging the superexchange interaction, typically determined as $\vec{D}_{12} \propto \sum_i \vec{n}_{1l_i} \times \vec{n}_{l_i2}$ (equation 2.13), where \vec{n}_{1l_i} is a normalized vector connecting the magnetic moment on site 1 with the ion l_i and \vec{n}_{l_i2} is a normalized vector connecting the ion l_i with the magnetic moment on site 2, is not straight forward, i.e., all Ni-Ni are coupled via three –O– bridges resulting in a different orientation of \vec{D}_{12} for each different superexchange pathway. Consequently estimation for \vec{D}_{12}

in a two-sublattice model is difficult. On the other hand, the splitting of the two lowest modes can be achieved also by the presence of nonaxial anisotropy field. In fact, our magnetization studies, presented above, strongly suggest that this term could be large and therefore needs to be taken into account. Finally, considering the refined magnetic structure (Figure 70a), we can conclude that it is impossible to say, which Ni-site and which superexchange path would values for B_A , B_E and B_{DM} obtained from the simple two-sublattice model correspond to. Hence, in order to get information about the particular superexchange pathways, more precise description of the system is needed, which we will introduce in the forthcoming section 5.5.3.

5.4.3 Angular dependence

In the next step, we have measured the angular dependence of the lowest resonance modes. The variation of the resonance field with the angle of rotation is shown in Figure 75b. A very strong variation of the resonance field with the angle is seen in the a^*b plane. Analogous but less dramatic dependence is seen for the rotations in the a^*c plane. This observation holds for both resonances on each side of the dip in the resonance-field–resonance-frequency relation. The angular dependence is so strong that we were able to follow the resonance modes only up to 15° away from the a^* , i.e., in the a^*b plane. In this plane, for angles larger than that angle, the resonance mode is already higher than the experimental Larmor frequency $\nu_L = 240$ GHz and thus becomes unobservable. We stress that a very pronounced angular dependence of the resonance modes is rather typical of antiferromagnetic resonance.

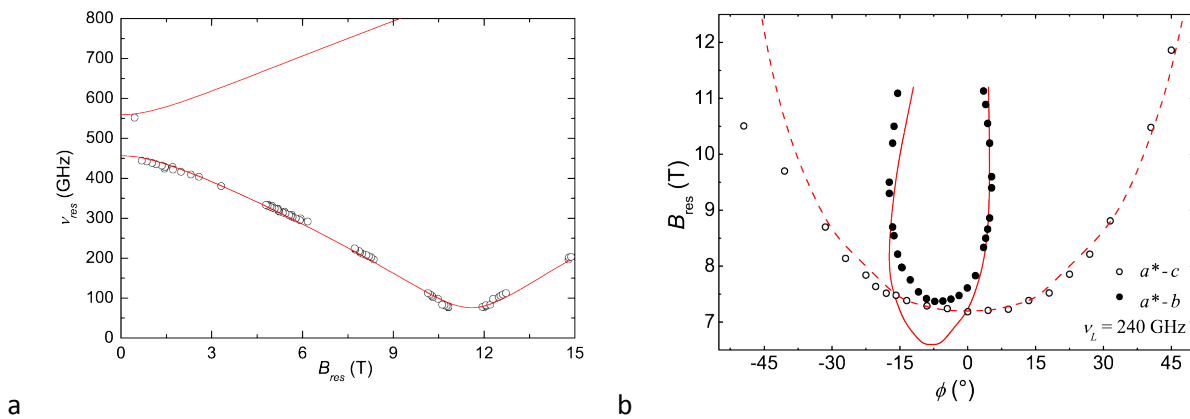


Figure 75: (a) The frequency dependence of the two lowest antiferromagnetic resonance modes (open circles) at $T = 4$ K. The solid line represents a fit to a model described in the text. (b) The angular dependence of the antiferromagnetic resonance mode in the a^*b plane (solid circles) as well as in the a^*c plane (open circles). The Larmor frequency was set to $\nu_L = 240$ GHz and the temperature was $T = 4$ K. Solid lines are fits to a model described in the text.

5.5 Calculations and discussion

5.5.1 Magnetic ordering and anisotropies

The $\text{Ni}_5(\text{TeO}_3)_4\text{Br}_2$ system unambiguously undergoes a transition to an antiferromagnetically ordered state below the Néel temperature $T_N = 29$ K. The magnetic unit cell is equal to the crystallographic one and it is made of two $[\text{Ni}_5\text{O}_{17}\text{Br}_2]$ units with oppositely aligned Ni^{2+} ($S = 1$) magnetic moments, giving a zero total magnetic moment. All Ni^{2+} ($S = 1$) magnetic moments lie in the a^*c plane, with two of them, Ni2 and Ni3, being nearly parallel, while the central Ni1 moment is significantly canted away. This implies strong magnetic anisotropies, which are reflected also in the magnetization measurements. These show a strong angular dependence and so the a^* axis was identified as the closest to the effective easy axis, the c axis as the closest to the hard axis (more precisely, the two magnetization axes are tilted by 30° away from the crystallographic axes), while the b axis was found to be the intermediate axis.

5.5.2 The phase diagram

The temperature and field ($\vec{B}||a^*$) dependences of the neutron diffraction, magnetization, magnetic torque, specific heat, and antiferromagnetic resonance imply, not only a rather complicated noncollinear magnetic structure, but also an intriguing temperature evolution of individual sublattice magnetizations. In particular, the transition from the PM to the AFM state (hereafter labelled as AFM1 phase) at $T_N = 29$ K is seen as a sharp peak in C_{mag} (Figure 71a), a pronounced change in M_c (inset I of Figure 73a), as well as the occurrence of the magnetic reflections in the neutron diffraction experiment (Figure 70b). This transition is almost independent of the applied magnetic field up to 23 T. Below T_N , however, a nonmonotonic temperature dependence of the magnetization as well as the intensity of (-201) and (-203) magnetic reflections suggest that Ni1 and Ni2,3 magnetic moments have different temperature dependences. Moreover, the heat capacity indicates a very broad bump at $T \sim 10$ K, which rapidly shifts to lower temperatures with increasing field. Around this temperature, a spin-flop-like transition becomes noticeable between 10 T and 15 T (depending on the chosen magnetization projection M_i) as an abrupt change in M_b (Figure 73b) as well as in M_{a^*} (Figure 72) and M_c (Figure 73a), where the corresponding changes are less sharp. The maxima, given by the peaks in the derivatives dM_{a^*}/dB and both dC/dB (indicating the changes in M_b and M_c), seem to occur at slightly different fields, but they get closer with decreasing temperature.

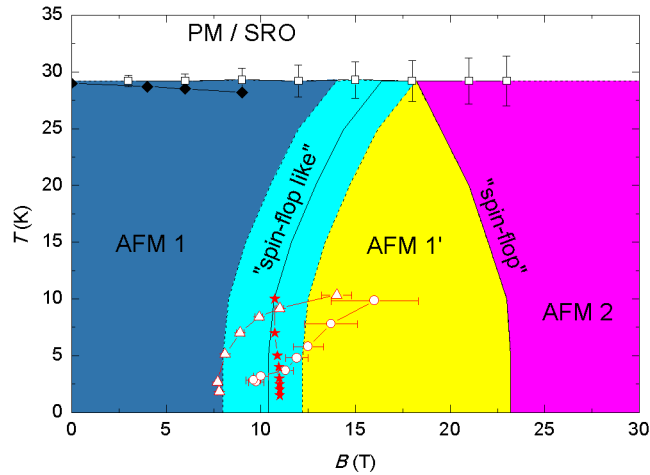


Figure 76: Phase diagram of the $\text{Ni}_5(\text{TeO}_3)_4\text{Br}_2$ compound. Empty circles and triangles stand for the maxima in dC/dH (torque measurements) corresponding to the changes in M_c (circles) and M_b (triangles), solid stars correspond to the peak in dM_{a^*}/dH obtained from magnetization measurements, solid black rhombuses represent peaks in the temperature dependence of the heat capacity, and black empty squares represent the sudden change in the $C(T)$ slope obtained from the torque measurements, corresponding to changes in M_c . The solid lines show the transitions predicted by our molecular-field model, while the dashed lines represent the transition-field boundaries obtained when tilting the applied field from the a^* by 5° , which corresponds to the experimental uncertainty of the crystal orientation.

We suggest that, at low temperatures, increasing the applied magnetic field along a^* axis above 10 T changes the arrangement of the magnetic moments and causes a transition from the in-plane AFM1 ordering to a more complex high-field AFM1' ordering, with the magnetic moments canted out of the ac plane. In Figure 76 we show the corresponding B - T phase diagram of $\text{Ni}_5(\text{TeO}_3)_4\text{Br}_2$ based on our heat-capacity and magnetization measurements. The AFM1-AFM1' transition is reminiscent of a spin-flop transition for a simple two-sublattice model. It is thus not surprising that it is seen as softening of the lowest AFMR mode. It becomes progressively more hindered with increasing temperature and is not observable any more above 15 K, where also the AFMR signal disappears (131). Finally, we note that the strong dependence of the spin-flop-like transition on the temperature and the orientation of the applied magnetic field, underline the importance of magnetic anisotropy for the magnetic ground state of $\text{Ni}_5(\text{TeO}_3)_4\text{Br}_2$.

5.5.3 Molecular-field model

In this section we extend the basic molecular-field model, developed in section 2.4.1, to properly describe our system. Based on the crystal structure, we expect the dominant superexchange interactions to take place among Ni^{2+} spins ($S = 1$) in the $[\text{Ni}_5\text{O}_{17}\text{Br}_2]$ basic building block. The Ni-Ni superexchange pathway includes oxygen bridges, but the superexchange coupling between the different Ni sites should differ from pair to pair. For instance, the distances between the Ni2 and Ni3 sites and between the Ni1 and Ni2 sites are 2.82 and 2.98 Å, respectively, and their $[\text{NiO}_6]$ octahedra connect via face sharing. The distance between the Ni1 and Ni3 is already larger, i.e., 3.29 Å, but the connectivity is now assured by edge sharing. Finally, these building blocks are connected with corner sharing so that the distances between the Ni sites on neighbouring $[\text{Ni}_5\text{O}_{17}\text{Br}_2]$ units increase to 3.4 Å (Ni3-Ni2), 3.57 Å (Ni3-Ni1), and 3.58 Å (Ni2-Ni3). Other Ni-Ni distances are already larger and the superexchange bridges involve several ligand atoms, making these superexchange interactions negligibly small. We also neglect the superexchange interactions between the layers, as already suggested by Mihaly et al. (56). A complete network of Ni sites in a layer projected along the reciprocal a^* direction with the notation of the superexchange coupling constants is shown in Figure 68. Since J_1 and J_5 couplings both act between the Ni2 and Ni3 sites, i.e., former within and latter between the neighboring basic units, only the Ni2-Ni3 effective superexchange coupling constant ($J_1 + J_5$) can be determined. The same argument applies also for the J_3 and J_4 superexchange couplings between Ni1 and Ni3 sites, and so the effective superexchange constant ($J_3 + J_4$) replaces them in our model.

As mentioned above, the $[\text{NiO}_6]$ octahedra are strongly distorted, so we will, in addition to the superexchange interaction, assume the presence of significant single-ion anisotropy. We stress that single-ion anisotropy is frequently very relevant for Ni^{2+} ions in distorted $[\text{NiO}_6]$ octahedral (143), (144), (145), (31). Furthermore, as already mentioned, there is almost no symmetry restriction for the Dzyaloshinsky-Moriya antisymmetric superexchange interaction, which is thus, in principle, allowed for each Ni pair.

A complete Hamiltonian of our system can therefore be written as

$$H = \sum_{i>j} \vec{S}_i \cdot \underline{J}_{ij} \cdot \vec{S}_j + \sum_j \vec{S}_j \cdot \underline{D}_j \cdot \vec{S}_j + \sum_{i>j} \vec{D}_{ij} \cdot (\vec{S}_i \times \vec{S}_j) + \mu_B \sum_j \vec{S}_j \cdot \underline{g} \cdot \vec{B}_0 \quad (5.3)$$

Here, the components of the above Hamiltonian are the superexchange interaction between nearest neighbours, single-ion anisotropy, Dzyaloshinsky-Moriya antisymmetric exchange interaction, and the Zeeman term. The components of the single-ion anisotropy tensor \underline{D}_j depend primarily on the local Ni^{2+} environment and thus are different for the Ni1, Ni2, and Ni3 sites. Applying the molecular field approximation, we can rewrite the above Hamiltonian as a magnetic free energy F per Ni site,

$$F = \sum_{i>j} \vec{M}_i \cdot \underline{A}_{ij} \cdot \vec{M}_j + \sum_j \vec{M}_j \cdot \underline{K}_j \cdot \vec{M}_j + \sum_{i>j} \vec{G}_{ij} \cdot (\vec{M}_i \times \vec{M}_j) + \frac{1}{g} \sum_j \vec{M}_j \cdot \underline{g} \cdot \vec{B}_0 \quad (5.4)$$

In the above free energy expression, we introduced ten magnetic sublattices ($i, j = 1, \dots, 10$) see Figure 68a for their numbering with corresponding magnetizations $\vec{M}_j = -Ng\mu_B \langle \vec{S}_j \rangle$, where N is the number of Ni^{2+} magnetic ions in the j -th sublattice, g is the g factor of the free electron, and $\langle \dots \rangle$ indicates the thermal average. The molecular field constants are defined as follows:

$$\underline{A}_{ij} = \frac{1}{N(g\mu_B)^2} \underline{J}_{ij} \quad (5.5)$$

$$\underline{K}_j = \frac{1}{N(g\mu_B)^2} \underline{D}_j \quad (5.6)$$

$$\vec{G}_{ij} = \frac{1}{N(g\mu_B)^2} \vec{D}_{ij} \quad (5.7)$$

Having written the expression for the magnetic free energy, we can follow the procedure presented in section 2.4.1 to obtain the expression for antiferromagnetic resonance, i.e., we calculate the mean-field $\vec{H}_j = \partial F / \partial \vec{M}_j$ acting on the sublattice magnetization \vec{M}_l ($l = 1, \dots, 10$) and assuming $\vec{M}_l = \vec{M}_{0l} + \vec{m}_l e^{i\omega t}$, where $\vec{m}_l \perp \vec{M}_{0l}$, we obtain the expression for $2l$ linear equations for l resonant modes. Unfortunately, in our experiments we were only able to detect the lowest two resonant modes, hence we cannot take the advantage of using all of the derived equations.

To sum up, we end up with expression for free energy, and expressions for the two lowest antiferromagnetic resonant modes, and a bunch of free parameters. Hence, before starting the calculations, we would first like to narrow down the number of free parameters.

5.5.4 Calculations of the single-ion anisotropies

It is obvious from the model described above that we are dealing with a very complicated magnetic structure and that large number of parameters is needed to adequately describe it. For this reason, we decided first to calculate the single-ion anisotropies and then to use these parameters as the input in the fitting procedure. Spin parameters were calculated in collaboration with Philip Tregenna-Piggott from the Laboratory for Neutron Scattering, ETHZ and Paul Scherrer Institute, Switzerland.

The orientation of the single-ion anisotropy tensor \underline{D} and its principal values were estimated by angular overlap model (AOM) calculations. The method proceeded in two steps. First, the ligand field matrix was constructed and diagonalized with 1000 unique directions of the magnetic field vector. This step was accomplished using program LIGFIELD developed by Bendix (146). AOM parameters for the Ni-O, Ni-Cl, and Ni-Br bonding interactions were estimated from values of 10Dq documented for homoleptic Ni²⁺ centres. Values for e_σ and e_π were derived assuming $e_\pi = 0.2 e_\sigma$. The parameter e_σ was assumed to vary with distance as a function of $1/r^5$ and e_π as a function of $1/r^6$. The Racah and spin-orbit coupling parameters were fixed at 80 % of their free-ion values, and the orbital Zeeman interaction reduced accordingly. Next, the calculated energies of the triplet ground state manifold were modelled by the general $S = 1$ spin Hamiltonian $H = \vec{S} \cdot \underline{D} \cdot \vec{S} + \mu_B \sum_j \vec{S}_j \cdot \underline{g} \cdot \vec{B}_0$. Least-squares refinement of the eigenvalues of the above Hamiltonian to the three lowest lying eigenvalues of the AOM calculations yielded the \underline{D} tensor and \underline{g} matrix in the reference coordination frame. The principal values were determined via the transformations $\underline{D}' = U_D^{-1} \underline{D} U_D$ and $\underline{g}' = U_g^{-1} \underline{g} U_g$. Here, \underline{D}' and \underline{g}' refer to the \underline{D} tensor and \underline{g} matrix in eigencoordinate frames in which they are diagonal. The transformation matrices U_D and U_g contain the direction cosines relating the two coordinate systems, from which the Euler angles can be calculated. The results of the calculations are summarized in Table 16. Here, we also introduced the standard planar anisotropy $E = \frac{1}{2}(D_{xx} - D_{yy})$ and $D = D_{zz} - \frac{1}{2}(D_{xx} + D_{yy})$ axial anisotropy constants.

It is important to emphasize the extent to which the single-ion anisotropy can be estimated from these AOM calculations. The ratio $E:D$ is governed principally by the angular disposition of the ligands, obtained from the crystallographic data, and the relative strength of the bonding interactions. We are therefore confident that our estimates of the bonding interactions are reasonable and hence the ratio of E to D should be quite reliable. We have allowed for covalency by reducing the Racah and spin-orbit coupling parameters to 80 % of their free-ion values. However, the reduction of these parameters could conceivably be somewhat different

with the result that the absolute magnitude of the splitting of the 3^A term is likely to differ from the values computed. Finally, we note that the calculated anisotropy of the Ni1 centre is very large with D_{zz} and D_{yy} of similar magnitude. In this instance, it is difficult to establish with certainty the orientation of the \underline{D} tensor by the least-squares fitting procedure adopted.

Table 16: Calculated components of the single-ion anisotropy tensors \underline{D} and the Euler angles α , χ , and γ defining their orientation in respect to the crystallographic system. See text for details.

parameter	Ni1	Ni2	Ni3
$D_{zz}(\text{K})$	23.83	6.14	-20.58
$D_{xx}(\text{K})$	-1.72	-1.17	12.41
$D_{yy}(\text{K})$	-22.11	-4.98	8.17
$D(\text{K})$	35.75	9.22	-30.87
$E(\text{K})$	10.20	1.90	2.12
$\alpha(^{\circ})$	89.99	359.76	309.69
$\chi(^{\circ})$	89.85	56.10	52.66
$\gamma(^{\circ})$	270.0	77.47	84.77

5.5.5 Calculations of the spin parameters

Only now, we can try to deduce the spin system parameters (J_{ij} , \underline{D}_j , \vec{D}_{ij}). To narrow down the number of parameters in the magnetic free energy (5.4) and make the problem tractable, we first make certain assumptions. As mentioned above, in the basic unit, the Ni2 and Ni3 moments are nearly collinear (Figure 68) as well as they have connecting --O-- bond angles $< 90^{\circ}$, so we will assume the ferromagnetic J_1 interaction between these two spins. On the other hand, the Ni1 moment tends to point in the opposite direction although tilted away from the direction defined by Ni2 and Ni3 moments. For this reason, we assume that the superexchange interactions between Ni2 and Ni1 J_2 , as well as between Ni3 and Ni1 J_3 , are antiferromagnetic. From the orientation of the spins in the two $[\text{Ni}_5\text{O}_{17}\text{Br}_2]$ units forming the magnetic unit cell (Figure 68), we anticipate the antiferromagnetic interactions J_6 . To account for tilting of the Ni moments in the a^*c plane, we use the calculated site dependent single-ion anisotropies (Table 16) but leave the scaling of the eigenvalues as a free parameter.

The simulation strategy was to model the free energy (5.4) in order to describe simultaneously the magnetic structure i.e., the equilibrium orientations obtained from the neutron diffraction (Figure 70a), the angular dependence of the magnetization (Figure 69c), and the frequency (Figure 75a) and angular (Figure 75b) dependence of the antiferromagnetic resonance data. The final set of parameters consistent with all experiments is given in Table 17. In order to obtain the magnetic structure Figure 70a, we also added the Dzyaloshinsky-Moriya exchange interactions between the Ni1 and Ni2 sites \vec{D}_{12} and between the Ni2 and Ni3 sites \vec{D}_{23} (Table 17). The fact that we were able to simultaneously describe three different experiments suggests that our parameters are close to the correct values.

Table 17: Summary of parameters (in Kelvin) used for fitting of the neutron diffraction, magnetization, and antiferromagnetic resonance data measured on $\text{Ni}_5(\text{TeO}_3)_4\text{Br}_2$ single crystal. The orientations of \underline{D}_i tensors are the same as in Table 16.

	$J_1 + J_5$	J_2	$J_3 + J_4$	J_6	D_1	D_2	D_3	\vec{D}_{12}	\vec{D}_{23}
x	-0.8	34.7	56.4	10.7	-0.8	-0.6	6.1	0	0
y	-19.6	18.4	49.6	2.0	-10.8	-2.4	4.0	-5.2	0.1
z	-1.2	5.8	12.6	25.4	11.6	3.0	-10.0	0	0

Based on the obtained parameters (Table 17), we can draw the following conclusions.

1. The effective ferromagnetic interaction between Ni2 and Ni3 is most likely a result of $< 90^\circ$ bonding Ni–O–Ni angles and seems to explain the relatively small value of the frustration. The derived frustration parameter $f = |\theta_{CW}|/T_N = 1.7$, which in comparison with the lower boundary, $f = 10$, for strongly frustrated materials (110), indeed implies that the triangular Ni^{2+} topology does not induce strong frustration effects. The remaining frustration is, in fact, a consequence of large magnetic anisotropies.
2. Similar magnitudes of superexchange interactions among the Ni^{2+} ($S = 1$) between and within $[\text{Ni}_5\text{O}_{17}\text{Br}_2]$ entities J_6 and J_2 respectively, suggests that the $[\text{Ni}_5\text{O}_{17}\text{Br}_2]$ cannot be considered as magnetically isolated units.
3. The determined single-ion anisotropies for Ni-sites are of the same order of magnitude as the superexchange interactions, hence their presence should strongly influence the $\text{Ni}_5(\text{TeO}_3)_4\text{Br}_2$ magnetic properties. Further, we stress that for the Ni3 site \underline{D} has a different sign than for Ni1 and Ni2 (see Table 16 and Table 17). Hence, it is likely that the Ni3 site anisotropy is responsible for the peculiar temperature dependence of the Ni moments detected below T_N by neutron diffraction as well as by the magnetization and specific heat measurements.
4. The large single-ion anisotropy constants originate from the strongly distorted Ni^{2+} octahedral surroundings. The difference in the single-ion anisotropy direction implied by the different directions of the octahedral deformations is the main reason for the Ni^{2+} moment tilting and for the noncollinear low-temperature magnetic structure.
5. At the same time, the magnetic anisotropies ($J_i^{\alpha\beta}$, $\alpha, \beta = x, y$) further suppresses quantum fluctuations arising from the geometrical frustration and stabilizes the long-range antiferromagnetic ordering below T_N . It is therefore clear that the single-ion anisotropy in addition to superexchange anisotropy plays a vital role in $\text{Ni}_5(\text{TeO}_3)_4\text{Br}_2$ system. Our results thus contradict the model proposed for isostructural $\text{Ni}_5(\text{TeO}_3)_4\text{Cl}_2$ by Mihaly et al. (56), where the single-ion anisotropy was neglected.

In order to understand how the applied magnetic field affects the spin order at low temperatures, we minimized the magnetic free energy (5.4) for $\vec{B}||a^*$ considering the calculated parameters (Table 17). This way the field dependence of the magnetization was calculated and the spin-flop-like transition was determined from the inflection points in the simulated $M(B)$ curves. In the zero-temperature limit the AFM1 to AFM1' transition is predicted at ~ 10 T (Figure 76). We stress that the transition field and the broadness of the peak in the $dM(B)/dB$ curves were found to be extremely sensitive to the applied magnetic field direction, i.e., deviation of the applied field for less than 5° causes the transition field to change for more than 1 T. We stress that such enhanced response directly reflects the complexity of the studied system. Thus, we suspect that the shift toward lower fields and the sharpness of the peak in Figure 73b are likely to be of experimental origin. The second peak at 11.6 T in the dC/dB curve at 2.7 K in Figure 73b is beyond the scope of our model and might reflect another transition due to higher order terms in the spin Hamiltonian.

In order to describe the magnetic response of $\text{Ni}_5(\text{TeO}_3)_4\text{Br}_2$ also at finite temperatures, we assume the temperature dependence of the sublattice magnetizations (147)

$$\vec{M}_i(T) = \vec{M}_i(0) B_S \left(\frac{\mu_B H_{eff}^{(i)}}{k_B T} \right), \quad (5.8)$$

where $H_{eff}^{(i)}$ is the effective magnetic field acting on a given sublattice,

$$B_S(x) = \frac{2J+1}{2J} \coth\left(\frac{2J+1}{2J}x\right) - \frac{1}{2J} \coth\left(\frac{x}{2J}\right) \quad (5.9)$$

is the Brillouin function, and $\vec{M}_i(0)$ is the sublattice magnetization at zero temperature. We further assume that the superexchange interactions and anisotropy constants are temperature independent. As a result, our model correctly predicts that the spin-flop-like field should increase with increasing temperature, matching well with the observed behaviour (Figure 76). We stress that the agreement between the theory and our measurements is particularly decent since all the parameter are fixed based on antiferromagnetic resonance and neutron-diffraction studies. Experimentally observed different transition fields for different magnetization components most likely originate from the small deviations of the crystal orientation between different experiments. To confirm this assumption, we calculated the spin-flop-like transition field for the tilt of the applied field from the a^* direction by 5° . The results show that all the measured transition fields up to ~ 10 K are still within the field region given by our model (dashed lines in Figure 76, which correspond to the tilt of the applied field from the a^* direction by 5°). Considering that our molecular-field model is valid at low temperatures and that at higher temperatures deviations from the average sublattice magnetization values are increased, discrepancy between the theoretical and experimental results above 10 K, i.e., above $\sim 0.4T_N$, is inevitable. The predicted Néel temperature is 40 K. The model could possibly be improved by introducing temperature-dependent superexchange interactions and anisotropy constants—similarly as done in ref. (147) — which would enable a more accurate estimation of the Néel temperature as well as potentially reproduce the observed strong temperature dependence of the spin-flop-like field at higher temperatures.

Lastly, in Figure 77 we show the calculated zero-temperature magnetic structures for $B = 0, 19$, and 30 T. The AFM1 phase, identified by AFMR and neutron-diffraction experiments (131), consists of antiferromagnetically arranged $[\text{Ni}_5\text{O}_{17}\text{Br}_2]$ clusters Figure 77c. In agreement with the magnetization measurements, our simulations suggest that the magnetic structure is almost completely field independent up to 10 T.

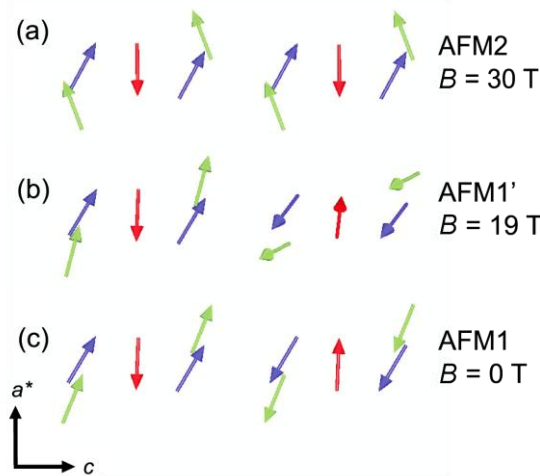


Figure 77: Calculated orientations of all ten sublattice magnetizations in the ac plane for the magnetic field \vec{B} applied in the a^* direction (the b axis is pointing out of the paper) for (a) $B = 30$ T, (b) $B = 19$ T, and (c) $B = 0$ T. Red, green, and blue arrows correspond to three nonequivalent sites: Ni1, Ni2, and Ni3, respectively.

At this point, the Ni^{2+} ($S = 1$) moments start to bend toward the crystalline b axis, marking the spin-flop-like transition to the AFM1' phase (Figure 77b). During this rearrangement, the magnetization component M_b starts to grow. The moments continue their reorientation up to the field of ~ 24 T, where the magnetic structure once more drastically changes. Above this field $\text{Ni}_5(\text{TeO}_3)_4\text{Br}_2$ can be described with another type of magnetic ordering (labelled as AFM2 phase and shown in Figure 77a). In this phase the arrangement is again

almost planar; however, it differs significantly from the AFM1 phase — the intercluster ordering becomes ferromagnetic, with central Ni^{2+} moment inside each cluster still being antiparallel to the other four. Such transition is a clear demonstration of the competition between intracluster and intercluster interactions. For $B > 24$ T the external magnetic field suppresses the intercluster AFM interactions but is still weaker than the leading intracluster AFM interactions. Additionally, we note that the AFM2 phase breaks the inversion symmetry and thus opens a possibility for magnetoelectric coupling as well as macroscopic electric polarization. However, the existence of the AFM2 phase, predicted by our simulations for $B > 24$ T, requires experimental verification by magnetic measurements in higher fields.

5.6 Summary and conclusion

In summary, our systematic temperature and magnetic field dependent heat-capacity, magnetization, magnetic torque, neutron diffraction, and antiferromagnetic resonance measurements allowed us to draw a B - T phase diagram up to 23 T and down to 1.5 K for the two-dimensional $\text{Ni}_5(\text{TeO}_3)_4\text{Br}_2$ compound. The contribution to the magnetic heat capacity observed at temperatures as high as $2.3T_N$ suggests a development of short-range magnetic correlations at rather high temperatures. Additionally, the short-range correlations are enhanced by the quasi-two-dimensional nature of the investigated spin system. Below $T_N = 29$ K, the B - T phase diagram is very rich. It consists of a number of low-temperature AFM phases governed by the presence of strong magnetic anisotropies and the competition between the intracluster and intercluster superexchange interactions. The zero-field AFM1 phase is characterized by a planar AFM arrangement of the two in-layer neighbouring $[\text{Ni}_5\text{O}_{17}\text{Br}_2]$ magnetic clusters within a magnetic unit cell. Unlike in $\text{FeTe}_2\text{O}_5\text{Br}$, magnetic order here preserves the crystal lattice inversion symmetry, and thus excludes a possibility for magnetoelectric coupling necessary for the establishment of macroscopic electric polarization. When the magnetic field is applied along the a^* axis, the spin-flop-like transition to the AFM1' phase occurs at approximately 10 T. Theoretical analysis of the data with the molecular field formalism suggests that the magnetic field does not affect all the $[\text{Ni}_5\text{O}_{17}\text{Br}_2]$ clusters in equal manner. The magnetic structure of clusters with the majority of the magnetic moments aligned close to the field direction stays almost intact, whereas the orientations of the Ni^{2+} magnetic moments in the other half of the clusters change from planar to a more complex out-of-plane arrangement. This transition is shifted to higher fields with increasing temperature, as indicated by our calculations. Finally, a stable AFM phase is predicted above 24 T, where $[\text{Ni}_5\text{O}_{17}\text{Br}_2]$ clusters are ordered ferromagnetically while the intracluster ordering of the central and the four surrounding moments remains antiferromagnetic. Interestingly, the AFM2 magnetic structure breaks the inversion symmetry, and thus opens a possibility for the magnetoelectric coupling. This prediction indeed makes the future search for the experimental proof of the existence of the AFM2 phase even more appealing.

At last, we stress that the observed richness of the phase diagram is a direct consequence of the competition between intracluster and intercluster superexchange couplings on the one hand and single-ion magnetic anisotropy on the other. The calculations results also suggest that the strong single-ion anisotropies in addition to the superexchange anisotropy prevail over the geometrical frustration and are crucial for the occurrence of the long-range magnetic ordering with the noncollinear sublattice structure. To conclude, both our measurements and our modelling show that building of layered systems from strongly coupled clusters might result in an intriguing sequence of AFM structures driven by the applied magnetic field.

6 Concluding remarks

In conclusion, we have investigated the impact of magnetic frustration on the magnetic ground state of two-dimensional systems of magnetic clusters with triangular geometry possessing lone pair electrons, namely $\text{FeTe}_2\text{O}_5\text{Br}$ and $\text{Ni}_5(\text{TeO}_3)_4\text{Br}_2$ compounds, and explore their magnetic and electric properties. The aim was to see, if Te^{4+} lone pair electrons, which were at first used solely from the synthesis point of view as a tool for forming low-dimensional structures, be as well considered as a coupling bridge between magnetic and electric degrees of freedom, i.e., does the roll of Te^{4+} as a bridging ion in the superexchange pathways between magnetic moments also mean that Te^{4+} lone pair electrons will act as a source of exchange-striction and consequently drive off-centre distortions, manifesting in macroscopic electric polarization.

In line of our research we used the following techniques. Magnetic susceptibility measurements (sections 4.2.1, 4.5.2, and 5.2.1) were employed to obtain bulk magnetic response and general anisotropies of the system. Magnetic torque and magnetization measurements in very high magnetic fields (section 5.3.2) enabled us to study the spin-flop transition. Neutron scattering measurements were essential for the determination of the low-temperature magnetic structure (sections 4.3.1, 5.2.2) and the temperature dependence of the correlation length above the Néel transition (section 4.5.4), where magnetic order is limited to the two dimensions; finally inelastic scattering was used to study spin waves (section 4.6.1). As local probe techniques we used electron (section 4.2.2) and nuclear magnetic resonance (sections 4.3.3 and 4.5.3) measurements to determine the temperature dependence of the spin correlation functions, investigate long-range magnetic ordering, as well as measure spin-gap and magnon spectra (section 5.4). Additionally, muon spin relaxation was measured (section 4.3.2) to probe evolution of short- and long-range ordered phases. Finally, dielectric measurements were employed to trace the electric polarization and track the ferroelectric transition in the applied magnetic field (sections 4.4.3 and 4.5.6). The impact of the electric polarization on the crystal lattice was investigated by precise thermal expansion (4.4.1) and synchrotron x-ray diffraction (section 4.4.2) measurements. The broad aspect of utilized experimental techniques enabled us a comprehensive as well as detailed insight into the investigated systems. In addition, our work has also significant theoretical aspect. This consists of the representation theory used to describe the magnetoelectric coupling mechanism in $\text{FeTe}_2\text{O}_5\text{Br}$ (section 4.4.4) as well as the molecular field model and Kubo-Tomita theory, which were employed to explain the behaviour of the antiferromagnetic resonance in $\text{Ni}_5(\text{TeO}_3)_4\text{Br}_2$ (section 5.5) and thus enabled us to determine the most significant magnetic anisotropies. The extensive summary and conclusion on the investigated systems has already been given in the end of chapters 4 and 5 thus we provide below only a short overview of the main experimental findings and their physical interpretation.

The most prominent result of our investigation is undoubtedly the discovery of the novel magnetoelectric multiferroic state in the $\text{FeTe}_2\text{O}_5\text{Br}$ system (chapter 4). This phase exists below $T_{N2} = 10.6$ K and it is probably provoked by magnetic frustration inducing incommensurate amplitude modulated magnetic structure, with eight different modulation phases. This breaks the inversion symmetry of the crystal structure, and thereby opens the possibility for macroscopic electric polarization. Further we propose that this effect is driven by exchange-striction mechanism involving sliding of the amplitude modulated magnetic waves that induces off-centre distortions of the superexchange bridging Te^{4+} ions, enforcing polarization of Te^{4+} lone pair electrons, which finally manifests as macroscopic electric polarization (section 4.4.4). Moreover, we manage to suppress electric polarization with magnetic field applied along the incommensurate direction of the magnetic order, which indicates that the responsible magnetoelectric coupling mechanism might indeed be applicable in the novel spintronic devices. Additionally, we identified a narrow temperature region, preceding the multiferroic phase, where high-temperature incommensurate magnetic phase exists. Since in this phase no trace of ferroelectricity has been detected, we assume that inversion symmetry of the crystal

lattice is preserved. Finally, we note that strong magnetic frustration and low dimensionality of the $\text{FeTe}_2\text{O}_5\text{Br}$ system manifest also as short range ordering effects, persisting far ($> 5T_N$) above Néel temperature.

On the other hand, the magnetic frustration in the $\text{Ni}_5(\text{TeO}_3)_4\text{Br}_2$ system is found to be less expressed. This is evident already from the lower value of the frustration factor, determined from the ratio between Néel and Curie-Weiss temperatures (section 5.2.1), as well as from the observed magnetic structure (section 5.2.2), which is considerably less complex in comparison to $\text{FeTe}_2\text{O}_5\text{Br}$ system. In fact, magnetic structure preserves the inversion symmetry of the crystal lattice, thus excluding the possibility for macroscopic polarization. The magnetic anisotropies and superexchange interactions determined from fits of field and angular dependences of antiferromagnetic resonance to the molecular field model seem to explain that, as anisotropies were found to be strong, thus favouring long-range magnetic ordering over the geometrical frustration. In addition, when magnetic field was applied perpendicular to the crystal layers, spin-flop like transition was observed at around 10 T. And further, when considering the obtained molecular field parameters, calculations predict another transition at ~ 24 T. The estimated magnetic structure of this phase however breaks the inversion symmetry, and thus open the possibility for ferroelectric order. Again, similar to $\text{FeTe}_2\text{O}_5\text{Br}$, low-dimensional nature of $\text{Ni}_5(\text{TeO}_3)_4\text{Br}_2$ system is evident from short-range ordering effects, which can be noticed up to $\sim 2T_N$.

In the end, magnetic frustration, imposed by low-dimensional triangular spin arrangement, is indeed responsible for reach magnetic phase diagrams observed in these compounds. The resulting magnetic phases are often extremely complex and have typically very low symmetry. This in particular, opens the possibility for intriguing new physical phenomena. Amazingly, following the synthesis of such systems, *p*-element cations with lone pair electrons (e.g., Te^{4+} , Se^{4+} , As^{3+} , and Sb^{3+}) are met. As lone pair electrons are considered to be stereochemically active, they are often assumed to be easily polarisable. Consequently, low-dimensional magnetically frustrated systems involving lone pair electrons introduce a great opportunity for electric polarization and complex magnetic ordering to coexist and possibly allow manipulation of the electric polarization with external magnetic field. This coupling might be further improved by the use of magnetic ions with high spin number, e.g., transition metal ions in high-spin electronic coordination. Hence we propose to look for new magnetoelectrics in the vast family of M-T-O-X compounds ($M = \text{Cu}, \text{Ni}, \text{Fe}$, $X = \text{Cl}, \text{Br}, \text{I}$, $T = \text{Te}, \text{Se}, \text{Sb}, \text{Bi}, \text{Pb}$), as they frequently possess strong magnetic frustration as well as *T* ions with stereochemically active lone-pair electrons.

7 Bibliography

1. *Quantum liquid in antiferromagnetic chains - a stochastic geometric approach to the haldane gap.* **Tasaki, H.** 1991, Phys. Rev. Lett., Vol. 66, p. 798.
2. *Spin-liquid ground-state of the half-filled kondo lattice in one dimension.* **Tsunetsugu, H., Hatsugai, Y. and Sigrist, M.** 1992, Phys. Rev. B, Vol. 46, p. 3175.
3. *Possible high-Tc superconductivity in the Ba-La-Cu-O system.* **Bednorz, J. G. and Müller., K. A.** 1986, Z. Phys. B, Vol. 64, p. 189.
4. *Iron-Based Layered Superconductor: LaOFeP.* **Kamihara, Y., et al.** 2006, J. Am. Chem. Soc., Vol. 128, p. 10012.
5. *Magnetic control of ferroelectric polarization.* **Kimura, T., et al.** 2003, Nature, Vol. 426, pp. 55-58.
6. *Electric polarization and memory in a multiferroic material induced by magnetic fields.* **Hur, N., et al.** 2003, Nature, Vol. 429, pp. 392-395.
7. *Magnetic phase control by an electric field.* **Lottermoser, T., et al.** 2004, Nature, Vol. 430, pp. 541-544.
8. **Mendels, P., et al.** 2007, Phys. Rev. Lett., Vol. 98, p. 077204.
9. **Helton, J. S., et al.** 2007, Phys. Rev. Lett., Vol. 98, p. 107204.
10. **Sachdev, S.** 1992, Phys. Rev. B, Vol. 45, p. 12377.
11. **Shastry, B.S. and Sutherland, B.** 1981, Physica B, Vol. 108, p. 1069.
12. **Zorko, A.** *Study of one- and two-dimensional magnetic systems with spin-singlet ground state - Thesis.* Ljubljana : Univeristy of Ljubljana, 2004.
13. **Ramirez, A. P.** 1994, Annu. Rev. Mater. Sci., Vol. 24, p. 453.
14. **Galy, J., et al.** 1975, J. Solid State Chem., Vol. 13, pp. 142-678.
15. *Crystal Structure and Magnetic Properties of a New Two-Dimensional $S = 1$ Quantum Spin System $Ni_5(TeO_3)_4X_2$ ($X = Cl, Br$).* **Johnsson, M., et al.** Chem. Mater., Vol. 15, pp. 68-73.
16. *Crystal structure and magnetic properties of $FeTe_2O_5X$ ($X = Cl, Br$): A frustrated spin cluster compound with a new Te(IV) coordination polyhedron.* **Becker, R, et al.** 2006, J. Am. Chem. Soc., Vol. 128, pp. 15469–15475.
17. **Johnsson, M., et al.** 2000, Chem. Mater., Vol. 12, p. 2853.
18. **Mayerova, Z., Johnsson, M. and Lidin, S.** 2005, J. Solid State Chem., Vol. 178, p. 3471.
19. **Takagi, R., et al.** 2006, Phys. Rev. B, Vol. 74, p. 014413.
20. *Visualizing the Role of Bi 6s “Lone Pairs” in the Off-Center Distortion in Ferromagnetic BiMnO₃.* **Seshadri, R. and Hill, N. A.** 2001, Chem. Mater., Vol. 13, p. 2892.
21. *Why are there so few magnetoelectric materials?* **Hill, N. A.** 2000, J. Phys. Chem. B, Vol. 104, pp. 6694-6709.

22. *Revival of the magnetoelectric effect.* **Fiebig, M.** 2005, J. Phys. D: Appl. Phys., Vol. 38, pp. R123-R152.
23. *Multiferroics: Different ways to combine magnetism and ferroelectricity.* **Khomskii, D. I.** 2006, J. Magn. Mater., Vol. 306, pp. 1-8.
24. *Multiferroic and magnetoelectric materials.* **Eerenstein, W., Mathur, N. D. and Scott, J. F.** 2006, Nature, Vol. 442, pp. 759-765.
25. *Multiferroics: a magnetic twist for ferroelectricity.* **Cheong, S. W. and Mostovoy, M.** 2007, Nature Mater., Vol. 6, pp. 13-20.
26. *Possible applications for magnetoelectric materials.* **Wood, V. E. and Austin, A. E.** 1973, Int., J. Magn., Vol. 5, pp. 303-315.
27. *Introduction to the proceedings of the 2nd international conference on magnetoelectric interaction phenomena in crystals, MEIPIC-2.* **Schmid, H.** 1994, Ferroelectrics, Vol. 161, pp. 1-28.
28. *Magnetoelectric phase control in a magnetic system showing cycloidal/conical spin order.* **Kimura, T. and Tokura, Y.** 2008, J. Phys.: Condens. Matter, Vol. 20, p. 434204.
29. *Ferroelectricity and giant magnetocapacitance in perovskite rare-earth Manganites.* **Goto, T., et al.** 2004, Phys. Rev. Lett., Vol. 92, p. 257201.
30. *Magnetically driven ferroelectric order in Ni₃V₂O₈.* **Lawes, G., et al.** 2005, Phys. Rev. Lett., Vol. 95, p. 087205.
31. *Crystal structure and magnetic properties of the new cobalt tellurite halide Co₅(TeO₃)₄X₂ (X = Cl, Br).* **Becker, R., et al.** 2007, Vol. 9, p. 223.
32. *Spin Amplitude Modulation Driven Magnetoelectric Coupling in the New Multiferroic FeTe₂O₅Br.* **Pregelj, M., et al.** 2009, Phys. Rev. Lett., Vol. 103, p. 147202.
33. *Magnetoelectric response to the applied magnetic field in FeTe₂O₅Br.* **Pregelj, M., et al.** 2010, in preparation.
34. **Fowler, M.** *Historical Beginnings of Theories of Electricity and Magnetism.* 1997.
35. *Origine de la Boussole 11. Aimant et Boussole.* **Shu-hua, Li.** 2, 1954, Isis, Vol. 45, p. 175.
36. *Zur Elektrodynamik bewegter Koerper.* **Einstein, A.** 1905, Annalen der Physik, Vol. 17, p. 891.
37. **Blundell, S.** *Magnetism in Condensed Matter.* New York : Oxford University Press, 2001.
38. **Slichter, C. P.** *Principles of Magnetic Resonance, 3rd Enlarged and Updated Edition.* Berlin : Springer-Verlag, 1990.
39. **Low, W.** *Paramagnetic Resonance in Solids, in Solid State Physics, Supplement 2.* [ed.] F. Seitz and D. Turnbull. New York : Academic Press, 1960. p. 8.
40. **Yosida, K.** *Theory of Magnetism.* Berlin : Springer-Verlag, 1996.
41. **Bencini, A. and Gatteschi, D.** *EPR of Exchange Coupled Systems.* Berlin Heidelberg : Springer-Verlag, 1990.

42. **Anderson, P. W.** 1959, Phys. Rev., Vol. 115, p. 2.
43. **Goodenough, J. B.** 1955, Phys. Rev., Vol. 100, p. 564.
44. **Kanamori, J.** 1959, J. Phys. Chem. Solids, Vol. 10, p. 87.
45. **Pilbrow, J. R.** *Transition ion electron paramagnetic resonance.* Oxford : Clarendon Press, 1990.
46. *A thermodynamic theory of "weak" ferromagnetism of antiferromagnetic.* **Dzyaloshinsky, I.** 1958, J. Phys. Chem. Solids, Vol. 4, p. 241.
47. *Anisotropic superexchange interaction and weak ferromagnetism.* **Moriya, T.** 1960, Phys. Rev., Vol. 120, p. 91.
48. *Moriya Interaction and the Problem of the Spin Arrangements in βMnS .* **Keffer, F.** 1962, Phys. Rev., Vol. 126, p. 896.
49. *Magnetic Inversion Symmetry Breaking and Ferroelectricity in TbMnO_3 .* **Kenzelmann, M., et al.** Phys. Rev. Lett., Vol. 95, p. 087206.
50. *The magnetic structures of the rare-earth manganates ErMn_2O_5 and TbMn_2O_5 .* **Gardner, P. P., et al.** J. Phys. C: Solid State Phys., Vol. 21, p. 5653.
51. *Amplitude-modulated spin structure in Er_5Sn_3 above 10 K.* **Semitelou, I. P. and Yakinthos, J. K.** J. Alloys Comp., Vol. 299, p. 55.
52. *Theory of the frustration effect in spin glasses: I.* **Toulouse, G.** 1977, Commun. Phys., Vol. 2, p. 115.
53. *Multi-Sublattice Magnetic Structure of KCuF_3 Caused by the Antisymmetric Exchange Interaction: Antiferromagnetic Resonance Measurements.* **Yamada, I. and Kato, N.** 1994 : s.n., J. Phys. Soc. Jpn., Vol. 63, p. 289.
54. *Resonance and high frequency susceptibility in canted antiferromagnetic substances.* **Herrmann, G.F.** 1963, J. Phys. Chem. Solids, Vol. 24, p. 597.
55. *Antiferromagnetism.* **Nagamiya, T., Yoshida, K. and Kubo, R.** 1955, Advances in Physics, Vol. 4, p. 1.
56. *Spin resonance in the ordered magnetic state of $\text{Ni}_5(\text{TeO}_3)_4\text{Cl}_2$.* **Mihály, L., et al.** 2006, Phys. Rev B, Vol. 74, p. 174403.
57. *The Renaissance of Magnetoelectric Multiferroics.* **Spaldin, N. A. and Fiebig, M.** 2005, Science, Vol. 309, p. 391.
58. **Mostovoy, M.** 2006, Phys. Rev. Lett., Vol. 96, p. 067601.
59. **Betouras, J. J. and al., et.** 2007, Phys. Rev. Lett., Vol. 98, p. 257602.
60. *Direct Transition from a Disordered to a Multiferroic Phase on a Triangular Lattice.* **Kenzelmann, M. and al., et.** 2007, Phys. Rev. Lett., Vol. 98, p. 267205.
61. **Lines, M. E. and Glass, A. M.** *Principles and Applications of Ferroelectrics and Related Materials.* Oxford : Clarendon Press, 1977.

62. *Spin current and magnetoelectric effect in noncollinear magnets.* **Katsura, H., Nagaosa, N. and Balatsky, A.V.** 2005, Phys. Rev. Lett., Vol. 95, p. 057205.
63. *Role of the Dzyaloshinskii-Moriya interaction in multiferroic perovskites.* **Sergienko, I. A. and Dagotto, E.** 2006, Phys. Rev. B, Vol. 73, p. 094434.
64. *Towards a microscopic model of magnetoelectric interactions in Ni₃V₂O₈.* **Harris, A. B., et al.** 2006, Phys. Rev. B, Vol. 73, p. 184433.
65. *Structural Anomalies and Multiferroic Behavior in Magnetically Frustrated TbMn₂O₅.* **Chapon, L. C., et al.** 2004, Phys. Rev. Lett., Vol. 93, p. 177402.
66. *Field-induced linear magnetoelastic coupling in multiferroic TbMnO₃.* **Aliouane, N., et al.** 2006, Phys. Rev. B, Vol. 73, p. 020102(R).
67. *Ferroelectricity in the Magnetic E-Phase of Orthorhombic Perovskites.* **Sergienko, I. A., Şen, C. and Dagotto, E.** 2006, Phys. Rev. Lett., Vol. 97, p. 227204.
68. **Kubo, R. and Tomita, K.** 1954, J. Phys. Soc. Jpn., Vol. 9, p. 888.
69. *Magnetic interactions in α -NaMnO₂: Quantum spin-2 system on a spatially anisotropic two-dimensional triangular lattice.* **Zorko, A., et al.** 2008, Phys. Rev. B, Vol. 77, p. 024412.
70. *Influence of non-diagonal dynamic susceptibility on the EPR signal of Heisenberg magnets.* **Benner, H., et al.** 1983, J. Phys. C, Vol. 16, p. 6011.
71. **Barnes, S. E.** 1981, Adv. Phys., Vol. 30, p. 801.
72. **Richard, P. M.** *Magnetic Resonance in One- and Two-Dimensional Systems, in Local Properties of Low-Dimensional Antiferromagnets.* [ed.] K. A. Müller. Amsterdam : Nord Holland Publishing Company, 1976. p. 539.
73. **Abragam, A.** *Principles of Nuclear Magnetism.* Oxford : Oxford University Press, 1961.
74. **Portis, A. M. and Lindquist, R. H.** *Magnetism.* [ed.] G. T. Rado and H. Suhl. New York : Academic Press, 1965. p. 357. Vol. 2A.
75. **Jaccarino, V.** *Magnetism.* [ed.] G. T. Rado and H. Suhl. New York : Academic Press, 1965. p. 307. Vol. 2A.
76. **Freeman, A. J. and Watson, R. E.** *Magnetism Vol. II.* [ed.] G. T. Rado and H. Suhl. New York : Academic Press, 1965. p. 167. Vol. 2A.
77. *Nuclear magnetic resonance in paramagnetic MnF₂.* **Shulman, R. G. and Jaccarino, V.** 1957, Phys. Rev., Vol. 108, p. 1219.
78. *Nuclear magnetic resonance in antiferromagnets.* **Moriya, T.** 1956, Prog. Theor. Phys., Vol. 16, p. 23.
79. **Heller, P.** *NMR and Neutron Scattering Studies Near Phase Transitions in Uniaxial Antiferromagnets, in Local Properties of Low-Dimensional Antiferromagnets.* [ed.] K. A. Müller. Amsterdam : Nord Holland Publishing Company, 1976, p. 445.
80. **Carlin, R. L.** *Magnetochemistry.* Berlin : Springer-Verlag, 1986. p. 41.

81. *Temperature and photo-induced phase transition in rubidium manganese hexacyanoferrate*. **Ohkoshi, S., Tokoro, H. and Hashimoto, K.** 2005, *Coord. Chem. Rev.*, Vol. 249, p. 1830.
82. *Electron, spin-wave, hyperfine, and phonon contributions to the low-temperature specific heat of $\text{La}_{0.65}\text{Ca}_{0.35}\text{MnO}_3$: Effects of magnetic fields and 16O/18O exchange*. **Fisher, R. A., et al.** 2001, *Phys. Rev. B*, Vol. 64, p. 134425.
83. *Scaling laws for dynamic critical phenomena*. **Halperin, B. I. and Hohenberg, P. C.** 1969, *Phys. Rev.*, Vol. 177, p. 952.
84. *Solid State Physics*. **Ashcroft, N. W. and Mermin, N. D.** s.l. : Cornell University, Orlando, 1976.
85. **Weinstock, H.** *SQUID sensors: fundamentals, fabrication, and applications*. Dordrecht, Netherlands : KluwerAcademic Publishers, 1996.
86. SQUID Magnetometer. *HyperPhysics*. [Online] Department of Physics and Astronomy, Georgia State University, 2005. <http://hyperphysics.phy-astr.gsu.edu/Hbase/hframe.html>.
87. *Small sample magnetometers for simultaneous magnetic and resistive measurements at low temperatures and high magnetic fields*. **Brooks, J. S., et al.** 1987, *Rev. Sci. Instrum.*, Vol. 58, p. 117.
88. *Cantilever magnetometry in pulsed magnetic fields*. **Naughton, M. J., et al.** 1997, Vol. 68, p. 4061.
89. *Active microlevers as miniature torque magnetometers*. **Rossel, C., et al.** 1996, Vol. 79, p. 8166.
90. **Squires, G. L.** *Introduction to the Theory of Thermal Neutron Scattering*. Mineola, New York : Dover Publications Inc, 1996.
91. The Cambridge Crystallographic Subroutine Library. [Online] <http://www.ill.eu/sites/ccsl/html/ccsl/doc.html>.
92. **Shirane, G., Shapiro, S. M. and Tranquada, J. M.** *Neutron scattering with a triple-axis spectrometer: basic techniques*. Cambridge : Cambridge University Press, 2002.
93. **Freeman, A. J.** 1959, *Acta. Cryst.*, Vol. 12, p. 261.
94. *Neutron-scattering study of antiferromagnetism in $\text{YBa}_2\text{Cu}_3\text{O}_{6.15}$* . **Shamoto, S., et al.** 1993, Vol. 48, p. 13817.
95. **Izyumov, Y.A. and Maleyev, S.** 1962, *Sov. Phys. JETP*, Vol. 14, p. 1668.
96. *Polarization Effects in the Magnetic Elastic Scattering of Slow Neutrons*. **Blume, M.** 1963, *Phys. Rev.*, Vol. 130, p. 1670.
97. *Spherical neutron polarimetry with MuPAD*. **Janoschek, M., et al.** 2007, *Physica B*, Vol. 397, p. 125.
98. *Inelastic neutron polarization analysis in low-dimensional systems*. **Regnault, L. P., et al.** 2004, *Physica B*, Vol. 345, p. 111.
99. SINQ. *Paul Scherrer Institut*. [Online] <http://sinq.web.psi.ch/>.
100. **Schenck, A.** *Muon Spin Rotation Spectroscopy: Principles and Applications in Solid State Physics*. Bristol and Boston : Adam Hilger Ltd, 1985.

101. **Science, Muons.** [ed.] S. L. Lee, S. H. Kilcoyne and R. Cywinski. Bristol : Institut of Physics Publishing, 1999.
102. **Schenck, A. and Gygax, F. N.** *Handbook of Magnetic Materials.* [ed.] K. H. J. Buschow. Amsterdam : North-Holland, 1995. p. 60. Vol. 9.
103. *Heavy-fermion systems studied by μ SR technique.* **Amato, A.** 1997, Rev. Mod. Phys., Vol. 69, p. 1119.
104. **Kubo, R. and Toyabe, T.** *Magnetic Resonance and Relaxation* . Amsterdam : North-Holland, 1967. p. 810.
105. **Dalmas de Reotier, P. and Yaouanc, A.** 1992, J. Phys.: Condens. Matter, Vol. 4, p. 4533.
106. **Debye, P.** *Polar Molecules.* New York : Dover Publications, 1929.
107. *Electric field induced critical points and polarization rotations in relaxor ferroelectrics.* **Kutnjak, Z. and Blinc, R.** 2007, Phys. Rev. B, Vol. 76, p. 104102.
108. *The giant electromechanical response in ferroelectric relaxors as a critical phenomenon* . **Kutnjak, Z., Petzelt, J. and Blinc, R.** 2006, Nature, Vol. 441, pp. 956-959.
109. **Selwood, P.W.** *Magnetochemistry.* New York : Interscience Publishers, 1943.
110. **Ramirez, A. P.** 1991, J. Appl. Phys., Vol. 70, p. 5952.
111. *Linear magnetic chains with anisotropic coupling.* **Bonner, J. C. and E., Fisher M.** 1964, Vol. 135, p. a640.
112. **Van Velck, J. H.** *The Theory of Electric and Magnetic Susceptibilities.* Oxford : University Press, 1932.
113. *Electron spin resonance lineshifts in paramagnetic copper-amino acid complexes.* **Calvo, R. and Passeggi, M.C. G.** 2000, J. Phys.: Condens. Matter, Vol. 2, p. 9113.
114. *Electron spin resonance studies of the onset of the magnetic order in intermetallic compounds.* **Taylor, R. H. and Coles, B. R.** 1975, J. Phys. F: Metal Phys., Vol. 5, p. 121.
115. *Dependence of elastic properties and ultrasonic velocities on the structure of vanadate lead tellurite glasses.* **Palanivelu, N. and Rajendran, V.** 2006, Phys. Stat. Sol. A, Vol. 203, p. 2347.
116. *Tellurite glasses Part 2. Anelastic, phase separation, Debye temperature and thermal properties.* **El-Mallawany, R.** 1999, Mater. Chem. Phys., Vol. 60, p. 103.
117. **Maleev, S. V., Bar'yaktar and Suris.** 1963, Sov. Phys. - Solid State, Vol. 4, p. 2533.
118. *Polarised neutrons and complex antiferromagnets: an overview.* **Brown, P.J.** 2001, Physica B, Vol. 297, p. 198.
119. **Brown, P. J. and Matthewman, J. C.** 2008, CCSL, p. 1897.
120. *FeTe₂O₅Br system: New ferroelectric with an incommensurate spin modulation.* **Zaharko, O., et al.** 2010, J. Phys.: Conf. Ser., Vol. 211, p. 012002.
121. *Muon spin relaxation study of the layered magnetoelectric FeTe₂O₅Br with spin amplitude modulated magnetic structure.* **Zorko, A., et al.** 2010, J. App. Phys., Vol. 107, p. 09D906.

122. **Lee, S. L., Kilcoyne, S. H. and Cywinski, R., [ed.]**. *Muon Science: Muons in Physics, Chemistry, and Materials*. Abingdon : Taylor & Francis Group, 1999.
123. *Commensurability and Defect-Induced Phason Gap in Incommensurate Systems*. **Blinic, R., et al.** 1985, Phys. Rev. Lett., Vol. 54, p. 79.
124. **Sheldrick, G. M.** *computer program SHELXL97*. University of Goettingen. Goettingen, Germany : s.n., 1997.
125. *Magnetoelectric phenomena in BaMnF₄ and BaMn_{0.99}Co_{0.01}F₄*. **Fox, D. L., Tilley, D. R. and Scott, J. F.** 1980, Phys. Rev. B, Vol. 21, pp. 2926-2936.
126. **Yasui, Y. and al., et.** 2008, J. Phys. Soc. Jpn., Vol. 77, p. 023712.
127. *NMR Imaging of the Soliton Lattice Profile in the Spin-Peierls Compound CuGeO₃*. **Horvatić, M., et al.** 1999, Phys. Rev. Lett., Vol. 83, pp. 420-423.
128. *Magnetization and universal sub-critical behaviour in two-dimensional XY magnets*. **Bramwell, S. T. and Holdsworth, P. C. W.** 1993, J. Phys. Condens. Matter, Vol. 5, p. L53.
129. **Chaikin, P. M. and Lubensky, T. C.** *Principles of condensed matter physics*. Cambridge : Cambridge University Press, 1995.
130. *Anomalous Magnetic Excitations of Cooperative Tetrahedral Spin Clusters*. **Prša, K., et al.** 2009, Vol. 102, p. 177202.
131. *Magnetic structure of the S=1 Ni₅(TeO₃)₄Br₂ layered system governed by magnetic anisotropy*. **Pregelj, M., et al.** 2007, Phys. Rev. B, Vol. 76, p. 144408.
132. *Temperature dependence of antiferromagnetic resonance mode in two-dimensional system Ni₅(TeO₃)₄Br₂*. **Pregelj, M., et al.** 2008, Physica B, Vol. 403, p. 950.
133. *Magnetic phase diagram of the two-dimensional antiferromagnet Ni₅(TeO₃)₄Br₂*. **Pregelj, M, et al.** 2009, Phys. Rev. B, Vol. 79, p. 064407.
134. *High-field ESR in a two-dimensional S = 1 spin system Ni₅(TeO₃)₄Br₂*. **Arčon, D., et al.** 2007, J. Magn. Magn. Mater., Vol. 316, p. E349.
135. **Zorko, A., et al.** 2006, J. Phys.: Condens. Matter , Vol. 19, p. 145278.
136. **Rodriquez-Carvajal, J.** 1993, Physica B, Vol. 192, p. 55.
137. **Kawamura, H.** 1998, J. Phys.: Condens. Matter, Vol. 10, p. 4707.
138. **Tarasenko, R., et al.** 2008, Acta Phys. Pol. A, Vol. 113, p. 481.
139. **Choi, M., et al.** 1991, Phys. Rev. B, Vol. 44, p. 9319.
140. **Cooper, B. R.** London : s.n., 1962, Proc. Phys. Soc., Vol. 80, p. 1225.
141. *Antiferromagnetic-Resonance Linewidths in MnF₂*. **Kotthaus, J.P. and Jaccarino, V.** 1972, Phys. Rev. Lett., Vol. 28, p. 1649.

142. *AFMR linewidth of two-dimensional antiferromagnets*. **Rezende, S.M. and Žekš, B.** 1975, Phys. Lett. A, Vol. 54, p. 135.
143. *Single-ion anisotropy of localized-electron compounds*. **Alders, D., Coehoorn, R. and de Jonge, W. J. M.** 2001, Vol. 63, p. 054407.
144. *Magnetism of a novel tetranuclear nickel(II) cluster in strong magnetic fields*. **Kataev, V., et al.** 2006, Vol. 51, p. 351.
145. *Magnetic studies of the $S = 1$ Heisenberg chain $[Ni(Prixa)_2(pyr)]_n$* . **Orendáová, A., et al.** 2003, Vol. 196, p. 278.
146. *LIGFIELD*. **Bendix, J.** s.l. : Department of Chemistry, University of Copenhagen, Denmark.
147. **Kaplan, S. G., et al.** 1993, Phys. Rev. B, Vol. 47, p. 5300.
148. *A method of controlling the sense of the screw spin structure*. **Siratori, K., et al.** 1980, J. Phys. Soc. Jpn., Vol. 48, p. 1111.
149. *Frequency dependence of magnetoelectric phenomena in $BaMnF_4$* . **Tilley, D. R. and Scott, J. F.** 1982, Phys. Rev. B, Vol. 25, pp. 3251-3260.
150. **Hayano, R. S., et al.** 1979, Phys. Rev. B, Vol. 20, p. 850.
151. *Antiferromagnetic resonance in MnF_2 over wide ranges of frequency and magnetic field*. **Hagiwara, M., et al.** J. Phys.: Condens. Matter, Vol. 8, p. 7349.
152. *Paramagnetic resonance line width in antiferromagnets*. **Mori, H.** 1963, Prog. Theor. Phys., Vol. 30, p. 57.
153. *Critical-point anomalies in the electron-paramagnetic resonance linewidth and in the zero-field relaxation time of antiferromagnets*. **Huber, D. L.** 1972, Phys. Rev. B, Vol. 6, p. 3180.
154. *The origin of ferroelectricity in magnetoelectric $YMnO_3$* . **Van Aken, B. B., et al.** 2004, Nature Materials, Vol. 3, p. 164.

8 Extended abstract in Slovene (Razširjen prevod v slovenščini)

8.1 Uvod

Zanimanje za nizkodimenzionalne spinske sisteme je v zadnjih nekaj desetletjih močno naraslo, saj le-ti pogosto kažejo nova nenavadna magnetna stanja, ki vodijo do novih zanimivih magnetnih pojavov, npr. spinske-tekoče faze v Haldanovih verigah (1), (2). Takšno obnašanje je še bolj izrazito v primeru, ko si spinsko-spinske interakcije nasprotujejo oz. tekmujejo za prevlado, saj to privede do tako-imenovane magnetne frustracije. Za to pa velja splošno prepričanje, da je močno povezana z magnetnimi lastnostmi v plastovitih visokotemperaturnih superprevodnikih (kuprati (3) in oksipniktidi (4)), z močno magneto-električno sklopitvijo v multiferroikih (5), (6), (7), kot tudi izjemno degeneracijo osnovnih stanj v sistemih s spini urejenimi v Kagomé (8), (9), (10), Shastry-Sutherland (11), (12) in še nekaterih drugih trikotnih vzorcih. Za vse te sisteme je značilno, da zaradi njihove posebne razporeditve magnetnih momentov - večinoma trikotne - ali zaradi nasprotujočih si magnetnih interakcij, vse izmenjalne interakcije v sistemu ne morejo biti zadoščene hkrati (13). Posledična magnetna frustracija lahko pripelje do močne degeneracije osnovnega stanja in s tem ojači vlogo kvantnih fluktuacij. Po drugi strani pa so ti sistemi zelo občutljivi na motnje, na primer, magnetne anizotropije tipa Dzyaloshinski-Moriya ali antisimetrične izmenjalne interakcije, ki lahko odpravijo degeneracijo, odprejo vrzel v spektru ekscitacij, zatrejo kvantne fluktuacije, in stabilizirajo magnetni red dolgega dosega. Posledično so realni frustrirani nizkodimenzionalni magnetni sistemi ponavadi zelo zapleteni in imajo zanimive magnetne lastnosti, ki lahko pomembno pripomorejo k nadaljnjemu tehnološkemu napredku. Po drugi strani, pa veliko opaženih pojavov še ni popolnoma razumljenih tako, da teče intenzivno iskanje novih modelnih sistemov, ki bi omogočili test obstoječih teorij.

Do nedavnega je bila večina realnih magnetno frustriranih sistemov odkrita na osnovi njihove topologije, določene iz strukturnih podatkovnih baz. Z drugimi besedami, znanstveniki so med že obstoječimi sistemi iskali tiste, v katerih bi lahko pričakovali geometrijsko frustracijo. Po drugi strani pa so bili poskusi sistematičnega načrtovanja novih frustriranih sistemov z novimi sintezni postopki presenetljivo redki. Premik se je zgodil v zadnjih nekaj letih, saj se je razvilo več novih sinteznih pristopov za izdelavo novih frustriranih magnetnih anorganskih spojin. Ena od sinteznih strategij, ki se je izkazala za zelo uspešno, je uporaba kationov z neveznim elektronskim parom. Za nevezni elektronski par so že Galy in ostali pokazali, da je njegova efektivna prostornina približno enaka prostornini O^{2-} iona (14). Posledica tega pa je, da se lahko ti elementi, če so zmešani s prehodnimi kovinam v prisotnosti halogenih ionov, obnašajo kot tako-imenovane "kemične škarje" (15), ki zmanjšajo število izmenjalnih poti med magnetnimi ioni in posledično oblikujejo nizkodimenzionalne magnetne strukture.

Dejanski sintezi koncept (16) temelji na pripravi oksohalidnih spojin, ki vključujejo katione v takem oksidacijskem stanju, kjer imajo stereo-kemično aktiven nevezni elektronski para (npr. Te^{4+} , Se^{4+} , As^{3+} , in Sb^{3+}). Prisotnost stereo-kemično aktivnega neveznega elektronskega para omogoča asimetrično ali enostransko koordinacijo dotičnega kationa. Poleg tega, tako močna Lewisova kislina (npr. Te^{4+}) v večini tvori vezi samo s kisikom, medtem ko se kationi prehodnih kovin v oksohalidnem okolju vežejo tako s kisikom kot halogenimi elementi. Kot rezultat, stereo-kemično aktivni nevezni elektronski pari v navezi z halogenimi ioni zmanjšujejo število vezi kar pripelje do bolj odprte strukture in povečanja možnosti za nizkodimenzionalno konfiguracijo. Ta sintezni koncept je bil uspešno uporabljen pri odkritju več podobnih spojin, npr. $Cu_2Te_2O_5X_2$ ($X = Cl, Br$) (17), $CuSb_2O_3Br$ (18), in $Cu_4Te_5O_{12}Cl_4$ (19).

Zelo zanimivo je tudi dejstvo, da so v ferroelektričnih materialih, npr. Bi^{3+} v $BiMnO_3$ (20), nevezni elektronski pari prepoznani kot nosilci električne polarizacije. Razlaga temelji na tem, da je nevezne elektronske pare zaradi stereo-kemične aktivnosti lahko polarizirati, to pa jih postavlja v vlogo gonilne sile za izven-centrične

strukturne spremembe, ki so bistvenega pomena za nastanek električne polarizacije v teh materialih. Tako se nevezni elektronski pari zdijo zelo primerni zato, da vzbudijo pojav magnetne frustracije in električne polarizacije hkrati, kar pa bi lahko pripeljalo do sklopitve med magnetnim in električnim redom.

Praktična realizacija soobstoja magnetne in feroelektrične ureditve je bila odkrita v tako-imenovanih multiferroičnih materialih (21), (22), (23), (24), (25). V primeru, ko je magneto-električne sklopitve močna, se da električno polarizacijo obračati z zunanjim magnetnim poljem (5), (6), in obratno, lahko se kontrolira magnetno ureditev z zunanjim električnim poljem (7). To pa obeta veliko za razvoj novih naprav iz področja spintronike in shranjevanja podatkov (26), (27). Tako obnašanje je bilo tipično opaženo v kompliciranih magnetnih ureditvah z zlomljeno simetrijo inverzije. To je v sistemih, kjer se električna polarizacija razvije simultano z inkomenzurabilnim magnetnim redom (28). Splošno prepričanje je, da je spiralni magnetni red ključen za pojav nelinearnega magneto-električnega pojava v perovskitnih manganitih $RMnO_3$ (29) (*R*-element iz skupine redkih zemelj) in $Ni_3V_2O_8$ (30), saj odstrani center inverzije in s tem omogoči feroelektrinčno ureditev. Klub temu pa so bili v dosedanjem obsežnem iskanju novih magneto-električnih multiferroikov nevezni elektronski pari tipično obravnavani zgolj kot izvor električne polarizacije; in ne kot sredstvo za sintezo nizkodimenzionalnih frustriranih magnetnih konfiguracij, pomembnih za vzpostavitev zapletene magnetne ureditve z zlomljeno simetrijo inverzije. Magnetno frustrirani materiali, ki vsebujejo nevezne elektronske pare, zato predstavljajo skoraj povsem neraziskano področje v raziskavah magneto-električne sklopitve.

Glavna vprašanja, ki predstavljajo motiv za delo predstavljeno v tej disertaciji, so torej: (i) kakšen je vpliv magnetne frustracije na osnovno magnetno stanje dvodimenzionalnih sistemov magnetnih skupkov s trikotnimi geometrijo, (ii) kakšne so njihove magnetne in električne lastnosti, in (iii) kako se različne prostorske stopnje, kot so spin, naboj, orbitalna ureditev, sklapljajo in urejajo v nizkodimenzionalnih magnetnih ureditvah s frustrirano strukturo. Poleg tega, smo bili med našimi raziskavami pozorni tudi na zanimive fizikalne pojave, ki bi bili lahko nekoč uporabni za široko uporabo. Predvsem smo se posvetili sistemom, ki vsebujejo katione v takem oksidacijskem stanju, kjer imajo stereo-kemično aktiven nevezni elektronski par, zlasti Te^{4+} . Prisotnost neveznega elektronskega para se odraža v zmanjšanem številu izmenjalnih poti med magnetnimi ioni, kar privede do tako-imenovane nizkodimenzionalne kristalne strukture. Poleg tega se nadejamo, da bo prisotnost neveznih elektronskih parov spodbudila težnjo preiskovanih sistemov k tvorbi izven-centričnih kristalnih sprememb, ki bi lahko privedle do vzpostavitve makroskopske električne polarizacije.

Natančneje, cilj tega dela je raziskati vpliv neveznega elektronskega para, pripadajočega Te^{4+} , v pred kratkim sintetiziranih sistemih $FeTe_2O_5Br$ (16) in $Ni_5(TeO_3)_4Br_2$ (15). Ta dva sistema sta bila narejena po zgoraj predstavljenem sinteznem konceptu, ki uporablja nevezni elektronski par kot tako imenovane "kemične škarje". Oba sistema imata plastovito monoklinsko struktura zgrajeno iz magnetnih skupkov. V prvem primeru, so Fe^{3+} ($S = 5/2$) ioni povezani preko kisikovih mostov v geometrijsko frustriran $[Fe_4O_{16}]$ skupek. V drugem primeru pa, so osnovni gradniki $[Ni_5O_{17}Br_2]$ enote, kjer so magnetni ioni Ni^{2+} ($S = 1$). V obeh primerih so skupki sestavljeni iz trikotno razporejenih magnetnih ionov, medtem ko so super-izmenjalne interakcije antiferromagnetne (16), (15). Pričakovati je torej magnetno urejanje na več nivojih: znotraj skupkov, znotraj plasti, in na koncu vzpostavitev tridimenzionalne magnetne ureditve pod 11 K za $FeTe_2O_5Br$ (16) in pod 29 K za $Ni_5(TeO_3)_4Br_2$ (15). Ne-nazadnje je vredno omeniti še to, da v $FeTe_2O_5Br$ sistemu vse super izmenjalne interakcije vključujejo Te^{4+} katione z neveznim elektronskim parom, in na ta način tvorijo potencialni most med magnetno in električno prostorsko stopnjo.

8.2 FeTe₂O₅Br sistem

FeTe₂O₅Br sistem je bil prvič sintetiziran leta 2006 (16). Ima plastovito strukturo in monoklinsko osnovno celico (glej Table 2) z izračunano gostoto 5.213 g/cm³. Plasti rastejo pravokotno na os a^* , med seboj pa jih vežejo šibke Van der Waalove vezi, kar namiguje na zelo šibko sklopitev med njimi (Figure 30). Izmed vrst ionov, ki sestavljajo kristalno strukturo FeTe₂O₅Br sistema, gre izpostaviti dve. Prvič, Te⁴⁺ (5s²5p⁰) katione s stereo-kemično aktivnimi neveznimi elektronskimi pari, ki kot že omenjeno, v kombinaciji z ioni prehodnih kovin tvorijo nizko dimenzionalno strukturo. Vrhu tega pa so nevezni elektronski pari lahko nosilci električne polarizacije. Druga pomembna vrsta ionov so Fe³⁺ (3d⁵) kationi, s spinskim kvantnim številom $S = 5/2$, saj so odgovorni za magnetne lastnosti FeTe₂O₅Br sistema. Natančen pogled pokaže, da sta v kristalni strukturi dve kristalografsko različni Fe mesti – Fe1 in Fe2, ki pa imata obe oktaedersko [FeO₆] koordinacijo. Štiri taka mesta so preko skupnih kisikov izmenično povezana v [Fe₄O₁₆]²⁰⁻ tetramer, ki je podoben rombu z eno diagonalo tako, da štiri možne izmenjalne poti potekajo po obodu (J_1), ena pa veže dva nasprotna si Fe1 (J_2) iona (Figure 31). Ker so si vsi Fe-O-Fe koti precej podobni (Table 3), so si najverjetneje podobne tudi izmenjalne interakcije. S strukturnega stališča so Te⁴⁺ ioni pomembni zato, ker tvorijo edini most med železovimi skupki, ki tvorijo trikotno ureditev znotraj plasti. Ker vse interakcije med Fe skupki potekajo preko Te⁴⁺ ionov, lahko pričakujemo močno sklopitev med magnetno izmenjalno interakcijo in polarizacijo neveznih Te⁴⁺ elektronskih parov.

S stališča jedrske magnetne in kvadrupolne resonance (odnosno NMR in NQR), kjer smo opazovali resonanco ^{81,79}Br jeder je zanimiva še lokalna okolica le-teh. Tudi v tem primeru imamo dve kristalografsko različni mesti – Br1 in Br2. Primerjava oddaljenosti njihovih najbližjih sosedov (Te) z osnovno Te-Br vezavno razdaljo kaže, da je Br1 najverjetneje povezan le z Te2, preko katerega posredno čuti tudi samo en Fe1 moment. Po drugi strani, pa je Br2 verjetno povezan z Te4 in Te2, kar ga sklaplja z vsaj tremi železi – Fe2 in dvema Fe1, zaradi česar pričakujemo, da bosta NQR in NMR signala nosila veliko informacije o obnašanju Fe momentov.

8.2.1 Magnetne lastnosti paramagnetne faze

Izrazito nizka magnetna dimenzionalnost sistema nakazuje možnost zanimivih magnetnih lastnosti. To nas je spodbudilo k obsežnim raziskavam, pri katerih smo uporabili vrsto različnih eksperimentalnih tehnik kot so meritve magnetne susceptibilnosti s SQUID-om, elektronske spinske resonance (ESR), muonske spinske relaksacije, termičnega raztezka, uklon rentgenskega sevanja, dielektrične susceptibilnosti, ^{81,79}Br jedrske magnetne in kvadrupolne resonance, elastičnega in neelastičnega nevtronskega sipanja.

Magnetno susceptibilnost lahko med sobno temperaturo in ~100 K lepo opišemo s Curie-Weissovom zakonom (Figure 32, enačba 4.1), če upoštevamo diamagnetni prispevek izračunan na osnovi Pascalovih konstant (Table 4). Ocenjena Curie-Weissova temperatura, $\theta_{CW} = -125$ (20) K, kaže na relativno močne antiferromagnetne izmenjalne interakcije. Z nižanjem temperature opazim počasen odklon od Curie-Weissovega obnašanja, pri ~50 K pa se pojavi širok maksimum (Figure 32), ki je tipičen za nizkodimenzionalne magnetne sisteme, saj gre za odraz razvoja magnetnih korelacij kratkega dosega (npr. znotraj plasti). Pri nadaljnjem ohlajanju, se susceptibilnost zmanjšuje vse do $T_N = 10.6$ K, kjer pride do jasne spremembe, ki odgovarja magnetnemu prehodu. Pod T_N postane izrazitejša tudi anizotropija sistema, saj susceptibilnost vzdolž b osi rahlo naraste, medtem ko v preostalih dveh smereh še bolj izrazito pade. Primerjava Néelove temperature z Curie-Weissovo temperaturo, tako imenovani faktor frustracije $f = |\theta_{CW}|/T_N \sim 11$, nam pove, da gre v sistemu za močno magnetno frustracijo. Po drugi strani pa so Becker in ostali (16) opaženo odvisnost relativno dobro opisali z modelom, ki predvideva relativno močne antiferromagnetne interakcije znotraj Fe-tetramerov, ki so v povprečju sklopljeni s šibkejšimi ferromagnetnimi interakcijami (enačba 4.2-4.7).

Za natančnejši vpogled v magnetne anizotropije smo se zatekli k lokalnim tehnikam, v tem primeru elektronski spinski resonanci. Pri sobni temperaturi vidimo jasen signal, katerega intenziteta, $\chi_{\text{ESR}} = 8.5 \cdot 10^{-2} \text{ Am}^2/(\text{T mol})$, ustreza izmerjeni magnetni susceptibilnosti. Lorentzova oblika spektralne črte je najverjetneje posledica zožitve zaradi močnih izmenjalnih interakcij (enačba 3.15), ki zamažejo razliko med dvema kristalografsko različnima Fe mestoma. Izmerjeni g -faktor, $g(\vec{B} \parallel a^*) \sim 2.008(1)$, je v skladu s pričakovanimi vrednostmi za Fe^{3+} ($S = 5/2$), med tem ko je velika širina signala, $\delta B_{1/2}(\vec{B} \parallel a^*) = 54.0 \text{ mT}$, najverjetneje izraz močnih magnetnih anizotropij. To se vidi tudi iz njene izrazite kotne odvisnosti (Figure 33). Temperaturna odvisnost intenzitete signala se do $\sim 130 \text{ K}$ obnaša podobno kot magnetna susceptibilnost, saj sledi Curie-Weissovi odvisnosti z ocenjenimi vrednostmi $\theta_{\text{CW}} = -141(10) \text{ K}$ in $C = 39.0(3) \text{ Am}^2 \text{ K}/(\text{T mol})$ ($\mu_{\text{eff}} = 5.56(5) \mu_{\text{B}}$) za $\vec{B} \parallel a^*$, v grobem pa je ta opis dober vse do $\sim 70 \text{ K}$. Pod to temperaturo pa je odstopanje izrazitejše. V nasprotju z SQUID meritvami, temperaturna odvisnost intenzitete nima širokega maksimuma pri 50 K , kar pripisujemo veliki širini signala in posledičnemu nenatančnemu prilagajanju enačbi 3.15. Hkrati pa je širjenje signala direktno povezano z razvojem magnetnih korelacij kratkega dosega, katerih obnašanje lahko ocenimo iz parametra $\delta H_{1/2} \chi_{\text{ESR}} T$ (Figure 35). Ta je v čisti paramagnetni fazi praviloma temperaturno neodvisen, z rastjo magnetnih korelacij pa se začne spreminjati. To spremembo je v našem primeru moč zaznati pri $\sim 45 \text{ K}$ ($\sim 4T_N$), v skladu s SQUID meritvami. Močne magnetne korelacije kratkega dosega so v končni fazi odgovorne tudi za tako močno razširitev, ki je kriva da signala pod 20 K ne moremo več zaznati.

Z namenom, da bi določili dejanski delež magnetnih korelacij nad in pod magnetnim prehodom smo se odločili izmeriti še specifično toploto sistema. Sam magnetni prehod se odraža kot očitna anomalija v drugače gladki temperaturni odvisnosti (Figure 35). Za določitev dejanskega magnetnega prispevka smo najprej odšteli prispevek kristalne mreže, ocenjen na osnovi enačbe 3.35. Očitno se magnetni prispevek razteza močno nad T_N , v skladu z SQUID in ESR meritvami. Kljub temu, pa celotna ocenjena entropija (enačba 3.39) odgovarja zgolj 26 % pričakovane $R \ln(6) = 14.9 \text{ J}/(\text{K mol})$ vrednosti. To kaže, da je najverjetneje naša ocena mrežnega prispevka nenatančna, saj predvideva, da je magnetni prispevek nad $\sim 25 \text{ K}$ zanemarljiv. Omeniti velja še to, da vse do 350 mK nismo opazili nobene druge anomalije, ki bi odgovarjala dodatnemu magnetnemu ali strukturnemu prehodu.

8.2.2 Nizkotemperaturna magnetno urejena faza

Za določitev magnetne strukture, smo se odločili za eksperimente z nevtronskim sipanjem. Preliminarne raziskave smo naredili na praškastem izostrakturnem $\text{FeTe}_2\text{O}_5\text{Cl}$ vzorcu. Iz razlike spektrov pri nizkih ($T = 1.5 \text{ K} \ll T_N$) in visokih temperaturah ($T = 20 \text{ K} > T_N$) smo lahko določili lego magnetnih vrhov (Figure 36), medtem ko primerjava spektrov posnetih pri 100 K in 20 K kaže razpršeno sipanje (Figure 37), ki odgovarja magnetnemu redu kratkega dosega. Spekter magnetnih vrhov v magnetno urejeni fazi je precej zapleten tako, da smo lahko iz njegove analize nedvoumno določili le magnetni valovni vektor $\vec{q} = (1/2 \ 0.463 \ 0)$, ki odgovarja inkomenzurabilni magnetni strukturi. Torej je nizkotemperaturna magnetna struktura cikloidna, helikoidalna ali amplitudno modulirana. Za pridobitev natančnejših informacij o magnetni strukturi smo raziskave nadaljevali na monokristalnih vzorcih, tokrat že na $\text{FeTe}_2\text{O}_5\text{Br}$ sistemu. Globoko v magnetno urejeni fazi (pri 1.5 K), smo izmerili intenziteto 48 magnetnih vrhov, kar pa nas žal ni pripeljalo k eni sami možni rešitvi magnetne strukture. Zato smo za določitev pravega modela magnetne strukture, izvedli še meritve s polariziranim nevtronskim sipanjem - 25 polarizacijskih matrik. Analiza vseh meritev nevtronskega sipanja skupaj (nepolariziranega in polariziranega) nam da en samo končno rešitev – amplitudno moduliran model (32), (120), kjer železove magnetne momente opišemo kot $S(i, k, l) = S_0 \cos(\vec{q} \cdot \vec{r}_i + \psi_{kl})$. Tu je \vec{r}_i vektor, ki definira položaj Fe momenta v i -ti celici, $S_0 = 4.02(9) \mu_{\text{B}}$ je amplituda magnetne modulacije, ki je enaka za vse magnetne momente, ψ_{kl} pa so faze, ki ustrezajo posameznim Fe momentom znotraj kristalografske osnovne

celice (Figure 38, Table 6). Očitno je simetrija kristalne strukture višja od simetrije odkrite magnetne strukture, saj je slednja izgubila center inverzije. S tem pa se odpira možnost za pojav električne polarizacije.

Za neodvisen test modela magnetne strukture, smo opravili meritve muonske spinske relaksacije (μ SR). Gre za meritve, pri katerih spremljamo precesijo muona v lokalnih magnetnih poljih. Najprej smo izmerili nabor muonskih relaksacijskih funkcij v šibkem prečnem magnetnem polju (Figure 40). Ta meritev nam je omogočila določiti delež vzorca, v katerem so magnetne korelacije (dolgega ali kratkega dosega) razvite že do te mere, da tam lokalna magnetna polja prevladajo nad zunanjimi. Rezultati kažejo, da so omenjene korelacije prisotne vse do ~ 20 K, kar je v skladu s pričakovanim obstojem magnetnega reda kratkega dosega. Naslednji korak so bile meritve v odsotnosti zunanjih polj. Te nam dajo informacijo o magnetnem redu dolgega dosega. Prvič, pojav oscilacij v relaksacijski krivulji nam pove, kdaj se magnetni red vzpostavi in drugič, oblika relaksacijske krivulje skriva informacijo o samem magnetnem redu. Po pričakovanju se oscilacije zares pojavijo pod T_N , njihovo obliko pa lahko precej dobro opišemo ob predpostavki, da imamo dve različni inkomenzurabilni porazdelitvi lokalnih polj. To kaže, da se muoni najverjetneje ustavljajo na dveh različnih kristalografskih mestih, hkrati pa potrjuje inkomenzurabilnost nizkotemperaturne magnetne strukture.

Raziskave na lokalnem nivoju smo nadaljevali z meritvami $^{79,81}\text{Br}$ jedrske kvadrupolne resonance (NQR). Ta pojav lahko opazujemo, ker imajo jedra s spinom $S > 1/2$ kvadrupolni moment Q , ki precesira v gradientu električnega polja (EFG). Slednji je tipično posledica porazdelitve elektronske gostote v okolici izbranega jedra. V našem primeru smo EFG izračunali za obe kristalografsko različni Br mesti na podlagi teorije gostotnih funkcionalov (DFT) - Table 7, kar nam je pri znanih $Q(^{79}\text{Br}) = 31.3 \times 10^{-30} \text{ m}^2$ in $Q(^{81}\text{Br}) = 26.2 \times 10^{-30} \text{ m}^2$ ($^{79}Q/^81Q = 1.19$), omogočilo določitev iskane kvadrupolne frekvence ν_Q . Natančnost izračuna se kaže v zelo dobrem ujemanju izmerjenih vrednosti (Table 8) z izračunanimi. Izmerjeni spektri Br1 in Br2 za oba izotopa pri 80 K kažejo enostavno Gaussovo obliko s šibkim širokim ozadjem, ki najverjetneje izvira iz manjše porazdelitve EFG vrednosti. Razmerje spektralnih širin in relaksacij za različna izotopa je obratno sorazmerno razmerju kvadratov njunih žiromagnetnih razmerji $(^{79}\gamma/^81\gamma)^{-2} = 1.162$, kar kaže, da je relaksacijski mehanizem pretežno magneten. Z ohlajanjem, se spinsko mrežna relaksacija ($1/T_1$) linearno zmanjšuje vse do ~ 40 K, kjer se ta trend prekine. Porast $1/T_1$ pod 25 K, ki se konča z izrazito divergenco pri T_N , povezujemo z vzpostavljanjem magnetnih korelacij, ki pospešijo magnetno relaksacijo v bližini faznega prehoda. Temperaturni odvisnosti spektrov za Br1 in Br2 sta nad magnetnim prehodom zelo podobni, saj se v obeh primerih ν_Q pri ohlajanju zvišuje (Figure 43), kar odgovarja povečanju EFG-ja kot posledici krčenja osnovne kristalne celice. Pod prehodom, pa se oba spektra močno spremenita. Ozka paramagnetna črta izgine razvije pa se spekter v obliki črke U, značilen za sinusno porazdelitev lokalnih polj, tipično za inkomenzurabilne sisteme. Samo 0.4 K nižje se spekter ponovno spremeni. Očitno smo priča dvema zaporednima magnetnima prehodoma – najprej iz paramagnetne faze v visokotemperaturno inkomenzurabilno fazo (HT-ICM), ki ji sledi še nizkotemperaturna faza (LT-ICM). Z nadaljnjim nižanjem temperature se na Br1 in Br2 mestih razvijeta popolnoma različna spektra. Na mestu Br1 dobimo relativno preprosto črto v obliki črke U (Figure 44a), med tem ko se na mestu Br2 razvijejo tri bolj ali manj neodvisne U črte (Figure 44b). Razlika je nedvomno posledica različne sklopitve z železovimi momenti, t.j. sklopitve Br1 z enim Fe mestom, medtem ko je Br2 sklopljen s tremi. Na podlagi te ugotovitve smo se lotili tudi natančnega opisa spektrov. Najprej smo EFG vrednosti pomnožili z 1.083 za Br1 in 0.88 za Br2, da smo prišli do točnega ujemanja ν_Q z izračunanimi vrednostmi. V nadaljnjem koraku pa smo kot proste parametre vzeli hiperfine sklopitvene tenzorje med Br in Fe mesti, torej enega za Br1 in tri za Br2. Končno smo uspeli oba spektra relativno dobro opisati (Figure 46) s hiperfinimi parametri podanimi v Table 9. V LT-ICM fazi je zanimiva tudi frekvenčna odvisnost relaksacije $1/T_1$ (Figure 45). V primeru Br1 se ta sklada s hipotezo, da so v območju polno razvitih magnetnih momentov (na robovih U spektra) osnovni vzbuditveni način fazoni, ki so energijsko »zelo poceni«, in s tem privedejo do

hitre relaksacije, medtem ko v območju majhnih magnetnih momentov (v centralnem delu U spektra) prevladujejo energijsko »dražji« amplitudoni, ki privedejo do počasnejše relaksacije. Odvisnost na mestu Br2 je bistveno bolj komplicirana.

Na koncu lahko rečemo, da vse uporabljene tehnike pri določanju nizkotemperaturne magnetne faze kažejo, da gre v LT-ICM fazi res za inkomenzurabilno amplitudno modulirano magnetno strukturo, ki zlomi kristalografsko simetrijo inverzije. Še več, opazili smo, da je nad LT-ICM fazo prisotna še HT-ICM faza, ki pa se po obliki Br1 in Br2 NQR črt zdi bolj simetrična kot LT-ICM faza.

8.2.3 Ferroelektrični prehod in njegova povezava z magnetizmom

Izguba simetrije inverzije v LT-ICM fazi nas je spodbudila k preučevanju obstoja električne polarizacije.

To raziskavo smo začeli z meritvami termičnega raztezka kristala, saj pri vzpostavitvi električne polarizacije pričakujemo tudi rahlo spremembo kristalne mreže. Z ohlajanjem se termični razteznostni koeficient vzdolž c smeri, α_c , počasi zmanjšuje, v skladu s pričakovanim krčenjem mreže (Figure 49a). Odstopanje od tega trenda postane očitno pod ~ 50 K, ko α_c postane negativen in pri ~ 20 K doseže minimum, kar si razlagamo kot posledico vzpostavljanja magnetnega reda kratkega dosega. Med nadaljnjim ohlajanjem α_c spet začne naraščati vse do 10.6 K, kjer opazimo v temperaturni odvisnosti α_c ostro špico (Figure 49b). Sovpadanje le-te z temperaturo magnetnega prehoda nedvomno kaže, da se vzpostavitev magnetnega reda odraža tudi na kristalni strukturi vzorca.

To nas je spodbudilo k natančnejšim raziskavam kristalne strukture z uklonom sinhrotronske rentgenske svetlobe. Pri teh meritvah smo se posvetili predvsem temperaturnemu intervalu okoli magnetnega prehoda. Pri ohlajanju nismo zaznali nobenih sprememb v simetriji kristalne strukture med 35 K in 5 K. Visoka kvaliteta meritev pa nam je omogočila tudi študijo posameznih medatomske razdalje. Iz jasnega razloga, ker imajo Te^{4+} stereo-kemično aktivne nevezne elektronske pare, nas je najbolj zanimala temperaturna odvisnost Fe-Te razdalje. In res, pri T_N opazimo majhno a jasno spremembo naklona v temperaturni odvisnosti le-teh, kar je lahko posledica premika Te^{4+} ionov zaradi polarizacije njihovih neveznih elektronskih parov.

Vsi te dokazi za odziv kristalne strukture na vzpostavitev magnetnega reda dolgega dosega govorijo v prid dejanskemu obstoju ferroelektrične faze. Da bi pridobili neizpodbiten dokaz, smo se odločili za izvedbo dielektričnih meritev. In res, temperaturna odvisnost realnega dela dielektrične konstante ϵ' , izmerjenega v električnem polju vzdolž c osi, kaže ostro špico, ki točno sovпада s temperaturo magnetnega prehoda (Figure 51a,c). Obstoj ferroelektrične faze je potrjen še z meritvijo električne polarizacije (Figure 51c) in izmerjeno histerezo zanko (Figure 51b). Izmerjena polarizacija je največja vzdolž c osi, $P(c) = 8.5(2) \mu\text{C}/\text{m}^2$ pri 5 K, med tem, ko je vzdolž a^* osi skoraj red velikost manjša, $P(a^*) = 1.0(1) \mu\text{C}/\text{m}^2$ pri 5 K. Polarizacije vzdolž smeri b nismo uspeli zaznat. Primerjava temperaturne odvisnosti električne polarizacije P in intenzitete enega izmed magnetnih vrhov kaže, da je $P \propto T^{0.5}$, kar je v nasprotju z obnašanjem v večini multiferroikov z močno magneto-električno sklopitvijo. To daje slutiti, da je v našem primeru za opaženo obnašanje odgovoren drugačen magneto-električen mehanizem, kar je najverjetneje povezano z dejstvom, da v $\text{FeTe}_2\text{O}_5\text{Br}$, za razliko od podobnih sistemov, vse izmenjalne interakcije potekajo preko Te^{4+} kationov, ki imajo nevezne elektronske pare.

Femenološka razlaga magneto-električnega pojava v inkomenzurabilnih helikoidalnih in spiralnih strukturah je tipično podana z izrazom $\vec{P} = [\vec{M}(\nabla \cdot \vec{M}) - (\vec{M} \cdot \nabla)\vec{M}]$ (58), kjer \vec{P} predstavlja električno polarizacijo, \vec{M} pa podmrežno magnetizacijo v vzorcu. Ta izraz za naš model magnetne strukture napove polarizacijo v a^*b ravnini, kar je v nasprotju z eksperimentalnimi rezultati. V naslednjem koraku smo zgornji izraz razširili z členom $\vec{P} \cdot \nabla(\vec{M})$, ki je pomemben v primeru, ko je \vec{P} sestavljen iz prostorsko homogenega in moduliranega

prispevka (59). Ker tudi ta razširitev ne napove prave smeri polarizacije, smo magneto-električni sklopitveni člen izpeljali s pomočjo reprezentacijske analize. Ta nam pove, da ima prostorska grupa, kateri pripada naša magnetna struktura, le dva simetrijska elementa – identiteto 1 in dvoštevno vijačno os 2_{1y} – in dve možni ireducibilni reprezentaciji Γ_1 in Γ_2 (Table 10). Primerjava eksperimentalno določenih faznih zamikov med amplitudno moduliranimi magnetnimi valovi s faznimi zamiki, ki jih predvidevata ireducibilni reprezentaciji, nam pove, da je naš strukturni magnetni model kombinacija obeh ireducibilnih reprezentacij. Ob upoštevanju tega kot tudi simetrijskih lastnosti magnetne strukture, lahko na koncu zapišemo sklopitveni člen podan z enačbo 4.11. Na podlagi tega pa lahko izpeljemo tudi izraza za intenziteto magnetnih vrhov (enačba 4.14) in električno polarizacijo (enačba 4.15), kot funkciji amplitude magnetnih valov in njihovih medsebojnih faznih zamikov. Končno lahko tako ob predpostavki, da imata amplituda magnetne modulacije kot tudi fazni zamik temperaturno odvisnost oblike $|T - T_N|^\beta$, opišemo nenavadno $P \propto I^{0.5}$ odvisnost. Na podlagi te analize sklepamo, da je za pojav električne polarizacije ključno »drsenje« amplitudno moduliranih magnetnih valov, ki preko izmenjalne-skrčitve Fe-O-Te-O-Fe mostov vzbudi polarizacijo telurjevih neveznih elektronskih parov.

8.2.4 Fazni diagram – meritve narejene v zunanjem magnetnem polju

Obstoj magneto-električne sklopitve bi se moral odražati v izrazitem odzivu ferroelektričnih lastnosti na zunanje magnetno polje in obratno, v odzivu magnetne strukture na zunanje električno polje. Po drugi strani, majhna vrednost električne polarizacije kaže, da bo veliko lažje zaznati vpliv magnetnega polja. Zato smo se odločili za natančno študijo magnetnih in dielektričnih lastnosti v zunanjem magnetnem polju.

Za natančno določitev faznih prehodov smo najprej opravili meritve specifične toplote v magnetnem polju vzdolž a^* (pravokotno na kristalne plasti). Iz rezultatov (Figure 52) je jasno razvidno, da obstajata dva zaporedna prehoda, ki sta močno odvisna od jakosti magnetnega polja. V odsotnosti polja prehoda tako-rekoč sovpadata; z naraščanjem polja pa temperatura visokotemperaturnega prehod raste nizkotemperaturnega prehod pa pada, tako da sta ti dve pri 9 T enaki $T_{N1} = 11.8(1)$ K in $T_{N2} = 9.4(1)$ K.

Magnetne lastnosti visoko- in nizkotemperaturne faze smo začeli preučevati z meritvami magnetne susceptibilnosti χ (Figure 53). V polju vzdolž a^* je izrazit le nizkotemperaturni prehod, visokotemperaturni pa je mogoče oceniti le zelo špekulativno iz šibkega prevoja v $d\chi/dT$. V nasprotju s tem, meritve v polju vzdolž b osi precej nazorno kažejo oba prehoda še posebej, če pogledamo $d\chi/dT$. Kot kaže se pri tej orientaciji z naraščajočim poljem temperatura visokotemperaturnega prehoda počasi zmanjšuje, med tem, ko je temperatura prehoda nizkotemperaturnega prehoda tako-rekoč konstantna. Končno pri ~ 4 T obe temperaturi sovpadeta sam prehod pa postane bolj oster/izrazit, kot da bi visokotemperaturna faza izginila. Odziv magnetne susceptibilnosti v polju vzdolž c osi pa je spet manj nenavaden. Kljub temu, da se dobro vidi le en prehod, se zdi, da se z naraščajočim poljem oba prehoda premikata k višjim temperaturam. Indikacije visokotemperaturnega prehoda očitno govorijo v prid hipotezi iz NQR-a, da sta oba prehoda zares magnetna.

Da bi dobili več informacije o značaju HT-ICM faze, smo nadaljevali preiskavo z lokalno tehniko – $^{81,79}\text{Br}$ jedrsko magnetno resonanco na mestu Br2. To smo pomerili v več različnih poljih (9.4 T in 4.7 T) in več različnih orientacijah ($\vec{B}||a^*$ in $\vec{B}||c$). Spekter izmerjen pri 80 K in polju 9.4 T je prikazan na Figure 54. Očitno gre za centralni črti obeh izotopov, ki ju spremljata po dva satelita. Dvojnost vseh črt, je najverjetneje posledica rahlega odstopanja \vec{B} od a^* , ki zlomi simetrijo 2_{1y} . Zanesljivost DFT izračunov smo dodatno preverili z meritvami kotne odvisnosti Br2 signala, ki kaže zelo dobro ujemanje meritev z računi. Temperaturna odvisnost centralne črte zelo jasno ponazarja odziv magnetne susceptibilnosti, kar omogoča jasno določitev izotropnega hiperfinega premika in posledično oceno hiperfine interakcije ~ 0.267 T/ μ_B . Omeniti velja, da je ta vrednost v skladu z vrednostmi ocenjenimi iz NQR meritev. Na Figure 57 je prikazan

temperaturni razvoj spektrov v okolici faznih prehodov, kjer široka črta pripada satelitu $^{79}\text{Br2}$ ozka pa centralnemu prehodu $^{81}\text{Br2}$. Pod prvim magnetnim prehodom se spekter močno spremeni, obe črti pa razvijeta U obliko, kar je razvidno iz pokazane simulacije. Spekter se ponovno spremeni pod T_{N2} , kjer pa je oblika črte zelo zapletena, kar kaže, da je LT-ICM faza precej bolj zapletena kot HT-ICM faza. Dodatne meritve pri 4.7 T kažejo podobno obnašanje (Figure 58). Tudi v tem primeru se zdi, da imajo črte v HT-ICM fazi U obliko. Zanimiva je še meritev temperaturne odvisnosti relaksacije, $1/T_{1r}$, kjer sta oba magnetna prehoda zelo lepo izražena kot dve zaporedni singularnosti. Meritve v magnetnem polju vzdolž c osi so se s stališča prepoznavanja spektra izkazale za bolj praktične, saj v tej orientaciji lahko $^{81}\text{Br2}$ centralne prehode spremljamo povsem izolirano – dva črti sta posledica zloma simetrije 2_{1y} osi zaradi majhnega odstopanja \vec{B} od a^* . Tu se lepo vidi, da imata obe črti v HT-ICM fazi enako obliko medtem ko se v LT-ICM fazi razlikujeta. To kaže na to, da je v HT-ICM fazi simetrija inverzije še prisotna, v LT-ICM fazi pa te ni več.

Da bi določili naravo HT-ICM faze, ali je amplitudno modulirana ali gre za kakšen drugačen magnetni red, smo se odločil za meritve nevtronskega sipanja v zunanjem magnetnem polju. Natančna meritev temperaturne odvisnosti intenzitete magnetnih vrhov potrdi rezultate NQR, da HT-ICM faza obstaja že pri $B = 0$ T. Njen obstoj pa je še bolj izrazit v polju vzdolž a^* smeri (Figure 60b). HT-ICM faza se od LT-ICM faze izrazito loči po temperaturni odvisnosti intenzitete magnetnih vrhov I , saj če privzamemo, da velja odvisnost $I \approx |T - T_N|^{2\beta}$, dobimo $\beta \sim 0.35(2)$ za HT-ICM fazo in $\sim 0.26(1)$ za LT-ICM fazo. Te vrednosti kritičnih eksponentov govorijo o tem, da ima HT-ICM tridimenzionalni značaj, LT-ICM pa dvodimenzionalnega, kar je v nasprotju z ostalimi rezultati. To je najverjetneje posledica tega, da I ni sorazmeren z M^2 , ampak je ta odvisnost zaradi temperaturne odvisnosti faz med magnetnimi valovi bolj komplicirana. Omeniti gre še to, da je položaj magnetnih vrhov v HT-ICM fazi temperaturno neodvisen, medtem ko se inkomenzurabilna vrednost valovnega vektorja v LT-ICM fazi razvija podobno kot intenziteta. V magnetnem polju vzdolž b osi (Figure 61), se jasno vidi, da se temperaturni interval HT-ICM faze s povečevanjem polja krči in pri 5 T tudi izgine, v skladu z magnetizacijskimi meritvami. Dodatno smo opravili še natančne meritve širin magnetnih vrhov, kar nam je omogočilo študijo temperaturnega razvoja magnetne korelacijske dolžine. Te rezultati (Figure 62) kažejo, da nad T_{N1} magnetni red kratkega dosega obstaja znotraj kristalnih plasti vse do ~ 40 K.

V nadaljevanju smo opravili še meritve temperaturne odvisnosti termičnega raztezka, ki pokažejo, da se v polju 6 T vzdolž c osi anomalija pri ~ 10.5 K rahlo pomakne k višjim temperaturam (Figure 63), v skladu z SQUID in NMR meritvami.

Da bi ugotovili ali gre v $\text{FeTe}_2\text{O}_5\text{Br}$ sistemu res za močno magneto-električno sklopitev in kaj se dogaja z električno polarizacijo v HT-ICM fazi, smo opravili meritve dielektrične konstante v $\vec{E}||c$ v vseh treh orientacijah magnetnega polja (Figure 64). Te kažejo, da je električna polarizacija prisotna zgolj v LT-ICM fazi, kar je v skladu z NMR in NQR rezultati, ki nakazujejo, da je v HT-ICM fazi še vedno prisoten center inverzije. Zelo zanimivo je obnašanje v magnetnem polju vzdolž b osi, saj anomalija v dielektrični konstanti pri ~ 4 T izgine. To je najverjetneje pomeni, da električna polarizacija izgine skupaj s HT-ICM fazo. Vsekakor je ta pojav zelo zanimiv z uporabniškega stališča, saj smo na ta način z zunanjim magnetnim poljem »ugasnili« električno polarizacijo v vzorcu.

Za konec smo preiskovali še magnetne ekscitacije z neelastičnim elektronskim sipanjem, ki kažejo, da so Goldstonovi nihajni načini precej potlačeni in da je večina intenzitete v ekscitacijah, ki imajo energijsko režo.

8.2.5 Povzetek

Če povzamemo, B - T fazni diagram $\text{FeTe}_2\text{O}_5\text{Br}$ sistema se sestoji iz visoko temperaturne paramagnetne faze, v kateri se pod ~ 60 K ($6T_N$) začnejo vzpostavljati magnetne korelacije kratkega dosega. Magnetni red dolgega dosega se vzpostavi pod T_{N1} , ko sistem preide v inkomenzurabilno HT-ICM fazo. Temu prehodu hitro (~ 1 K

nižje – odvisno od jakost magnetnega polja) sledi prehod v LT-ICM fazo, kjer inkomenzurabilna amplitudno modulirana magnetna struktura, odstrani center inverzije in vzbudi makroskopsko električno polarizacijo. Ta pojav pripisujemo delovanju izmenjalne-skrčitve Fe-O-Te-O-Fe izmenjalnih poti, ki privede do polarizacije telurjevih neveznih elektronskih parov. Z zunanjim poljem lahko močno vplivamo na temperaturo faznih prehodov, in v primeru ko je polje vzdolž b osi večje od 4 T tudi »ugasnemo« električno polarizacijo. Naši rezultati kažejo, da se spleča iskati nove magneto-električne multiferroike med M - T - O - X spojinami ($M = \text{Cu}, \text{Ni}, \text{Fe}, X = \text{Cl}, \text{Br}, \text{I}, T = \text{Te}, \text{Se}, \text{Sb}, \text{Bi}, \text{Pb}$), saj pogosto združujejo prisotnost magnetne frustracije in neveznih elektronskih parov.

8.3 $\text{Ni}_5(\text{TeO}_3)_4\text{Br}_2$ sistem

Odkritje magneto-električne sklopitve v $\text{FeTe}_2\text{O}_5\text{Br}$ sistemu, nas je spodbudilo k raziskavam $\text{Ni}_5(\text{TeO}_3)_4\text{Br}_2$ sistema, ki je plod istega sinteznega koncepta ter kaže podobne strukturne lastnosti. Prav tako ima $\text{Ni}_5(\text{TeO}_3)_4\text{Br}_2$ sistem plastovito strukturo in monoklinsko osnovno celico, pripadajočo prostorski grupi $C2/c$, ki ima tako kot $\text{FeTe}_2\text{O}_5\text{Br}$ simetrijo inverzije. Znotraj osnovne celice so tri kristalografsko različna Ni^{2+} ($S = 1$) magnetna mesta, od katerih imata $\text{Ni}1$ in $\text{Ni}2$ oktaedrsko koordinacijo z kisikovimi ioni, $\text{Ni}3$ pa je povezan z petimi kisikovimi in enim bromovim ionom. Ni ioni so preko kisikov povezani v $[\text{Ni}_5\text{O}_{17}\text{Br}_2]$ enoto, ki jo sestavljata dva trikotnika, stikajoča se v $\text{Ni}1$ (Figure 68). Te enote so preko svojih O^{2-} ionov povezane v NiO plasti, ki so ločene s Te^{4+} in Br^- ioni.

8.3.1 Magnetne lastnosti v nizkih magnetnih poljih

Temperaturna odvisnost magnetne susceptibilnosti na Figure 69a,b kaže, da njeno obnašanje pri visokih temperaturah (< 80 K) lahko opišemo z Curie-Weissovim zakonom (enačba 4.1), s $\theta_{CW} = -44(5)$ K in $C = 75(2)$ $\text{Am}^2\text{K/mol T}$. Dobljena konstanta ustreza efektivnemu magnetnemu momentu $\mu_{eff} = 3.45(5) \mu_B$, kar za $S = 1$ sistem odgovarja g -faktorju $g = 2.35$, v skladu z predhodnimi meritvami (135), (15). Pri $T_N = 29$ K je opaziti anomalijo, ki ustreza prehodu v magnetno urejeno stanje. Pod prehodom pride do izrazite razlike med meritvami pri $\vec{B}||a^*$, $\vec{B}||b$ in $\vec{B}||c$, kar kaže na močno anizotropijo sistema. Iz natančne meritve kotne odvisnosti v urejeni fazi (Figure 69c) lahko določimo celo približno orientacijo magnetnih momentov, saj vzdolž njih pričakujemo najmanjšo, pravokotno na njih pa največjo magnetno susceptibilnost. Tako dobimo, da momenti ležijo v ac ravnini, zamaknjeni približno 30° od a^* proti c osi. Na koncu velja pogledati še razmerje $|T_N/\theta_{CW}|$, ki kaže na bistveno nižjo stopnjo magnetne frustracije, kot v $\text{FeTe}_2\text{O}_5\text{Br}$ v sistemu.

Magnetno strukturo urejene faze, smo določili iz meritev nevtronskega sipanja. Izkaže se, da je nizkotemperaturna (5 K) magnetna struktura dvodimenzionalna, z nagnjenimi magnetnimi momenti (Figure 70a). Njena simetrija ohranja center inverzije, kar onemogoča pojav makroskopske električne polarizacije. Zanimivo je tudi različno obnašanje temperaturne odvisnosti magnetnih vrhov (Figure 70b), ki odgovarjajo med seboj pravokotnim komponentam magnetnih momentov, kar nakazuje spreminjanje orientacije momentov. Na primer (-203) vrh kaže $A(1 - T/T_N)^{2\beta}$ obnašanje z $\beta = 0.25(1)$, ki ustreza kritičnemu eksponentu za plastovite trikotne antiferromagnetne sisteme (137), med tem ko ima (-201) vrh bistveno bolj skokovito odvisnost. Dodatne meritve intenzitet magnetnih vrhov pri 15 K pa kažejo celo, da se na različnih Ni mestih magnetni momenti obnašajo različno.

8.3.2 Meritve v magnetnem polju

Občutljivost frustriranih sistemov na zunanje motnje nas je spodbudila k raziskavam vpliva zunanjega magnetnega polja. Za to smo uporabili naslednje tehnike: meritve specifične toplote, magnetizacije in magnetnega navora.

Temperaturna odvisnost specifične toplote, C_p , jasno kaže ostro špico pri T_N (Figure 71a). Magnetni prispevek, C_{mag} , ki ga dobimo po odštevanju ocenjenega mrežnega prispevka C_{latt} (enačba 3.35), ima dobršen

del tudi nad T_N (Figure 71b). To potrjuje izračunana entropija, saj se skoraj 30 % celotne vrednosti, ki se sicer ujema z pričakovano vrednostjo $5R \ln(2S + 1) = 45.7 \text{ J / (K mol)}$, razvije šele nad T_N (Figure 71d). S tem pa tudi jasno kaže na prisotnost magnetnih korelacij kratkega dosega nad T_N in posledično potrjuje izrazito dvodimenzionalnost sistema. Zunanje magnetno polje vzdolž a^* osi, ki ne vpliva na T_N , se izrazito pozna v odvisnosti pod 15 K (Figure 71b), ki pa jo pripisujemo spremembi orientacije magnetnih momentov, opaženi že pri nevtronskem sipanju.

Magnetni odziv smo še bolj natančno sledili z meritvami kompletnega odziva magnetizacije na zunanje polje. To smo dosegli tako, da smo standardne meritve magnetizacije, ki merijo odziv magnetizacije vzdolž magnetnega polja - $\vec{M}||a^*$ (M_{a^*}), dopolnili z meritvami magnetnega navora, saj smo iz teh lahko dodatno ocenili odziv še v pravokotnih smereh - $\vec{M}||b$ (M_b) in $\vec{M}||c$ (M_c). Pri nizkih temperaturah (1.5 K) temperaturna odvisnost dM_{a^*}/dB kaže jasen vrh pri $\sim 11 \text{ T}$ (Figure 72). Ta odgovarja spremembi smeri magnetnih momentov oz. tako-imenovanemu spinskemu preskoku (spin-flop), ki mu bomo zaradi ne povsem ostre oblike v našem primeru raje rekli »blagi spinski preskok«. Z višanjem temperature pa ta prehod postaja še manj izrazit. Podoben odziv smo opazili tudi za M_b in M_c , le da je odziv pri M_b bolj oster. Poleg tega lahko iz temperaturne odvisnosti M_c vidimo, da je temperatura Néelovega prehoda povsem neodvisna od polja. Zanimivo je še to, da Néelov prehod v M_b sploh ni opazen, kar je najverjetneje posledica lege magnetnih momentov v ac ravnini.

8.3.3 Meritve antiferromagnetne resonance

Z namenom, da bi določili osnovne člene v spinskem Hamiltonianu, smo opravili magnetno resonančne meritve v območju od 10 do 550 GHz v poljih do 15 T. Signala paramagnetne resonance nismo uspeli zaznati, kar je najverjetneje posledica izjemno širokega signala. Antiferromagnetno resonanco pa smo lahko zaznali šele pod 15 K, precej pod $T_N = 29 \text{ K}$ (Figure 74a), ki ga pri Larmorjevi frekvenci $\nu_L = 324 \text{ GHz}$ opazimo pri polju 5.05 T vzdolž a^* . Pri nadaljnjem ohlajanju, se ta izrazito oži - z 1.8 T pri 15 K na 0.07(1) T pri 1.5 K, njegov položaj pa se tudi rahlo spreminja (Figure 74b). Opažena zožitev signala je sorazmerna s $T^{2.8}$ in je najverjetneje posledica magnonskega sipanja, medtem ko je odvisnost resonančnega polja najverjetneje posledica spreminjanja orientacije magnetnih momentov.

V naslednjem koraku smo se posvetili odvisnosti resonančnega polja od zunanjega magnetnega polja pri nizkih temperaturah (4 K). V skladu s pričakovano odvisnostjo za antiferromagnente sistem, opaženo tudi v izostrukturalnem $\text{Ni}_5(\text{TeO}_3)_4\text{Cl}_2$ sistemu (56), se resonančna frekvenca z naraščajočim poljem ($\vec{B}||a^*$) najprej zmanjšuje od 450 GHz pri 0.7 T do $\sim 80 \text{ GHz}$ pri 10.7 T, potem pa začne naraščati (Figure 75a). Ta prevoj, je jasen indikator blagega spinskega preskoka, kar je v skladu z meritvami magnetizacije. Poleg tega gre poudariti, da smo pri 550 GHz in polju $\sim 0.7 \text{ T}$ opazili tudi naslednji resonančni način. Razlika med osnovnim in drugim resonančnim načinom v odsotnosti polja kaže, da so poleg anizotropije kristalnega polja, tipično odgovorne za končno vrednost osnovnega resonančnega načina, prisotne tudi anizotropije izmenjalne interakcije (npr. Dzyaloshinsky-Moriya ali anizotropna izmenjalna interakcija).

Dodatno smo izmerili še kotno odvisnost resonančnega polja pri izbrani Larmorjevi frekvenci 240 GHz (Figure 75b). Opazimo lahko, da je kotna odvisnost veliko močnejša, ko smo polje vrteli znotraj a^*b kot v primeru rotacije v ac ravnini, kar je v skladu z magnetno susceptibilnostjo, kjer je razlika med odzivom vzdolž a^* in b smermi bistveno večja kot med a^* in c smermi.

8.3.4 Izračuni

Da bi dejansko prišli do členov, ki sestavljajo spinski Hamiltonian $\text{Ni}_5(\text{TeO}_3)_4\text{Br}_2$ sistema, smo se odločili eksperimentalne rezultate opisati z modelom molekularnega polja (enačbe 5.3-5.7), kjer smo upoštevali izotropno in anizotropno izmenjalno interakcijo, anizotropije kristalnega polja, antisimetrično Dzyaloshinsky-

Moriya izmenjalno interakcijo in seveda tudi vpliv zunanega magnetnega polja. Na osnovi magnetne strukture, smo v obzir vzeli 10 magnetnih pod mrež, ki pripadajo Ni mestom označenim na Figure 68a. Zaradi očitno velikega števila prostih parametrov – šest različnih izmenjalnih interakcij (z vsemi anizotropijami) in tri različne anizotropije (tenzorji), smo se odločili število le-teh zmanjšati. V ta namen smo na osnovi modela, ki upošteva prekrivanje orbital (angular overlap model - AOM) in pomočjo programa LIGFIELD (146) izračunali anizotropije kristalnega polja za vsa tri Ni mesta (Table 16). Narava tega izračuna je taka, da so njegove ocene anizotropije dobre, medtem ko je njihova absolutna velikost relativno slabo določena. V naslednjem koraku smo skrčili število različnih izmenjalnih poti na štiri, saj znotraj našega modela ne moremo ločiti različnih interakcij, ki potekajo med istimi pod mrežami.

Za izračun parametrov modela molekularnega polja, smo simulirali izmerjene vrednosti kotne odvisnosti magnetizacije, orientacije magnetnih momentov določenih iz nevtronskega sipanja, kot tudi odvisnosti antiferromagnetne resonance od orientacije in jakosti magnetnega polja. Rezultati računov, so predstavljeni v Table 17, primerjava z meritvami pa je ponazorjena z rdečimi črtami na Figure 69c, Figure 75a in Figure 75b. Opaziti je, da pomembno vlogo igrajo anizotropije, med katerimi je še posebej izrazita anizotropija izmenjalnih interakcij, ki je najverjetneje posledica znatnega prispevka elektronske orbitalne vrtilne količine. Precej močne anizotropije kristalnega polja na Ni mestih pa so posledica nesimetrične razporeditve sosednjih kisikovih ionov. Ob upoštevanju izračunanih parametrov molekularni model napoveduje prehod v novo magnetno fazo pri ~ 24 T (Figure 77), za katero pa je značilno, da nima centra inverzije s čimer odpira možnost za nastanek električne polarizacije. Še več, ob privzeti temperaturni odvisnosti pod mrežne magnetizacije (enačba 5.8) lahko kvantitativno opišemo tudi pomik blagega spinskega preskoka k nižjim poljem s padajočo temperaturo.

8.3.5 Povzetek

Na sliki Figure 76 kažemo celoten B - T fazni diagram $\text{Ni}_5(\text{TeO}_3)_4\text{Br}_2$ sistema. Z ohlajanjem sistem pri $T_N = 29$ K preide v planarno magnetno urejeno fazo z rahlo nagnjeni magnetnimi momenti, katerih orientacija se ustali šele pri nizkih temperaturah. Z povečevanjem zunanega magnetnega polja vzdolž a^* smeri – pravokotno na kristalne ravnine, sistem pri ~ 11 T doživi blag spinski preskok, ki mu po napovedih računov sledi izrazitejši spinski preskok pri ~ 24 T. Za razliko od magnetne ureditve pri nizkih poljih napovedana faza v visokih poljih izgubi center inverzije, kar potencialno omogoči pojav električne polarizacije. Širše območje blagega spinskega prehoda na Figure 76 označuje interval vrednosti magnetnega polja pri eksperimentalni negotovosti orientacije kristala za 5° . Zanimivo, v nasprotju s trendom, ki ga kaže blagi spinski preskok, se magnetno polje predvidenega spinskega preskoka (pri ~ 24 T) med ohlajanjem povečuje. Omeniti gre še pojav magnetnega reda kratkega dosega, katerega efekti so opazni vse do $\sim 2T_N$.

Na koncu velja izpostaviti pomen magnetnih anizotropij, ki so ključne za opisan fazni diagram. Gre za to, da magnetne anizotropije prevladajo nad geometrijsko frustracijo in s tem omogočijo sistemu, da pri nizkih temperaturah vzpostavi magnetno urejeno stanje.

8.4 Končne ugotovitve

V našem delu smo preučevali vpliv magnetne frustracije na osnovno magnetno stanje dvodimenzionalnih sistemov magnetnih skupkov s trikotno geometrijo, ki vsebujejo katione z neveznimi elektronskimi pari, in raziskovali njihove magnetne in električne lastnosti. Cilj je bil ugotoviti, če inkorporacija omenjenih kationov v izmenjalne poti med magnetnimi ioni lahko pripelje do izmenjalne-skrčitve in posledične magneto-električne sklopitve. To študijo smo izvedli na dveh modelskih sistemih, t.j. $\text{FeTe}_2\text{O}_5\text{Br}$ in $\text{Ni}_5(\text{TeO}_3)_4\text{Br}_2$, ki ustrezata omenjenim strukturnim zahtevam. V toku teh raziskav in z željo, da bi oba sistema kar se da dobro

preučili, smo uporabili številne eksperimentalne metode, vključujoč makroskopske meritve, sipalne in lokalne tehnike.

Glavni rezultat naše raziskave je nedvomno spoznanjem, da je $\text{FeTe}_2\text{O}_5\text{Br}$ sistem multiferroik, v katerem je za pojav električne polarizacije odgovorna vzpostavitev inkomenzurabilnega amplitudno moduliranega magnetnega reda dolgega dosega (32). Natančno spremljanje temperaturne odvisnosti kristalne strukture kaže, da nastanek električne polarizacije spremlja premik neveznih elektronskih parov Te^{4+} . To potrjuje hipotezo, da je električna polarizacija res rezultat izven-centričnih strukturnih sprememb, ki so posledica premika neveznih elektronskih parov. Kot razlago opaženega, predlagamo nov mehanizem magneto-električno sklopitve, ki vključuje izmenjalno-skrčitev, do katere pride zaradi drsenja sosednjih inkomenzurabilnih amplitudno moduliranih magnetnih valov. S tem se zlomi tudi simetrija inverzije, kar odpre možnost za pojav makroskopske električne polarizacije. Meritve v zunanjem magnetnem polju, so nam razkrile, da obstaja tik nad multiferroično fazo še visokotemperaturna inkomenzurabilna magnetna faza, kjer pa električna polarizacija ni bila opažena. To najverjetneje pomeni, da ta faza še ohranja center inverzije. Še več, direkten dokaz močne magneto-električne sklopitve predstavlja opaženo izginotje električne polarizacije v nizkotemperaturni fazi pri dovolj velikem zunanjem magnetnem polju (~ 4 T) vzdolž inkomenzurabilne smeri (33). Z drugimi besedami, odkrili smo, da lahko električno polarizacijo v $\text{FeTe}_2\text{O}_5\text{Br}$ sistemu z dovolj velikim magnetnim poljem »izklopimo«, kar pa je zelo zanimivo s stališča uporabe v novih spintronskih napravah. Očitno $\text{FeTe}_2\text{O}_5\text{Br}$ sistem predstavlja nov razred multiferroičnih spojin in razširja močno magneto-električno sklopitve, do sedaj odkrito le v komenzurabilnih ali inkomenzurabilnih helikoidalnih/spiralnih magnetnih strukturah, tudi na inkomenzurabilno amplitudno modulirane strukture. To odkritje občutno poveča obseg kandidatov za močan magneto-električni efekt pri sobni temperaturi, ki je bistven s širšega uporabniškega stališča.

Po drugi strani, preiskava $\text{Ni}_5(\text{TeO}_3)_4\text{Br}_2$ sistema razkriva, da ima le-ta manj zapleteno magnetno strukturo, ki tudi ohranja simetrijo inverzije kristalne mreže. S tem pa je izključena tudi možnost za pojav makroskopske električne polarizacije. Opis kotne in poljske odvisnosti antiferrromagnetne resonance na osnovi modela molekularnega polja kaže, da je nižja raven magnetne frustracije in enostavnejša magnetna struktura najverjetneje rezultat močnih magnetnih anizotropij. Poleg tega smo odkrili, da magnetno polje pravokotno na kristalne plasti povzroči blag spinski preskok (spin-flop) pri približno 10 T. Izračuni na osnovi molekularnega polja, ob predpostavki ocenjenih magnetnih anizotropij, napovedujejo še en podoben prehod pri ~ 24 T. Zanimivo je, da predvidena magnetna struktura te faze nima več centra inverzije in tako odpira možnosti za vzpostavitev feroelektrične ureditve.

Skratka, naše raziskave so v skladu z delovno hipotezo, ki trdi, da lahko nizkodimenzionalni magnetni sistemi zares razvijejo zapletene magnetne strukture in da so nevezni elektronski pari v teh sistemih najverjetnejši nosilci električne polarizacije. Poleg tega, tekmovanje med magnetno frustracijo in magnetnimi anizotropijami privede do bogatih faznih diagramov, ki so sestavljeni iz številnih zanimivih faz. Ti ugotovitvi sta nam spodbuda za nadaljnje iskanje zanimivih magnetnih pojavov na področju nizkodimenzionalnih geometrijsko frustriranih magnetnih materialov, ki vsebujejo nevezne elektronske pare, npr. med $M\text{-T-O-X}$ spojinami ($M = \text{Cu, Ni, Fe, X} = \text{Cl, Br, I, T} = \text{Te, Se, Sb, Bi, Pb}$), saj te pogosto združujejo prisotnost magnetne frustracije in neveznih elektronskih parov.

IZJAVA

Izjavljam, da je ta disertacija plod lastnega znanstveno-raziskovalnega dela.

Ljubljana, 15. 6. 2010

Matej Pregelj